ACTIVE SUPERELASTICITY IN THREE-DIMENSIONAL EPITHELIA OF CONTROLLED SHAPE

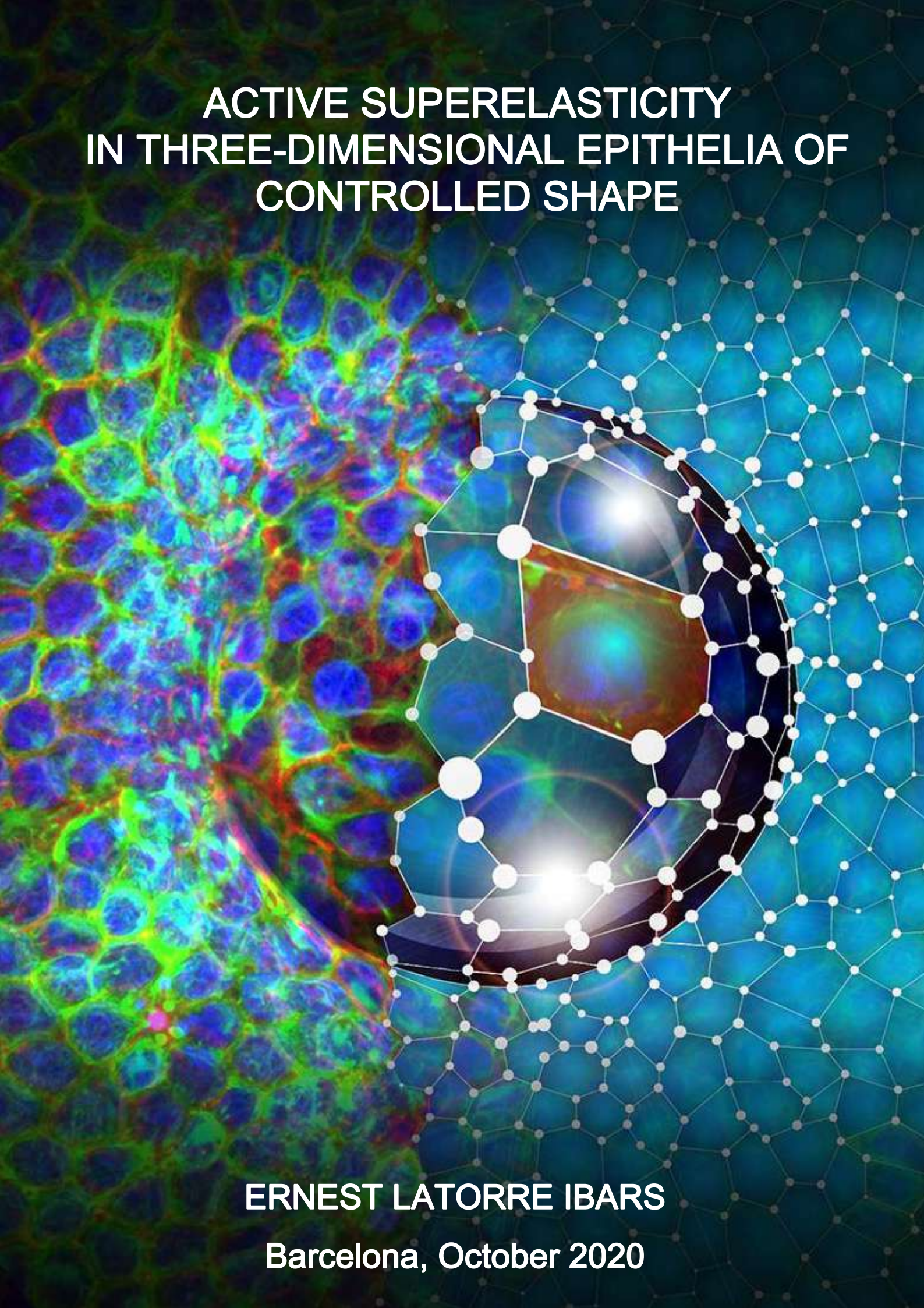

ERNEST LATORRE IBARS

Barcelona, October 2020

PhD program in Applied Mathematics

Active superelasticity in three-dimensional epithelia of controlled shape

DISSERTATION SUBMITED IN PARTIAL FULFILLMENTS OF THE REQUIREMENTS FOR THE DEGREE

DOCTOR OF PHILOSOPHY

Doctoral thesis by:
Ernest Latorre Ibars

Thesis advisors:
Dr. Marino Arroyo Balaguer and Dr. Xavier Trepat Guixer

Department of Civil and Environmental Engineering
Barcelona, October 2020

A l’Anna i als meus pares

ABSTRACT

Fundamental processes in development and physiology are determined by the three-dimensional architecture of epithelial sheets. How these sheets deform and fold into complex structures has remained unclear, however, because their mechanical properties in three-dimensions have not been accessed experimentally. By combining measurements of epithelial tension, shape, and luminal pressure with mathematical modeling, here we show that epithelial cell sheets are active superelastic materials. We develop a new approach to produce massive arrays of epithelial domes with controlled basal shape and size. By measuring 3D deformations of the substrate and curvature of the dome we obtain a direct measurement of luminal pressure and epithelial tension. Observations over time-scales of hours allow us to map the epithelial tension-strain response, revealing a tensional plateau over several-fold areal strain reaching 300%. We show that these extreme nominal strains are accommodated by a highly heterogeneous stretching of individual cells, with barely deformed cells coexisting with others reaching 1000% areal strain, in seeming contradiction with the measured tensional uniformity. This phenomenology is reminiscent of superelasticity, a mechanical response generally attributed to microscopic material instabilities in metal alloys. We provide evidence that this instability is triggered in epithelial cells by a stretch-induced dilution of the actin cortex and rescued by the intermediate filament network. Finally, we implement a mathematical model that captures both the tension/strain relationship and strain heterogeneity. Our study unveils a new type of mechanical behavior -active superelasticity- that enables epithelial sheets to sustain extreme stretching under constant tension.

ACKNOWLEDGMENTS

I would like to start by expressing my deepest gratitude to my PhD advisors, Marino Arroyo and Xavier Trepat. You have been a constant support, a source of inspiration and a true example of people that fight and work hard for what they actually love which I dare to say that, in your case, is discovering and learning new things. I am very proud of having worked together with both of you in this fascinating project. You will always be a reference for me.

I would like to thank all the members of the Trepat and the Roca-Cusachs groups at IBEC. You are a big family and I am already missing you a lot. In particular, I will start thanking Laura Casares who introduced me in the lab and who trained me experimentally to follow up the project that she started and that today crystalizes in this thesis. Thanks to Léo Valon for contributing to this project and for being a guidance when I started.

Thank you, Manu, for being the best mate ever. We have made a very good team during these years and I am sure that in a way or another we will continue collaborating together. Thank you, Carlos. We had the chance to travel a lot making fun and enjoying many moments. You have been my reference biologist and I consider you a friend. Special thanks also to Natalia who brightened every day at the lab and helped me in anything I asked or needed. Thank you Ariadna, Nimesh and Tom for following up the project, working with domes. I will also like to thank Raimon from whom I learned many things on how to analyze data and with who I shared many of my personal views. And being non-exhaustive, many thanks to Macià, Juanfra, Sabrina, Marina U., Pilar, Anna, Sefora, Dobryna, Leone, Anabel-Lise, Victor, Roger, Alberto, Marc, Ignasi, Gerardo, Marija, Oriol, Xarxa, Jenny, Ion, Laura, Marina P and Pere.

I would also like to give special thanks to the members of the Arroyo team, starting by Alejandro who was always there to help me in the coding parts and also to debate about life. Thank you Sohan for your great contribution to this work. And thanks to the rest of the team: Nikhil, Caterina, Jordi, Adam, Waleed, Dimitri, Guillermo, Francesco and Chiara.

I would like to thank all my friends for making everything easy and my life funnier: David, Carles, Àlex, Òscar, Sebastià C., Sebastià M. and Simó.

A big thank to my family for their unconditional support and because they taught me the important things in life: to my parents Ana and Ernest and to my brother Andreu and my sister Rosa. Also, thanks to all my grandparents that have contributed to build the person

who I am now. A big thank to Rosa Mari, my mother in-law that is for me as a second mother.
My biggest gratitude goes to my wife, Anna, who is the person that has supported me the most during all this time. Thank you, I love you.
Finally, I would like to thank the funding that I have received during my PhD, coming from the Generalitat de Catalunya AGAUR (2017-FI-B1-00068) and from the European Research Council (Consolidator Grant 616480 and Consolidator Grant 681434).

CONTENTS

LIST OF FIGURES

1 INTRODUCTION

1.1 Introduction to mechanobiology

Mechanics is the branch of science that studies how bodies react to physical forces and deformations. Mechanics can nowadays be widely applied to accurately model many physical phenomena and to solve engineering problems.

Many biological processes involve shape changes (deformation). We can find representative examples during morphogenesis or when performing routinely breathing, heart beating or peristaltic movements in mammals. Those deformations **are ultimately caused by forces of active origin and thus are also governed by mechanics**. This fact has been acknowledged by authors such as D'Arcy Thompson in his famous 'On growth and form'[1], where the author claimed that physical laws and more specifically mechanics is at the core of morphogenesis. Following this idea, he stated that the shape, the size and the physiology of many biological structures may be largely determined by forces. In the seminal paper[2], Turing focused on chemical patterning but was aware of the role of mechanics when asserting that *"[...]the description of the state consists of two parts, the mechanical and the chemical. The mechanical part of the state describes the positions, masses, velocities and elastic properties of the cells, and the forces between them. In the continuous form of the theory essentially the same information is given in the form of the stress, velocity, density and elasticity of the matter."*. However, with the emergence of molecular biology and the various omics, the role of mechanics in biology has been largely overlooked. Reviving the role of mechanics in biology, the multidisciplinary field of mechanobiology **has emerged in recent years. It applies mechanics and physics to biology and tries to unveil how forces, deformations and movement are determinant in biological processes such as development, cell differentiation, physiology or disease**.

Mechanobiology applies at several scales, ranging from complete organisms and full organs such as the lungs, the heart or the guts to the smaller cellular scales as in epithelial tissues that line the internal cavities of the body. Mechanobiology also covers even smaller subcellular scales, for instance understanding the mechanical determinants of the

organelle morphogenesis and physiology. At the cellular scale, we have overwhelming evidence that cells are able to sense changes of their mechanical micro-environment and to detect mechanical cues (**mechanosensing**) and that they are able to respond to these cues by different means such as initiating biochemical cascades (**mechanotransduction**). Moreover, it is known that this response to mechanical signals is a dynamical process and that there is a crosstalk between mechanics and the involved biochemical pathways[3, 4]. It has been showed that cell fate (cell differentiation) is affected by mechanical cues as the stiffness of the extra cellular matrix (ECM)[5]. Gene expression can also be mechano-regulated by the nuclear translocation of some transcriptional factors such as YAP/TAZ mediated by the mechanical coupling of the cell cytoskeleton and the nucleus[6]. At the tissue scale, there are several collective migration modes that are governed by the forces that cells exert onto their ECM and by the stresses that are transmitted between neighboring cells[7] such as collective durotaxis (cells are guided by the stiffness gradient of the ECM)[8] or plithotaxis (cells are guided by the direction of maximal principal stress)[9]. Mechanics is also crucial for wound healing[10] or in morphogenesis where pressure and physical forces can drive the creation of new structures such as in the lung development[11]. Tissue homeostasis is, in general, governed by physical forces and stress by directly regulating mitosis[12], by an increased cell division rate at high levels of tension or high levels of stretch[13], by the induction of cell extrusion for crowded monolayers that have lower levels of stress[13, 14] and by the topological rearrangement of cells[15].

1.2 Epithelial tissues and epithelial architecture

Epithelial tissues are ensembles of cells with a very well-defined architecture that line internal organs and cavities of animal bodies and perform many biological functions. In terms of shape, epithelial cells can be squamous, cuboidal or columnar. These cells are always tightly packed forming a continuous layer with almost no intercellular spaces. Epithelia can be organized as a single layer (monolayer) of cells or a multilayered structure. They are barriers against pathogens, and they participate in many processes as wound healing, sensing, absorption, secretion, transport or morphogenesis[16].

Epithelia are most often attached to an extracellular matrix (ECM), which is soft, fluid filled and made of fibrous proteins such as fibronectin, collagen or laminin. Epithelia are

innervated and not vascularized, and thus cells must obtain oxygen and metabolites through diffusion from the ECM or from the surrounding medium. Both individual epithelial cells and the epithelium are polarized. The basal side, which is the one adhering to the ECM is structurally different from the apical side, which is facing the bathing medium. Epithelial cells exhibit strong junctions between them, which are crucial for epithelial mechanics because they mediate the transmission of physical forces and stresses from cell to cell and from cell to the ECM[16].

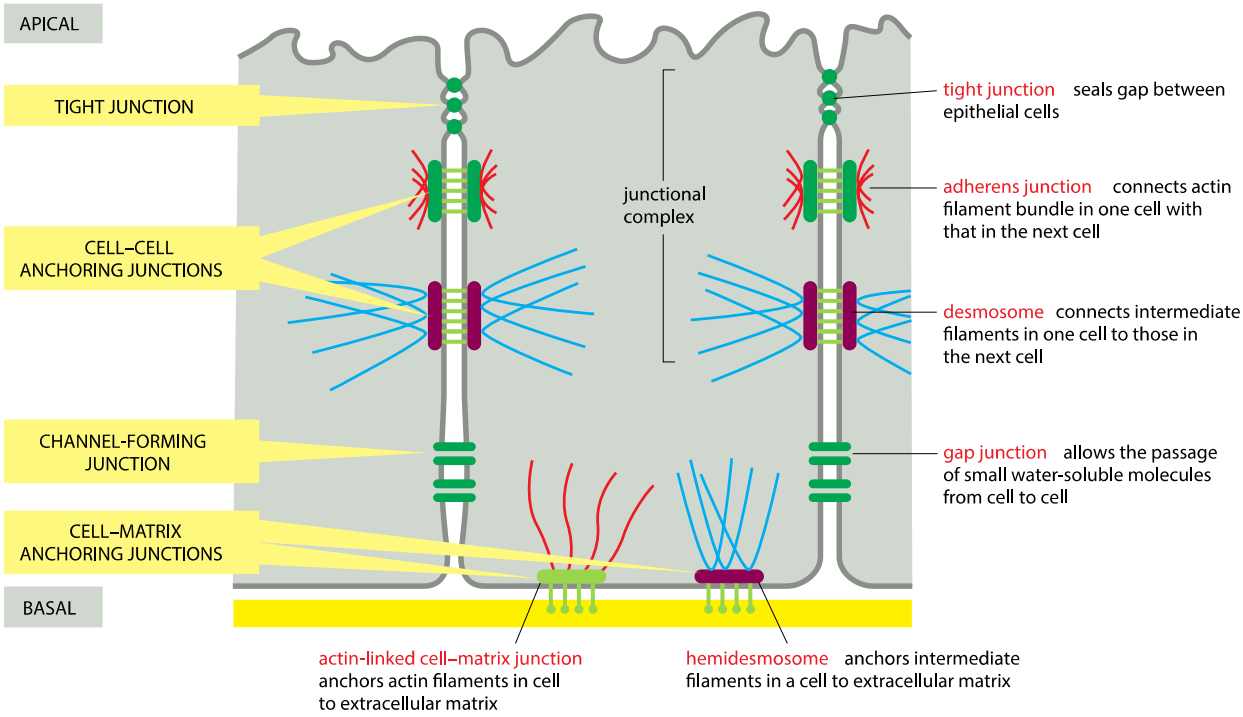

Figure 1: ***Cell junctions of epithelial cells.*** *Summary of the cell junctions (including cell-cell and cell-matrix junctions) found in a vertebrate epithelial cell. They are classified according to its main function. The polarity of the cells, and the tissue, seen by the differences between the apical and the basal side is also shown. Adapted from [16].*

Cell-cell and cell-matrix junctions can be summarized in three groups depending on their function, having also different molecular basis[16], (Figure 1):

- **tight junctions** (TJ, Figure 2), also called occluding junctions, seal the interface between cells and make of the epithelium an impermeable layer. They separate the basolateral compartment and the apical side that faces the medium. The proteins involved are claudins, occludins and tricellulin, together with the organizational proteins of the *zonula occludens* (ZO-1, ZO-2 and ZO-3 among others).

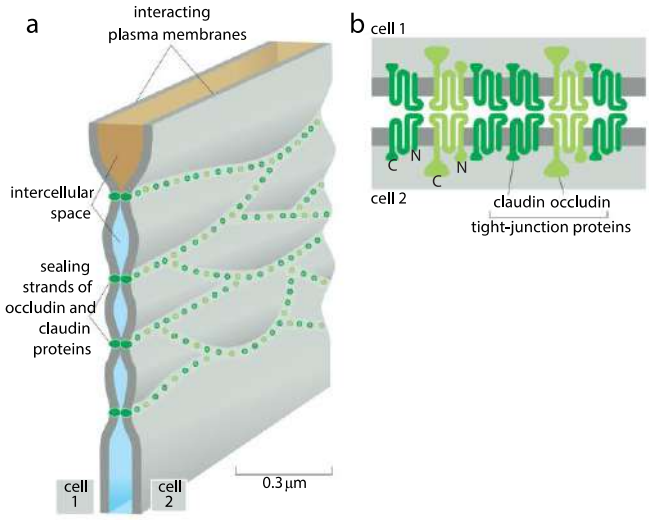

Figure 2: ***Tight junction. a****, Schematic view of a tight junction between two neighboring cells. The sealing strands ensure the impermeability of the junction.* ***b****, Molecular representation of the claudin and occludin interaction at the sealing strand of a tight junction. Adapted from [16].*

- **gap junctions** (GJ, Figure 3), also called communicative junctions, create a channel between two adjacent cells and connect the cytoplasm of both cells to enable the exchange of molecules. In vertebrates, the gap is made by the channel-forming protein family connexins (innexins for the gap junctions of the invertebrates).

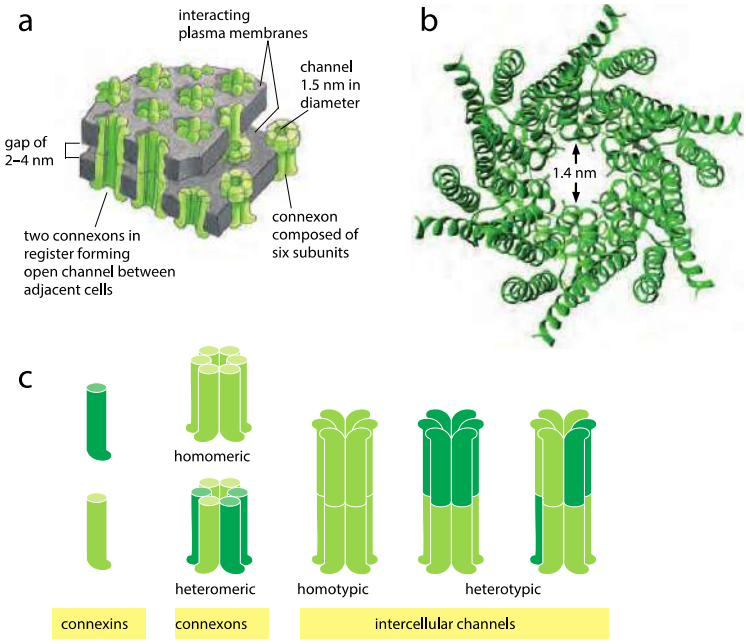

Figure 3: ***Gap junction. a****, Picture of a gap junction connecting the plasma membrane of two adjacent cells.* ***b****, Structure of the homomeric connexon of an intercellular channel.* ***c****, Connexins organize to form connexons that will form the intercellular channels. Adapted from [16].*

- **anchoring junctions,**

  that include adherens junctions (AJ, Figure 4) and desmosomes (Figure 5), transmit physical forces and stresses between the cytoskeleton of neighboring cells. Adherens junctions link actin filaments of adjacent cells through classical cadherins and its adaptor proteins (alpha-catenin, beta-catenin, plakoglobin, p120-catenin and vinculin). Adherens junctions are known to be mechanosensitive and

a site where mechanotransduction takes place. Alpha-catenin unfolds when it is under tension and it exposes a cryptic binding site for vinculin, enabling the binding of more actin filaments to the junction and thus promoting the strengthening of the junction.

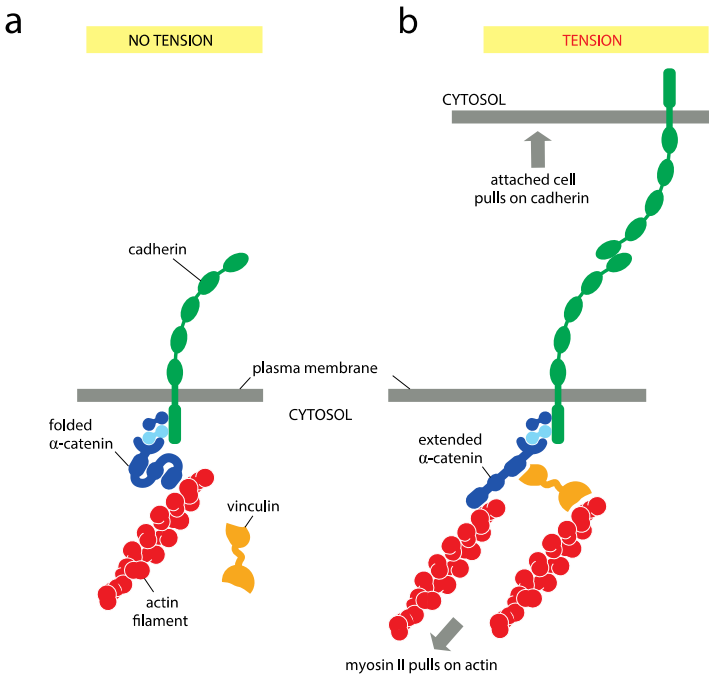

Figure 4: ***Anchoring junction is a site of mechanotransduction. a,*** *Actin filaments are bound to the cadherins through the adaptor proteins (alpha-catenin, beta-catenin and p120-catenin. Without tension, alpha-catenin is folded.* ***b,*** *When the attached cell pulls, the junction is under tension and alpha-catenin unfolds, exposing a cryptic binding site for vinculin, promoting actin recruitment and thus the strengthening of the junction. Adapted from [16].*

Desmosomes (Figure 5) link intermediate filaments of two adjacent cells through nonclassical cadherins as desmoglein and desmocollin and its adaptor proteins (plakoglobin, plakophilin and desmoplakin).

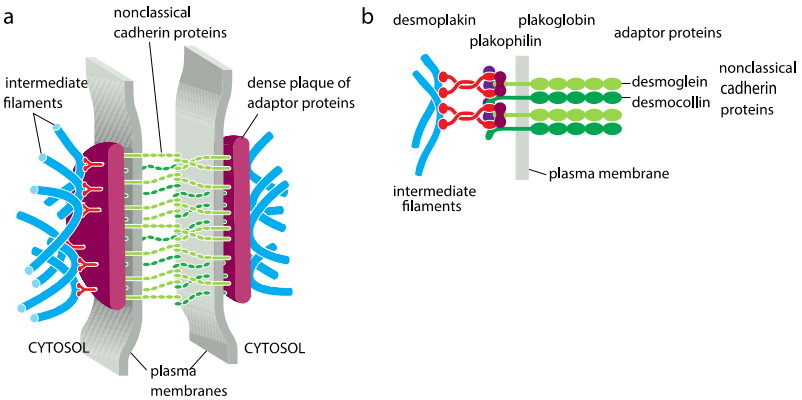

Figure 5: ***Desmosome. a****, General scheme of a desmosome.* ***b****, Molecular structure of the desmosome. Desmoglein and desmocollin are the nonclassical cadherins that link adjacent cells in desmosomes. The intermediate filaments are bound to the adaptor proteins (desmoplakin, plakophilin and plakoglobin). Adapted from [16].*

Cell-matrix junctions are also considered anchoring junctions and include the actin-linked cell-matrix junctions (Figure 6), which link the actin cytoskeleton to the ECM through integrins and their adaptor proteins (talin, kindlin, vinculin, paxillin, and focal adhesion kinase among others). When these junctions are stable, durable and large they are called **focal adhesions**. It is known that

mechanotransduction takes place in this kind of junctions when, under tension, talin unfolds, exhibiting a cryptic binding site for vinculin and promoting the growth of the focal adhesion, resulting in a junction strengthening (reinforcement)[17].

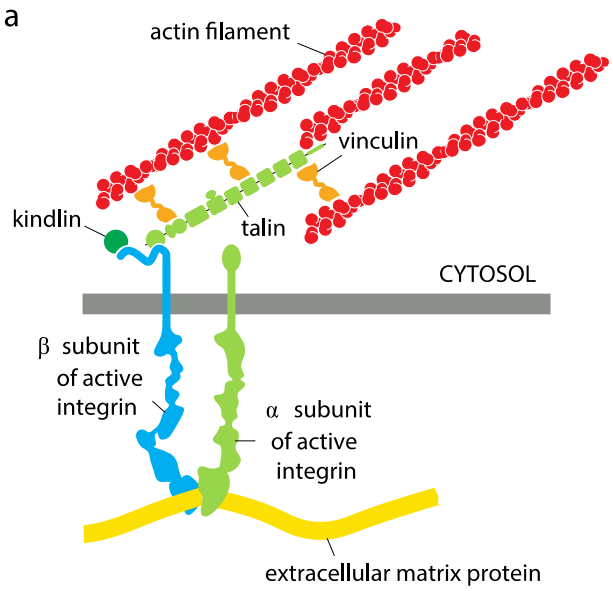

Figure 6: ***Actin-linked cell-matrix junction.*** ***a****, Actin filaments are linked to the ECM fibers through integrin proteins by the adaptor proteins talin, vinculin and kindlin among others. This junction is also a site of mechanotransduction, and it takes place when, under tension, talin unfolds, exhibiting a cryptic binding site for vinculin and promoting the growth of the junction complex. Adapted from [16].*

Hemidesmosomes (Figure 7) are the cell-matrix junctions, which link the intermediate filaments to the collagen type XVII of the ECM through alpha6-beta4-intengrins and with the adaptor proteins (plectin and BP230).

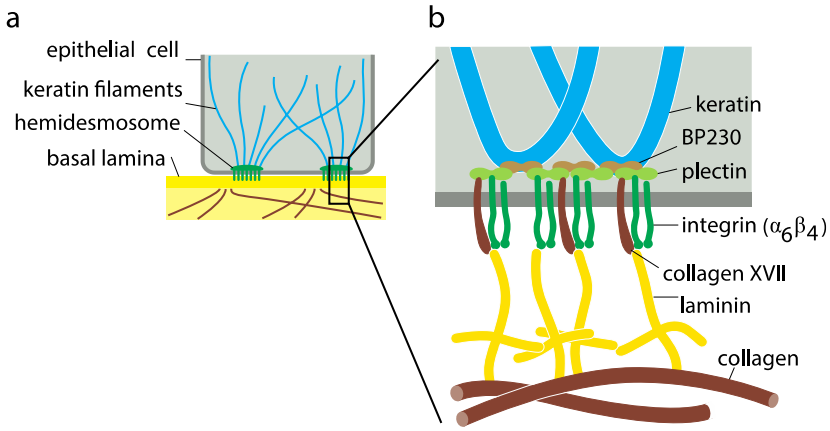

Figure 7: ***Hemidesmosome.*** ***a****, Intermediate filaments (keratin filaments) in epithelial cells are linked to the collagen XVII fibers of the ECM through hemidesmosomes.* ***b****, Molecular structure of an hemidesmosome. The keratin bundles are bound to the integrin alpha6-beta4 via adaptor proteins BP230 and plectin. Adapted from [16].*

1.3 Structure of the thesis

This thesis is structured in the following main chapters:

- In the second chapter we define the **general and specific aims of the thesis**.
- The third chapter is an **introduction to epithelial mechanics** and a **review of the different existing techniques to measure active mechanical stress in living tissues**. This work has been published:
    - Gómez-González M.*, **Latorre E.***, Arroyo M. and Trepat X. Measuring mechanical stress in living tissues. *Nature Reviews Physics* **2**, 300-317, doi:10.1038/s42254-020-0184-6 (2020). *co-first authors.
- In the fourth chapter we present a newly developed technique to **measure stress in curved epithelia that are forming 3D domes**. It represents a novel approach to obtain, under certain assumptions, a stress in the cell monolayer just from mechanical equilibrium without assuming any constitutive behavior for the epithelium.
- In the fifth chapter, we develop a simple mathematical model for the **dome's hydraulic transport** across the epithelium, which we use to quantify transepithelial permeability, osmotic pumping rate and the absolute osmolarity of dome's internal medium from measurements in the epithelial domes setup.
- Finally, in the sixth chapter we apply dome's experimental setup as a material bulge test to measure the epithelial stress at different strains and thus to investigate the constitutive behavior of the epithelial living tissue as we would do for an engineering material. Combining observations of tissue and cellular shape, luminal pressure and cytoskeletal dynamics, a new 3D vertex model accounting for all these features, and various perturbations of the system, we identify unexpected features such as their ability to sustain extreme deformations at a constant tension in a reversible manner. We termed this new mechanical behavior **active superelasticity** in analogy to superelasticity, which is a behavior known for some metal alloys.

The results of chapters 4, 5 and 6 have been published in the following article:

- **Latorre, E.**, Kale, S., Casares, L., Gómez-González, M., Uroz, M., Valon, L., Nair, R.V., Garreta, E., Montserrat, N., del Campo, A., Ladoux, B., Arroyo, M., Trepat, X. Active superelasticity in three-dimensional epithelia of controlled shape. *Nature* **563**, 203-208, doi:10.1038/s41586-018-0671-4 (2018)

2 GENERAL AND SPECIFIC AIMS OF THE THESIS

2.1 General aim

The general aim is **to study the mechanics of three-dimensional epithelia of controlled size and shape.**

2.2 Specific aims

1. To review the state-of-the art of stress measuring techniques in living tissues.
2. To develop a new technology to measure tractions, pressure and tension in epithelial tissues of controlled size and shape in three dimensions.
    a. To implement a new experimental approach by using microcontact printing over soft polydimethylsiloxane (PDMS) gels to induce the formation of blister-like epithelial structures (here after called domes).
    b. To measure dome mechanics by combining Traction Force Microscopy (TFM) and the equilibrium equation for a thin axisymmetric membrane under uniform pressure.
    c. To verify that dome tension is perturbed by pharmacological alterations of the cytoskeleton.
3. To study epithelial hydraulics at the origin of dome formation.
    a. To theoretically model dome swelling and de-swelling based on an active ionic pumping and water permeation mechanisms.
    b. To experimentally measure epithelial permeability and ionic pumping rate from volume dynamics under controlled osmotic shocks.
4. To investigate epithelial rheology of curved three-dimensional cell monolayers.
    a. To obtain experimental stress-strain relations for epithelial domes.
    b. To develop and implement a computational vertex model of the domes in 3D.
    c. To study the analogy between constitutive relations of epithelial layers and those of known materials.
    d. To test experimentally some features of the found material behavior.

3 INTRODUCTION TO EPITHELIAL MECHANICS AND STRESS MEASUREMENT IN LIVING TISSUES

3.1 Epithelial mechanics

3.1.1 Mechanics of epithelial cells

Individual cell mechanics collectively determine epithelial mechanics. Cell-cell and cell-matrix junctions (see section 1.2) transmit physical forces and stresses between adjacent cells and between cells and the extra-cellular matrix (ECM). In turn, cell mechanics emerges essentially from the active forces generated in the cell cytoskeleton, mainly at the cell cortex, and it depends on their properties and architecture. Adhesion forces between cells are also determinant for epithelial mechanics.

3.1.1.1 The cytoskeleton and the cell cortex

The cytoskeleton is a filamentous structure that confers stiffness and mechanical stability to the cell. It is made of polymerized proteins belonging to three different families: **actin filaments** (microfilaments), **microtubules** and **intermediate filaments**. Despite the fact that these three families of proteins have different mechanical properties, distinct dynamics and different biological functions, they all work together in a collective way to shape the cell, to permit locomotion, to confer stiffness and strength and to spatially organize the organelles in the cytoplasm.

Apart from the mentioned proteins, there are many other accessory proteins that are bound to the filaments and participate in the cytoskeleton regulation, into the linkage between filaments and between the filaments and other cell elements. They include the **motor proteins**, as myosin, that are bound to actin and that can contract upon converting the chemical energy, coming from ATP hydrolysis, to mechanical energy. They are responsible of exerting **active physical forces**. We call those forces 'active' because they need a spent of energy to be exerted. Actin filaments are, together with myosin motors, the most important family of proteins for cell mechanics, forming a contractile system that is sometimes called **actomyosin**. Microtubules are responsible of organizing the organelles. They coordinate intracellular transport and form the mitotic spindle. Intermediate filaments line the inner face of the nuclear envelope, protecting the DNA.

They are forming bundles in the cytosol that are believed to participate into cell mechanics in a passive way, behaving as cables.

For animal cells (in fact, for most eukaryotic cells without cell wall), the **cell cortex** is the most relevant element of the cytoskeleton for cell mechanics. As depicted in Figure 8, the cell cortex is a thin quasi-two-dimensional layer adjacent to the plasma membrane (around 200nm thick). It is a gel composed of actin filaments, myosin motor proteins and actin binding proteins that crosslink the network that is highly dynamic. The cortex undergoes constant turnover of constituent proteins and crosslinkers, and it is capable of being remodeled in seconds. The cortex is also responsible of creating and maintaining polarity for epithelial cells, making differences between the apical and the basolateral sides of the cell.

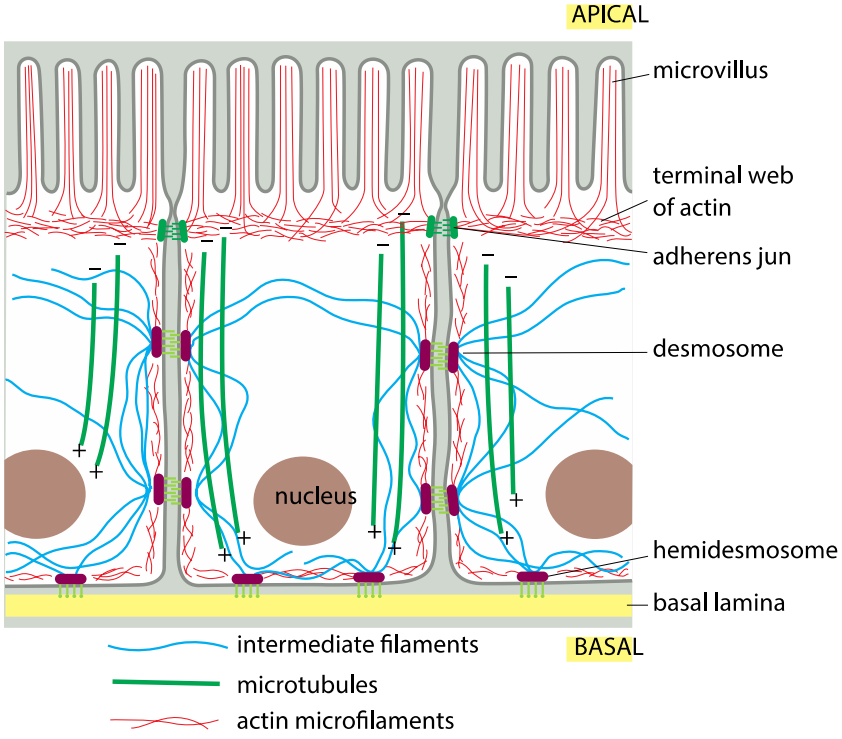

Figure 8: ***Cytoskeleton of epithelial cells.*** *The cytoskeleton includes the intermediate filaments, the microtubules and the microfilaments (actin). The cortex is composed by the actin filaments that underlie the plasma membrane. The cortex confers mechanical stability, transmits and exerts the forces through the molecular motors (myosin) and determines and maintain the epithelial cell polarity. Adapted from [16].*

Actin exists in two different states: G-actin, which is the monomeric actin that is free in the cytoplasm, and F-actin, which is the polymerized actin, also called filamentous actin. **Actin filaments (F-actin) exhibit structural polarity**, having two different ends called **plus** (also called **barbed end** it is the end where polymerization dominates over disassembly) and **minus end** (also called **pointed end**, where disassembly mostly takes

place), (Figure 8). F-actin polymerization is primarily done by adding ATP-linked G-actin to the plus end of the filament. After adding the subunit to the barbed end, the ATP hydrolyzes to ADP, resulting in ADP-F-actin and the elongation of the filament. 'Old' ADP-F-actin is disassembled by depolymerization and by severing, transforming F-actin to the monomeric G-actin[18]. F-actin is structured in two different networks depending on which actin-nucleator (also called actin assembly factor) is formed by:
On the one hand, the **actin-related protein 2/3 (ARP2/3) complex** induces the formation of dense branched networks that are necessary to generate active forces that deform the plasma membrane as in protrusion during cell locomotion or during endocytosis. On the other hand, **formins and Ena/VASP (Enabled/vasodilator-stimulated phosphoprotein)-homology proteins** promote the creation of linear filaments of F-actin which associate in bundles that form the cytokinetic ring, filopodia, actin cables or stress fibers (Figure 9).

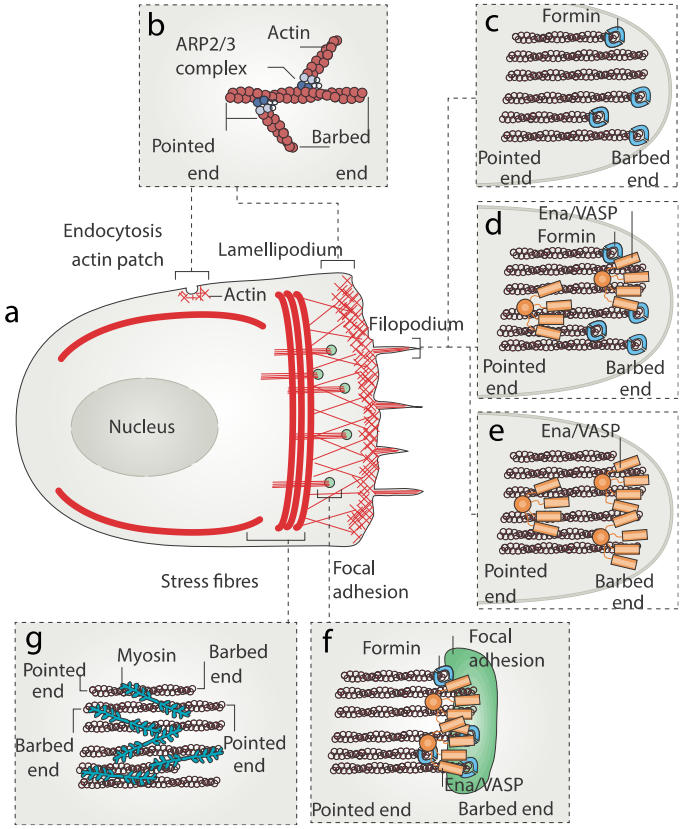

Figure 9: ***F-actin can be polymerized in two different architectures: branched (induced by ARP2/3 complex) or linear (induced by formins or Ena/VASP).*** ***a****, Mammalian cell exhibiting two different F-actin architectures.* ***b****, The ARP2/3 complex promotes a branched actin network that participates in the endocytic actin patch and is also present in the lamellipodia.* ***c****,* ***d****,* ***e****,* ***f****,* ***g****, Formins and Ena/VASP induce the formation of linear F-actin that forms the filopodia (**c-e**), the focal adhesions (**f**) and the stress fibers (**g**). Adapted from [18].*

The size and the architecture of the F-actin network is crucial to correctly develop its biological function at every side of the cell. Moreover, these are dynamic structures that are continuously being polymerized and depolymerized, so the temporal control of the size, distribution and balance between the two different architectures is also determinant for its proper function. This network turnover is controlled by the Actin Binding Proteins

(ABPs) and by signaling pathways that are very complex and that convert external or internal stimuli in the activation or inhibition of the actin assembly factors (ARP2/3 complex and formins or Ena/VASP). In the classical view of actin dynamics, the signaling pathways include three main RHO GTPases (RAC1, CDC42 and RHOA) that are able to activate or inhibit the actin assembly factors. For example, most formins are autoinhibited and the RHOA GTPase is able to release the autoinhibition (Figure 10a), promoting the polymerization of linear formin-mediated F-actin (Figure 10b). In case of CDC42, it is able to release the autoinhibition of the Wiskott-Aldrich syndrome protein (WASP) that in turn activates the ARP2/3 complex (Figure 10c), inducing the polymerization of branched actin networks (Figure 10d). The stability of the G-actin pool is maintained by profilin and thymosin beta4 that prevent them to be polymerized. The disassembly is done by severing or by depolymerization and it is mediated by many Actin Binding Proteins (ABPs) such as cofilin/ADF (actin depolymerization family) among others (Figure 10e).

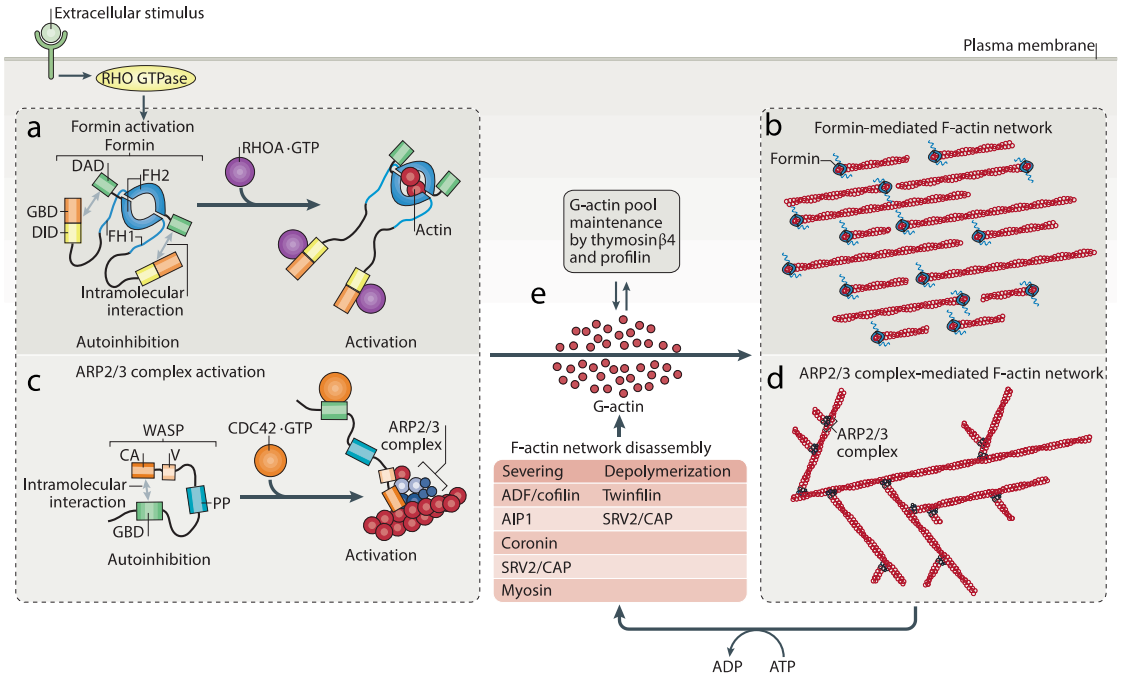

Figure 10: ***Classical view of actin turnover. a****, RHOA (a RHO GTPase) is able to release the autoinhibition of formin (FH: formin homology; DAD: diaphanous autoregulatory domain; DID: DAD-interacting domain; GBD: GTPase-binding domain).* ***b****, Releasing of formin autoinhibition promotes the formation of linear F-actin.* ***c****, CDC42 (a RHO GTPase) is able to release the autoinhibition of the Wiskott-Aldrich syndrome protein (WASP) that in turn promotes the activation of the ARP2/3 complex. (CA: acidic domain, V: WH2 domain, PP: polyproline domain).* ***d****, Branched actin network is formed when the ARP2/3 complex is activated through WASP.* ***e****, Profilin and thymosin beta4 stabilize and maintain the pool of monomeric G-actin. Both linear F-actin and branched networks are disassembled by severing or depolymerization mediated by several Actin Binding Proteins (ADF: actin depolymerization proteins, AIP1: actin interacting protein 1, CAP-SRV2: adenylyl cyclase associated protein). Adapted from [18].*

The role of signaling pathways is much more complicated than described here because there can be intricated crosstalk between the different pathways [18].

Recent studies[18] add more complexity to the actin turnover by taking into account the **finite amount of the G-actin pool** (Figure 11f), introducing an **internetwork competition for the monomeric actin** (Figure 11). The F-actin homeostasis depends then on the signaling pathways that are activated upon internal or external stimuli but it also depends on other factors such as the equilibrium between the G-actin that is sequestered and prevented to polymerize (Figure 11e), the G-actin that becomes linear F-actin mediated by formin, Figure 11a, (or Ena/VASP; Figure 11d) competing with the G-actin that becomes ARP2/3 complex mediated branched F-actin (Figure 11b). The homeostasis is also dependent on the stabilization of F-actin through actin binding proteins such as myosin at stress fibers (Figure 11c). The **disassembly is also crucial for actin homeostasis because it replenishes the G-actin pool**.

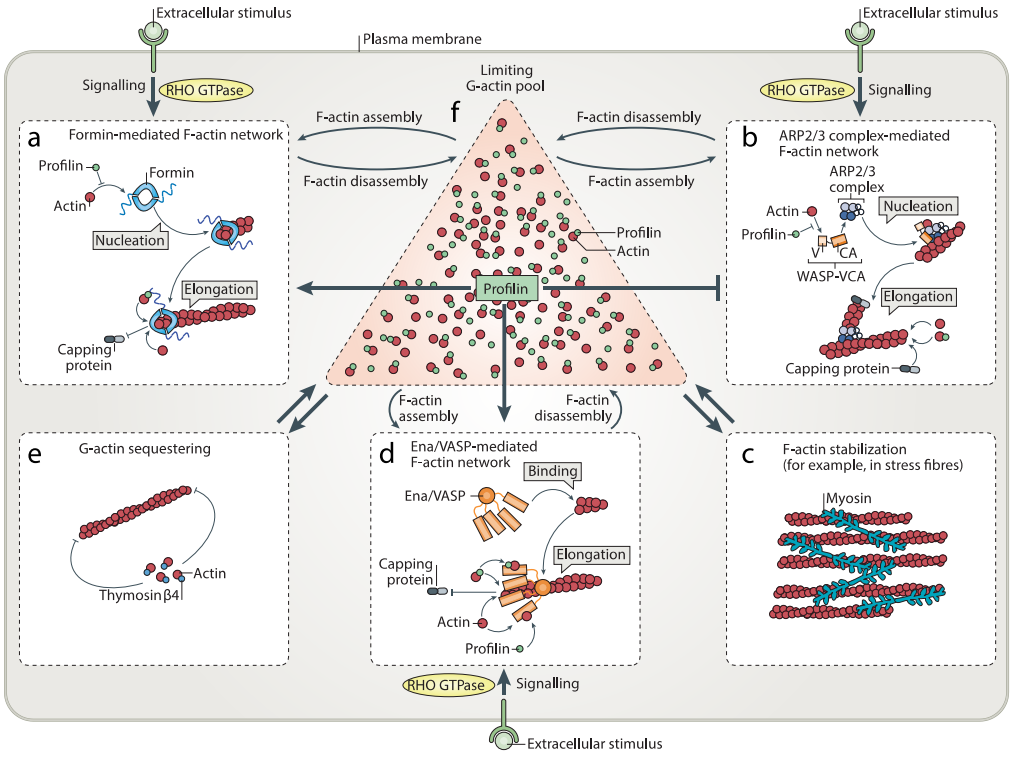

Figure 11: ***Updated actin turnover model including finite G-actin pool and internetwork competition to achieve F-actin homeostasis. a****, Signaling pathways involving RHO GTPases induce the formation of formin-mediated F-actin network.* ***b****, ARP2/3 complex mediated F-actin is formed upon signaling coming from RHO GTPases.* ***c****, F-actin is stabilized via actin binding proteins such as myosin in stress fibers.* ***d****, Ena/VASP mediated F-actin is formed upon signaling coming from RHO GTPases.* ***e****, Thymosin beta4 is able to sequester monomeric G-actin and prevent it from polymerization.* ***f****, There is a limiting monomeric G-actin pool that is controlled by profilin that establishes a competition and exists in equilibrium between the assembly and disassembly of the different networks of actin described in (**a**), (**b**) and (**d**). It also competes with the thymosin sequestered G-actin (**e**) and the fraction of F-actin of the different networks that is stabilized (**c**). Adapted from [18].*

3.1.1.2 Cell surface tension

As explained in the previous section, the cell cortex is the main determinant of cell mechanics. The **cell cortex is under tension**, called cortical tension, as a result of the active contractile physical forces that are exerted by myosin motor proteins.

The resultant mechanical stress and tension at the cell surface, called **cell surface tension**, defined as the **force per unit length acting on a cross-section of the cell surface**, will be largely determined by the cortical tension. To generate active forces, myosin motors are able to pull actin filaments by the hydrolysis of ATP. Active generated forces at the cortex have been found to be thermodynamically out of equilibrium, violating the Fluctuation-Dissipation theorem and thus coming from a truly active consumption of energy produced by myosin motors and recapitulated in vitro[19]. It is believed that **myosin-II** isoforms are the responsible of generating the majority of active forces but there are more proteins from the myosin superfamily that are also able to generate active forces[20]. Some studies show that actin dynamics can also generate forces in a myosin-independent manner by combining polymerization and depolymerization of the actin network with the attachment of barbed-end tracking proteins[20]. Moreover, the balance between the different actin network architectures also controls the cortical tension as shown in [21].

The cortical tension is believed to act against the hydrostatic pressure existing in the cell cytoplasm, equilibrating it for cells that are in isolation and explaining the spherical shape that cells adopt in suspension (Figure 12a). This hydrostatic pressure is the difference between the internal pressure of the cell cytoplasm and the pressure of the external medium and it is osmotically controlled by the cell by ionic transport[22].

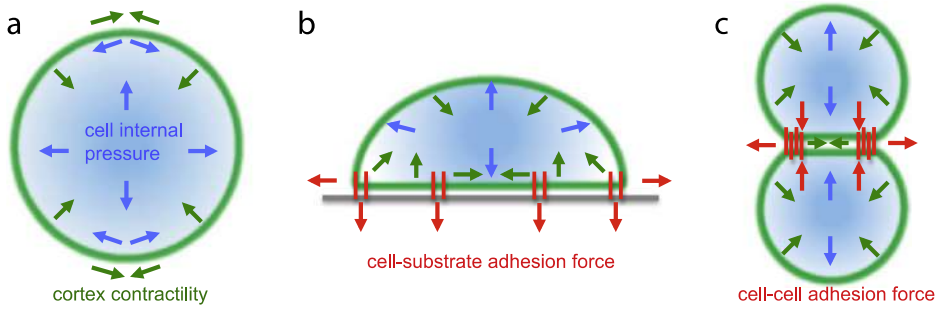

*Figure 12: **Active cortical tension balances internal hydrostatic pressure. a**, In isolated cells in suspension, the outward expansion forces comes from the hydrostatic pressure. They are equilibrated by the contractile forces acting actively at the cell cortex. **b**, For isolated but attached cells, the cell-substrate adhesion forces add forces that reduce the effective surface tension at the substrate contact, increasing the substrate interface and producing cell spreading on the surface. **c**, For a doublet of cells, there is a similar effect as in (**b**), lowering the effective surface tension at the contact zone and increasing the cell-cell contact area. Adapted from [23].*

For cells that are attached to a substrate (Figure 12b) or in doublets (Figure 12c), the adhesion forces lower the effective surface tension, giving rise to an increase of the contact area and therefore inducing cell spreading on the substrate or an increase of the cell-cell contact area in a doublet.

Single cell mechanics is then the resultant of the balance between hydrostatic pressure difference, cortical tension and adhesive forces and because of this, it has been modeled as the capillary behavior of soap bubbles that also equilibrate the hydrostatic pressure difference with surface tension, relating the curvature, the difference in pressure and the surface tension via Laplace's law (see Force inference section at 3.2.4.5). Surface tension is, for soap bubbles, a **passive** force per unit length that comes from the physics of the surfactants and that is the result of the molecular interactions at the interface. It is a constant parameter at a fixed temperature and pressure. As for soap bubbles, the contractile tension of the cortex may generate an apparent elastic response upon cell (or bubble) indentation that is independent of intrinsic elasticity that the cortex may exhibit at short time-scales. This apparent elastic behavior upon indentation is the result of increasing the surface area of the cell (bubble) at nearly fixed volume, hence mechanically working against surface tension. It is used sometimes to characterizes changes in the cortex mechanical properties via atomic force microscopy (AFM) indentation. In turn, for cells, it is a global cellular parameter that could depend on cortical tension, cell geometry among other parameters [20].

There are other mechanical elements that may influence epithelial cell mechanics as the passive intermediate filaments, the poromechanical properties of the cytoplasm, the mechanical properties of the nucleus and the plasma membrane tension.

The mechanical variables that play a role in cell mechanics are known: **cortical tension, hydrostatic pressure and adhesive forces.** Despite this fact, the big challenge is that the three of them can be actively tuned in a very complex, coupled and not completely understood manner. Regarding cortical tension, there are several signaling pathways that can alter or affect myosin activity (among other motor proteins). Cortical tension can also be modulated by a remodeling of the actin cortex during biological processes such as cell division or locomotion or a change of its architecture. Hydrostatic pressure is in turn coupled to the osmotic pressure difference between the cytoplasm and the external medium. It can be tuned by ion pumping or transport across the plasma membrane in response of many external stimuli. Finally, adhesion forces depend on cell-cell and cell-matrix junctions and in all the protein complexes that form them.

To sum up, these three mechanical variables coarse grain all these processes in values that can be experimentally assessed by different techniques (section 3.2) and that are related between them and to the geometry of the cell. The active nature of living cells makes that, in contrary to what happens to passive surfactants as soap bubbles, the surface tension value is not constant and can change, even locally, to adapt the cell to perform the necessary biological processes. The same happens to adhesive forces or to hydrostatic pressure.

3.1.2 Mechanics of epithelial tissues

Epithelial tissues are sets of epithelial cells as explained in 1.2. Its mechanics emerge from the mechanics of single cells, taking into account that within a tissue, cells are able to transmit physical forces to neighboring cells (via cell-cell anchoring junctions, section 1.2) and they can also transmit forces to the extracellular matrix (via cell-matrix junctions, section 1.2). Because of the adhesion forces when cells are in contact, its surface tension is lowered at the cell-cell interface as in Figure 12c. When, instead of a cell doublet, we have a tissue with many cells, the result is that they describe shapes which are close to a network of polyhedra (Figure 13).

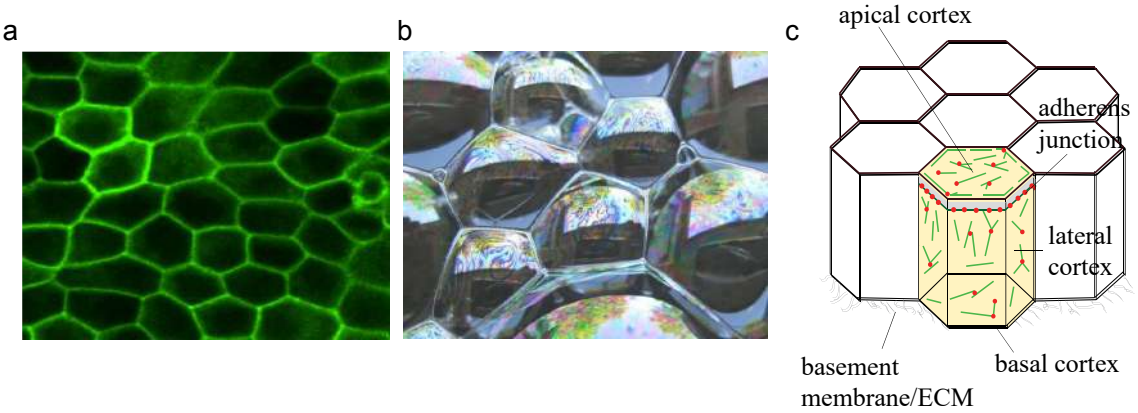

Figure 13: ***Epithelial tissues are made of polyhedral-like cells and resemble soap bubbles. a****, Apical plane of MDCK CIBN-GFP cells, taken with a spinning disk microscope.* ***b****, Soap bubbles that are in contact, image obtained from: http://www.meteoptix.de/Seife/Soap03.jpg.* ***c****, Epithelial cells within a tissue are idealized as polyhedra. Apical, basal and lateral cortices may define different apical, lateral and basal cortical tensions. Adapted from [24].*

Seen from an apical view, epithelial cells in confluent tissues resemble polygons (Figure 13a). They seem a collection of soap bubbles (Figure 13b) and the way mechanics is described came from the theoretical work done for the soap bubbles.

There were two opposing theories describing how individual cell mechanics scale in a collective fashion to obtain the mechanics of epithelial tissues that is summarized in a coarse-grained manner by a **tissue surface tension (TST)**. The first theory, proposed by Steinberg[25-27] was called **differential adhesion hypothesis (DAH)** and postulated that tissue surface tension comes, in analogy to passive fluids, from adhesive forces between the constituent cells. Cells were treated as point objects and then TST is proportional to the intensity of the adhesion energy between cells (represented experimentally mostly by the E-Cadherin levels at the cell-cell junctions). DAH has been proven successful to explain cell sorting in many tissues[28, 29]. The opposing theory is called **differential interfacial tension hypothesis (DITH)**, also called differential surface contraction hypothesis (DSCH) and proposed by Harris[30] and extended by Brodland[31] including some cohesive interactions (not relevant for TST). It postulates that the origin of tissue surface tension is the actomyosin contraction, relating the tissue surface tension to the individual tension of cell interfaces. The current understanding in the field, suggested by recent studies[32-34], is that both theories are complementary and **adhesion and cortical tension of individual cells are co-regulated and both participate in determining the tissue surface tension**. More precisely, **adhesion forces mechanically couple cortices from adjacent cells and the reduction of surface tension at the interfaces of contact acts as an effective adhesion, permitting the increase of cell-cell contact area.** Adhesive forces, which tend to expand the area of cell-cell junctions, compete then with the actomyosin contractile forces, which tend to reduce the contact area, to give rise to a global tissue surface tension, also called **net tension**.

Epithelia behave as a solid-like material or a fluid-like depending on the timescales and those properties emerge from the fact that the actomyosin cortex is a dynamical network. For small or fast deformations where cortical remodeling cannot happen, epithelia behave as a solid material whereas for longer time-scales both cortical remodeling and also topological rearrangements of the cells can occur, leading to a fluid-like behavior[15].

Vertex models are a mathematical framework used to recapitulate this behavior. They define a discrete set of points, called vertices that have precise coordinates for the polygon-like cells. A vertex model includes:

1. A work function capable of taking into account the differential mechanical work done by a perturbation on the position of the vertices. It includes the contribution coming from surface tension conjugated to surface area changes, the pressure that

is conjugated to cell volume changes and the line tension that can exist in actin belts conjugated to its change of length.

2. An evolution principle for the vertices, normally introducing the instantaneous minimization of the work function between topological rearrangements.
3. Rules to resolve topological reconfiguration of the vertices.

A more detailed formulation of vertex models is presented in section 3.2.4.5.

Vertex models have been proven successful to qualitatively assess epithelial mechanics[24] but, as in epithelia there are many coupled biological pathways including actomyosin contractility and actin network dynamics[18, 20, 21], adhesion remodeling[35], osmotic regulation of cell volume[22], mechanosensing at different places[13] and junctions (cell-cell[16] and cell-matrix[17]) a **quantitative understanding of epithelial rheology and mechanical behavior is still missing**.

3.2 Measuring active mechanical stress in living tissues

Adherent animal cells are able to generate mechanical stresses to move, divide, remodel, and sense their mechanochemical microenvironment. The generation and transmission of stresses in a tissue can give rise to collective cellular phenomena of diverse complexity, from the relatively simple contraction of striated muscle to the intricate folding of an epithelium. The role of mechanical stresses in biological systems is particularly apparent in early development, when cellular layers of different identity undergo pronounced 3D movements to shape tissues[36]. However, living tissues are mechanically active throughout life. For instance, the intestinal epithelium self-renews every 3-5 days through a series of mechanical functions such as division, migration and extrusion[37, 38]. Mechanical stresses also play a critical role in wound healing, where they enable cell migration towards the wounded area and supracellular contraction to seal the wound[10]. Conversely, aberrant stresses mediate devastating diseases such as myopathies or cancer[39, 40]. Unlike in passive materials, stresses in living tissues are transduced by cells to trigger and regulate biological responses[41]. For example, an increase in tension causes cell proliferation whereas a decrease induces cell extrusion[12, 13, 42].

A number of tools have been developed to measure mechanical stress over multiple length scales, from the single molecule to the entire organ. Here we will review technologies to

measure stress in tissues with cellular and subcellular resolution. Because our focus will be on stress, we will exclude technologies to measure other relevant mechanical quantities such as stiffness, viscoelasticity or poroelasticity. Therefore, we will not discuss techniques such as magnetic tweezers[43, 44], optical tweezers[45, 46], acoustic tweezers[47], atomic force microscopy[48], micropipette aspiration[49], microindentation[50], microplate actuators[28], Brillouin microscopy[51, 52], or tissue dissection and relaxation[53]. The reader is referred to excellent recent reviews on these techniques[54-65].

We begin reviewing fundamental concepts in continuum mechanics, which might be familiar to most physicists and engineers but not to the broad biomedical community interested in cell and tissue mechanobiology. We continue presenting the techniques developed to measure tissue stress *in vitro* and *ex vivo*, starting with the techniques applicable to 2D cultures, such as 2D traction force microscopy, micro-pillar arrays, monolayer stress microscopy and tensile tests of cultured tissues. We then introduce the methods applied to 3D cultures, including 2.5D and 3D traction force microscopy. We finally discuss the techniques compatible with *in vivo* samples, such as servo-null methods, inclusions, FRET sensors, laser ablation and force inference.

3.2.1 The concept of stress and traction

A force is an interaction that tends to deform or change the velocity of an object. Forces acting on any material can be classified as internal or external. For a given cell in a tissue, internal forces are generated by subcellular components such as the actomyosin cytoskeleton, whereas external forces are exerted by the surrounding extracellular matrix (ECM) or neighboring cells. The mechanics of deformable continuum materials is not formulated in terms of force, however, but rather in terms of force per unit area, a physical quantity known as **stress**. The need for the concept of stress can be simply understood by noticing that the same force applied over smaller or larger areas of a material will cause a different deformation.

The force per unit area acting on any internal or external surface of a material is called **traction vector** $\vec{T}$. It is assumed that the traction vector only depends on the location within the material and on the unit normal vector $\vec{n}$ to the surface (Cauchy's stress postulate). Therefore, the traction vectors that act on opposite sides of a surface are equal in magnitude and opposite in sign (Newton's 3rd law) (Box 1). In general, the traction

vector is not perpendicular to the surface, and it can be decomposed into normal $\vec{t}_n$ and tangential $\vec{t}_t$ vector components. Normal tractions can be compressive (negative) or tensile (positive) depending on their sign relative to $\vec{n}$ (Box 1).

As there are infinitely many surfaces passing through a point A, there are also infinitely many traction vectors acting on that point. Therefore, to fully characterize the stress state of a tissue we introduce the stress tensor field $\boldsymbol{\sigma}(A)$, a second order mathematical entity that contains all the stress information at a given point A. It can then be proven that the traction vector $\vec{T}$ depends in a linear way on $\vec{n}$:

$$\vec{T} = \vec{n} \cdot \boldsymbol{\sigma}(A). \tag{1.1}$$

BOX 1: The traction vector

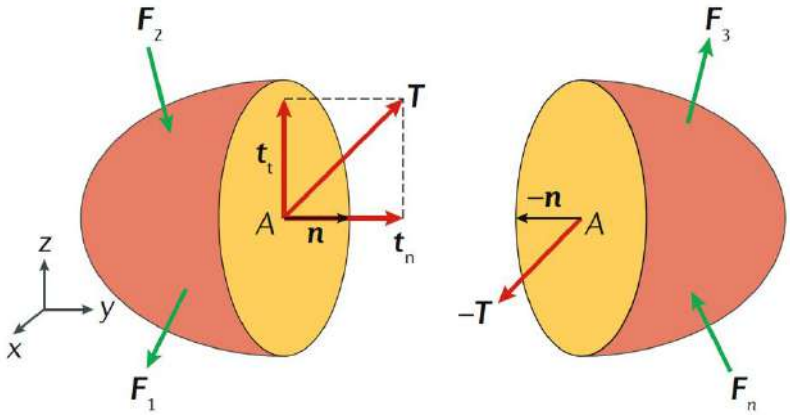

Box 1: *Geometric representation of the traction vector, $\vec{T}$ (red), acting at point A of a body subject to external forces (green arrows).*

A given body can be cut by infinitely many imaginary planes passing through a point A. Each cut will define two sub-bodies and a pair of surfaces with outer normal vectors $\vec{n}$ and $-\vec{n}$. The traction vector $\vec{T}$ is defined as the force between these adjacent surfaces divided by their surface area. It is linearly related to the stress tensor and to the normal vector by Cauchy's stress theorem, Eq. (1.1). The traction vector may have any direction relative to the surface. Therefore, it is conveniently decomposed into its normal ($\vec{t}_n$, indicating compression or tension) and tangential ($\vec{t}_t$, indicating shear) vector components:

$$\vec{t}_{\mathrm{n}} = \left(\vec{T} \cdot \vec{n}\right) \cdot \vec{n} = (\vec{n} \cdot \boldsymbol{\sigma} \cdot \vec{n}) \cdot \vec{n}, \tag{1.2}$$

$$\vec{t}_{\mathrm{t}} = \vec{T} - \vec{t}_{\mathrm{n}} = \vec{n} \cdot \boldsymbol{\sigma} - (\vec{n} \cdot \boldsymbol{\sigma} \cdot \vec{n})\, \vec{n}. \tag{1.3}$$

Normal tractions can be tensile (pulling) when they point in the direction of the outer normal $\vec{n}$, or compressive when they point in the opposite orientation (pushing). In the specific case of TFM, the surface of interest where tractions are defined is the interface between cells and their ECM.

At any point A, the stress tensor $\boldsymbol{\sigma}(A)$ is a 3x3 symmetric matrix (Box 2).

BOX 2: The stress tensor

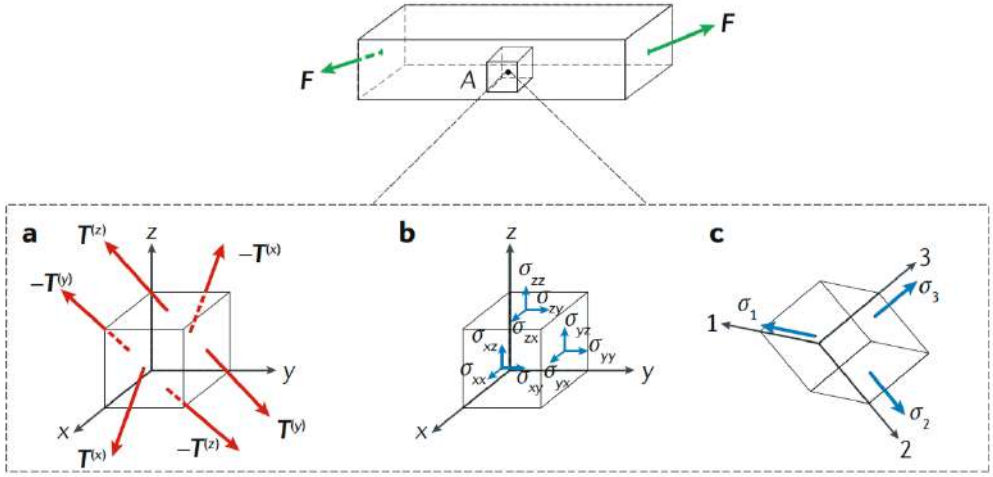

Box 2: *Geometric representation of the stress tensor* $\boldsymbol{\sigma}$ *at point A of a body under a load F.*

There are infinitely many traction vectors $\vec{T}$ acting on a point A as there are infinitely many planes cutting through that point. The stress state at point A is, however, completely defined by 6 orthogonal planes infinitely close to A (defining an infinitesimal cube centered in A), and their associated tractions (Box 2a). In equilibrium, the traction vectors in parallel faces are equal and opposite and, therefore, only three traction vectors, $\vec{T}^{(x)}$, $\vec{T}^{(y)}$ and $\vec{T}^{(z)}$ are needed to describe the stress state at point A. For any given coordinate system, the components of these three traction vectors (Box 2b) can be organized in a 3x3 matrix called the stress tensor $\boldsymbol{\sigma}$, which owing to balance of angular momentum is symmetric:

$$\boldsymbol{\sigma} = \begin{bmatrix} \sigma_{xx} & \sigma_{xy} & \sigma_{xz} \\ \sigma_{xy} & \sigma_{yy} & \sigma_{yz} \\ \sigma_{xz} & \sigma_{yz} & \sigma_{zz} \end{bmatrix}. \tag{1.4}$$

As a result of the spectral theorem, we can always find an orthonormal coordinate system where the matrix is diagonal (Box 2c).

$$\boldsymbol{\sigma} = \begin{bmatrix} \sigma_1 & 0 & 0 \\ 0 & \sigma_2 & 0 \\ 0 & 0 & \sigma_3 \end{bmatrix} \tag{1.5}$$

When $\boldsymbol{\sigma}$ has a diagonal form, its three independent values (its eigenvalues) are called principal stresses ($\sigma_1 \geq \sigma_2 \geq \sigma_3$). When they are equal, the stress state is called hydrostatic or spherical, and in any orthonormal coordinate system $\boldsymbol{\sigma}$ is proportional to $\mathbf{1}$, the identity 3x3 matrix. For instance, fluids at rest have a uniform (independent of A) stress state of the form

$$\boldsymbol{\sigma} = -P \cdot \mathbf{1} = \begin{bmatrix} -P & 0 & 0 \\ 0 & -P & 0 \\ 0 & 0 & -P \end{bmatrix}, \tag{1.6}$$

where P is the pressure. In this situation, the traction vector $\vec{T}$ is always parallel to $\vec{n}$ and thus perpendicular to any surface (the tangential component of the traction is identically zero) and compressive of magnitude P.
In a general case, the stress tensor $\boldsymbol{\sigma}$ can always be decomposed in its spherical or hydrostatic part (that produces tractions perpendicular to any surface) and its remaining deviatoric part:

$$\boldsymbol{\sigma} = \boldsymbol{\sigma^{sph}} + \boldsymbol{\sigma^{dev}}, \tag{1.7}$$

$$\begin{aligned} \boldsymbol{\sigma^{sph}} &= \frac{\mathbf{1}}{\mathbf{3}}\left(\sigma_{xx} + \sigma_{yy} + \sigma_{zz}\right) \cdot \mathbf{1} = \sigma_m \cdot \mathbf{1} \\ &= \begin{bmatrix} \sigma_m & \mathbf{0} & \mathbf{0} \\ \mathbf{0} & \sigma_m & \mathbf{0} \\ \mathbf{0} & \mathbf{0} & \sigma_m \end{bmatrix}, \end{aligned} \tag{1.8}$$

$$\begin{aligned} \boldsymbol{\sigma^{dev}} &= \boldsymbol{\sigma} - \boldsymbol{\sigma^{sph}} \\ &= \begin{bmatrix} \sigma_{xx} - \sigma_m & \sigma_{xy} & \sigma_{xz} \\ \sigma_{xy} & \sigma_{yy} - \sigma_m & \sigma_{yz} \\ \sigma_{xz} & \sigma_{yz} & \sigma_{zz} - \sigma_m \end{bmatrix}. \end{aligned} \tag{1.9}$$

The deviatoric part, which is represented as a traceless matrix, is responsible for the shear stresses.

When modeling thin objects such as plates placed parallel to the (x-y) plane, it may be justified to assume that the traction vector normal to the top and bottom free surfaces of the plate is identically zero and that the stress tensor does not depend on z. Since the normal vector to those surfaces is parallel to the z-direction, the stress tensor takes the form

$$\boldsymbol{\sigma} = \begin{bmatrix} \sigma_{xx} & \sigma_{xy} & 0 \\ \sigma_{xy} & \sigma_{yy} & 0 \\ 0 & 0 & 0 \end{bmatrix}. \tag{1.10}$$

These conditions are referred to as *plane stress*. Under these conditions, the stress state becomes two-dimensional, and an interaction of the thin plate with a substrate (e.g. a measured traction between a cell monolayer and its substrate) becomes a body force rather than a surface traction, see Eqns. (1.17)-(1.18).

Depending on the geometry of the material and the loading conditions, it can adopt distinct forms. We illustrate the most characteristic of such forms in Box 3, using the process of blastocyst implantation as an example.

BOX 3: Stress tensor in biological tissues

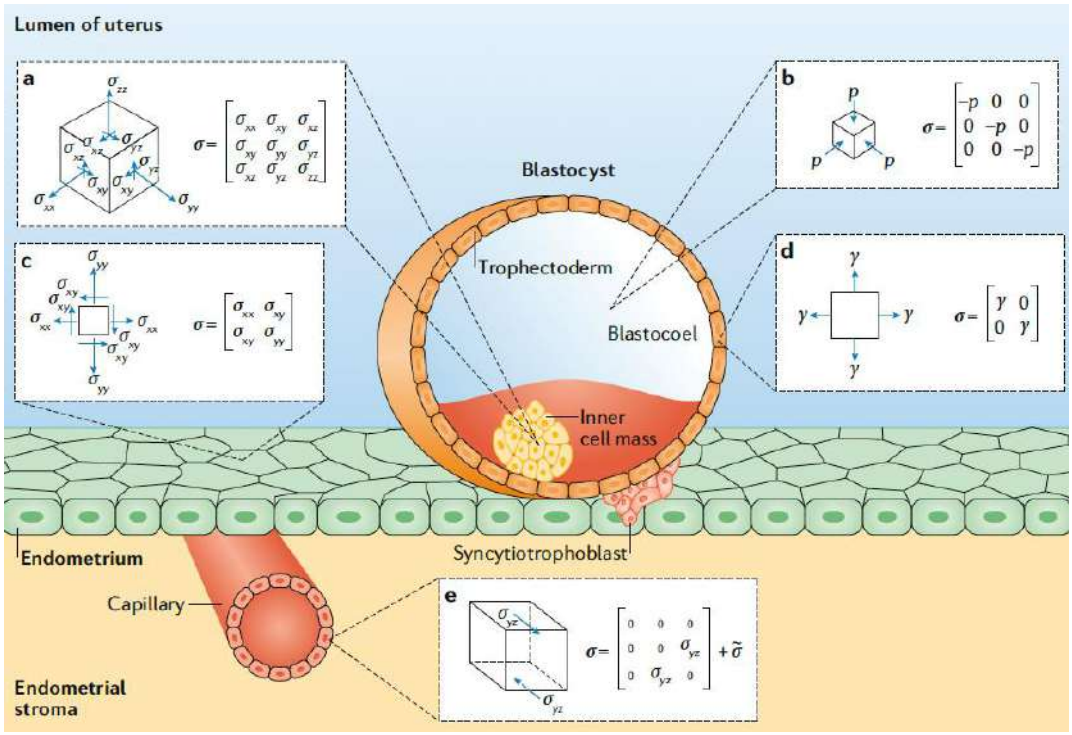

Box 3: *Illustrative sketch of different representative stress states that are present during embryo implantation.*

The stress tensor $\boldsymbol{\sigma}$ is, in general, a 3x3 symmetric full matrix, where all normal and tangential elements are non-zero (Box 3e). However, for specific geometries and loading conditions, it will adopt simplified forms. Here, we illustrate some characteristic mechanical configurations by using the process of blastocyst implantation as an example[66].

The inner cell mass (Box 3e) is a 3D body in a 3D stress state, and therefore $\boldsymbol{\sigma}$ is in general a 3x3 full matrix. By contrast, the blastocoel (Box 3c) is a fluid filled cavity in a 3D hydrostatic state, and thus $\boldsymbol{\sigma}$ is a 3D diagonal matrix whose elements are equal. The endometrium (Box 3a) is a flat monolayer in a state of plane stress. Therefore, $\boldsymbol{\sigma}$ can be reduced to a full 2D matrix, with both normal and tangential components. Conversely, the blastocyst's wall (trophectoderm) (Box 3b) is in a state of capillary (surface) tension due to the internal pressure exerted by the blastocoel. $\boldsymbol{\sigma}$ is then reduced to a 2D diagonal matrix with equal diagonal components. Finally, the endothelial surface of a blood capillary is subjected to a combination of shear stress, hydrostatic pressure and surface tension. $\boldsymbol{\sigma}$ can then be expressed as a sum of two matrices, one with only shear components owing to blood flow and one with a more complex structure due the vessel geometry, hydrostatic pressure and surface tension, generally expressed in cylindrical coordinates (Box 3d).

Force balance in a tissue is defined by Newton's second law. For a tissue in equilibrium modeled as a continuum material and ignoring inertial forces, Newton's second law is expressed in terms of the stress tensor as (see Box 4 for the derivation)

$$\nabla \cdot \boldsymbol{\sigma} = -\vec{b}, \tag{1.11}$$

where $\nabla \cdot$ indicates the divergence operator, which applied to the stress tensor produces a vector expressing the out-of-equilibrium force density in the material, and where $\vec{b}$ is an externally applied force density.

BOX 4: Equilibrium equation for a continuum

The resultant $\vec{R}$ of all external forces applied on a sub-volume V of a tissue bounded by the surface S is the sum of all surface forces acting on its boundary and of all body forces acting on its volume:

$$\vec{R} = \int_{\mathrm{S}} \vec{T}\,\mathrm{dS} + \int_{\mathrm{V}} \vec{b}\,dV = \int_{\mathrm{S}} \boldsymbol{\sigma} \cdot \vec{n}\,\mathrm{dS} + \int_{\mathrm{V}} \vec{b}\,dV = \int_{\mathrm{V}} (\nabla \cdot \boldsymbol{\sigma} + \vec{b})dV, \tag{1.12}$$

where the last step was obtained by invoking the divergence theorem.
Newton's second law can then be written as:

$$\vec{R} = \int_{\mathrm{V}} \left(\nabla \cdot \boldsymbol{\sigma} + \vec{b}\right) dV = \int_{V} \rho\, \vec{a}\; dV. \tag{1.13}$$

where $\vec{a}$ is the acceleration and ρ is the mass density. Despite the fact that tissues are dynamic systems that change in time, we can assume that they relax instantly to their closest state of mechanical equilibrium[24]. In this approximation, the tissue is said to be in a quasi-equilibrium state, which since the sub-volume is arbitrary, results in equilibrium Eqn. (1.11):

$$\int_{\mathrm{V}} \left(\nabla \cdot \boldsymbol{\sigma} + \vec{b}\right) dV = 0 \quad \Rightarrow \quad \nabla \cdot \boldsymbol{\sigma} = -\vec{b}. \tag{1.14}$$

When there are no body forces acting on a tissue, i.e. $\vec{b} = \vec{0}$, the internal stress gradients balance themselves at each point of the tissue:

$$\nabla \cdot \boldsymbol{\sigma} = \vec{0}. \tag{1.15}$$

Box 4: *Derivation of the equilibrium equation for a continuum.*

When there are no external forces applied to the system, i.e. $\vec{b} = \vec{0}$, the internal stresses are balanced at every point and the divergence in Eqn. (1.11) is identically zero. The above equilibrium equation, together with its boundary conditions, govern the mechanics

of the system. In 3D, $\boldsymbol{\sigma}$ has 6 independent components and the equilibrium (vector) equation only provides 3 independent equations. In 2D, where stress is sometimes referred to as tension, $\boldsymbol{\sigma}$ has 3 independent components and equilibrium provides 2 independent equations. In general, we need extra conditions, called constitutive equations, to have a closed problem. Constitutive equations model the stress-generation mechanisms of the material under consideration, and for a living tissue they may include elastic (relating stress and deformation), viscous (relating stress and deformation rate), and active (involving internal consumption of chemical energy) components. The simplest of these relations is provided by isotropic linear elasticity, which relates $\boldsymbol{\sigma}$ and the deformation in a linear way through two coefficients: Young's modulus E and Poisson's ratio ν. Constitutive equations of higher complexity are used when elasticity is not applicable, invoking viscosity[67], hyperelasticity[68], superelasticity[69], plasticity[70], viscoelasticity[65], poroelasticity[71] or polarity[72]. For some particular cases with highly symmetric geometries, such an expanding cell monolayer (3.2.2.3), the stress can be fully determined without specifying the constitutive equation by simply invoking equilibrium[69, 73].

3.2.2 Techniques to measure stress in tissues cultured in 2D

Biological tissues display great variability in their geometrical and mechanical configuration (Box 3). Leukocytes can crawl as single cells on 2D surfaces and invade the 3D ECM during the inflammatory response; epithelial cell monolayers cover the internal and external surfaces of our body, often withstanding a 2D plane stress (Box 2); the early mammalian embryo behaves as a thin walled spherical vessel under pressure; a tumor is a 3D material subjected to compressive stress due to its growth and to stromal forces. Each of these systems displays different mechanical states, and thus requires different techniques to measure the generated stresses. In the following sections, we will discuss techniques developed to measure stress in living tissues and their range of applicability. We will first review techniques applicable to *in vitro* and *ex vivo* 2D systems, while later sections will focus on *in vitro* and *ex vivo* 3D samples and *in vivo* systems. The techniques discussed in this section, together with their main features and selected bibliography, are summarized in Table 1.

3.2.2.1 Traction Force Microscopy in 2D (TFM 2D)

Traction Force Microscopy (TFM) is the first and most standard technique used to measure the tractions exerted by single cells and tissues on soft elastic substrates. A first qualitative implementation of TFM showed that single cells were able to wrinkle a thin and soft silicon rubber substrate on which they were adherent[74]. Subsequent improvements attempted the quantification of the tractions underlying such deformations by modeling the substrate as a flat thin membrane under plane stress[75-77]. Following these seminal contributions, the technique was reformulated to its current implementation, which measures the 2D tractions exerted by cells on flat substrates of known thickness[78]. Typical substrates are polyacrylamide (PAA) and soft polydimethylsiloxane (PDMS) gels, which are transparent, tunable in stiffness and can be coated with ECM proteins. As detailed in a number of studies and reviews, TFM 2D directly measures the displacements that cells generate on the upper surface of their underlying substrate[79, 80]. These displacements are measured relative to a reference state typically obtained by detaching all the cells from the substrate and thus relaxing it to its non-deformed configuration (Figure 14a and Figure 14b). Displacements are entirely caused by the tractions that cells exert on the substrate and they are computed by imaging fiducial markers that are embedded in the substrate or attached to its surface. Recent implementations of TFM 2D eliminate the need to image the relaxed configuration by distributing the markers into a regular array that serves as theoretical reference[68, 81].

Different strategies are available to obtain the tractions that cause the measured surface displacements. In all cases, mechanical equilibrium Eqn. (1.11) (Box 4) is imposed to the substrate, and a constitutive behavior is chosen to establish a closed problem. The substrate is commonly considered uniform and isotropic, and its constitutive behavior is typically assumed linear elastic, with known Young's modulus E and Poisson ratio ν. TFM 2D can be used when the out-of-plane tractions exerted by the sample tissue are negligible compared to the in-plane tractions, yielding a 2D traction vector on the substrate surface[82].

By also assuming a simple geometry (as a half-space or a finite thickness substrate) and small displacements (infinitesimally smaller than any relevant dimension of the gel),

several computational methods have been developed to obtain the tractions. These methods take advantage of linear superposition and of the availability of analytical forms for the Green's function of the problem, which provides the displacement field in the substrate under the action of a point surface load. In most cases, tractions are calculated as the solution to an inverse problem, typically computed in Fourier space to accelerate computational performance[82, 83]. In some applications, the inversion can also be performed in real space using the Boundary Element Method[78]. Regardless of the specific computational formulation, the inverse problem is mathematically ill-posed, and because of the long-ranged decay of the Green's function, the computed tractions are very sensitive to small variations or noise in the displacement data. This difficulty can be mitigated by using regularization techniques during the solution of the inverse problem[84, 85] or Bayesian methods[86]. When the previous hypotheses do not hold, as for example when the substrate is not uniform because there is a gradient of stiffness (E), when the geometry of the substrate is complex, or when there are large displacements, tractions need to be computed from the displacements using the Finite Element Method (FEM)[87].

A different strategy is to directly compute the substrate deformation from the spatial derivatives of the displacement field[88]. The stress tensor $\boldsymbol{\sigma}$ is then directly computed from the deformation using the constitutive equation of the substrate material. Finally, the traction vector is obtained simply as $\vec{T} = \vec{n} \cdot \boldsymbol{\sigma}$. The main shortcoming of this approach is the noise in the displacement field, which arises from optical microscopy limitations, from the image analysis algorithms and from the material heterogeneities of the substrate. Noise in the measurements are strongly amplified when calculating the displacement derivatives, and the calculated $\boldsymbol{\sigma}$ might not satisfy the equilibrium Eqn. (1.11).

TFM has been pivotal in the emergence and growth of the field of mechanobiology. At the single cell level, TFM made visible for the first time the tractions that cells exert when they migrate[78], divide[89] and interact with their mechanical environment[3, 90]. At the tissue level, TFM has been used to establish how cells coordinate local traction generation during collective cell migration[7], how mechanical waves propagate in a cell monolayer[91], and how cells combine different motility modes to heal wounds[10].

Other discoveries enabled by TFM include collective durotaxis[8], kenotaxis[92] and cell jamming[93]. Whereas most TFM experiments have been performed using cultured monolayers, the technique has also been applied to tissue explants[94].

Key advantages of TFM over other techniques are its straightforward implementation, its potential to be applied at different scales, and its high versatility, which has enabled its use in physics and engineering problems[80] such as wetting[67, 95], fracture[96, 97] or adhesion[98-100] both in living and inert materials. A major disadvantage is that retrieving the tractions from the displacements is an ill-posed problem and thus it is very sensitive to experimental noise. Furthermore, TFM 2D is by definition restricted to measuring tangential in-plane tractions, but deformations on flat gels might be due to out-of-plane tractions, resulting in errors in the traction field measured with TFM 2D[101, 102].

3.2.2.2 Micropillars

The use of micropillars to measure tractions exerted by a tissue is conceptually similar to TFM, but the continuous flat gel substrate is substituted by a discrete array of vertical slender micropillars of micron-size cross-section, typically fabricated with PDMS[103]. Because of the localized nature of adhesion to the substrate, micropillars measure an integrated traction over a small region, that is, a net force. Micropillars are physically anchored at their bottom and free at their tip, in a vertical cantilever beam configuration. Cell attachment is restricted to the pillar top surface, which defines the area of force application (Figure 14c and Figure 14d). The in-plane component of the forces applied on the substrate can be calculated from the displacements of the micropillars tips. Owing to the inherent locality and discreteness of the mechanical problem, the implementation of the technique is mathematically and computationally simpler than TFM. For deflections much smaller than the micropillar length, applied net force and tip displacement are linearly related through the elastic spring equation

$$\mathrm{F} = \left(\frac{3\,\mathrm{EI}}{\mathrm{L}^3} \right) \delta, \qquad (1.16)$$

where F is the applied force, E is Young's modulus, I is the moment of inertia, L is the length of the micropillar and δ is the measured displacement. Eqn. (1.16) is only valid for slender pillars, i.e. with a length larger than 10 times their radius, of uniform cross-section. Micropillars are microfabricated following a regular lattice, which provides a

reference from which deflection can be calculated. Particle tracking software is used to find the centroid of each tip and its location is compared to the theoretical position of the pillar in the ideal lattice. According to Eqn. (1.16), the substrate stiffness and stiffness gradient felt by the cells can be modified by tuning the pillar material, length[103] and/or cross section[104]. A variant of this technique uses only two thick vertical micropillars[105, 106]. Contractile cells, such as fibroblasts[105] and cardiomyocytes[105, 106] are seeded between them surrounded by ECM proteins, mimicking a three-dimensional microtissue. Because the pillars are not slender and lack uniform cross-section, their response is not linear as in Eqn. (1.16), and their force-deflection curve needs to be experimentally calibrated.

Arrays of micropillars have been used to quantify forces during single and collective cell migration[10, 103, 107], yielding force patterns comparable to those reported by TFM. In static monolayers, micropillar arrays have been exploited to study the tangential forces helping neutrophils to transmigrate through the endothelium[108]. This technique has also been used to study the role of tractions in the healing of wounds[10], and to elucidate the role of leading cells in collective cell migration[109]. By modifying the geometrical properties of the micropillars, i.e. length and cross-sectional shape, cells were shown to increase the force generated with increasing the stiffness of the pillar[110] and to elongate in the direction of highest stiffness[104]. This approach has also been employed to study the link between rigidity sensing of the environment and cancer cell growth[111].

Compared with TFM 2D, micropillar-based traction microscopy has the advantage of providing a direct local interpretation of the relation between applied force and pillar deflection. Tracking the displacements of the pillars is simpler than following patterns of bead markers, and cells do not need to be detached to capture a reference image, given that the reference position of the pillars is calculated from an ideal grid. Furthermore, the mathematical and computational methods to calculate the forces are straightforward. A final advantage of micropillar arrays is that they provide a way to create stiffness gradients in the substrate by varying the shape of the pillars rather than their material properties. However, this technique presents some drawbacks, mostly associated with the discrete nature of the adhesion of cells to the pillars. Indeed, micropillar arrays provide the cells with topological cues affecting their behavior. Moreover, despite a correct substrate functionalization, cells still tend to enter the empty space between pillars. This

technique requires very slender micropillars, which poses microfabrication and handling challenges. Furthermore, it only allows us to measure in-plane displacements of the micropillar tips, and thus vertical tractions are disregarded. Given that the actual relaxed position of the micropillars might deviate from their ideal location, the use of a theoretical reference image introduces random noise in the deflection and, therefore, in the force measurement. Finally, the presence of a deformable substrate under the pillars has been reported to induce an overestimation of the tractions applied by the tissues under study and, consequently, correction factors need to be introduced and validated[112].

3.2.2.3 Monolayer Stress Microscopy

Given the traction field exerted by a tissue on a flat substrate and invoking simple force equilibrium arguments and mechanical assumptions, it is possible to calculate the internal stress distribution in the tissue (Figure 14e and Figure 14f). This approach, generally known as Monolayer Stress Microscopy (MSM), was first proposed to measure the average internal stress in a single cell[73]. This idea was then applied to measure the internal tension distribution in an expanding cell monolayer[7], and later on, in cell doublets[113, 114], triplets[115] and larger cell clusters[116].

In MSM, the cell monolayer is modeled as a very thin flat plate under plane stress conditions[9, 117]. In this 2D setting, the equilibrium Eqns. (1.11) take the form (Box 4)

$$\frac{\partial \sigma_{xx}}{\partial x} + \frac{\partial \sigma_{xy}}{\partial y} = \frac{T_x}{h}, \tag{1.17}$$

$$\frac{\partial \sigma_{xy}}{\partial x} + \frac{\partial \sigma_{yy}}{\partial y} = \frac{T_y}{h}, \tag{1.18}$$

where σ_{xx}, σ_{yy} and σ_{xy} are the components of the stress tensor in the tissue, h is the mean height of the monolayer, and T_x and T_y are the tractions measured by TFM 2D, which in this 2D approximation take the role of $\vec{b}$ in Eqn. (1.11). These two partial differential equations, insufficient to determine the three unknown stress components, are then complemented by the Michell-Beltrami compatibility condition

$$\left(\frac{\partial^2}{\partial x^2} + \frac{\partial^2}{\partial y^2}\right)(\sigma_{xx} + \sigma_{yy}) = \frac{1+\nu}{h}\left(\frac{\partial T_x}{\partial x} + \frac{\partial T_y}{\partial y}\right). \tag{1.19}$$

This equation implicitly assumes a linearly elastic isotropic behavior of the tissue. The MSM inference of the tissue stress is then obtained by solving Eqns. (1.17)-(1.19) with suitable boundary conditions[9, 117].

This approach requires knowledge of Poisson's ratio ν of the monolayer, but not its Young's modulus E. An alternative approach has been proposed to calculate the monolayer internal stresses from the substrate displacements (rather than tensions) by solving the elasticity equations for the monolayer[118]. This approach has the advantage of not requiring the calculation of the tractions exerted on the substrate and allowing for non-uniformities in E and ν of the monolayer. However, uncertainties in the values of the monolayer's mechanical properties will greatly impact the calculated tensions.

For monolayers that cannot be modeled as elastic and isotropic, Eqn. (1.19) does not hold, and the problem is underdetermined unless a constitutive model is assumed. A Bayesian inversion method, Bayesian Inversion Stress Microscopy (BISM), has been proposed to solve Eqns. (1.17)-(1.18) independently of a constitutive model[119]. This approach, which can be interpreted as an unbiased regularization, is in principle devoid of free parameters and has been shown to be robust with respect to the underlying statistical model.

Recently, a mathematical framework has been developed to quantify bending moments in the cell monolayer from the out-of-plane tractions exerted on the substrate[120]. The problem is decomposed into a plane MSM state (governed by Eqns. 1.17-1.19), and a bending state induced by the out-of-plane components of the traction vector[120, 121].

MSM has been pivotal in describing emerging phenomena such as plithotaxis, i.e. the tendency of cells to follow the direction of maximum principal stress[9], active de-wetting of epithelial islands[67], collective durotaxis of epithelial monolayers[8], cell extrusion at topological defects[72], and the role of mechanical interactions between follower cells in the emergence of leaders during epithelial migration[122].

Monolayer Stress Microscopy has the advantage of accessing the internal stresses of a tissue, as opposed to the interactions of the tissue with its surrounding environment, in a non-invasive way. However, it is built around the assumption of uniform elastic mechanical properties of the tissue and restrictive geometric constraints such as considering a flat monolayer with uniform thickness. These limitations are absent in formulations of MSM in quasi-1D configurations, such as cell chains or monolayers expanding from a rectangular pattern[91]. In 2D monolayers, the impact of MSM

assumptions in the recovered stress field has been analyzed in detail[117]. Monolayer mechanical properties are dependent on cell type and microenvironment, and they might not be fully described by an elastic constitutive equation[69]. Similarly, cell monolayers might not present a uniform height. Finally, the original implementation of MSM makes the assumption of planar stress state, which might not be applicable to all types of monolayers. This limitation has been partially addressed by including the bending moments of the monolayer[120].

3.2.2.4 Suspended monolayers

A direct tensile testing of *in vitro* and *ex vivo* cell cultures can be performed by using suspended cell monolayers[123]. These tensile assays enable the quantification of both the rheology of the monolayer[123] and its stress response to mechanical deformations[124]. In these experiments, a freely suspended cell monolayer is attached at its two ends to one rigid and one flexible rod, used as manipulators to apply a given strain or stress, and as transducers to measure the conjugated stress or strain exerted by the monolayer[125] (Figure 14g and Figure 14h). The suspended monolayer is physically and optically accessible, enabling the direct visualization of the tissue while being stretched.

Tensile tests of suspended cell monolayers have been used to characterize mechanical properties at the tissue, cellular and subcellular scales[123], and these experiments have been computationally simulated with vertex models[126]. Tensile tests have also been applied to study the contribution of cell division to stress relaxation and tissue homeostasis[127], with results well-captured by vertex model simulations[128]. More recently, tensile tests have shown that the stress response of cell monolayers to applied strains is controlled by the actomyosin cortex both in cell monolayers grown *in vitro* and in multilayered explants of *Drosophila* larval wing discs cultured *ex vivo*[124]. Furthermore, compression tests have been used to study the mechanoresponse of the actomyosin cytoskeleton, and to identify a buckling threshold above which monolayers remain folded[129]. Finally, mechanical probing of curls formed at the edges of suspended monolayers provides a method to measure the out-of-plane mechanics of tissues[130].

The biggest advantage of this technique is its ability to perform tensile and compression tests of a cell monolayer devoid of matrix, hence directly testing the cellular material. Moreover, it is very well suited to image the cell monolayer while being manipulated,

potentially enabling the combination with computational force inference methods (section 3.2.4.5). The technique has the disadvantage of requiring a very specialized and low-throughput protocol for sample preparation and testing.

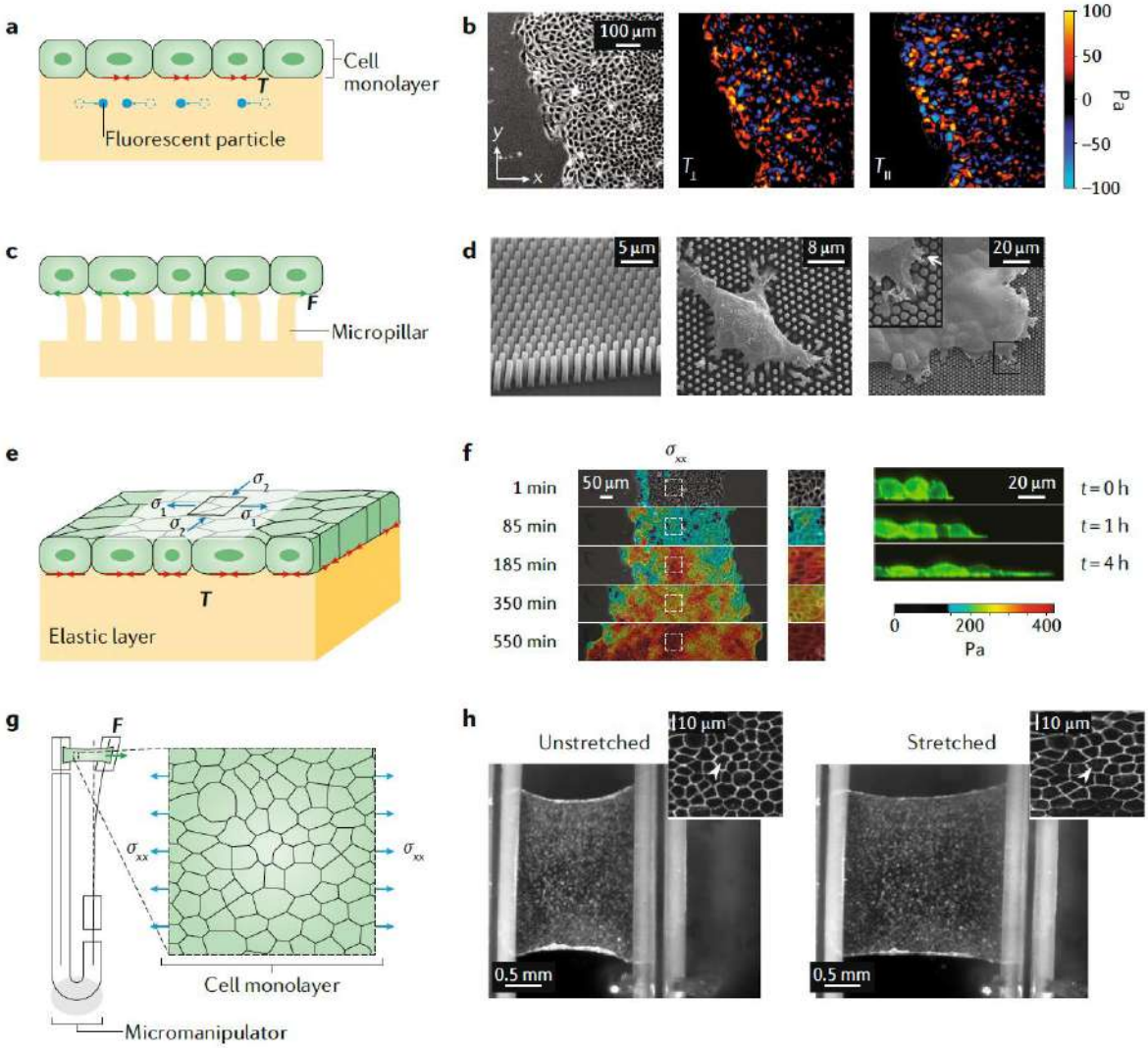

Figure 14: ***Techniques used to measure tractions and internal stresses in 2D tissues****.* ***a****, In TFM 2D, a flat elastic gel is synthetized, and a tissue is allowed to attach to its surface. Cells exert tractions on the substrate and the resulting deformation can be tracked by adding fluorescent particles in or onto the substrate and comparing their position with an image of the substrate at rest. Tractions are then calculated by using different computational and analytical approaches.* ***b****, Representative TFM 2D experiment. Phase contrast image of a flat cell monolayer on top of a polyacrylamide gel (left) together with the tractions exerted by the cells in the directions parallel (center) and perpendicular (right) to the advancing edge[7].* ***c****, In the micropillar technique, cells are seeded on top of an array of micropillars, whose deflection is proportional to the locally applied force.* ***d****, Representative micropillar experiment. Scanning electron micrograph of a micropillar array (left) with a single cell (center) and a cell monolayer (right) lying on top of it[107].* ***e****, Using MSM, the internal stresses of a flat cell monolayer can be calculated from the tractions it applies on an elastic substrate.* ***f****, Representative MSM experiment. Expanding cell monolayer with overlaid color-coded internal stresses calculated with MSM[91] (left). Side view of an expanding monolayer (right).* ***g****, The tensional state of a flat monolayer can be directly measured and controlled with a micromanipulator.* ***h****, Representative suspended cell monolayer experiment. Monolayer before (center) and after (right) stretch applied with a micromanipulator[131]. Insert: zoom in a region of a monolayer before and after stretch[125].*

3.2.3 Techniques to measure stress in tissues cultured in 3D

Specific techniques have been developed to measure the tractions and stresses in tissues cultured in 3D. They will be discussed here and summarized in Table 1.

3.2.3.1 Traction Force Microscopy in 3D

It is well known that cells impose 3D displacements on their extracellular matrix by applying 3D forces[132]. Even when attached to flat surfaces, tissues exert normal forces on their substrate. These normal forces are sometimes comparable in magnitude to their in-plane counterparts[133, 134]. In those cases, TFM 2D is not a valid approach, and a different technique needs to be used. A natural extension to TFM in 2D (section 3.2.2.1) is to relax the hypothesis of zero normal tractions at the substrate surface. In this extension, a 3D displacement field of the top layer of the substrate needs to be measured to infer the 3D traction vector field (Figure 15a and Figure 15b). This method is also known as 2.5D because it involves calculating a 3D traction field applied on a 2D substrate. To obtain 3D tractions from 3D measured displacements, the same mathematical and computational approaches that were explained for TFM 2D can be used. Under the assumptions of a uniform, isotropic and linear elastic substrate, with simple geometry and small displacements, 3D traction fields were first calculated from displacements by following a direct approach and evaluating the constitutive elastic equation for the substrate[135, 136]. Subsequently, a Boundary Element Method was proposed to generalize Dembo and coworkers' solution[78], by considering an incompressible substrate ($\nu = 0.5$) and thus uncoupling the normal and tangential problems[137]. Alternatively, 3D tractions fields can be calculated from displacements using the Fourier transform and the known Green's function for the problem[101]. For other cases, where the aforementioned hypotheses do not hold, a Finite Element Method is needed[133].

To study some physiological processes such as tumor invasion or angiogenesis it may be more pertinent to measure the tractions exerted by a tissue embedded in a 3D ECM. The quantification of a 3D traction field from a 3D displacement field is fundamentally more challenging from the conceptual, experimental and computational points of view (Figure 15c and Figure 15d). A central conceptual hurdle of this technique is that cells continuously synthetize and remodel their ECM and, as a consequence, it is unclear if the measured displacements are produced by the tractions exerted by the cells or if they are

the result of remodeling of the ECM[64]. Furthermore, the 3D imaging of the ECM completely surrounding the tissue might be too aggressive for the sample and induce phototoxicity. Another problem arises from the fact that the physiological 3D ECM includes fibers and thus cannot be modeled by linear elasticity. An early implementation of TFM 3D estimated the traction exerted by the invading front of a cancer spheroid embedded in a Matrigel matrix by tracking the motion of embedded microparticles[138]. This approach is limited by the assumption of linear elasticity, the measurement of the particle displacements in only one plane through bright field illumination, and the assumption that the traction force points in the direction of the average particle displacement. However, this work paved the way for more sophisticated studies. To tackle some of the problems of TFM 3D, some researchers have used well-characterized viscoelastic materials such as agarose[139] or engineered synthetic matrices that behave as linear elastic materials[140]. Other groups have characterized the non-linear constitutive behavior for physiologically relevant ECMs such as collagen gels[70, 141]. Recently, a simplification of TFM 3D has been applied to tumor spheroids[142]. By taking advantage of the approximately spherical geometry of the tissue and assuming spherical symmetry of the stress state, only an equatorial plane of the spheroid and the ECM is imaged. The radial far-field displacements of the ECM are measured as a function of the distance to the spheroid, and a scalar value of the tissue contractility is calculated through a Finite Element Method. In a particularly simplified implementation of TFM 3D, spherical tissues such as cancer spheroids[143] and blastocysts[144] are encapsulated within a spherical hydrogel drop. By measuring the radius and wall thickness of the hydrogel capsule, the normal stresses exerted by the spherical tissues are inferred.

TFM in 2.5D has been used to elucidate the interplay between normal and tangential forces during single cell migration[134], the influence of 3D traction stresses in the protease-dependent invasion of cancer[145], and diapedesis of leukocytes through a vascular endothelial monolayer[146]. It has also been employed to simultaneously measure traction forces and the substrate's Poisson's ratio from the displacements of fiducial markers at different substrate locations[147]. TFM 3D has been used to describe the invasion, in physiologically relevant conditions, of healthy[140] and disease model cells[141].

The main advantage of TFM in 2.5D is that it builds on top of TFM 2D, keeping its experimental and analytical simplicity while qualitatively improving the scope of its

measurements by correctly quantifying 3D tractions. However, this technique also shares the drawbacks of TFM 2D, such as the high sensitivity to experimental noise. With regard to TFM 3D, its biggest benefit is the ability of using physiologically relevant ECMs. The main limitation is the need to deal with non-linear constitutive behaviors and 3D materials that can be degraded and remodeled by the cells. Furthermore, these techniques are affected by the current imaging limitations of 3D optical microscopy, such as a lower resolution in the z direction compared to the in-plane resolution, and a decline in image quality with the thickness of the sample.

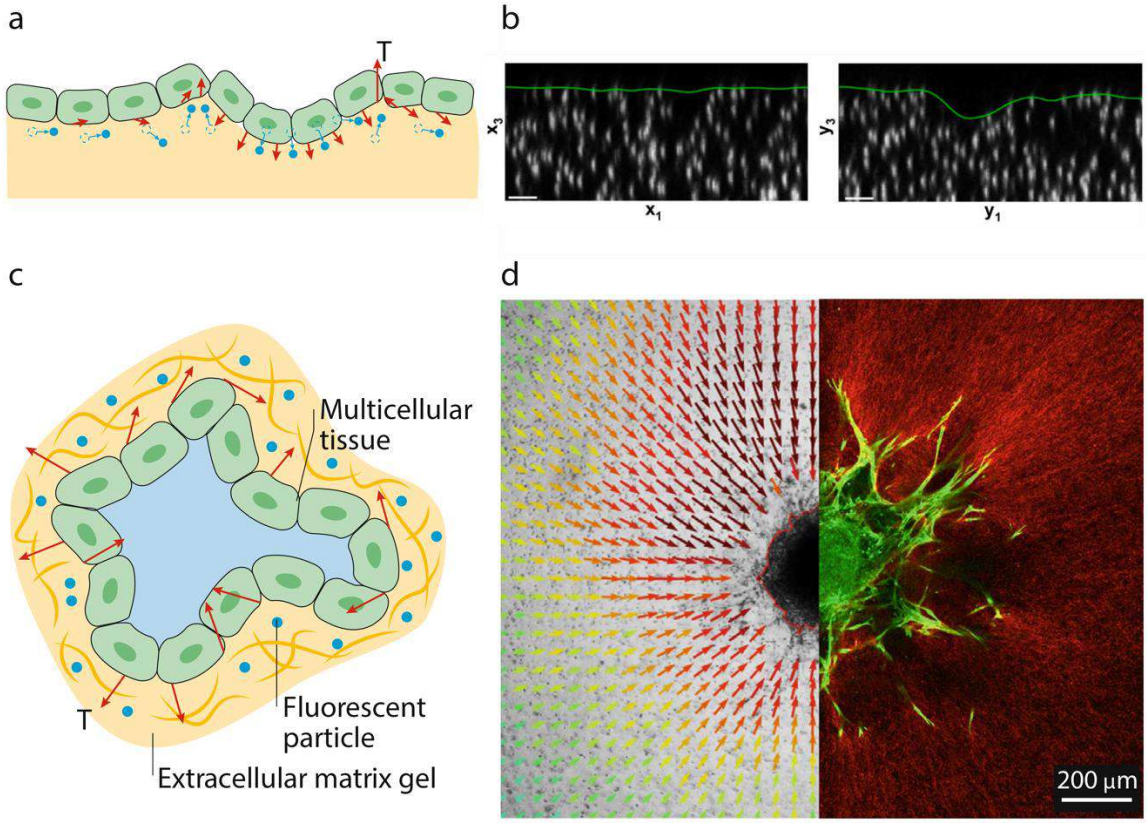

Figure 15: ***Techniques used to measure tractions and internal stresses in 3D tissues in vitro. a****, In TFM 2.5D, a tissue is seeded on top of a 2D elastic substrate, and the displacements of the substrate are measured in 3D. From these displacements, the 3D traction field can be calculated.* ***b****, Cross section of the undeformed (left) and deformed (right) gel surfaces. The deformation is caused by the locomotion of a Schwann cell. Adapted from[136].* ***c,*** *By applying TFM 3D to tissues grown inside a deformable matrix with particle tracers, the full 3D displacement field can be measured, and from it the full 3D traction field can be inferred.* ***d****, Representative TFM 3D experiment. Breast cancer spheroid embedded in a 3D collagen I matrix. Bright field image with superimposed ECM displacements (left) and fluorescent image of the spheroid and matrix (right) (courtesy of Nadine Grummel, David Böhringer and Ben Fabry).*

3.2.4 Techniques to measure stress in vivo

The techniques discussed in the previous sections relied on the possibility of growing or explanting tissues on artificial matrices. Here, we discuss the techniques available to measure tractions and stresses *in vivo*. They are summarized in Table 1.

3.2.4.1 Servo null methods for measuring luminal pressure

The development of closed cavities with a pressurized fluid-filled lumen is crucial for morphogenesis at different scales, from tissues to organs[148]. The hydrostatic pressure in such cavities can be measured by directly puncturing the lumen with a micropipette connected to a micropressure measuring system (Figure 16a and Figure 16b). Although the quantitative measurement of pressure in animals dates back to the eighteenth century[149], the measurement of luminal pressure in micron-size tissue structures was more recently achieved thanks to the development of servo-null devices[150]. These devices use a glass micropipette filled with a saline solution electrolyte of very low electrical impedance, much lower than the luminal contents under study. When the tip is punctured into a fluid-filled pressurized cavity, the luminal content will be pushed inside the tip, effectively increasing the electrical impedance measured at the micropipette. A servomechanism is then used to read the impedance at the tip and send a signal to a pressure transducer that will push the electrolyte towards the lumen until the original impedance is restored. The counterpressure applied by the transducer is assumed to be the pressure of the luminal cavity[151].

Although servo-null methods were originally developed to measure the pressure in the microcirculation[150, 152], they have been extensively used in diverse systems and length-scales, from the cytoplasm[153, 154] to whole animal organs[155-158]. Servo-null methods have also shown to be powerful tools for quantifying pressure in tissues. They were used early on to characterize pressurized domes formed by *in vitro* grown epithelia[159], a tissue system where luminal pressure is key for its correct 3D morphogenesis. They have also been used to assess the key role of luminal pressure during the development of the embryonic heart of zebrafish[160] and chicken[161] embryos, as well as for quantifying the relation between luminal pressure and successful brain formation of chicken embryos[162]. More recently, experiments at different stages of mouse blastocyst formation have shown that luminal pressure regulates cell fate

specification and tissue patterning by influencing cell division and positioning[163]. Servo-null methods have also been used to study the mechanoregulation of tissue morphogenesis via hydraulic feedback in the developing inner ear of zebrafish[164].

Despite their unique potential to measure pressure at the microscale, servo-null methods present several disadvantages. Typically, the tip resistance and compliance are neglected, overlooking a possible quantitative bias in the pressure measurements. From an experimental perspective, the meticulous filling of the tip needs to be assessed at all times, given that even small bubbles will highly impact the measurement. Moreover, puncturing micropipettes are prone to clogging, affecting the pressure readings. Finally, the probing tips need to be exceptionally thin to avoid leakage at the puncture site. Thus, this technique is highly complex and prone to very subtle but catastrophic errors both in the data collection and interpretation[165].

3.2.4.2 Inclusions

A novel approach to measuring tissue stress *in vivo* and *in vitro* is based on introducing force transducers into the tissue and reading out their output signal through optical means (Figure 16c and Figure 16d). The probes used in these techniques need to have controlled size, shape and known visco-poro-elastic properties. Moreover, their mechanical properties must be stable in time. For this reason, cells themselves cannot be used as force transducers, and these techniques resort to synthetic inclusions[71].

The first reported application of exogenous inserts as force transducers used fluorescently labeled liquid microdroplets of biocompatible fluorocarbon oils coated with adhesion molecules[166]. These microdroplets are injected into a tissue, and their 3D shape is imaged through confocal microscopy. By knowing the surface tension of the microdroplet and assuming a spherical reference configuration, part of the deviatoric stress (Box 2) locally applied on the surface of the microdroplet can be calculated. A critical step of this method is the assumption of constant and uniform surface tension of the microdroplets. This surface tension can be modified when proteins are adsorbed on the microdroplet's surface, and thus it needs to be saturated with surfactants prior to injection[63]. One fundamental limitation of this implementation is the use of incompressible liquids, which impairs the measurement of the hydrostatic stress component and of the full deviatoric stress component (Box 2). This limitation has been overcome by using elastic

reporters[167]. Furthermore, the use of exotic liquids such as ferromagnetic fluids enables the active application of forces on the surrounding tissue[168].

A similar approach uses poroelastic polyacrylamide hydrogel microbeads rather than oil droplets[169, 170]. Thanks to their poroelastic nature, these microbeads are able to report on the hydrostatic stress component (the pressure). When the microbeads are subjected to a hydrostatic stress, their polymer volume fraction changes and, consequently, the diffusion time of a small fluorescent tracer varies. By measuring this diffusion time one can calculate the hydrostatic component of the stress applied on the microbeads. A more advanced approach uses alginate hydrogel microbeads with fluorescent nanobeads embedded in them[171]. A Fast Iterative Digital Volume Correlation (FIDVC) algorithm[172] applied to microbead images enables the calculation of the full deformation configuration of each microbead. The full stress state on the microbead surface is then calculated from the deformation by using a Finite Element Method.

A novel and promising generation of transducers for force measurement of *in vivo* specimens are Lanthanide-doped nanoparticles[173, 174]. These nanoparticles change their molecular structure when subjected to a mechanical stress, effectively varying their fluorescence emission intensity[175]. They can be used as force reporters in the nano- to micro-Newton regime[176]. Although these nanoparticles have been extensively used as bioprobes[173], they remain to be used as force transducers in biological applications. In the same vein, Whispering Gallery Mode Microlasers are micron-sized deformable optical microresonators able to emit laser light pulses with a frequency dependent on their geometry[177], and thus enabling the quantification of their deformation from their emission spectrum. These reporters have been inserted into the cytoplasm of contractile cardiomyocytes and in zebrafish hearts to monitor cell and organ contractility[178], but they remain to be used as direct force reporters.

Oil microdroplet force transducers have been employed to study the stresses exerted by tooth mesenchymal cells in mandible explants *ex vivo*[166] and in 3D multicellular spheroids *in vitro*[179]. Conversely, elastic hydrogel force transducers have been used to measure the hydrostatic stress in 3D multicellular spheroids[169, 170]. Maps of the complete stress tensor have been obtained both in 3D tumor spheroids *in vitro* and in zebrafish embryos *in vivo* by using viscoelastic hydrogel force transducers[171].

The main advantage of force transducers is their ability to report the 3D internal stresses both *in vitro* and *in vivo*[166]. Thanks to their size and to their mechanical and chemical properties, their injection does not compromise embryo viability. One limitation of using microdroplets as force transducers is the need to know the surface tension of the microdroplet, and the assumption that it does not change when the microdroplet is injected into the sample. Moreover, they only enable the measurement of some components of the stress tensor. These two disadvantages can be overcome by using hydrogel reporters[167, 169-171, 180]. Additional limitations include that the introduction of an exogenous body into the tissue might impact the measured stress distribution and affect tissue biochemical interactions, for example by serving as a potential sink for lipophilic growth factors or by altering diffusion patterns in the tissue.

3.2.4.3 FRET tension sensors

FRET (Förster Resonance Energy Transfer) tension sensors are composed of a molecular spring of known elastic constant and a fluorescence complex reporting the spring elongation[181, 182] (Figure 16e and Figure 16f). Sensors can be either encoded genetically or synthesized and coupled to an inert material. Different molecular springs have been designed and their elastic properties and force range have been characterized *in vitro*[183, 184]. The elongation reporter system comprises two fluorophores, a donor and an acceptor, with different but overlapping excitation and emission spectra[174]. The rate of energy transfer between the two fluorophores, first described by Theodore Förster[185], has the form:

$$K_{FRET} \sim \frac{\kappa^2 J\, k_f}{n^4 r^6}, \tag{1.20}$$

where κ is the relative dipolar orientation between the donor and acceptor, J is the integral of the overlap between the donor emission and acceptor excitation spectra, k_f is the radiative emission rate of the donor, n is the refraction index of the medium and r is the distance between the donor and the acceptor[174]. Because the rate of energy transfer depends on the separation between fluorophores, it can be converted into a tension readout after careful calibration.

FRET tension sensors have been extensively applied to the study of force transmission at focal adhesions in single cells[184]. At the multicellular level, they have been used to

study intercellular tension in endothelial cell monolayers subjected to fluid shear[186], to elucidate the mechanical role of E-cadherin during collective cell migration in the *Drosophila* ovary[187], and to characterize the tension sustained by E-cadherin and desmosomes[188] during cell stretch[189] and swelling of epithelial acini[190], among other applications.

FRET tension sensors have the advantage that they are genetically encoded and, therefore, they can be expressed in virtually any living tissue, both *in vitro* and *in vivo*. Moreover, they have the potential to report the forces sustained by different cellular components. They are non-invasive and can be used with a relatively high throughput. Despite the enormous potential of this technique, it presents several limitations that restrict its range of applicability and question the interpretation of its results[191]. It is typically assumed that FRET sensors are surrounded by a medium with the index of refraction of water, but local concentration changes might greatly impact the measurements[174, 192]. Furthermore, it is assumed that the FRET sensor emission will only be affected by the applied tension, but local chemical interactions with the microenvironment might impact its spring constant or introduce hysteresis[62, 63]. The readout of FRET sensors is affected by fluorophore stability, and its quality is severely decreased in thick samples, where the signal to noise ratio is reduced[62, 174]. Another drawback of the technique is that it can measure tension but not compression[62]. Importantly, it only provides the magnitude of tension, not its direction[63]. Finally, besides these technical considerations, it is worth emphasizing that molecular tension does not necessarily reflect tissue stress. Indeed, tissue stress is supported by many different proteins arranged in parallel, and the tensional state of one of such proteins does not necessarily reflect the stress of the tissue.

3.2.4.4 Laser ablation

Laser ablation is used to assess the stress state of cohesive tissues. It is based on simultaneously severing a group of cells to generate a sudden force imbalance. The movement of cells surrounding the ablated area to recover mechanical equilibrium is then used to compute relative values of stress before ablation[193, 194] (Figure 16g and Figure 16h). The ablation is performed with near-infrared femtosecond lasers or pulsed UV lasers. Strain and stress anisotropy can be quantified by ablating a supracellular annular region of the tissue[195] or by severing circular areas[196].

The main assumptions underlying this technique are that the tissue is at mechanical equilibrium before and after the cut, that the ablation is able to release tissue tension, and that, during relaxation, dissipative forces outweigh inertia[195, 197]. By further assuming that dissipation is due to tissue viscosity and friction, the initial recoil velocity and its spatial profile provide information about the stress-to-viscosity and the friction-to-viscosity ratios[195]. However, given the complex rheological nature of tissues, it might not be accurate to assume a pure viscous response or uniform frictional properties, and therefore data from laser ablation experiments needs to be combined with an appropriate analysis of tissue rheology[198, 199]. The combination of non-uniform or anisotropic rheological descriptions with Finite Element models can provide more accurate interpretations of laser ablation experiments[199].

Laser ablation has been extensively used to study early morphogenesis and wound healing. For example, it has been used to show that dorsal closure in the *Drosophila* embryo is mechanically governed by the contractile forces exerted by purse strings at the leading edge of the lateral epidermis and by the actomyosin cortex of amnioserosa cells[197, 200]. By ablating one amnioserosa cell, researchers showed that dorsal closure is favored by acto-myosin pulsed apical constrictions that pull on the epidermis[201]. Ion flux between cells has also been related to the generation of contractile forces, measured with laser ablation during dorsal closure[202]. In the *Drosophila* embryonic tissue, laser ablation showed that a contractile actomyosin cable forms along the wound margin, acting as a purse string[203]. In the zebrafish embryo, the tissue tension has been related to the orientation of the spindle by measuring and manipulating the stress state using laser ablation[204].

The main advantages of laser ablation are that it can be used *in vivo* and in a wide variety of tissues, and its relatively easy implementation in many optical microscopy setups. As a major drawback, this technique only offers relative stress measurements unless a tissue rheology is assumed. Moreover, the measurement damages the sample severely, thereby impeding time-lapse recordings. Finally, current laser ablation implementations and analysis are largely restricted to a single optical plane, which prevents a full study of curved tissues.

3.2.4.5 Force inference

Geometric Force inference methods compute the internal force balance of a tissue from images of the cellular contours (Figure 16i and Figure 16j). Internal forces include surface tensions (arising from the cortical cytoskeleton, adhesion proteins, or the plasma membrane), internal pressures, and the elastic and viscous response of the cellular components[64]. By neglecting inertial forces, viscous dissipation and elastic contributions (assuming long time scales), only two force sources are generally considered: cellular surface tensions and internal pressure. Force inference methods assume that tensions and pressures equilibrate at the vertices of the junctional network and at cell-cell interfaces, where Laplace's law, relating surface tension, pressure difference and curvature is invoked:

$$\Delta P = \gamma H, \tag{1.21}$$

where γ is the surface tension, H is the mean curvature and ΔP is the pressure difference.

With the assumptions mentioned above, relative tensions and pressures can be calculated without the need for a specific constitutive model of the system. Therefore, the tensions and pressure differences calculated with inference methods are determined up to a scaling constant factor, which can be obtained through an independent technique such as micropipette aspiration[205, 206] or TFM[207].

The assumptions behind force inference methods for epithelial tissues can be formalized using vertex models[24, 208] (Box 5).

BOX 5: Vertex models

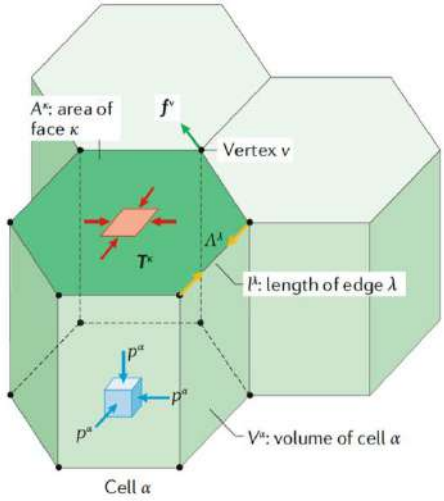

Box 5: *Illustrative representation of the parameters and variables of a vertex model: vertex ν, edge λ, face κ, cell α, edge length l^{λ}, face area A^{κ}, cell volume V^{α}, vertex applied force f^{ν}, edge tension Λ^{λ}, surface tension T^{κ} and cell pressure p^{α}.*

A vertex model describes the geometry of a tissue as a set of vertices marking the confluence of three or more cells, i.e. triple junctions. The mechanical description of vertex models can be formulated by means of the work function, with an internal and an external component:

$$\delta W = \delta W_i + \delta W_e. \tag{1.22}$$

The external work differential accounts for any external force applied on the vertices

$$\delta W_e = -\sum_{vertex\ \nu} f_e^{\nu} \delta x^{\nu}. \tag{1.23}$$

The internal work differential can be generally written as

$$\delta W_i = \sum_{cell\ \alpha} -P^{\alpha}\delta V^{\alpha} + \sum_{surface\ \kappa} T^{\kappa}\delta A^{\kappa} + \sum_{edge\ \lambda} \Lambda^{\lambda}\delta l^{\lambda} - \sum_{vertex\ \nu} f_i^{\nu}\delta x^{\nu}, \tag{1.24}$$

where α labels each cell, κ and λ label each cell surface and edge, respectively, and ν labels each vertex. δV^{α}, δA^{κ}, δl^{λ} and δx^{ν} represent variations in cell volume, surface area, edge length and vertex position, respectively; while P^{α}, T^{κ}, Λ^{λ} and f_i^{ν} indicate each cell's intracellular pressure, surface and line tensions, and internal dissipative forces applied on each vertex. A particular dissipative process is the internal viscosity of the epithelium, that can be modeled as

$$f_i^{\nu} = \sum_{vertex\ \nu', j} \alpha_{ij}^{\nu'} \frac{dx_j^{\nu'}}{dt}. \tag{1.25}$$

The equations describing the system are simplified for 2D flat monolayers, where the cells are assumed to be columnar and to have a uniform height. Thus, in Eqn. (1.24), the cell area takes the role of cell volume and the cell interfaces are treated as line edges with uniform line tension. Other energy functionals alternative to that in Eqn. (1.24) have been proposed in the literature[209], with similar results.

In a vertex model, the arrangement of cells in the tissue is described by a set of vertices that define the intersection of three or more cells. The mechanical state of the monolayer can be described by a work function, W, accounting for the work performed by cellular pressure and by surface tensions as the configuration of the tissue is perturbed. The out-of-balance forces at each vertex in the model can then be computed as

$$f^{\nu} = -\frac{\delta W}{\delta x^{\nu}}, \tag{26}$$

where f^{ν} represents the total force acting on vertex ν, δW is the variation of work function and δx^{ν} denotes the variation of the position of vertex ν along the coordinate x^{ν} (Box 5). Mechanical equilibrium requires that $f^{\nu} = 0$, providing one equation per vertex, which linearly depends on the unknown pressure and tension of adjacent cells. Thus, it is possible to establish an algebraic system of equations for cell pressure and surface tension just from the geometrical information of the epithelium[210]. However, by imposing force-balance at the vertices where multiple cells meet, this system of equations is underdetermined[211]. Different approaches have been used to make the problem overdetermined, so the force balance equation can be solved in the least squares sense. One option is to assume uniform tension, thereby reducing the unknowns to only the cell pressures[212]. This simplification is exact for foams and has been applied to model specific tissues such as the ommatidia of the *Drosophila* retina[213]. Alternatively, it can be assumed that every cell has the same pressure, keeping only the tensions as unknowns in the force equilibrium equation[214]. In a different approach, by observing that most of the cell interfaces in epithelia are under positive tension, Bayesian statistics have been applied to reduce the number of unknowns while calculating both internal pressures and cortical tensions[211].

Recently, force inference has been combined with TFM 2D (section 3.2.2.1) to study motile confluent epithelia, in an experimental setup similar to MSM[207] (section 3.2.2.3). By knowing the tractions applied by the epithelial tissue, this approach enables the calculation of both the absolute tissue tensions and pressures as well as the rheology of the monolayer. All the previous methods model the cell edges as straight lines between vertices, a geometry that is not always seen in epithelia. By relaxing the straight cell interface assumption, the force balance equations become overdetermined[215]. This method, called CellFIT-2D[215] or Laplace inference[216], demands a much higher accuracy of image segmentation algorithms to detect the curvature of cell

boundaries[217]. Furthermore, the curvature of a cell-cell boundary in a 2D image will be smaller in general than that of the actual 3D surface. Laplace inference is well suited for tissues with high cell-edge curvature that is uniform along each cell boundary. However, for small or non-uniform curvatures along a cell edge, it is prone to artifacts and errors that propagate to cell neighbors. These errors are shown to increase with increasing tissue size[216].

The problem of geometric force inference in 3D has been undertaken as an extension of CellFIT-2D called CellFIT-3D[218]. The geometry of the sample is detected by segmentation of 3D image stacks. Due to the complexity of accurately segmenting fluorescent 3D images of cells and the subsequent extraction of surface curvatures, CellFIT-3D is only used to calculate cell tensions, while a natural theoretical extension to calculate pressures is suggested. In experimental setups where slow motions cannot be assumed, the introduction of viscosity in the force balance equation is required. In those cases, vertex models have been used to calculate the viscosity component of the internal forces of a cell monolayer[219, 220]. In an approach called *Cinemechanometry* (CMM)[208] or *Video Force Microscopy*[221], cell pressures and tensions have been computed from the time evolution of the monolayer shape.
Geometric Force Inference methods have been successfully applied *in vivo* to study the mechanics of development in *Drosophila*[221, 222] and *C. elegans* [223]. They have also been pivotal to understand the role of cell shape and mechanical stress orientation in mitosis in *ex vivo* models of *xenopus* tissue[224]. Among other contributions, force inference methods have also been used to study the process of hair-cell determination in the avian cochlea[214], and the effect of interstitial fluid osmolarity in the tissue surface tension in progenitor cell segmentation during gastrulation of the Zebrafish embryo *in vivo*[225].

Force inference methods have many advantages[63]: they are non-destructive, only requiring imaging of the tissue, they make minimal assumptions about the origin of the forces, they are well suited to be combined with other methods such as suspended monolayers (section 3.2.2.4), and they provide cellular and tissue resolution. Limitations include that they assume positive and constant tensions along each cell edge, which might not be true for wiggly junctions[216]; they only calculate ratios of tensions and pressure differences unless other techniques such as micropipette aspiration are used to provide

absolute measurements of tensions[205, 206]; they depend on the accurate segmentation of the cell contour in the tissue; and the calculation is currently limited to tractions transmitted between cells by contact, disregarding any force exerted by the cells on the substrate. The assumptions behind force-inference methods can be systematically tested in various ways, including the geometrical inspection of the junctional network (wiggly junctions or non-uniform curvature being signs of non-compliance), the *a posteriori* quantification of the error in the force-balance equations $f^{\nu} = 0$, or comparisons with measurements relying on other techniques such as servo-null pressure measurements, extended micro-pipette aspiration or laser ablation tension measurements[216]. Furthermore, observation of cellular processes with mechanical consequences but not accounted for in the conceptual framework underlying force inference, such as protrusive behavior, cortex polarization or the presence of actin belts, may require reconsideration of the results or refinements of the underlying model.

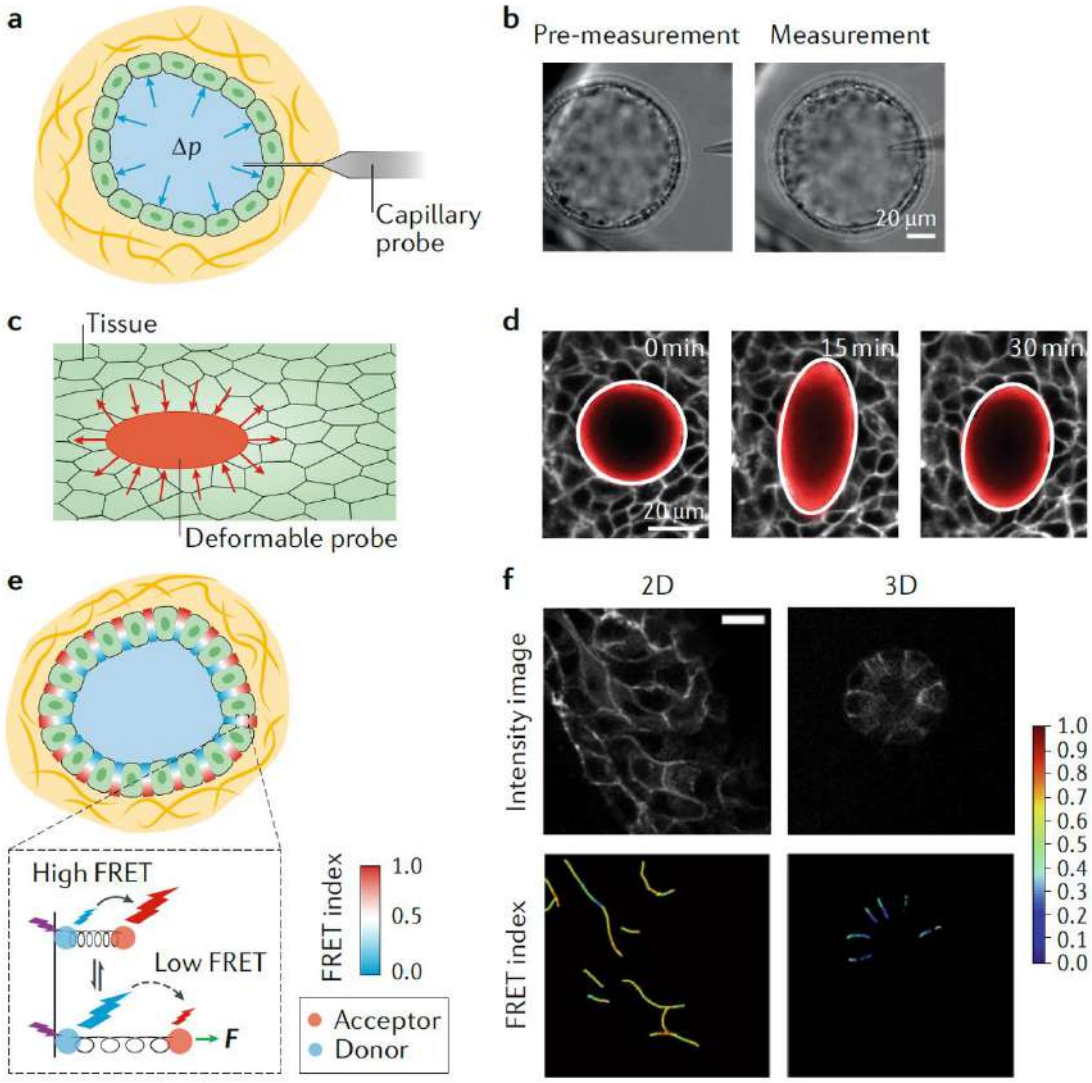

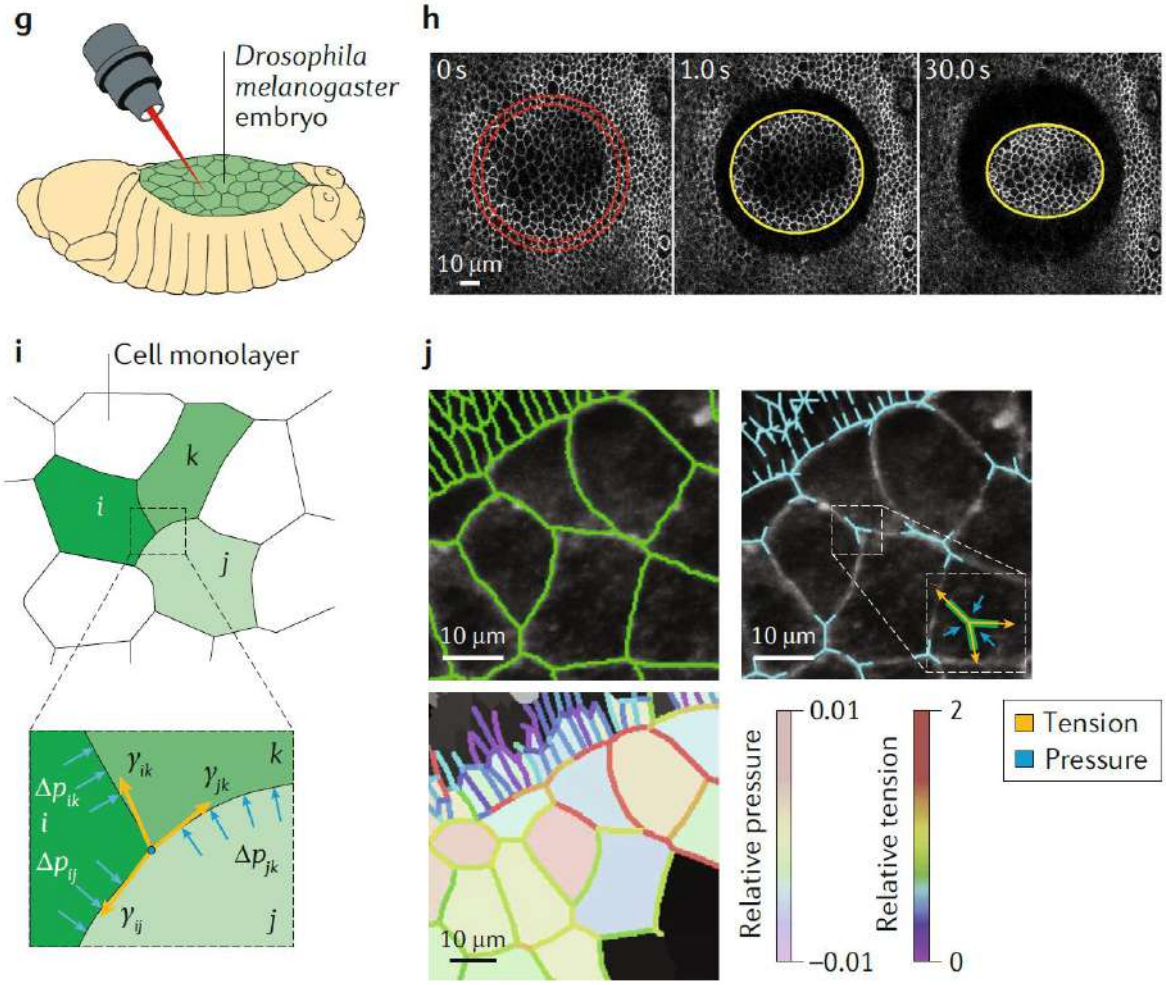

Figure 16: ***Techniques to measure internal stresses in vivo****.* ***a****, Servo null methods measure the luminal pressure of a tissue by inserting a capillary probe directly into the lumen.* ***b****, The servo-null applied to the luminal cavity of a mouse blastocyst before (left) and during (right) measurement[163].* ***c****, Inert deformable probes can be inserted in a specimen to assess its local stress state.* ***d****, Liquid drop inserted in a tissue, before (left) and after (center and right) deformation[226].* ***e****, FRET sensors are genetically encoded molecular springs whose deformation is reported by a pair of resonant fluorophores.* ***f****, Junctional tension reported by FRET sensors in an epithelial monolayer and in an epithelial acinus[190].* ***g****, In the laser ablation technique, a specimen is cut by using a pulsed laser, and its internal stress is released.* ***h****, Circular laser cut (left) performed in a Drosophila melanogaster embryo, and asymmetric retraction (center and right) of the cut patch due to the differential internal tension along the x and y axes[195].* ***i****, With force inference methods, cellular pressures and inter-cellular tensions can be inferred from the geometry of the tissue.* ***j****, Illustration of a force inference method. Cell monolayer segmentation (left), tension and pressure location (center), and calculated values for the cellular pressure and cell-junction tension (right)[64, 217].*

3.2.5 Summary and discussion of pros & cons

A large and diverse suite of techniques is now available for researchers to measure stress with subcellular resolution in living tissues (see summary in Table 1). These techniques remain experimentally and computationally challenging, but their use is becoming

progressively widespread thanks to the increased availability of open source software[79] and standardized protocols. No technique is a one-size-fits-all solution, and there are a number of considerations that need to be taken into account before deciding which technique is more suitable to address a specific question. The highest resolution is provided by tools to measure stress in 2D cultured monolayers, but these flat monolayers do not capture essential features of tissues *in vivo*. Conversely, *in vivo* technologies might have more physiological relevance, but they generally do not provide absolute values of stress. The techniques reviewed here are not only relevant to illuminate biological processes in development, homeostasis and disease, but also to advance our understanding of active matter physics. In this context, measuring stress in reductionist tissues like micropatterned monolayers, or even unidimensional multicellular chains, is the pertinent strategy to address questions such as what are the master equations that govern the dynamics of aggregates of active particles. A general problem of the techniques reviewed here is that they are still limited to a relatively low throughput. Overcoming this limitation is crucial to bring mechanobiology from the basic science arena to applications in industry and medicine.

To summarize this section:

- Mechanical stresses generated by cells determine the fate, form and function of living tissues.
- Several techniques have been developed to measure tissue stress with subcellular resolution.
- State-of-the-art technologies enable high-resolution mapping of time-varying stress fields in 2D and 3D cell cultures. 3D methods are much more recent and less reliable. **Most discoveries in mechanobiology are based on 2D measurements and also based on 2D experimental setups** (section 3.2.2).
- Measuring stresses in vivo remains an outstanding challenge that is currently addressed through the combination of image-based computational modelling and the insertion of soft inclusions in tissues of interest.

Table 1: Technique Summary

Technique	Measured quantity	Output	Strengths	Limitations	Bibliography
2D IN VITRO AND EX VIVO					
2D Traction Force Microscopy	2D displacement of the substrate's top surface.	2D traction vector.	Absolute measurement. Simple implementation. Mechanical properties of the substrate can be tuned.	Very sensitive to noise. Neglects out-of-plane tractions.	[3, 7, 8, 10, 67, 68, 74-102]
Micropillars	2D displacement of pillar tip.	2D traction force.	Absolute measurement. No reference image is needed. Clear physical interpretation of the measured force.	Discrete adhesion. How topography affects cell behavior is unclear. Deformable substrate under pillars affects measurements.	[10, 103, 104, 106-112]
Monolayer Stress Microscopy	Displacement of the substrate.	Local internal monolayer stress tensor.	Accesses local internal stresses of the tissue.	Linear, uniform and isotropic elasticity is generally assumed for the tissue. Uniform thickness is assumed.	[7-9, 67, 72, 73, 91, 113-122, 227]
Suspended monolayers	Cantilever displacement.	Average internal monolayer stress.	Stress or strain are imposed by the user.	Local stress is not obtained.	[123-129]
3D IN VITRO AND EX VIVO					
2.5D Traction Force Microscopy	3D displacement of a gel substrate.	3D traction vector.	3D traction can be measured.	Anisotropic 3D point spread function. Very sensitive to noise (high quality measured displacements are needed). Computational complexity.	[69, 101, 102, 133-137, 145-147]
3D Traction Force Microscopy	3D displacement of the ECM surrounding the tissue.	3D traction vector.	3D traction can be measured. Physiologically relevant ECM.	Anisotropic 3D point spread function. Non-linear material behavior of the surrounding ECM. Cells remodel and degrade ECM. Computational complexity.	[70, 132, 138-144]
IN VIVO					
Servo-null methods (pressure gauges)	Electrical resistance at the capillary tip.	Luminal pressure.	Direct access to luminal interstitial pressure.	Invasive. Complex experimental setup.	[150-165]
Inclusions	Inclusion shape/ deformation.	Local tissue stress tensor components.	Able to report 3D tissue stress.	Only accesses stress value near to the inclusion. Might perturb force transmission in the tissue. Requires microinjection in vivo	[71, 166-171, 179, 180, 226]
FRET sensors	Fluorescence intensity.	Local tension at the molecular level.	Genetically encoded. Local measurement.	Only reports tension, not compression. Calibration issues. No directional information. Unclear effect of the surrounding medium and fluorophore stability.	[174, 181-190, 192]
Laser ablation	Recoil velocity.	Relative tissue stress.	High spatio-temporal control of the perturbation. Easy implementation.	Invasive. Relative measurements unless viscosity of the tissue is assumed.	[193-204]
Force inference	Tissue shape.	Relative local internal stress.	Very simple experimental implementation. Non-invasive.	Only relative measurements. Computational complexity. Highly sensitive to segmentation noise.	[24, 69, 205-215, 217-225]

Table 1: Summary of the techniques available to measure the mechanical stresses of living tissue

4 MEASURING STRESSES IN THREE-DIMENSIONAL EPITHELIA OF CONTROLLED SHAPE

4.1 Introduction

The acquisition of a three-dimensional structure by epithelial sheets is a remarkable mechanical phenomenon that requires a tight control of cellular deformation, mechanical stress, and luminal pressure. How these mechanical variables evolve together to shape three-dimensional epithelia is unknown, however, because current techniques to map epithelial mechanics are largely restricted to two-dimensional layers seeded on a flat substrate[91, 228-230] or freely standing between cantilevers[231] (as explained in 3.2.2). Currently, there are very few 3D techniques to measure forces and stresses, and the existent ones have many drawbacks and hypothesis to be assumed (section 3.2.3). To fill this gap, here we report direct measurements of traction, tension, pressure and deformation in three-dimensional epithelial monolayers of controlled size and shape. In this chapter **we present a new technique to investigate the mechanics of three-dimensional epithelia that will be analogous to a bulge test in material science, applied to monolayers of cells.** The main idea is to take profit of a remarkable feature of some epithelial cell lines that are known to spontaneously form blister-like structures called domes.

4.2 Micropatterned epithelial domes

To shape epithelial monolayers in 3D, we used transmural pressure as morphogenetic driving force. We seeded MDCK cells on a soft PDMS substrate that was homogeneously coated with fibronectin except for micropatterned non-adhesive areas of precise size and shape (Figure 17). A more detailed explanation about the gel fabrication and the micropatterning technique (micro-contact printing) is described in the APPENDIX ranging from 8.4.1 to 8.4.5.

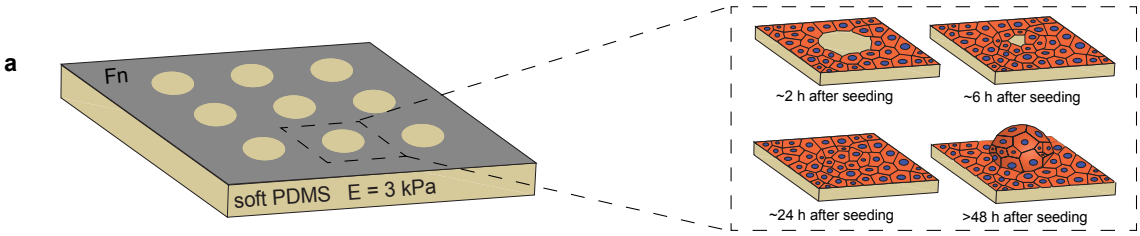

Figure 17: ***Generation of epithelial domes of controlled size and shape****. a, Scheme of the process of dome formation.*

A few hours after seeding, cells covered the adherent regions of the gel and, with time, they invaded the non-adherent areas through mechanisms independent of substrate adhesion. Since adherent MDCK cells are known to actively pump osmolytes in the apico-basal direction [232-234], we reasoned that fluid pressure should build-up over time in the interstitial space between cells and the impermeable substrate, leading to tissue delamination from the substrate precisely in the non-adherent regions. In agreement with this rationale, we observed the spontaneous formation of large multicellular epithelial domes closely following the micropatterned shapes (Figure 18).

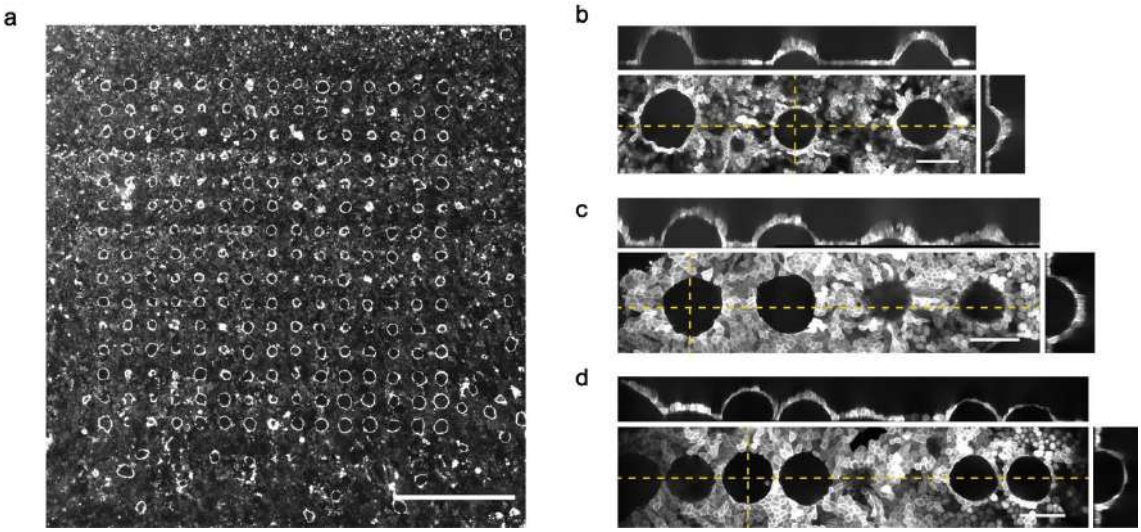

Figure 18: ***Experimental images of epithelial domes. a****, Top view of an array of 15×15 epithelial domes (representative of n =10 micropatterned substrates). Scale bar, 1 mm.* ***b-d****, Confocal x-y, y-z and x-z sections of MDCK-LifeAct (see 8.4.7 for details on the cell lines) epithelial domes with a circular basal shape and varying spacing (representative of n=10 micropatterned substrates). Scale bar, 100 µm.*

This approach allowed us to analyze large arrays of 3D epithelial domes with highly reproducible basal shapes such as circles, rectangles and stars (Figure 18, Figure 19).

If adhesive protein concentration was high enough, domes did not delaminate beyond the predefined non-adhesive pattern. In contrast with spontaneous doming by progressive delamination [232-239], our strict control of dome footprint allowed us to decouple

epithelial mechanics from cell-substrate adhesion and gave us access to large variations in the ratio between dome height and basal size [240].

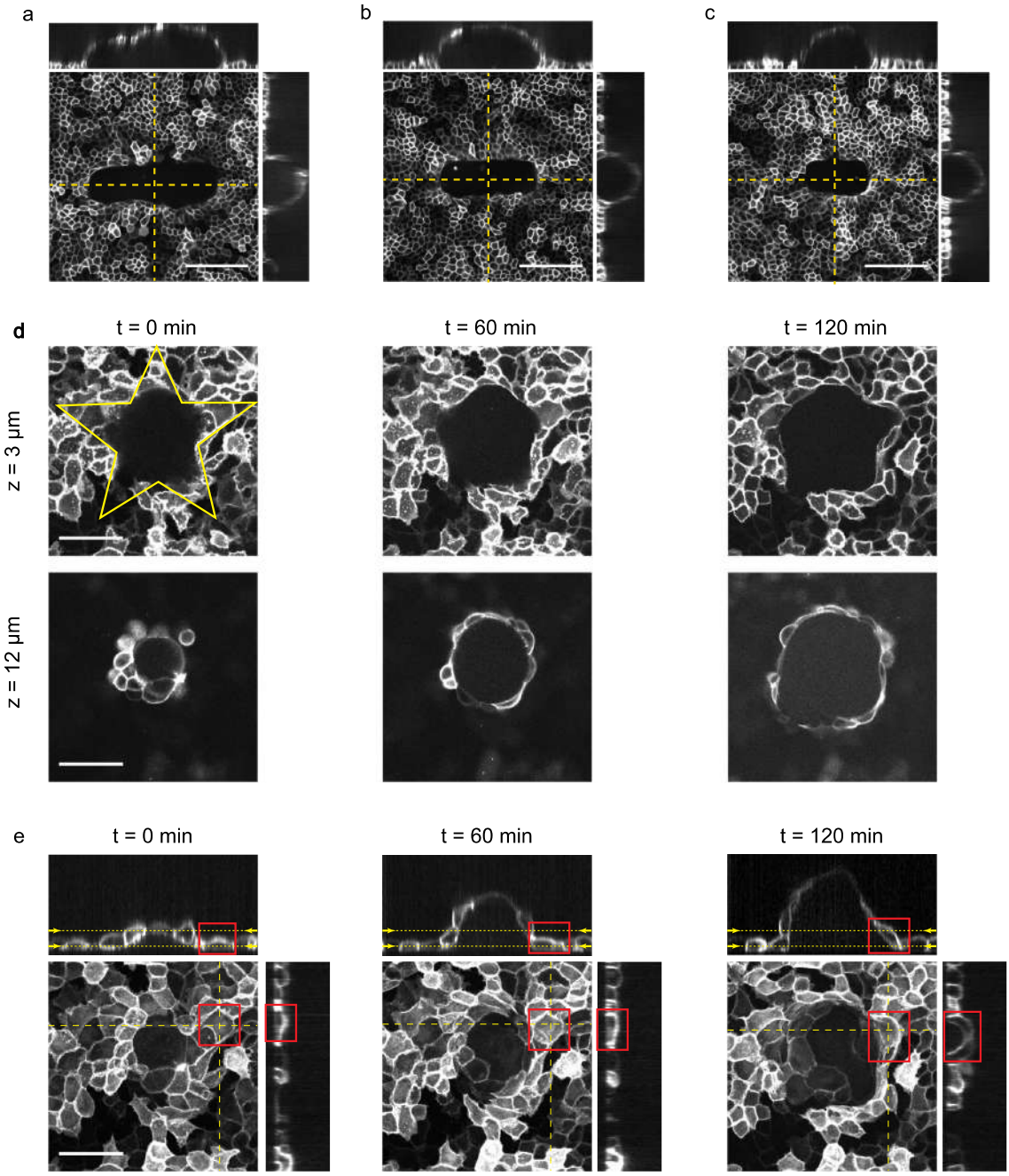

Figure 19: ***Domes can have different basal shapes. a-c,*** *Confocal x-y, y-z and x-z sections of domes with rectangular basal shapes and varying size. MDCK-CAAX cells. Scale bar, 100 µm (representative of n=3 micropatterned substrates).* ***d****, Time evolution (0, 60 and 120 min) of a representative dome with a star-shaped footprint. The patterned footprint (yellow) was obtained from images of the fibrinogen-labelled substrate. Each row shows a different z-plane (labelled by doted yellow lines in the x-y profiles in* ***e*** *(n=3 micropatterned substrates). Scale bar, 50 µm.* ***e****, Time evolution (0, 60, 120 min) of the same star-shaped dome showing the rare delamination of a single cell (red rectangle) at one tip of the star. Images are maximum intensity projections with confocal x-z and y-z sections along the yellow dashed lines (n=3 micropatterned substrates). Scale bar, 50 µm.*

4.3 Measurement of dome mechanics

To measure mechanics of the domes, we focused on circular patterns and implemented 3D traction microscopy (explained in 3.2.3.1 and in the methods section 8.4.6) to determine the three components of tractions at the surface of the soft PDMS substrate (Figure 20). This forces per unit area are the ones exerted by the fluid inside the cavity and the cells from the monolayer over the substrate.

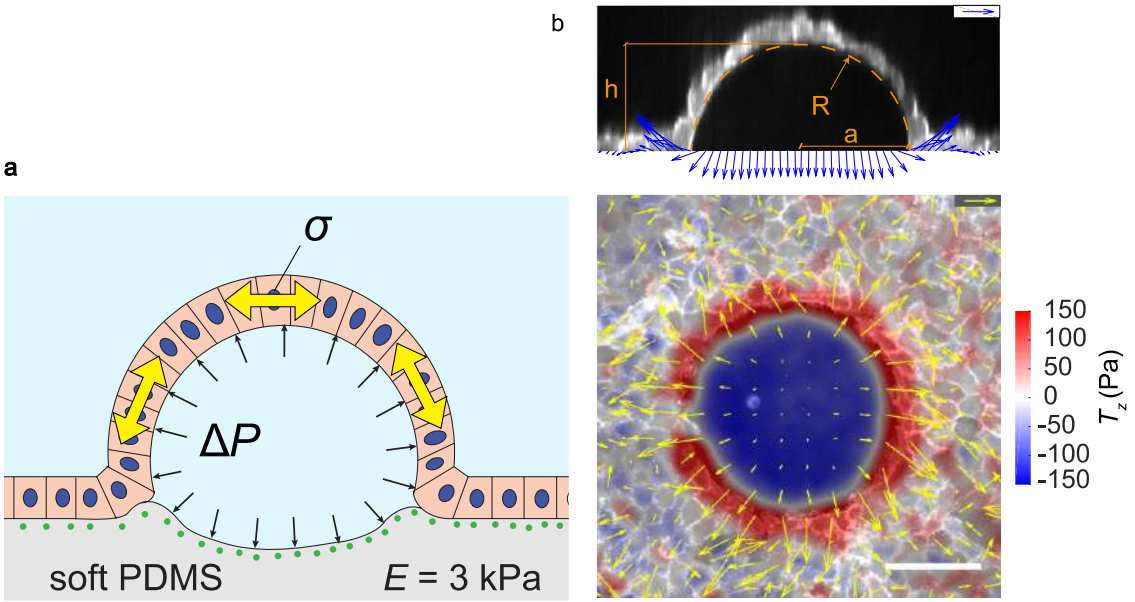

Figure 20: ***Measurement of luminal pressure and dome tension. a****, Scheme of dome mechanics. The lumen is under uniform pressure ⊿P (black arrows) and the free-standing monolayer is under surface tension σ (yellow arrows).* ***b****, Traction vectors of a dome of MDCK-LifeAct cells. Top: lateral view. Bottom: 3D traction maps overlaid on a top view of the dome. Yellow arrows represent in-plane components and the color map represents the vertical component. Scale bar, 50 µm. Scale arrows, 150 Pa (representative of n=13 domes).*

Tractions in the adherent regions showed large 3D fluctuations without a clear spatial pattern (Figure 20b). By contrast, non-adherent areas exhibited systematic normal and nearly uniform negative tractions that indented the gel substrate. In a narrow annular region of ~10 µm at the interface between adherent and non-adherent areas, the traction vector consistently exhibited a positive normal component pulling the substrate upward. These observations, along with the morphology of epithelial domes, established that the lumen was in a state of hydrostatic pressure, and that the free-standing part of the monolayer sustained tension to balance this pressure (Figure 20a).

We then wondered if we could map the tensional state of the dome, even though constituent cells did not directly generate tractions on the substrate. To do so, we examine in the next section the mechanics of such a system and the relation with its geometry.

4.3.1 Mechanics of a thin axisymmetric membrane under uniform pressure

We model here the mechanics of epithelial domes by idealizing them as structural membranes, that is, surfaces supporting a two-dimensional tangential tensional state [15, 229, 231], subject to uniform transmural pressure. Such a model neglects bending moments, consistent with the sharp contact angle of our domes, or out-of-plane shear stresses in the epithelial layer. We further assume that the dome shape is axisymmetric, in agreement with our observations, and that the stress state is also axisymmetric. As a result, the principal directions of the curvature and the surface stress tensors are the circumferential and meridional directions, and local shape and surface tension can be characterized by the radii of curvature ρ_c (in the circumferential direction) and ρ_m (in the meridional direction) and the principal surface tensions σ_c and σ_m along these directions. As shown in [241], under this setting the local statements of balance of linear momentum in the normal and tangential directions can be written as:

$$\sigma_c = \frac{\Delta P}{2}\left(2 - \frac{\rho_c}{\rho_m}\right)\rho_c \tag{4.1}$$

$$\sigma_m = \frac{\Delta P}{2}\rho_c \tag{4.2}$$

Our measurements show that epithelial domes very closely resemble spherical caps of radius R (Figure 20b), and hence $\rho_c = \rho_m = R$. The equations above then reduce to:

$$\sigma_c = \sigma_m = \sigma = \frac{\Delta P R}{2} \tag{4.3}$$

that is a state of isotropic surface tension obeying Laplace's law. Since our observations show that pressure and curvature are uniform to a very good approximation, surface tension should also be nearly uniform on our domes and it can be represented by the scalar value σ. Such a tense spherical membrane should exert tractions on the substrate tangential to the surface of the dome. However, measured tractions at the rim of the adhered region were generally not tangential to the domes (Figure 20b), suggesting that both the tense free-standing monolayer and the adjacent planar tissue contributed to the forces transmitted by marginal cells on the substrate.

Laplace's law allowed us to measure epithelial tension of the domes since the negative normal traction in the non-adherent regions provides a direct readout of ΔP, and R could be measured from confocal stacks. We found tissue tensions in the mN/m range, of the same order of magnitude than previous measurements in 2D monolayers [229, 231].

4.3.2 Tension measurements are able to capture drug perturbations

To test the principle behind our tension measurement, reminiscent of the bulge test to characterize materials at the macroscale [242, 243], we perturbed the system with Rho Kinase inhibitor Y-27632 (see methods in 8.4.8), known to reduce tissue tension [244]. Because the epithelial barrier has finite permeability to water, the enclosed volume, and hence R, cannot change instantaneously upon this perturbation. Consequently, Laplace's law requires tension relaxation be paralleled by a pressure drop. This prediction was confirmed by our measurements. Immediately after the perturbation, volume and curvature remained continuous whereas luminal pressure exhibited a discontinuous ~3-fold drop (Figure 21, Figure 22).

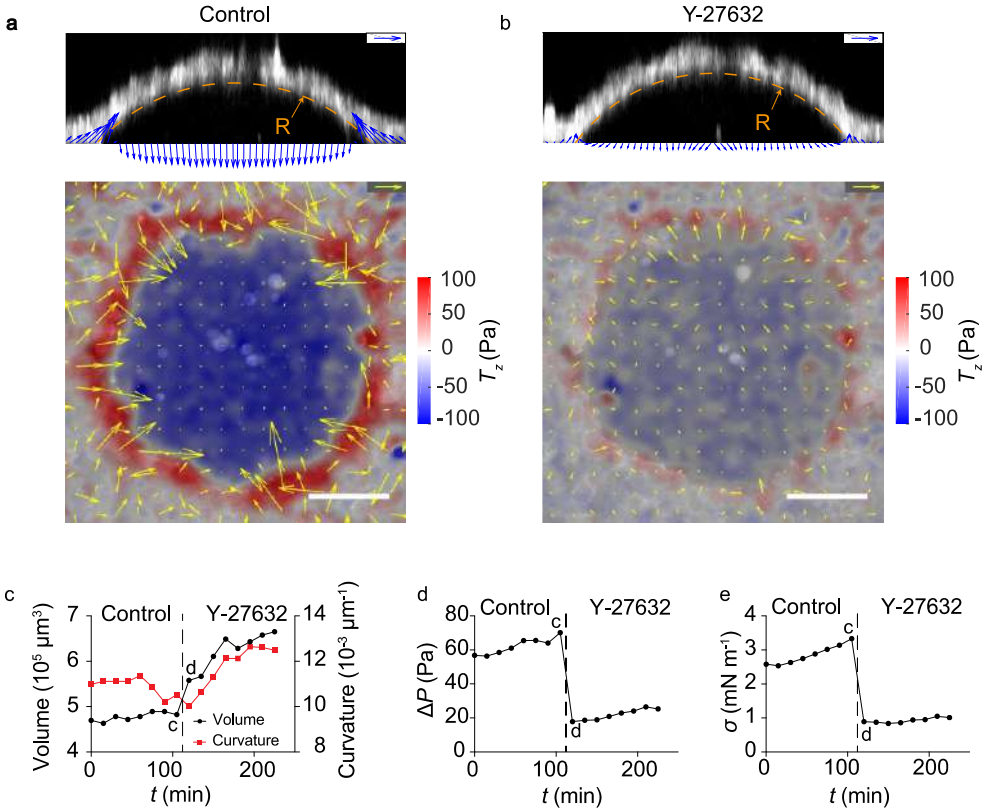

Figure 21: ***Perturbing the dome with Y27632. a**, **b**, Tractions exerted by MDCK-LifeAct cells before (Control) and after 5 min incubation with 30 µM of Y-27632. Scale bar, 50 µm. Scale arrows, 75 Pa. **c-e**, Time evolution of dome volume and curvature (c), pressure (d) and tension (e) before (Control) and after adding Y-27632. The time points corresponding to panels **a** and **b** are labelled in **c-e** (representative of n=3 domes).*

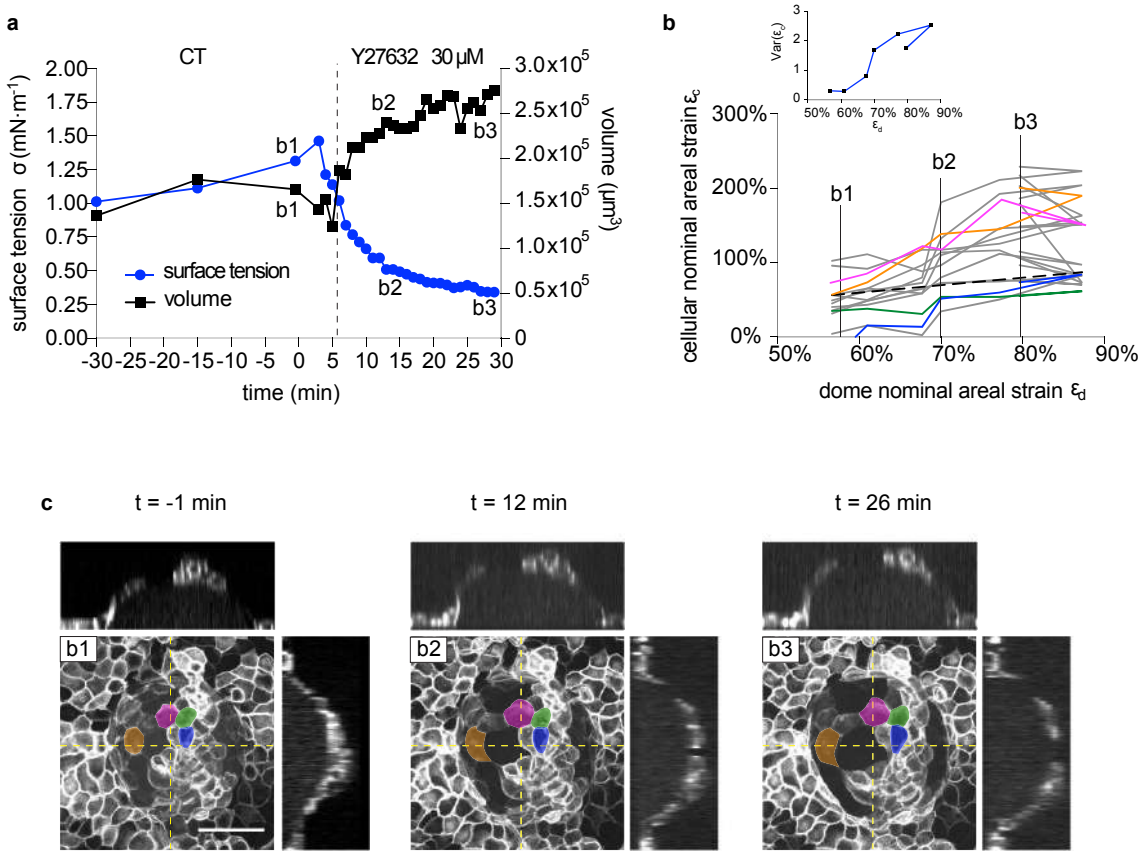

Figure 22: ***Dome response to inhibition of tension.*** ***a****, Time evolution of surface tension and volume of a representative dome in response to Y27632 (30 µM, added at t = 0 min).* ***b****, Cellular areal strain ε_c as a function of dome nominal areal strain ε_d during dome swelling. Only a subset of cells is represented and most cells with $\varepsilon_c < \varepsilon_d$ have been omitted for clarity. Colored lines represent the cells labelled in* ***c****. Dashed line represents the relation $\varepsilon_c = \varepsilon_d$. The inset represents the variance of ε_c within the dome as a function of ε_d.* ***c****, Maximum intensity projection and x-z and y-z confocal sections of an epithelial dome of MDCK-CAAX cells before (-1 min) and after (12 min, 26 min) addition of Y27632 (30 µM, added at t = 0 min). The time evolution of colored cells is depicted in* ***b*** *using the same color code. Scale bars, 50 µm. Data are representative of n=3 experiments.*

We also observed that domes progressively swelled after tension/pressure relaxation, suggesting a poro-mechanical coupling by which the mechanical perturbation drove water permeation across the epithelial membrane. Since Y-27632 could be affecting not only contractility but also permeability [245], we conducted a separate set of experiments to examine water transport by subjecting domes to hyper-osmotic shocks while monitoring dome volume which are included in the next chapter 5.

4.4 Summary and discussion

Epithelial domes are, in short, a micro-bulge test that follows the same mechanical principles as the bulge test that is used in material science. With this technique, we are able to induce the formation of axisymmetric and non-axisymmetric shapes and we can also control the spatial distribution up to a certain degree which, in the end, is limited by the micro-contact printing technique. The size of the basal footprint of the domes is also limited by the fact that, in general, cells are not able to close very big gaps that are not coated with any ECM protein such as fibronectin. In our study, MDCK cells were able to close, at maximum, gaps of about 100 μm in diameter. This is a limitation of the technique and new experimental setups should be put in practice to overcome it.

Epithelial domes very closely followed a spherical cap geometry (Figure 20b), which implies that their surface tension σ was isotropic and uniform. Under this geometric configuration, σ in the dome must obey Laplace's law $2\sigma = R\Delta P$, where ΔP is the transmural pressure and R the radius of curvature of the spherical cap. Under the hypothesis stated in the section 4.3.1 (considering the dome monolayer as a membrane made of an isotropic material) the reciprocal is also true and thus, the only possible shape for a membrane that has a uniform and isotropic tension and that is bounded by a circle is a spherical cap. Moreover, Laplace's law is nothing but applying the conservation of linear momentum or, equivalently, stating that the dome is in mechanical equilibrium. As explained in Box 4, the equilibrium equation for a continuum media in which we neglect body forces is $\nabla \cdot \boldsymbol{\sigma} = \mathbf{0}$. This equation applied to a curved surface in the normal direction is precisely Laplace's law. **We are in a very special case in which, thanks to the symmetry of the problem, we do not need any constitutive equation for the epithelia to completely determine the stress state at every point of the dome**. It is also very remarkable that the stress state can be summarized just with a single scalar value which is the surface tension σ that is uniform all over the dome.

Interestingly, tractions at the rim of the adhered region $\boldsymbol{T}$ were generally not tangential to the domes, (as one could expect for a capillary system) suggesting that both the tense free-standing monolayer and the adjacent planar tissue contributed to the forces transmitted by marginal cells on the substrate (Figure 20a).

5 EPITHELIAL HYDRAULIC TRANSPORT

5.1 Dome hydraulics

In this chapter, we describe experiments probing transepithelial transport across domes and theoretical models to interpret these experiments. We show that our experimental setup enables not only mechanical measurements but also an absolute and non-invasive quantification of transepithelial transport.

5.2 Main hypotheses

Dome swelling is thought to be driven by active ionic pumping across the monolayer towards the interstitial space between cells and the substrate, followed by passive water transport to equilibrate the osmotic imbalance[232-239]. Ionic and water transport across the monolayer can occur both at the dome location and in the adherent part of the monolayer[239], and therefore transport into or out of the lumen under a dome can in principle occur (1) through the free-standing epithelial membrane and/or (2) through exchanges between the lumen and the interstitial space below the adherent monolayer.
In our system, transport across the free-standing epithelial membrane seemed to be much larger than ionic or hydraulic leaks between the lumen and the interstitial space below the adherent monolayer.
We observed swollen domes in close vicinity (about 15 μm) of non-adherent patterns that were not successfully invaded by cells, Figure 23a. The lumen of one dome was separated from a second lumen or the medium by one or two adherent cells. These observations suggest that the ionic and hydraulic screening lengths as defined in[246] are smaller than the typical cell size. These screening lengths measure the relative ease between lateral transport under the adherent monolayer and across it and indicate the length over which osmotic/hydraulic pressure under the adherent monolayer is screened from a free edge (here, the medium or a lumen). If these screening lengths were larger, osmotic/hydraulic differentials between neighboring lumens would quickly equilibrate through interstitial fluxes and dome dynamics would become coupled. Similarly, domes two cells apart from the free medium would not form.

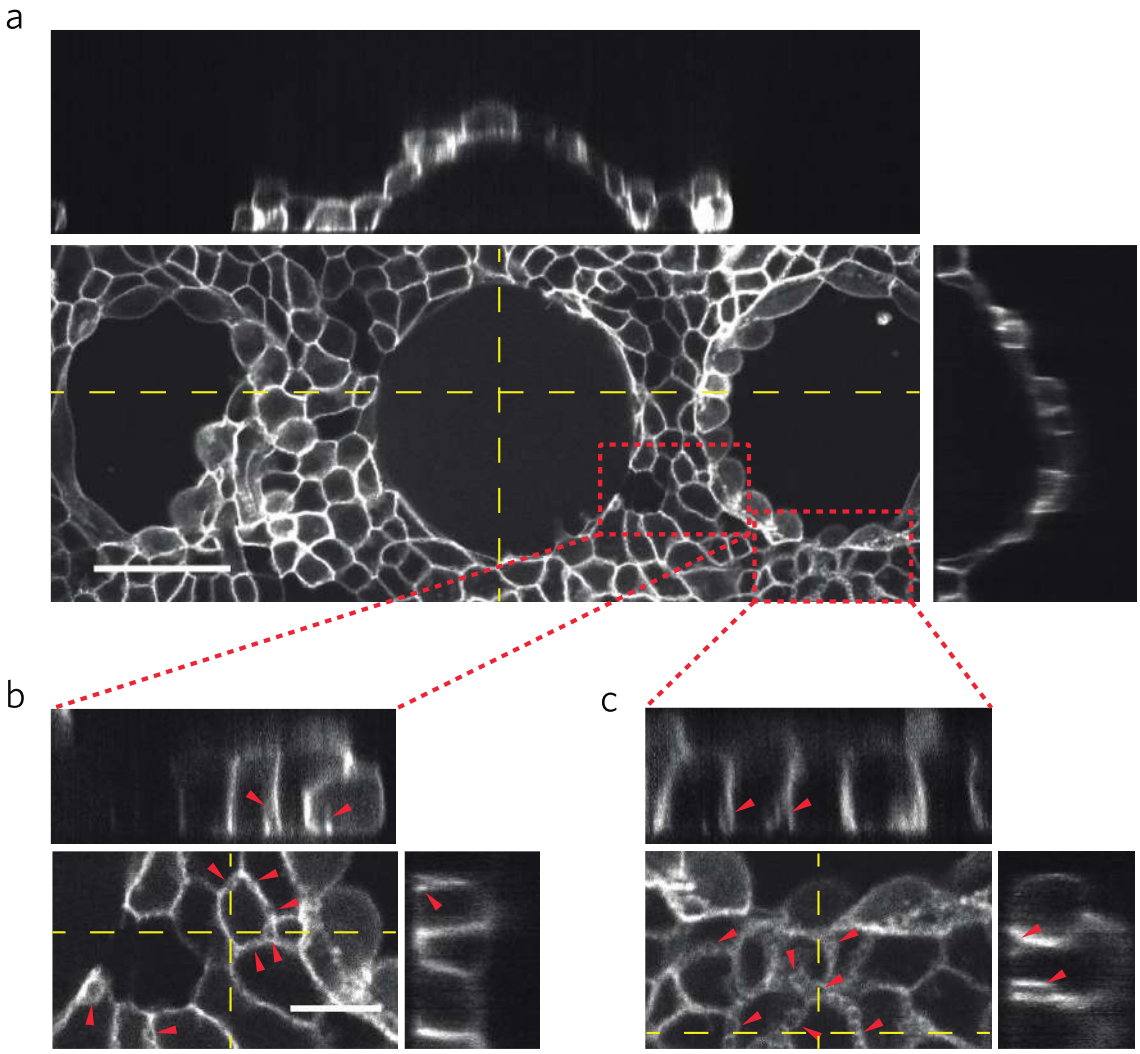

Figure 23: ***Domes can grow near opened holes. a****, Representative example of a MDCK dome surrounded by two micropatterned areas that had not been invaded by cells. Confocal image of the basal plane (center) along with x-z and y-z sections along the dashed yellow lines. Scale bar, 50 µm.* ***b-c,*** *Confocal basal plane along with x-z and y-z sections along the dashed yellow lines for the areas marked by dashed red rectangles in* ***a****. Red arrowheads indicate micron-sized basal bubbles between cells. Scale bar, 10 µm.*

Further supporting the absence of significant lateral leaks, we systematically observed micron-sized basal bubbles, predominantly located at cell-cell junctions but also at the basal membrane, which indicate significant pressurization of the interstitial fluid[97, 247], Figure 23b and Figure 23c. This pressurization, presumably a result of active ionic pumping across the adherent monolayer, was capable of partially separating the plasma membranes of adjacent cells or of delaminating the basal membrane from the substrate. These bubbles allow us to estimate the pressure in the interstitial space. Their radius of curvature is of about 1 micron, about two orders of magnitude smaller than that of domes. Since cortical tension is in the order of 1 mN/m[97], similar to that in domes, these rough

estimations together with Laplace's law suggest that pressure in the basal bubbles is much larger than in the lumens. Since basal bubbles are systematically present in the very close vicinity of lumens or free edges, these observations further suggest that the ionic/hydraulic screening lengths are very small in our system.

In summary, our data suggests that ionic/hydraulic transport underneath the adherent monolayer was very small compared to trans-epithelial transport in our experiments, leading to very small ion/water exchange between the interstitial space under the adherent monolayer and the lumen under a dome. Consequently, we account for water and ion transport only across the dome surface to model luminal dynamics. We model the lumen as a fluid cavity enclosed by a semi-permeable membrane allowing passive water permeation, actively pumping osmolytes and capable of withstanding mechanical tension (the free-standing monolayer) and an impermeable substrate. In agreement with our observations, we assume that domes conform to a spherical cap geometry with radius of curvature R.

5.3 Stresses, pressures and tensions

We denote by p_w the water pressure in the medium, or water chemical potential, and by π the osmotic pressure, which according to the van't Hoff equation can be approximated as $\pi = \bar{R}TM$, where $\bar{R}$ is the gas constant, T is the absolute temperature, and M is the osmolarity of the solution. Assuming that the medium is a Newtonian fluid, the stress tensor of the solution is $\boldsymbol{\sigma} = 2\eta\boldsymbol{d} - (p_w + \pi)\,\boldsymbol{Id}$, where η is the viscosity, $\boldsymbol{d}$ is the rate-of-deformation tensor and $\boldsymbol{Id}$ is the identity tensor. As discussed in the previous section 4.3, we assume that surface tension in the epithelial monolayer is uniform and isotropic, and denoted by σ.

5.3.1 Osmolarity can be assumed to be uniform

Since our domes are dynamically evolving out-of-equilibrium, osmolarity could be non-uniform and the viscous stresses in the fluid could play a mechanical role. Since M is governed by a diffusion equation, the osmolarity equilibration time will be in the order of $t_{\text{diff}} \approx L^2/D$, where $L \approx 10^{-4}\ m$ is the characteristic dome size and D is the molecular diffusion coefficient. Taking a typical value of $D \approx 10^{-9} m^2/s$ and according to this argument, osmolarity will become homogeneous after $t_{\text{diff}} \approx 10\ s$ in a length-scale commensurate to L, i.e. in the luminal solution or in the external solution around the

dome. Since the typical time-scales of our experiments are much longer, we can assume that M is uniform in the luminal and in the external solutions, although in principle there will exist an osmolarity jump across the epithelial barrier $\Delta M = M^{lum} - M^{ext}$.
As a result, the osmotic pressure π is constant in the luminal solution and it is also constant in the external solution. They are noted, respectively, π^{lum} and π^{ext}. The osmotic pressure π can exhibit a jump across the semi-permeable membrane, $\Delta\pi = \pi^{lum} - \pi^{ext}$ because of the active ionic transepithelial pumping.

5.3.2 Water pressure can be assumed to be uniform

We can estimate the viscous stresses in the medium as $\sigma^{visc} \approx \eta V/L$, where V is a typical velocity during dome dynamics. The most rapid events are dome collapses, which can last a few minutes and displace the epithelial barrier by about 50 μm. With these estimates, $\sigma^{visc} \approx 10^{-5}$ Pa. When compared with the Laplace pressures measured in our experiments in the order of 100 Pa, we conclude that viscous stresses can be neglected. This further allows us to conclude that p_w is uniform in the luminal (p_w^{lum}) and external solutions (p_w^{ext}), since balance of linear momentum in the fluid neglecting the hydrostatic effect of gravity (which in our experiments produces hydrostatic pressure differences at the scale of the dome of at most 0.5 Pa) becomes $\nabla p_w + \bar{R}T\nabla M = 0$ and we have argued in the previous paragraph that $\nabla M = 0$. Despite the epithelial membrane is assumed to be permeable to water, p_w can exhibit jumps across the barrier, $\Delta p_w = p_w^{lum} - p_w^{ext}$ since it offers a dynamical resistance to water permeation.

5.4 Water permeation across the semi-permeable barrier

We model this passive water permeation adapting Darcy's law to the present setting, as commonly done for semi-permeable membranes[248], and assume that the permeation velocity v of water across the membrane flowing into the luminal cavity follows the relation $Kv = -\Delta p_w$, where K is a permeation coefficient. K is an effective coefficient accounting for the permeability of the plasma membrane, the presence of water channels such as aquaporins, the porosity of the cytosol, and the hydraulic pericellular permeability through cell-cell junctions. Since Δp_w is uniform and assuming K is uniform, we conclude that v is uniform. Thus, we can compute the rate of luminal volume as $\dot{V} = vS$, where S is the surface area of the dome.

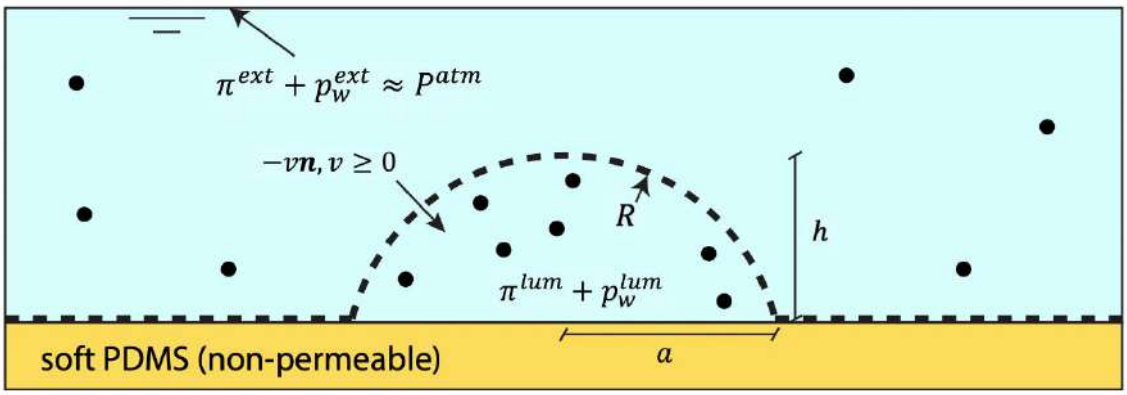

Figure 24: ***Domes are idealized as a semi-permeable membrane****. At the top surface, the boundary condition relates the atmospheric pressure (neglecting the pressure of the vapor in air) with the external osmolarity and chemical potential of the water. The permeation velocity of water across the membrane flowing into the luminal cavity is denoted by* v*.* p_w^{lum} *and* π^{lum} *are the luminal water chemical potential and luminal osmotic pressure, both uniform.* p_w^{ext} *and* π^{ext} *are the external water chemical potential and external osmotic pressure, also uniform.* R, a *and* h *are, respectively, the radius of curvature, the basal radius and the height of the dome.*

5.5 Mechanical equilibrium normal to the membrane

Laplace's law applied to our spherical domes under constant tension reduces to $2\sigma/R = \Delta p_w + \Delta\pi$. Importantly, our 3D traction force microscopy technique allows us to access the total mechanical pressure difference between the lumen and the external solutions, $\Delta p_w + \Delta\pi$, which is equal to the measured normal traction in the non-adherent region, t_n experimentally determined by averaging the point-wise measurements. Thus, we can determine the tissue surface tension as $\sigma = R\, t_n/2$.

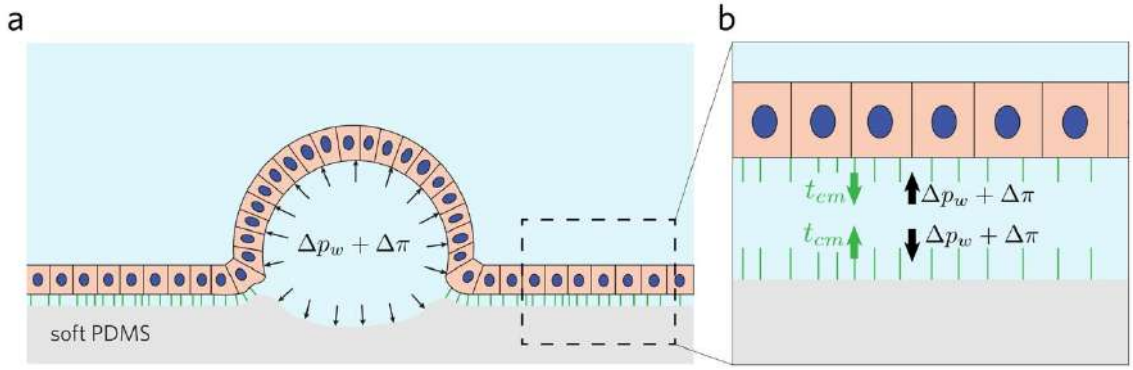

Figure 25: ***Dome mechanics****.* ***a****, Under the dome, the substrate experiences a normal traction equal to* $\Delta p_w + \Delta\pi$*.* ***b****, By mechanical equilibrium on the adherent monolayer, cell-matrix tractions are opposite in sign and equal in magnitude to* $\Delta p_w + \Delta\pi$ *in the interstitial space. Consequently, the substrate underneath the adherent monolayer experiences zero net traction.*

5.6 A typical scenario during a swelling phase

During a swelling phase, $\dot{V} > 0$ and therefore the permeation velocity v is also positive. For this flow to occur, Darcy's law requires that $\Delta p_w < 0$. From the cell medium specification, we have $M^{ext} \approx 250$ mOsm/l, corresponding to $\pi^{ext} \approx 644$ kPa. At the free surface, the solution is in contact with the atmosphere and thus, neglecting the pressure of the vapor in air, we have $\pi^{ext} + p_w^{ext} \approx P^{atm} \approx 100$ kPa. Thus, we conclude that $p_w^{ext} \approx -544$ kPa. Since $\Delta p_w < 0$ during swelling, we conclude that p_w^{lum} is also negative and larger in magnitude.

Epithelial blisters are clearly pressurized and tense ($\sigma > 0$), and therefore $\Delta p_w + \Delta\pi > 0$. Since $\Delta p_w < 0$, we conclude that $\Delta\pi > 0$ and of larger magnitude, consistent with the notion that the cell monolayer is actively pumping osmolytes towards the luminal space.

5.7 Volume dynamics during osmotic perturbations and measurement of the epithelial osmotic permeability

At time-scales faster than the spontaneous volume dynamics, it is possible to manipulate the dome luminal volume by osmotically perturbing the system. In hyperosmotic shock experiments, we suddenly increased the osmolarity of the external medium by 100 mOsm/l (see 8.4.8 for details on the experimental methods), and hence increased π^{ext} by 260 kPa. Because at the free surface the water and osmotic pressures still need to satisfy $\pi^{ext} + p_w^{ext} \approx P^{atm}$, this perturbation will result in a concomitant decrease in p_w^{ext} by a significant magnitude in a very short time (thanks to water incompressibility). However, neither π^{lum} nor p_w^{lum} will be affected in a very short time-scale after the perturbation. As a result of the perturbation, $\Delta p_w > 0$, which will drive water out of the luminal cavity as observed experimentally in Figure 26.

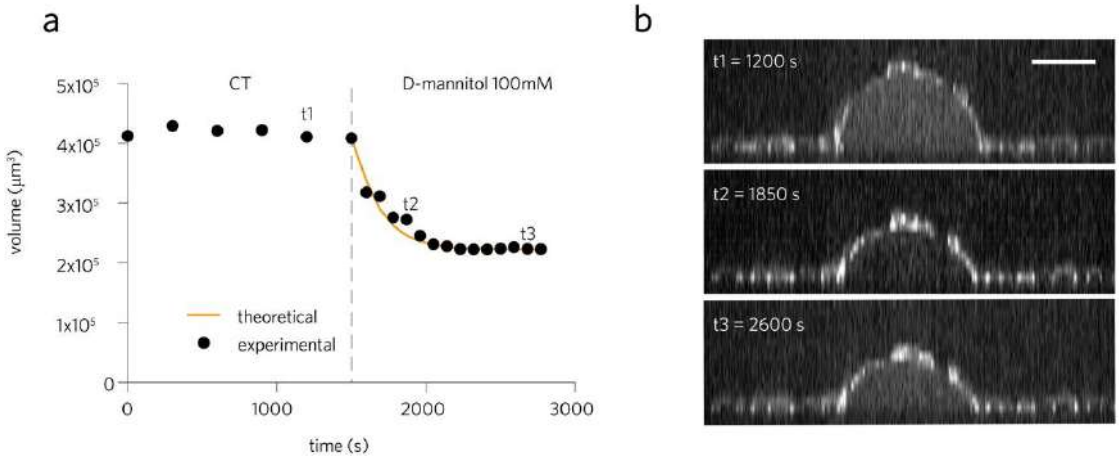

Figure 26: ***Dome deflates with a hyperosmotic shock. a****, Volume time evolution after the hyperosmotic shock with D-mannitol 100 mM.* ***b****, y-z sections at different steps of the volume decrease shown in* ***a*** *induced by the osmotic shock. Scale bar, 50 µm. Data are representative of n=3 experiments.*

Assuming that in the time-scale of the perturbation the number of moles of osmolytes in the luminal cavity N^{lum} remains constant, the osmotic pressure jump can be written as:

$$\Delta\pi = \bar{R}T\frac{N^{lum}}{V} - \pi^{ext} \tag{5.1}$$

where the luminal volume V can be measured experimentally from confocal stacks and π^{ext} is given by the external medium after perturbation and known. As discussed earlier, the mechanical pressure difference can be computed as:

$$\Delta p_w + \Delta\pi = t_n \tag{5.2}$$

from the measurement by traction force microscopy of the normal traction t_n. Finally, Darcy's law can be written as:

$$K\frac{\dot{V}}{S} = -\Delta p_w \tag{5.3}$$

where the permeation coefficient K is not known. Combining these three equations, we obtain the following ordinary differential equation governing the luminal volume dynamics:

$$K\frac{\dot{V}}{S} - \bar{R}T\frac{N^{lum}}{V} + \pi^{ext} + t_n = 0 \tag{5.4}$$

During osmotic perturbation experiments, variations in t_n are in the order of 10 Pa whereas variations in π^{lum} are of hundreds of kPa. In other words, osmotic pressures overwhelmingly dominate mechanical pressures in setting osmotic flows. We can therefore neglect t_n in this equation. With this assumption, this equation predicts the volume:

$$V_\infty = \frac{\bar{R}TN^{lum}}{\pi^{ext}} \tag{5.5}$$

at steady state, but, before active pumping can significantly change N^{lum}. Since V_∞ can be measured (Figure 27a) and π^{ext} is data, this equation allows us to estimate N^{lum} at the moment of the perturbation.

Since the domes can be accurately described as spherical caps with a fixed basal radius a and height h, we have:

$$V = \frac{\pi h}{6}(3a^2 + h^2), \quad S = \pi(a^2 + h^2), \tag{5.6}$$

and hence,

$$\dot{V} = \frac{\pi\dot{h}}{6}(3a^2 + h^2) + \frac{\pi h}{3}h\dot{h} = \frac{\pi\dot{h}}{2}(h^2 + a^2) = \frac{\dot{h}}{2}S \tag{5.7}$$

A simple manipulation allows us to rewrite the volume dynamics equation in a non-dimensional form as:

$$\frac{V_\infty}{V(t)} = 1 + \frac{K}{2\pi^{ext}}\dot{h}(t) \tag{5.8}$$

Therefore, according to this theory the inverse of the non-dimensional volume should be affinely related to the rate of change of the height, with the linear coefficient providing a measurement of K. We find that the experimental data for multiple domes collapses on

this master curve (Figure 27b), and using a linear least squares fit, we find that $K \approx 1.2 \cdot 10^{13}$ Pa·s/m. Osmotic permeability is often expressed as a velocity P_f related to K as:

$$P_f = \frac{\bar{R}T}{KV_w} \tag{5.9}$$

where V_w is the volume of 1 mol of water molecules at the temperature T. From our estimate for K, we obtain $P_f = 1.1 \cdot 10^{-3}$ cm/s in accordance to what has been published before[249-251] for MDCK cells using volume measurements with confocal microscopy, and about twice of the osmotic permeability of the plasma membrane of these cells[250, 251].

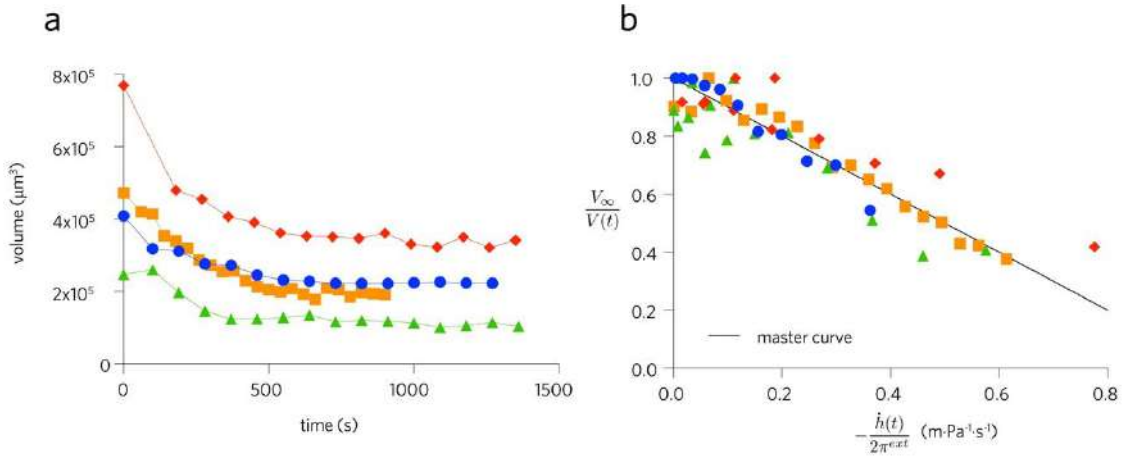

Figure 27: ***Volume dynamics during osmotic shocks collapse over a master curve. a****, Time evolution of dome volume just after perturbing the osmolarity with D-mannitol 100 mM (different colors represent different domes), n=4 domes.* ***b****, Collapse over a master curve eq. 5.8 of the experimental data shown in* ***a****. n=4 domes.*

5.8 Estimation of ionic pumping flux

Having measured K, we can revisit the volume dynamics of the domes over a longer time-scale. During a swelling phase, we can estimate the absolute number of moles of osmolytes in the luminal cavity and the ionic pumping rate across the epithelial barrier. Indeed, it follows from the volume dynamics equation that:

$$N^{lum}(t) = \frac{V(t)}{\bar{R}T}\left[K\frac{\dot{V}(t)}{S(t)} + \pi^{ext}\right] \tag{5.10}$$

Finally, the osmotic pumping rate per unit area q, can be computed as:

$$q(t) = \frac{\dot{N}^{lum}(t)}{S(t)} \tag{5.11}$$

Using this theory, our experimental data indicates that during events of dome swelling (Figure 28), the pumping rate is nearly constant, but exhibits variability between different swelling events, in the range 0.04 to 0.14 μmol/(cm^2·hour), comparable to previous electrical measurements of Na transport across MDCK monolayers[233, 252].

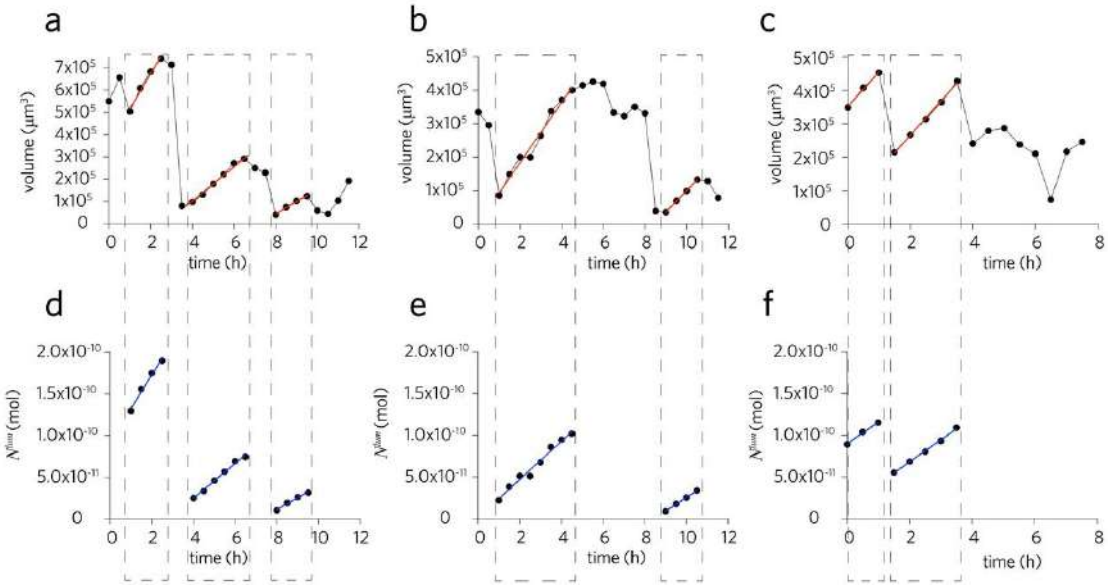

Figure 28: ***Dome volume dynamics and osmolarity. a-c****, Time evolution of dome volume during spontaneous fluctuations for n=3 different domes. During the swelling phases, volume increases almost linearly in time.* ***d-f****, Time evolution of the absolute number of osmolytes in the luminal cavity. During the swelling phases,* N^{lum} *increases almost linearly in time. n=3 domes.*

5.9 Summary and discussion

Volume dynamics under osmotic perturbations were consistent with a simple physical picture in which the epithelial barrier behaves like a semi-permeable membrane actively pumping osmolytes at nearly constant rate. Moreover, our results indicate very limited fluid transport between the lumen and the interstitial space under the adhered part of the monolayer.

These assumptions are consistent with the experimental measurements because the timescale for dome volume's dynamics is much longer than the one for the diffusion of the osmolytes. We can also note that the coarse graining done when assuming Darcy's law is reasonable because the length scale that we are interested in is much greater than the thickness of the cell monolayer. Therefore, further detailed modelling should be done if one is interested in local changes of cell volume or in the local ionic transport.

Using volume measurements in time, after a controlled hyper-osmotic shock, we are able to determine the transepithelial osmotic water permeability. We obtained $Pf = 10^{-3}$ cm/s, similar to other published data[249] and about twice the permeability of the plasma membrane of MDCK cells[250, 251].

The specific transport rate of osmolytes was found in the range 0.04 to 0.14 μmol/(cm^2 h), comparable to previous electrical measurements of Na transport across MDCK monolayers[233, 252]. We also measured total amount of osmols inside the lumen (Figure 28d-f).

Thus, our experimental setup enables not only mechanical measurements but also an absolute and non-invasive quantification of transepithelial transport, transepithelial permeability, the total amount of mols that are inside the cavity and also the active pumping rate of osmolytes. Using hypo-osmotic shocks we should be able to increase dome's volume and also to calculate the permeability of the epithelia. Moreover, **hyper- and hypo- osmotic shocks could be seen as possible mechanisms to exogenously interfere with the spontaneous variation of dome's volume. It could be a way to drive the 'micro-bulge mechanical test'.**

As a future perspective, this experimental setup can be used to test how different drugs are able to change the transepithelial permeability in a simple and non-invasive way.

6 ACTIVE SUPERELASTICITY

6.1 Constitutive relation between dome tension and strain

In the absence of pharmacological or osmotic perturbations and over timescales of hours, epithelial domes exhibited large volume fluctuations (Figure 29).

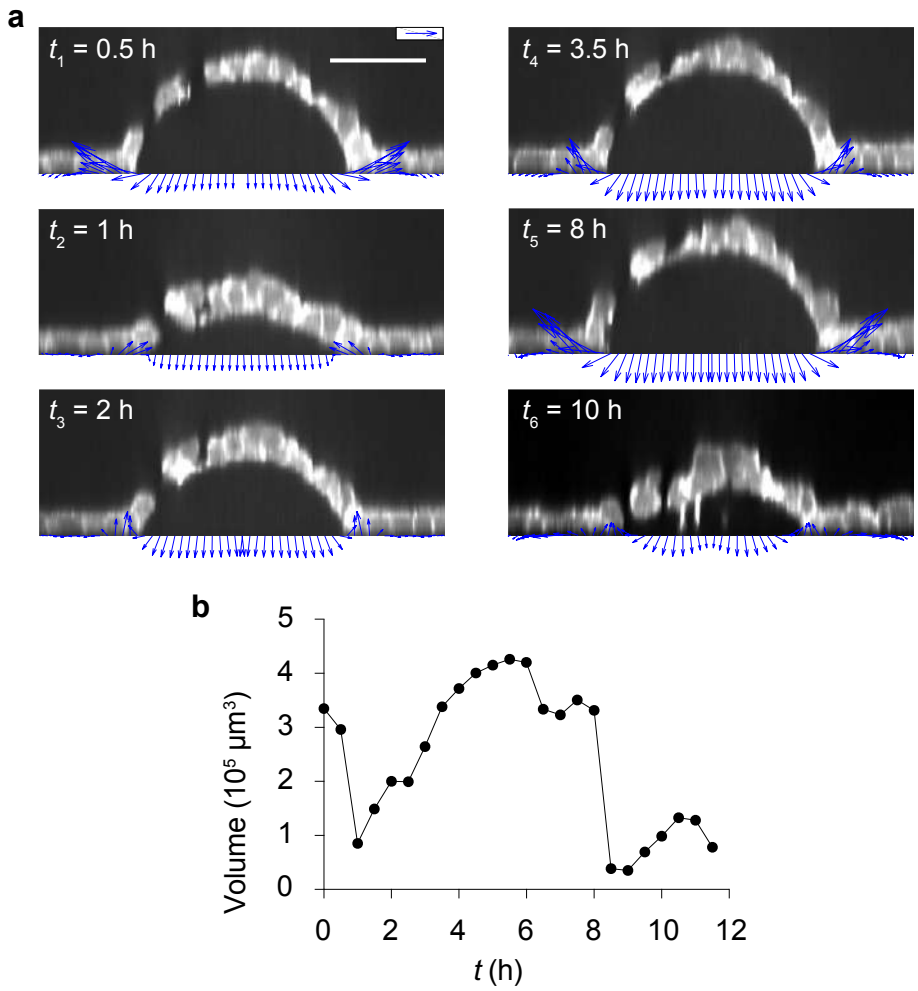

Figure 29: ***Dome volume dynamics showing the traction forces evolution. a****, Spontaneous time evolution of tractions in a MDCK-LifeAct dome (y-z section). Scale bar, 50 µm. Scale arrows, 150 Pa. Regions in the dome monolayer lacking fluorescence signal correspond to unlabeled cells, not to gaps.* ***b****, Time evolution of spontaneous fluctuations in dome volume (representative of n=9 domes, each sampled over various time points).*

These fluctuations involved periods of slow swelling and deswelling combined with sudden volume drops, often up to total dome collapse and subsequent rebirth. The magnitude of collapse events, presumably caused by localized disruptions of epithelial

integrity, and the duration of swelling phases exhibited high variability (Figure 29 and Figure 30).

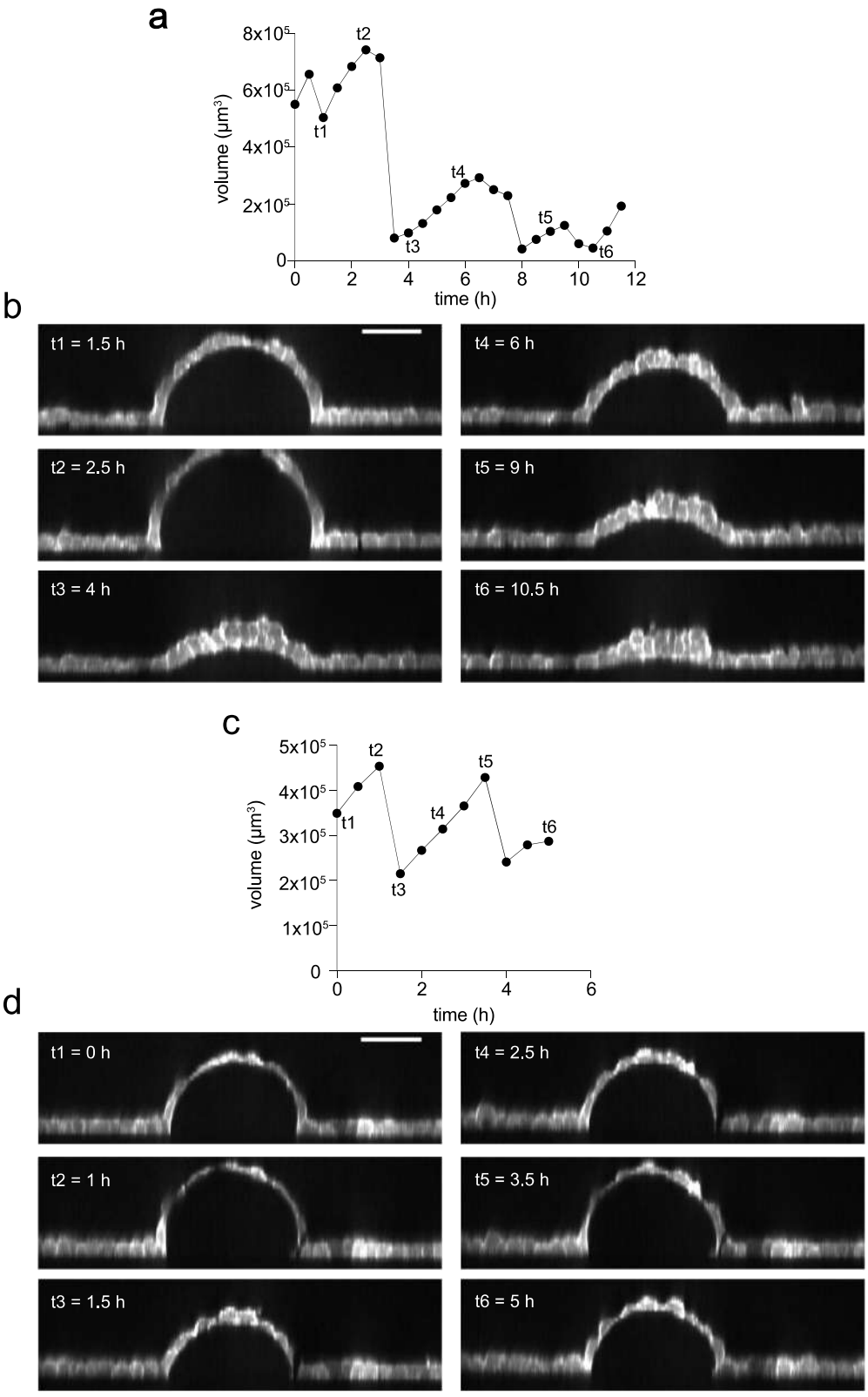

Figure 30: ***Dome volume dynamics during spontaneous fluctuations. a, c,*** *Time evolution of the dome volume in experiments that last 12 h and 6 h respectively. Cells are MDCK-LifeAct.* ***b, d,*** *Confocal x-z sections of domes during these experiments. Data representative of n=10 experiments. Scale bars, 50 µm.*

To test if dome deswelling is due to a cell-cell junction failure, we experimentally weakened them using EGTA (ethylene glycol-bis(β-aminoethyl ether)-N,N,N′,N′-tetraacetic acid) which is a well-known calcium chelator (see section 8.4.8 for details of the methods). This caused a rapid collapse of the domes and provoked visible gaps at tri-cellular junctions (Figure 31).

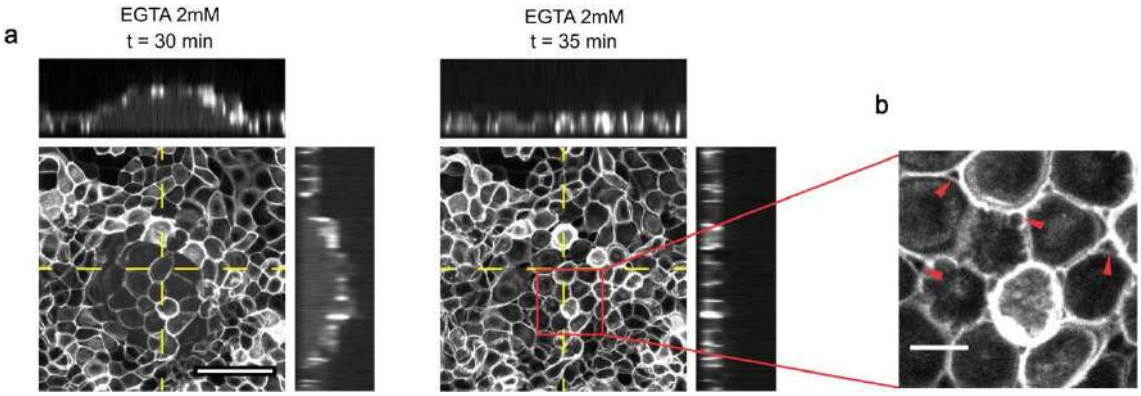

Figure 31: ***Weakening cell-cell junctions with EGTA provoked dome collapse. a,*** *Maximum intensity projection and corresponding x-z and y-z profiles showing the collapse of a MDCK-CAAX dome after treatment with EGTA 2mM (30 min and 35 min after EGTA addition). Data representative of n=3 experiments. Scale bar, 50 µm.* ***b,*** *After dome collapse, gaps (red arrowheads) were apparent at tricellular junctions. Scale bar, 10 µm.*

During the spontaneous volume fluctuations, we tracked luminal pressure and dome geometry, which provided a record of **epithelial tension measurements at different degrees of swelling** (Figure 32). To examine these data, we represented tension in the free-standing tissue as a function of nominal areal strain of the dome $\varepsilon_d = (h/a)^2$, defined as the difference between the actual area of the dome $\pi(h^2+a^2)$ and the area of the non-adhesive region in the substrate πa^2, normalized by the latter (see Figure 20b or Figure 24 for a definition of h and a). All domes exhibited tensions of ~1 mN/m at small strains. At moderate strains (below 100%), tension progressively increased following a highly reproducible law. Beyond this point, tension exhibited larger scatter but appeared to reach a plateau at ~2 mN/m for areal strains up to 300% (Figure 32c, Figure 33). It is very important to highlight that the deformation process described in those figures is **reversible** and that the points correspond to different domes sampled over various time points. This means that the constitutive behavior described correspond to several cycles of swelling or de-swelling of the domes.

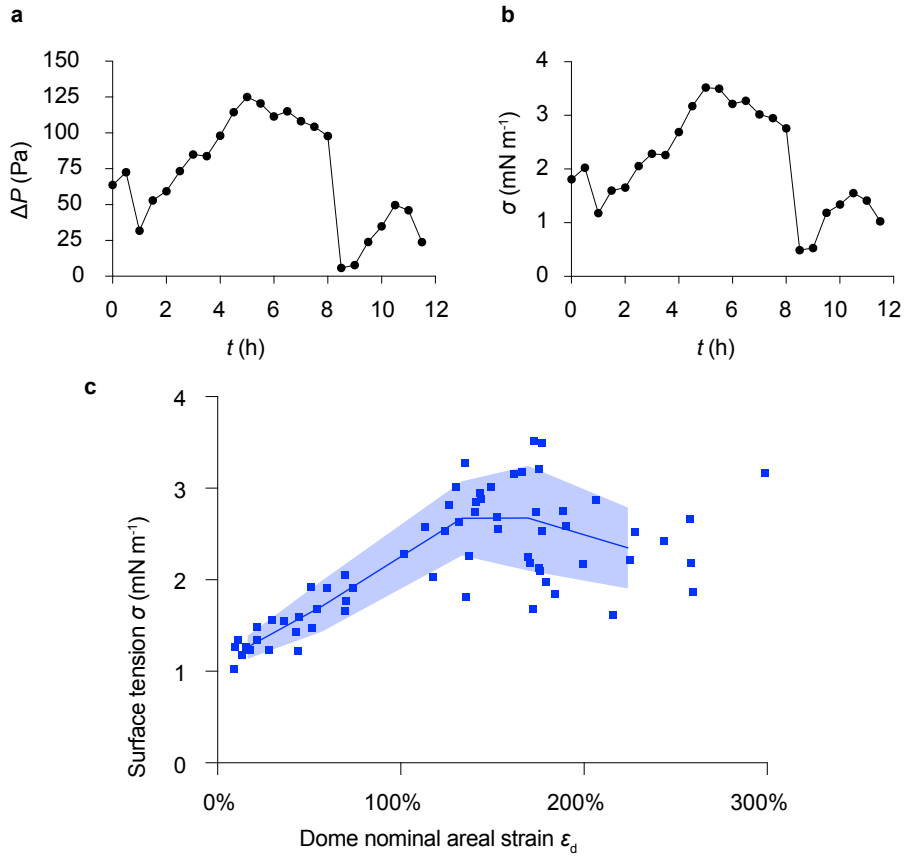

Figure 32: ***Constitutive relation between dome tension and strain. a-b,*** *Time evolution of spontaneous fluctuations in pressure ΔP* ***(a)*** *and surface tension σ* ***(b)*** *(representative of n=9).* ***c,*** *Surface tension in the free-standing sheet as a function of nominal areal strain of the dome ε_d (n = 9 domes, each sampled over various time points). The solid line and shaded area indicate mean ± SD obtained by binning the data (n = 14 points per bin). Cells are MDCK LifeAct.*

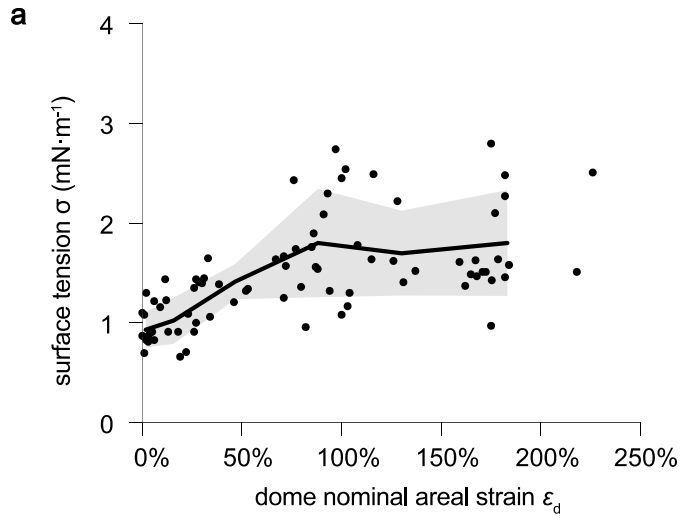

Figure 33: ***Tension/strain relations in MDCK-CAAX cells. a****, Relation between surface tension and areal strain for MDCK-CAAX cells. Data include measurements at different time points from n = 9 domes. The tension/strain relation is qualitatively similar to the one obtained for MDCK-LifeAct cells (Figure 32c), with small quantitative differences. The solid line and shaded area indicate the mean ± SD obtained by binning the data (n = 14 points per bin).*

The very existence of this plateau is remarkable, as it reveals that epithelial domes maintain tensional homeostasis while undergoing deformations that change their area by up to 4-fold. Human epithelial colorectal adenocarcinoma cells (Caco-2), which are also known to form spontaneous domes, showed a plateau at similar tension but lower strain (Figure 34; see the Table 2 in 8.1 for a list of cell lines known to form domes).

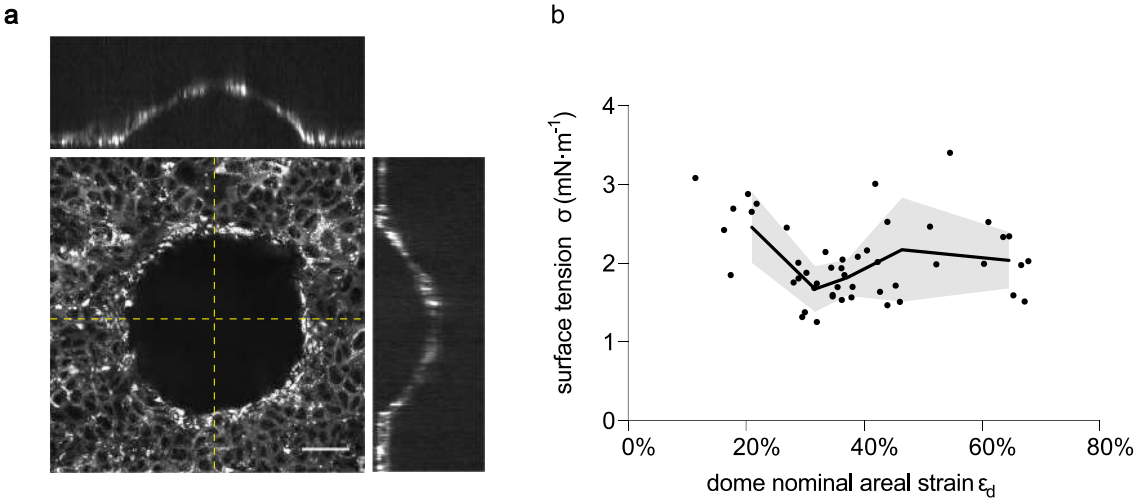

Figure 34: ***Caco-2 cells also form domes and they also exhibit a plateau in the stress-strain curve. a,*** *Image of a representative Caco2 cell dome labelled with Bodipy FL C16 dye (n=3 micropatterned substrates). (Confocal x-y, x-z and y-z sections). Scale bar, 50 µm.* ***b****, Relation between surface tension and areal strain for Caco2 cells. Data include measurements at different time points from n = 6 domes. Caco2 cells show a tensional plateau throughout the probed strain range. The solid line and shaded area indicate the mean ± SD obtained by binning the data (n = 10 points per bin).*

A number of mechanisms could contribute to such tensional homeostasis, including directed[253] or accelerated[13] cell division, junctional network rearrangements[15], and cell exchange between domes and the adjacent adhered tissue. Visual examination of the domes showed that cell division and live cell extrusion were rare events. Moreover, the number of cells above the non-adherent region remained constant during the several-fold increases in dome area (Figure 35).

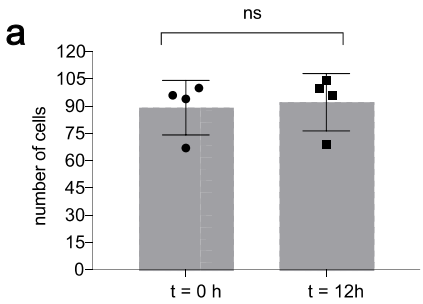

Figure 35: ***Number of cells in domes is constant. a****, Quantification of the number of cells in circular domes at two time points 12 h apart (n=4 domes). ns, not significant (P = 0.4571), two-tailed Mann-Whitney test. Data shown as mean ± SD.*

We thus concluded that the tension-strain response of the tissue had to depend on the mechanics of cell stretching.

To understand the strain-tension relation of the dome monolayer, we developed a theoretical vertex model in 3D[254, 255]. The model is based on the well-established observation that **the major determinant of epithelial cell mechanics is the actin cortex**[256] (see also the section 2). In the time-scales of our experiments, this thin cytoskeletal network behaves like a fluid gel, capable of developing contractile tension thanks to myosin motors[256-258]. In 3D vertex models, these active tensions act along lateral (γ_l) and apico-basal (γ_{ab}) faces of polyhedral cells and penalize their area increase (Figure 36).

6.2 3D vertex model of epithelial domes

6.2.1 An elementary (and analytic) 3D vertex model with polyhedral cell geometry

We develop here a 3D vertex model[254, 255] to understand epithelial mechanics under stretch in our domes. The key modeling assumptions are discussed first.

Cells in an epithelial monolayer are modeled as polyhedra with polygonal apical and basal faces and rectangular lateral faces. We denote by A_i the apico-basal area of the i −th cell, by P_i its perimeter, by t_i the cell thickness, assumed to be constant for simplicity, and by $A_{l,i} = P_i t_i$ the lateral area of cell-cell contacts. We denote by $A_{0,i}$ a convenient reference apico-basal area of the i −th cell, for instance that before dome swelling. See Figure 36:

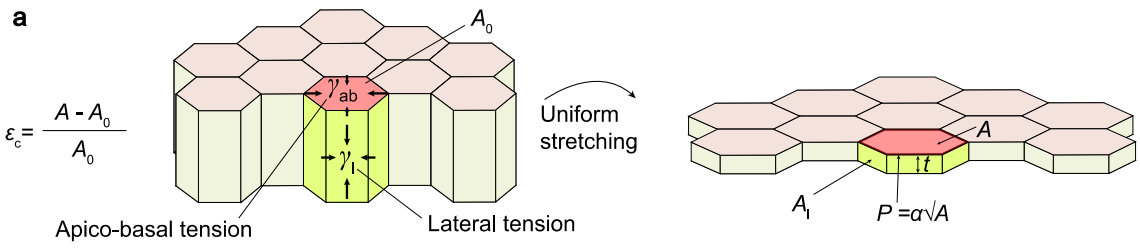

Figure 36: ***Model assumptions and geometry for the 3D vertex model. a****, Scheme of an idealized monolayer, made of regular hexagonal cells, undergoing uniform equi-biaxial stretching and representing model assumptions.*

6.2.1.1 Cortical surface tensions

The major determinant of epithelial mechanics is the active contractile tension produced by the actomyosin cytoskeleton (see section 3.1.1.1). Our experimental observations of cells in epithelial domes did not show any evidence of an apical cortical belt. Instead, they showed a rather uniform thin actin layer lining cell boundaries. Therefore, we included active surface tensions produced by the actin cortex along cell faces but did not include an apical line tension. Since cells in domes are detached from the matrix, we did not include a negative adhesive tension along basal faces.

We assume that the actin cortex exerts an isotropic and constant surface tension γ, which can be different in the apico-basal faces, γ_{ab}, and in the lateral faces, γ_l. Because apico-basal faces are not adherent, tension along these faces is contractile, $\gamma_{ab} > 0$. The lateral tension γ_l models the combined effect of cortical contractility and adhesive negative tension at cell-cell contacts. We assume that $\gamma_l > 0$, implying a dominance of contractile over adhesive tensions along lateral cell-cell contacts[32] and in agreement with the geometry of the contact angles between cells in our observations.

6.2.1.2 Virtual work function

Epithelial mechanics in vertex models results from an effective energy or virtual work function, which here is expressed per unit undeformed apico-basal area for the i-th cell as:

$$\delta W_i = \gamma_{ab} \frac{\delta A_i}{A_{0,i}} + \gamma_l \frac{\delta A_{l,i}}{A_{0,i}} = \gamma_{ab} \frac{\delta A_i}{A_{0,i}} + \gamma_l \frac{(t_i \delta P_i + P_i \delta t_i)}{A_{0,i}} \qquad (6.1)$$

This function expresses the virtual work required to vary the apico-basal and lateral cell areas, A_i and $A_{l,i} = P_i t_i$.

6.2.1.3 Assuming constant cell volume

In agreement with previous observations[231], we assume that cell volume remains constant, $A_i t_i = V_{0,i}$, as cells are stretched. This incompressibility constraint can be imposed explicitly by setting the cell thickness to $t_i = V_{0,i}/A_i$.

6.2.1.4 Uniform stretching of an epithelial sheet

Since our observations show that the tissue in domes accommodates large nominal strains by cell stretching, we examine first the mechanics of an idealized planar tissue made out of regular hexagonal cells and subjected to uniform isotropic stretch. Since stretching is uniform and isotropic, the regular hexagonal shape of the cells is preserved during deformation. With this geometry, we can relate the cell perimeter to its apico-basal area by $P = \alpha\sqrt{A}$, where $\alpha = 6\sqrt{2/(3\sqrt{3})}$. The subscript i is dropped for this idealized case as all cells in the tissue are assumed to be identical and undergoing the same deformation. Thus, invoking cell incompressibility, the virtual work function per unit reference (apico-basal) area for the tissue can be written as:

$$\delta W = \gamma_{ab}\frac{\delta A}{A_0} + \frac{\gamma_l}{A_0}\left[\frac{V_0}{A}\delta P + P\delta\left(\frac{V_0}{A}\right)\right] = \left(\gamma_{ab} - \gamma_l\frac{\alpha V_0}{2}\frac{1}{A^{3/2}}\right)\frac{\delta A}{A_0} \qquad (6.2)$$

Introducing the cellular strain $\varepsilon_c = A/A_0 - 1$, we can write the virtual work as:

$$\delta W = \left(\gamma_{ab} - \frac{\alpha V_0}{2A_0^{3/2}}\frac{\gamma_l}{(1+\varepsilon_c)^{3/2}}\right)\delta\varepsilon_c \qquad (6.3)$$

The tissue surface tension is the quantity work-conjugate to areal strain, and can thus be computed as:

$$\sigma = \frac{\delta W}{\delta\varepsilon_c} = \gamma_{ab} - k\frac{\gamma_l}{(1+\varepsilon_c)^{3/2}} \qquad (6.4)$$

where $k = \alpha V_0/(2A_0^{3/2}) = \alpha t_0/(2\sqrt{A_0})$ is a geometrical non-dimensional constant and $t_0 = V_0/A_0$ is the reference cell thickness. Since in this analysis the idealized tissue is uniformly stretched, all cells behave identically and Eq. 6.4 can be interpreted as the tension-strain relation of a single cell, and thus be regarded as the local constitutive relation of the tissue.

Equation 6.4 captures the saturation of tissue tension σ towards γ_{ab} as cells experience increasing areal strains ε_c. Since A_0 and V_0 define the reference state of the cells and they

are measurable from experiments, γ_l/γ_{ab} is the only free model parameter controlling the shape of the cellular constitutive relation, see Figure 37.

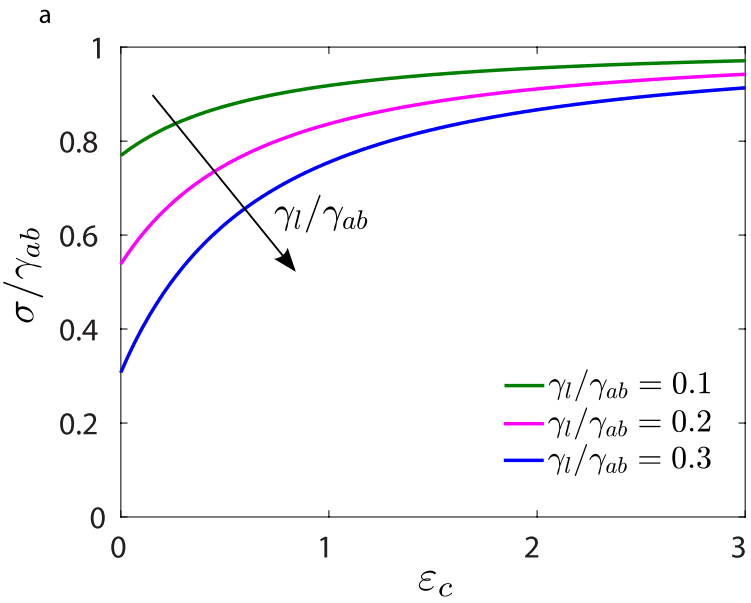

Figure 37: ***Cellular constitutive behavior with the free parameter γ_l/γ_{ab}. a****, According to the cellular constitutive relation given by Eq. 6.4, the tissue tension σ saturates to γ_{ab} with increasing cellular areal strain ε_c. The ratio γ_l/γ_{ab} determines the tissue tension in the reference configuration, at $\varepsilon_c = 0$. In the plots, the reference cell thickness is twice the reference cell edge length s_0, $t_0 = 2s_0 = P_0/3$, resulting in $k = 4/\sqrt{3}$.*

6.2.2 Computational vertex model of epithelial domes

To consider a situation closer to the experiments, we develop next a computational version of the vertex model described above. We simplify the kinematics of the polyhedral cells in the tissue by assuming that apical and basal faces are parallel to each other, hence defining a uniform cell thickness. The tissue configuration is then defined by a polygonal tessellation of a surface in 3D, each polygon representing an average of the apical and basal faces. Thus, the degrees of freedom in our computational model are the 3 Cartesian coordinates of each vertex, $\boldsymbol{r_a}$, in the polygonal network.

The vertices of an initially planar polygon in the network are not constrained to maintain their co-planarity during tissue deformation. To define the apico-basal area A_i of each cell, we triangulate the corresponding polygon using the barycenter (mean coordinate) of the cell vertices. The summation of the areas of the triangles formed by the edges of the cell and the barycenter approximates A_i. Once the apico-basal area is computed, the cell thickness is determined from the cell incompressibility constraint $t_i = V_{0,i}/A_i$. The perimeter of a cell can be easily computed from its polygon. Thus, given the 3D polygonal

tesselation of the surface, we can compute all the quantities required to evaluate the virtual work function of a tissue with N cells:

$$\delta W(\boldsymbol{r};\delta\boldsymbol{r}) = \sum_{i=1}^{N} \delta W_i A_{0,i} = \sum_{i=1}^{N} \left(\gamma_{ab}\delta A_i + \gamma_l \left[\frac{V_0}{A_i}\delta P_i - \frac{P_i V_0}{A_i^2}\delta A_i \right] \right), \quad (6.5)$$

where $\boldsymbol{r} = \{\boldsymbol{r_1}, \boldsymbol{r_2}, \dots, \boldsymbol{r_a}, \dots, \boldsymbol{r_M}\}$ collects the vertex coordinates. Since δA_i and δP_i can be expressed in terms of the virtual displacements of the vertices, $\delta\boldsymbol{r_v}$, we can identify the forces acting on the vertices from the relation:

$$\delta W(\boldsymbol{r};\delta\boldsymbol{r}) = -\sum_{v} \boldsymbol{f_v}(\boldsymbol{r}) \cdot \delta\boldsymbol{r_v} \quad (6.6)$$

Tissue configurations in mechanical equilibrium can be obtained by equating the virtual work to zero for all virtual vertex displacements, leading to $\boldsymbol{f_v}(\boldsymbol{r}) = 0$ for all vertices in the absence of any external forces[254].

This model does not consider a possible asymmetry between apical and basal faces, which could induce spontaneous curvature, or an explicit modeling of the monolayer bending rigidity[259]. It focuses on the capillary mechanics of the cell monolayer, as suggested by our experiments.

The reference configuration of the vertex model is generated by a Voronoi tessellation using cell center positions extracted from an experimental micrograph. The vertices outside the non-adherent region below the dome are fixed, and only vertices inside this region are allowed to move. The volume trapped between the epithelial sheet and the substrate can also be computed from the vertex positions, $V(r)$. Dome swelling is modeled by subjecting the system to a nonlinear constraint that fixes the dome volume $V(\boldsymbol{r}) = V^* \geq 0$. We can describe the mechanics of this constrained system by introducing the Lagrangian:

$$\delta\mathcal{L} = \delta W - \lambda[\delta V - \delta V^*] \quad (6.7)$$

where the Lagrange multiplier λ corresponds to the transmural pressure difference ΔP. By making the Lagrangian zero for arbitrary virtual vertex displacements and virtual pressure changes, we obtain a nonlinear set of equations expressing balance of network and pressure forces at each vertex and enforcing the enclosed volume constraint. In our

calculations, V^* is incrementally increased/decreased in small steps δV^* to model dome swelling/deswelling. This model describes the quasi-static limit of the dome inflation process where the tissue instantaneously relaxes to a mechanically equilibrated configuration after each increment in V^*. We describe in the APPENDIX (8.2) a modification of this model accounting for kinetic effects related to the reconfiguration of the cell cortex during dome dynamics.

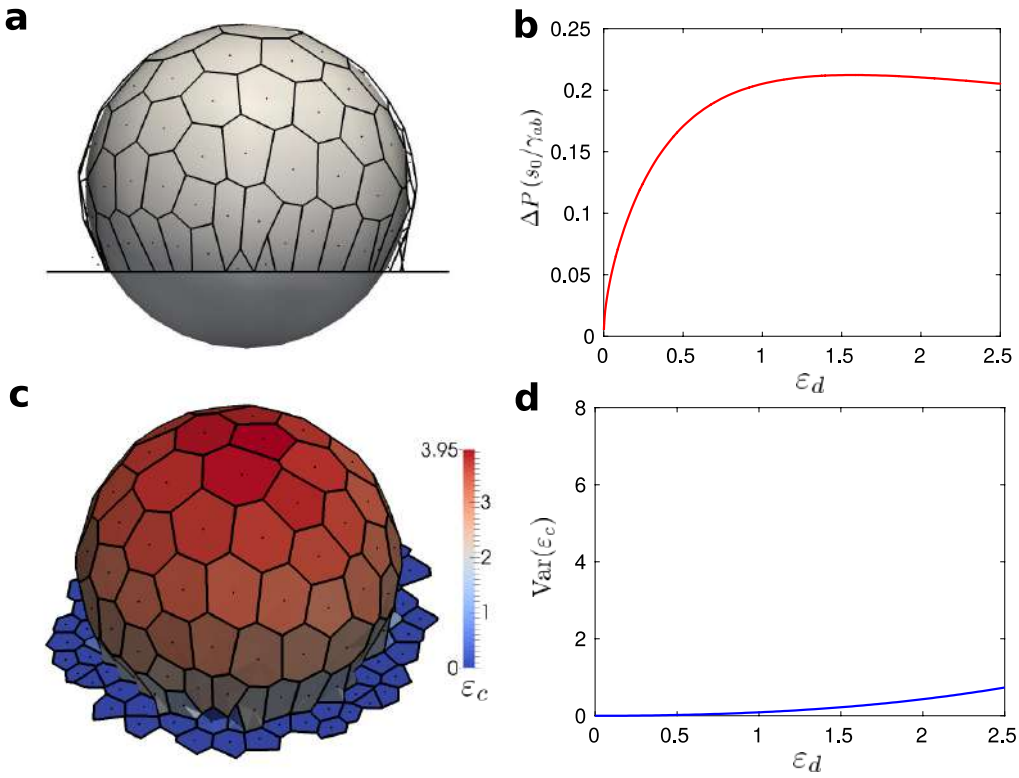

Figure 38: ***Computational vertex model of epithelial domes****.* ***a,*** *An example of equilibrated dome shape approximated closely by a spherical cap at* $\varepsilon_d = 2.5$*.* ***b,*** *The normalized transmural pressure difference* $\Delta P(s_0/\gamma_{ab})$*, computed as the Lagrange multiplier during the constrained minimization algorithm, is a non-monotonic function of the nominal dome strain* ε_d*.* ***c,*** *Slight non-uniformity of cell areal strain* ε_c *distribution on the dome at* $\varepsilon_d = 2.5$*, caused by a boundary effect.* ***d,*** *Variance in the cellular areal strains* ε_c *as a function of the dome nominal strain* ε_d*. The parameter for this simulation is* $\gamma_l/\gamma_{ab} = 0.25$*, which is also used for Figure 39.*

Before applying the first enclosed volume increment, the reference configuration at $V^* = 0$ is equilibrated. Based on experimental observations, we choose a reference cell thickness of $t_0 = 2s_0$ for all cells, where $s_0 \approx 6.75$~μm is the mean cell edge length obtained from experimental observations. The system of nonlinear equations determining the vertex locations is solved in MATLAB[260].

In Figure 38 as well as in Figure 39, we consider a dome of basal radius $a = 7.5s_0$, whose volume is increased incrementally in steps of $\delta V^* = 20s_0^3$. In these calculations, we set

$\gamma_l/\gamma_{ab} = 0.25$. We find that equilibrated dome geometries very closely follow spherical caps as in the experiments, see Figure 38a. This is consistent with a previous theoretical study that predicts residual in-plane shear modulus and bending modulus for a 3D vertex model similar to that considered here[259].

For a given equilibrium configuration, we compute the dome radius R from the radius of its footprint a and from its height h (Figure 20b), and compute the nominal areal strain of the dome as:

$$\varepsilon_d = \frac{A_{\text{dome}}}{\pi a^2} - 1 = \left(\frac{h}{a}\right)^2 \tag{6.8}$$

where $A_{\text{dome}} = \pi(a^2 + h^2)$ is the surface area of the spherical cap. The pressure difference ΔP is an outcome of the numerical calculation. Having obtained R and ΔP from the mechanically equilibrated configurations of the system, we can compute the tension in the computational tissue using Laplace's law

$$\sigma = \frac{R\Delta P}{2} \tag{6.9}$$

Tissue tension calculated following this procedure as a function of ε_d is represented in Figure 39:

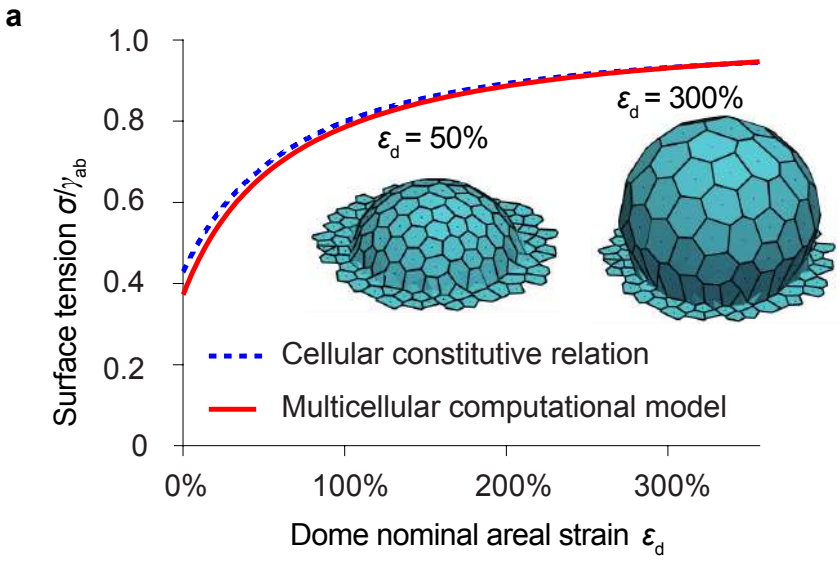

Figure 39: ***Stress-strain curve from the vertex model. a****, Normalized dome surface tension as a function of areal strain calculated with the vertex model. The dashed blue line represents the cellular constitutive relation in Eq. 6.4, based on a sheet of identical hexagonal cells under uniform strain ($\varepsilon_d = \varepsilon_c$). The solid red line is the result of a multicellular computational vertex model for a dome with an initial geometry obtained experimentally. Insets: computed dome shape at 50% and 300% nominal areal strain.*

It agrees remarkably well with the cellular constitutive relation given by Eq. 6.4, and captures the plateau of σ towards γ_{ab} with increasing ε_d. Interestingly, during dome swelling, our model predicts a non-monotonic variation of ΔP with ε_d, see Figure 38b. We finally note that, because of the fixed boundary conditions imposed by the substrate-bound vertices at the edge of the dome, the distribution of the cell areal strain ε_c is not uniform. The areal strain experienced by cells decreases from the dome apex towards its edge, see Figure 38c. This boundary effect produces a mild cellular strain heterogeneity, Figure 38d, quantitatively and qualitatively different from that reported in Figure 40 or in Figure 41a-d of the next section.

6.3 Epithelial domes exhibit superelastic behavior

6.3.1 Cell strain heterogeneity

Although this simple theoretical framework, described in the previous section, captured the overall tension-strain relationship (the tensional plateau is already predicted by the vertex model and it is explained because the area of lateral faces decreases with cell stretching and, hence, tissue tension converges to apico-basal tension), **it missed a remarkable experimental feature; during swelling and de-swelling events, we systematically observed cells that barely changed area coexisting with others that reached cellular areal strains up to 1000%, five times more than the average dome stretching** (Figure 40, Figure 41).

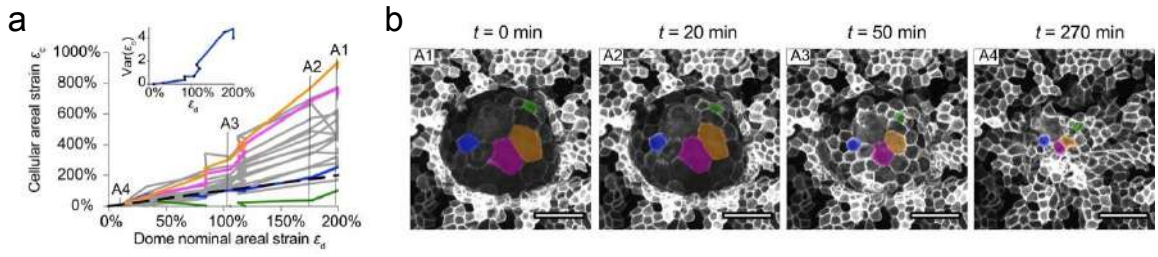

Figure 40: ***Strain heterogeneity among the constituent cells of a dome. a****, Cell strain ε_c versus dome strain ε_d during a deflation event for a subset of cells. Colored curves correspond to cells labelled in* ***b****. Dashed line: $\varepsilon_c = \varepsilon_d$. Variance of ε_c versus ε_d (inset).* ***b****, MDCK-CAAX deflating dome. Scale bar, 50 µm.*

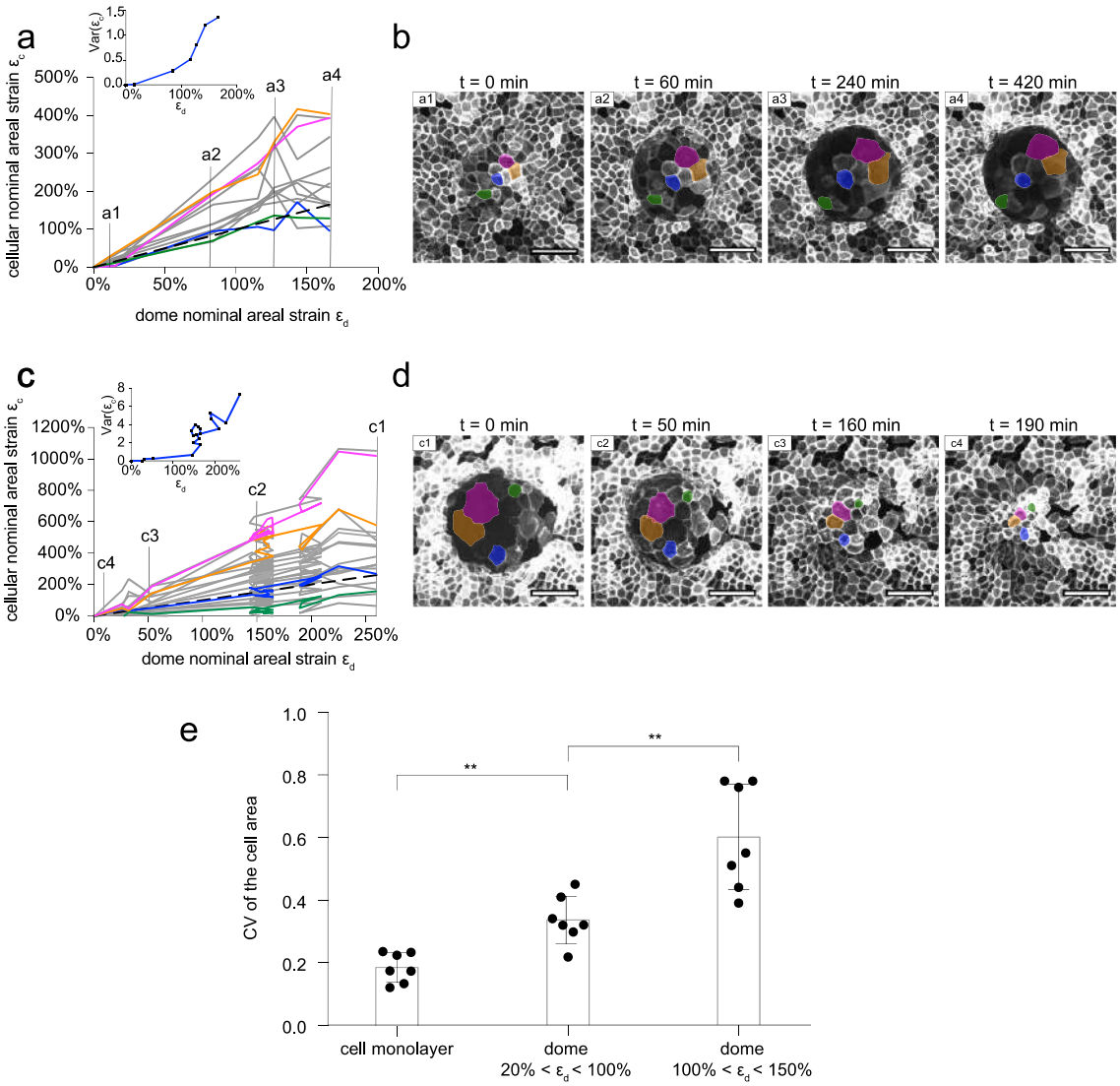

Figure 41: ***Dome cells exhibit large strain heterogeneity****. **a**, Cellular areal strain ε_c as a function of dome nominal areal strain ε_d during dome swelling. Only a subset of cells is represented and most cells with $\varepsilon_c < \varepsilon_d$ have been omitted for clarity. Colored lines represent the cells labelled in **b**. Dashed line represents the relation $\varepsilon_c = \varepsilon_d$. The inset represents the variance of ε_c within the dome as a function of ε_d. **b**, Maximum intensity projection of an epithelial dome of MDCK-CAAX cells at 4 different time-points of the swelling event described in **a**. The time evolution of colored cells is depicted in **a** using the same color code. Scale bars, 50 µm. **c** and **d** represent the same as **a** and **b** for a different dome of MDCK-CAAX cells during slow deflation. **e,** Coefficient of variation (CV, defined as standard deviation divided by mean) of MDCK-CAAX cells in a 2D adherent cell monolayer, in weakly inflated domes (20%-100% areal strain), and in highly inflated domes (100%-150%). The coefficient of variation is a non-dimensional indicator of heterogeneity. The CV was calculated by measuring area of 10 cells in n = 7 cell monolayers, n = 7 weakly inflated domes, and n = 7 highly inflated domes (**P= 0.0041, **P=0.0041 from left to right, two-tailed Mann-Whitney test). Data are shown as mean ± SD.*

This extreme heterogeneity in cellular strain is reminiscent of that observed in highly stretched epithelia in vivo such as the trophoblast in human and mouse blastocysts[261, 262]. **Both in epithelial domes and blastocysts** (see methods for the animal culture, the blastocyst extraction and its immunofluorescence at sections 8.4.16, 8.4.17 and 8.4.18),

strain heterogeneity would seem in contradiction with their spherical shape, which implies tensional uniformity (Figure 41 and Figure 42).

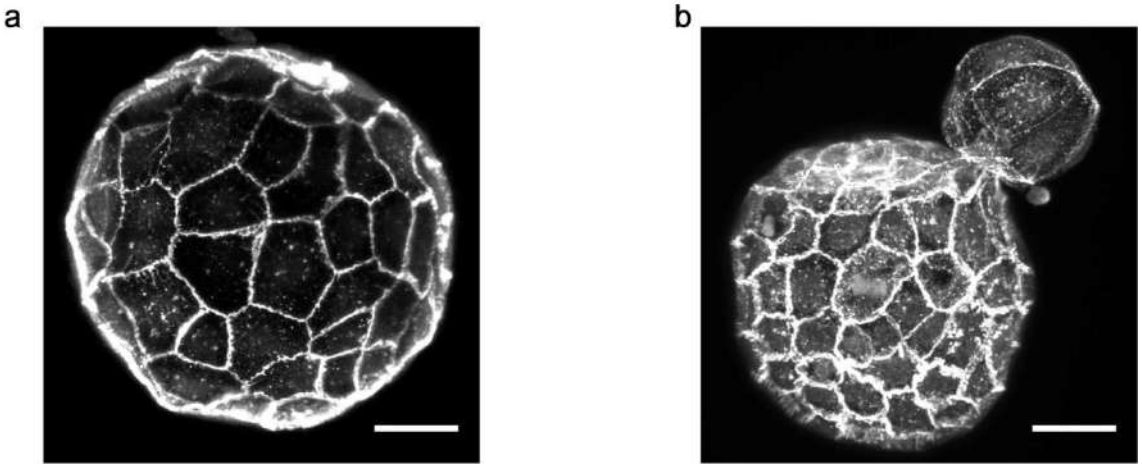

Figure 42: ***Strain heterogeneity in mouse blastocysts. a-b****, Mouse blastocysts (E-cadherin labelled) exhibiting cell area heterogeneity in the trophectoderm, particularly during hatching (g) (n=4). Scale bars, 25 µm.*

Interestingly, heterogeneity of cellular strain increased sharply beyond areal strains of ~100% (Figure 40, Figure 41). This strain threshold coincides with the onset of the tensional plateau and with the increase in the scatter of tissue tension (Figure 32).

6.3.2 Epithelial superelasticity

Taken together, **our experiments show that epithelial domes exhibit very large reversible deformations and a tensional plateau during which superstretched constitutive elements coexist with barely stretched ones**. These uncommon material features are defining hallmarks of superelasticity, a mechanical behavior observed in some inert materials such as Nickel-Titanium alloys[263]. These materials are able to undergo large and reversible deformations at constant stress by heterogeneously switching between low- and high-strain phases[263]. The microscopic trigger of superelasticity is a mechanical instability resulting from strain-softening of the material. In the case of Nickel-Titanium (and for other metal alloys), the mechanical instability is based in a change in the crystallographic structure of the metal. The atomic lattice changes its spatial configuration and thus it changes the volume that it occupies. Both phases coexist at the solid state and macroscopically they are undistinguishable. This is very different from plasticity or damage because this phase transformations are reversible when the applied deformation is ceased.

We reasoned that, in analogy with this behavior, cell monolayers might behave as superelastic materials by switching from barely stretched to superstretched cellular states at constant tension. To explore this possibility further, we sought to find a **strain-softening mechanism** that would explain the mechanical instability underlying the transition between the two strain phases.

Since cellular deformations increased the surface area of the actin cortex by over 3-fold (the apico-basal area is able to increase much more, up to 11-fold, but then the lateral area also decreases a lot due to volume preservation, giving a final increase of the actin cortex area by over 3-fold at maximum), we hypothesized that **strain-softening could arise from the limited availability of cytoskeletal components**[18, 264]. Indeed, scarcity of cytoskeletal components could lead to stretch-induced cortical dilution, which if sufficiently pronounced could impair the ability of the cortex to generate active tension[21] (see the discussion in the next section). To test this hypothesis, we incorporated cortical dynamics to the 3D vertex model.

6.3.3 Cortical depletion and cellular strain-softening

6.3.3.1 Modeling the cortical depletion

To model the state of the actin cortex, we use the cortical areal density ρ, that is the amount of cortical material per unit surface area. If the 3D density of this gel is fixed (the amount of cortical material per unit volume within the thin cortical layer), then ρ is directly related to the cortical thickness. We note that in our coarse-grained model, ρ is an effective density accounting for the different molecular components of the actin cortex. In active-gel models of the actomyosin cortex[265, 266], the polymerization rate r_p is assumed to be constant because (1) actin polymerization is triggered by nucleators at the plasma membrane, and thus r_p should be independent of ρ and (2) it is assumed that there is an excess of cytoplasmic cortical material ready for polymerization, and thus r_p should be independent of the cytoplasmic concentration of these materials. On the other hand, depolymerization rate is assumed to be proportional to ρ, $r_d = k_d$. This model of actin turnover has quantitatively described a number of controlled experiments[267, 268].

The balance between polymerization and depolymerization sets a steady-state cortical areal density:

$$\rho = \frac{r_p}{k_d} \tag{6.10}$$

Thus, according to this model, cortical density is independent of cell deformation.

Since the surface area of the actin cortex can increase in stretched cells on epithelial domes by more than three-fold, we hypothesize that **the assumption of infinite availability of cortical components leading to constant cortical density may break down**. The notion that a limited availability of cortical components may influence the size of cytoskeletal networks is consistent with recent work showing that the limited amount of actin monomers controls the competition between different types of actin networks[18, 264]. See also the section 3.1.1.1 for a more detailed presentation of this updated actin turnover model that includes a finite a limiting monomeric G-actin pool.
To examine this idea, we develop next an alternative minimal model. We denote by m the total mass of cytoskeletal material within a cell, which we assume to be fixed and split between a cortical fraction and a cytosolic fraction. We denote by C the cytosolic concentration of dissolved cytoskeletal components, by $V_{0,i}$ the cell volume, and by $A_{c,i} = 2A_i + P_i t_i$ the surface area of the cell envelope, i.e.~that of the cortex. The statement of conservation of mass of cytoskeletal components is then:

$$m = CV_{0,i} + \rho A_{c,i} \tag{6.11}$$

In this model, the dissolved cytoskeletal components are no longer kept at constant chemical potential; instead, C depends on cellular deformation. Accordingly, we modify the polymerization rate following a first-order kinetic relation $r_p = k_p C$, obtaining at steady state:

$$k_p C - k_d \rho = 0 \tag{6.12}$$

The steady state assumption is justified since dome dynamics are much slower than the actin turnover timescale (tens of seconds to a minute).
Fixing $V_{0,i}$, m and the rate constants and combining these two equations we find:

$$\rho = \frac{m}{A_{c,i} + \frac{k_d}{k_p} V_{0,i}} = \frac{m/A_{0,i}}{\frac{A_{c,i}}{A_{0,i}} + \omega} \tag{6.13}$$

where,

$$\omega = \frac{k_d}{k_p} \frac{V_{0,i}}{A_{0,i}} \tag{6.14}$$

Thus, this model predicts cortical depletion as cells become stretched and the cortex area $A_{c,i}$ becomes larger. Considering an idealized cell monolayer composed of regular hexagonal cells and uniformly stretched, as in the section 6.2.1.4, the cortical depletion as a function of cellular areal strain ε_c can be made explicit. In this case, we find:

$$\rho = \frac{m/A_0}{2[1 + \varepsilon_c + k(1 + \varepsilon_c)^{-1/2}] + \omega} \tag{6.15}$$

where the non-dimensional quantity ω controls the rate of decrease of ρ with ε_c. This relation is represented in Figure 43 for the choice of parameters $\omega = 10$, normalized by the reference cortical density ρ_0 at $\varepsilon_c = 0$ and assuming $t_0 = 2s_0$ as before:

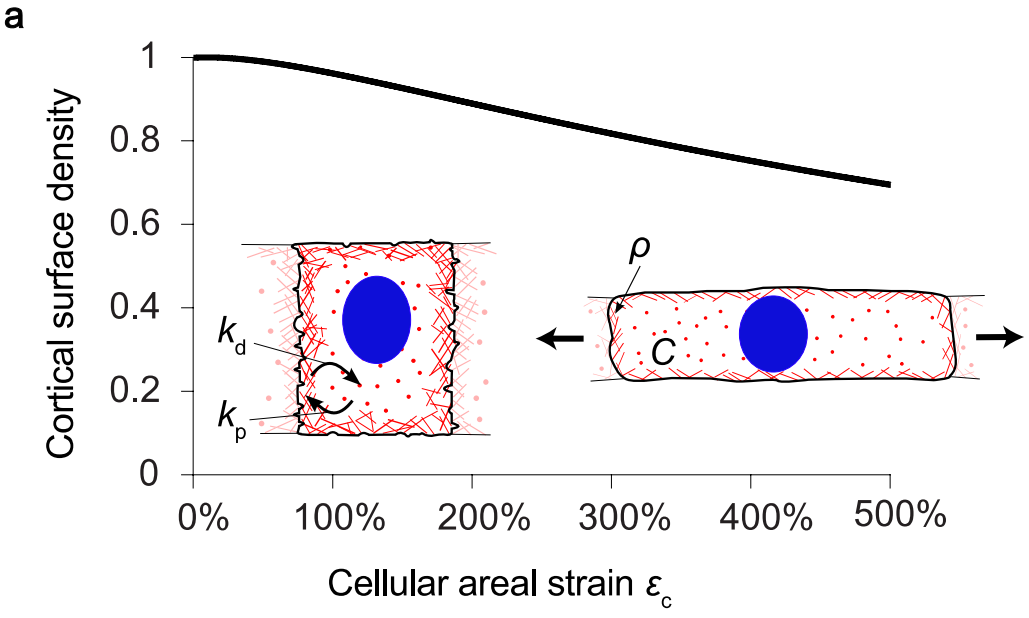

Figure 43: ***Stretch-induced cortical dilution. a****, Illustration of the model accounting for limited availability of cytoskeletal components. We fixed the total mass* m *of cytoskeletal material in a cell, which includes the cytosolic fraction (concentration of dissolved components* C *times cell volume* V_0*) and the cortical fraction (*ρ *times cortex area* A_{cortex}*),* $m = CV_0 + \rho A_{cortex}$*. We considered first-order polymerization and depolymerization kinetics for the cortex with rate constants* k_p *and* k_d*, resulting in* $k_p C = k_d \rho$ *at steady state. These two equations predicted a progressive depletion of cortical surface density* ρ *with increasing cellular areal strain* ε_c*.*

6.3.3.2 Experimentally testing the stretch-induced cortical dilution

To test this hypothesis of a cortical dilution induced by stretch, we measured cortical surface density ρ in cells located at the apex of fixed domes and represented it as function of cell strain ε_c. We first fixed the domes and stained the F-actin using phalloidin (see methods in section 8.4.9). These experiments showed that superstretched cells systematically exhibited less dense cortices (Figure 44, Figure 45).

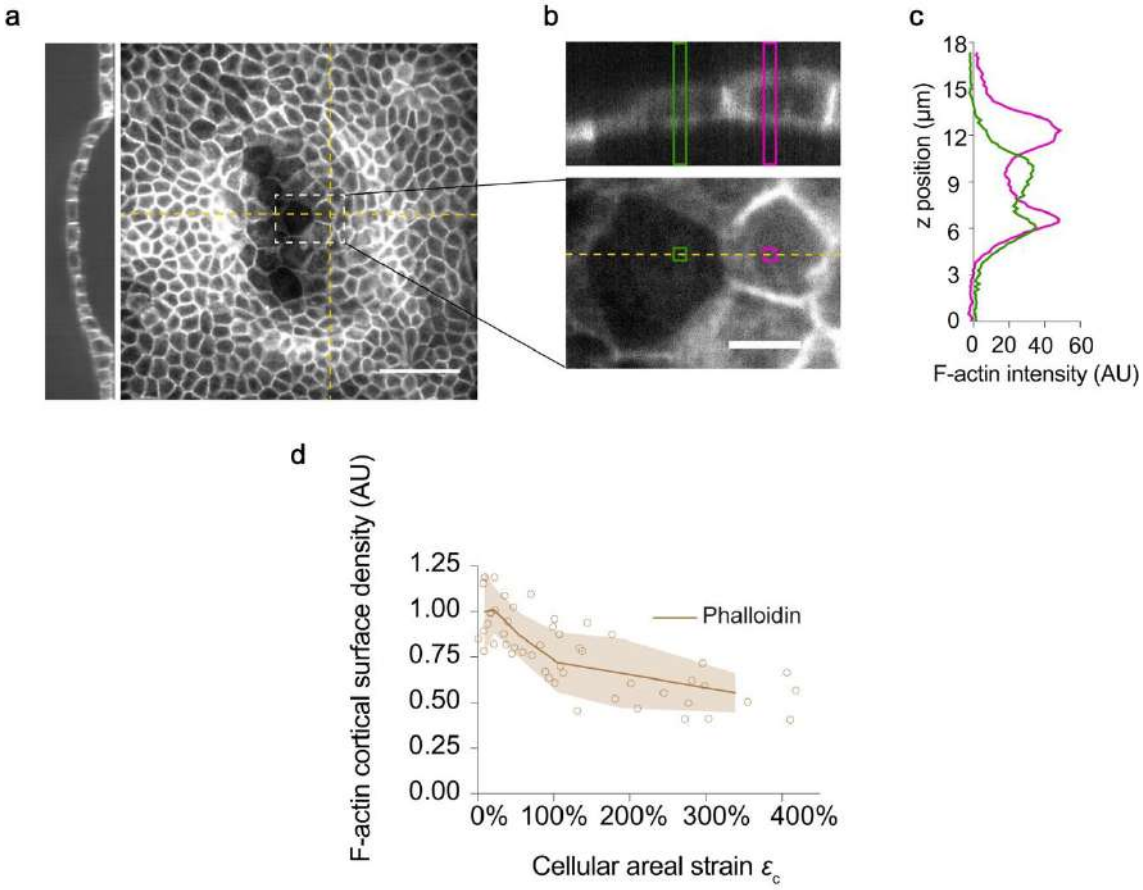

Figure 44: ***Stretch-induced cortical dilution shown in fixed domes. a****, Sum of intensity projection and confocal section of a dome stained for F-Actin (phalloidin). Scale bar, 50 µm.* ***b****, Zoom of representative cells. Scale bar, 10 µm.* ***c,*** *F-actin intensity (arbitrary units) along the bands marked in* ***b****.* ***d****, Normalized cortical F-Actin density (phalloidin) versus cellular strain (n=68 cells from 5 domes).*

Moreover, live imaging of cells labelled with SiR-actin (see methods in section 8.4.7) showed that the actin cortex became progressively and reversibly diluted with cell stretching (Figure 46).

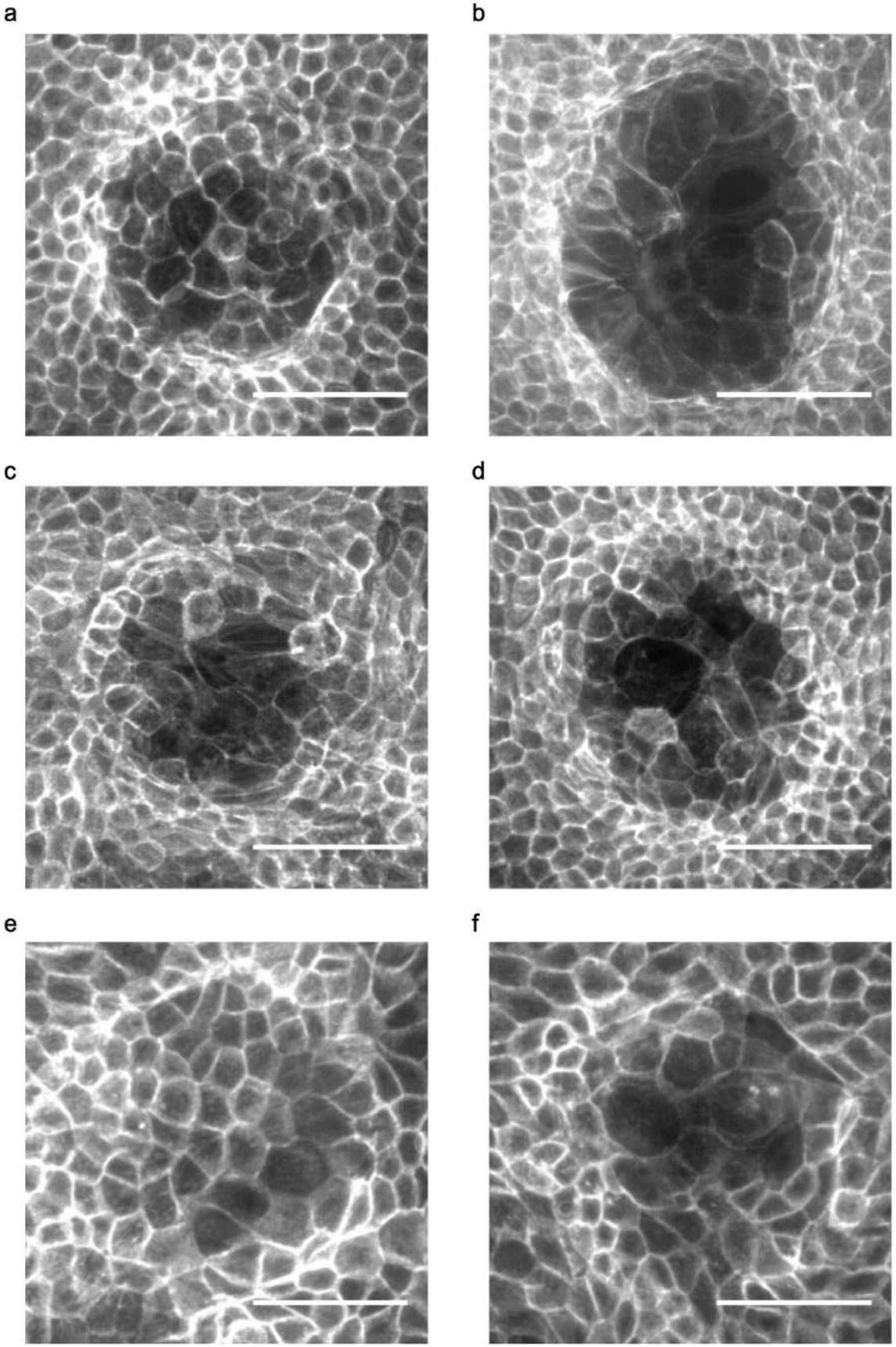

Figure 45: ***Superstretched cells display lower F-Actin cortical surface density. a-f****, Sum of intensity projection of epithelial domes stained for F-Actin (phalloidin), n=5. Scale bars, 50 µm.*

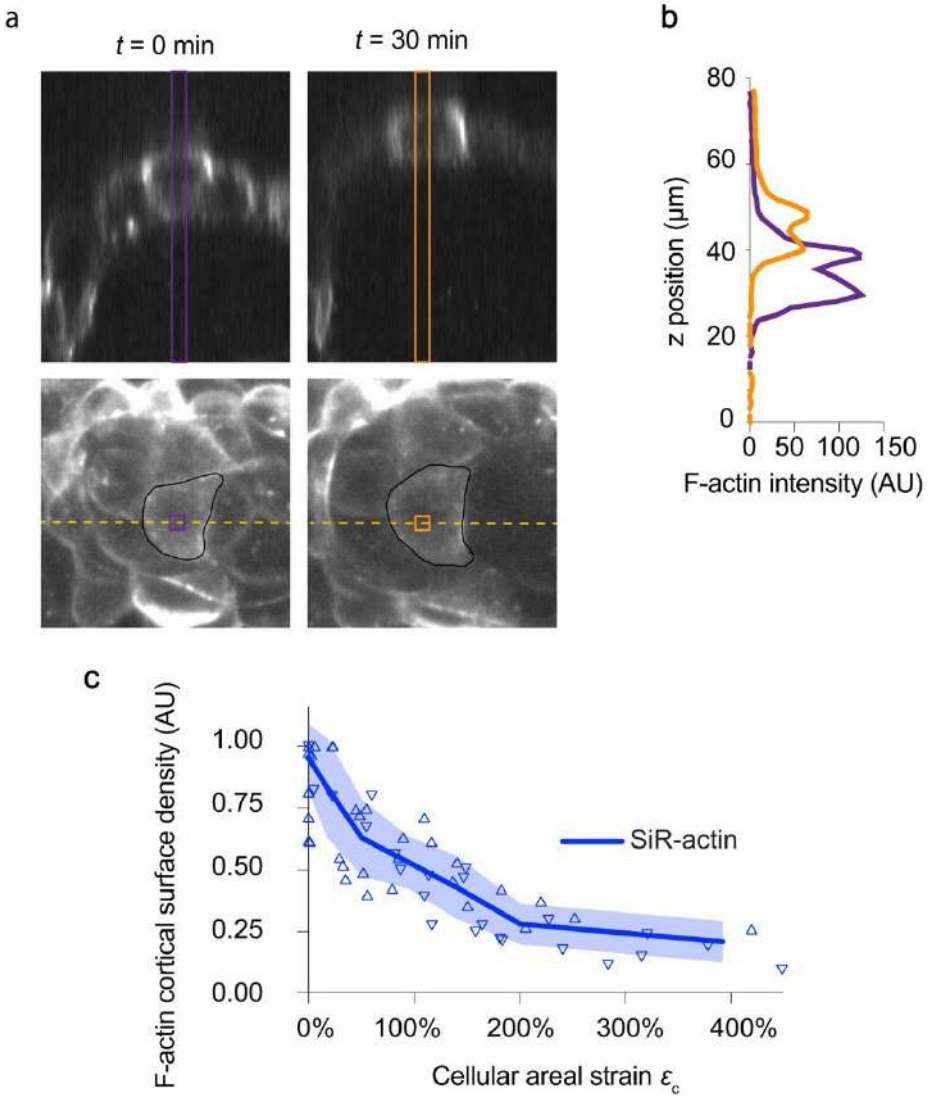

Figure 46: ***Stretch-induced cortical dilution shown in live imaging. a****, Live imaging of the cortex (SiR-actin) of a cell located at the apex of a dome at two different time points of a swelling event (0 min and 30 min).* ***b****, Intensity profiles along the purple and orange bands shown in* ***a*** *for the two time points. This representative example illustrates cortical dilution during stretching, as further quantified in* ***c*** *for 7 domes.* ***c****, Normalized cortical F-Actin density (measured using SiR-actin in live cells, measured in AU) as a function of the cellular areal strain. The data set includes 26 cells from 7 domes sampled at different time points both during swelling (upward triangles) and deswelling events (downward triangles).*

6.3.3.3 Strain-softening as a result of cortical depletion

Recent studies on reconstituted systems[269], cell extracts[268] and living cells[21] suggests a complex relation between cortical tension and various characteristics of the actomyosin network, including myosin activity, network architecture, connectivity, turnover or density. In particular, by examining cells with different network architecture, Chugh et al.[21] showed that cortical density may not always positively correlate with cortical tension. However, it is reasonable to expect that, irrespective of network

architecture, cortical tension will decrease when the cortex becomes very diluted. This idea is consistent with the recent quantitative analysis of actomyosin dynamics by Malik-Garbi et al.[268], who suggest a linear scaling between active tension and network density across a variety of conditions determining cortex architecture and turnover. It is also consistent with the work of Chugh et al.[21], who through experiments and theory conclude that there exists an optimal thickness for maximal tension, but also that at low-enough thicknesses tension decreases with decreasing thickness. Based on this rationale, we assume here a linear relation between cortical active tension γ and ρ, in agreement with most active gel models of the actomyosin cortex[265, 266].

With this assumption and if cortical components are in infinite supply leading to Eq. 6.10, we obtain that surface tension in the cortex is constant and independent of cellular deformation. We thus recover the standard vertex model given by Eq. 6.1, which predicts a monotonously increasing cellular tension-strain relationship, see Figure 38. In contrast, accounting for cortical depletion, and assuming that γ_{ab} and γ_l are proportional to ρ with possibly a different coefficient of proportionality, we obtain:

$$\gamma_{ab} = \gamma_{ab,0}\frac{\rho}{\rho_0} = \gamma_{ab,0}\frac{\frac{A_{c,0}}{A_{0,i}} + \omega}{\frac{A_{c,i}}{A_{0,i}} + \omega} \tag{6.16}$$

where $\gamma_{ab,0}$, ρ_0 and $A_{c,0}$ are the active tension, the cortical areal density and the cortex surface area in the reference configuration. Similarly, we have:

$$\gamma_l = \gamma_{l,0}\frac{\rho}{\rho_0} = \gamma_{l,0}\frac{\frac{A_{c,0}}{A_{0,i}} + \omega}{\frac{A_{c,i}}{A_{0,i}} + \omega} \tag{6.17}$$

From this expression, it is clear that increasing cortex area $A_{c,i}$ (or cellular strain ε_c) will lead to a reduction in the active tensions, thereby softening the epithelial sheet.

Accounting for cortical depletion, the virtual work function of one cell per unit reference area becomes:

$$\delta W_i = \frac{\rho}{\rho_0}\left(\gamma_{ab,0}\frac{\delta A_i}{A_{0,i}} + \gamma_{l,0}\frac{\delta A_{l,i}}{A_{0,i}}\right) \tag{6.18}$$

This expression can be directly used in the computational 3D vertex model described in 6.2.2. Considering a uniformly stretched idealized tissue made out of regular hexagonal cells, the effective energy density becomes:

$$\delta W = \frac{\rho}{\rho_0}\left(\gamma_{ab,0} - \gamma_{l,0}\frac{k}{(1+\varepsilon_c)^{3/2}}\right)\delta\varepsilon_c \tag{6.19}$$

where,

$$\frac{\rho}{\rho_0} = \frac{2(1+k)+\omega}{2[1+\varepsilon_c + k(1+\varepsilon_c)^{-1/2}]+\omega} \tag{6.20}$$

From these expressions, it is straightforward to compute the cellular constitutive relation as:

$$\sigma = \frac{\delta W}{\delta\varepsilon_c} = \frac{\rho}{\rho_0}\left(\gamma_{ab,0} - \gamma_{l,0}\frac{k}{(1+\varepsilon_c)^{3/2}}\right) \tag{6.21}$$

The constitutive relation accounting for cortical depletion is compared with the relationship given by Eq. 6.4 in Figure 47.

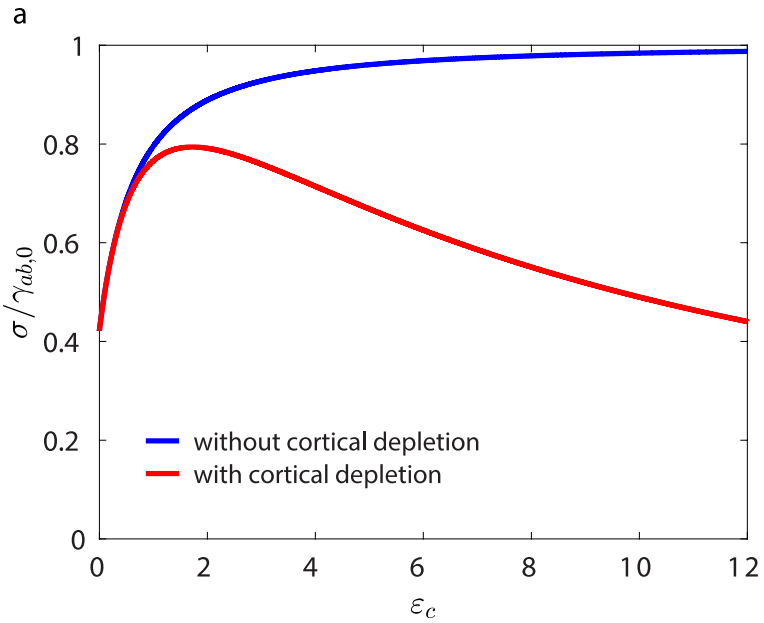

Figure 47: ***Cellular constitutive relation with and without softening by cortical depletion****.* ***a****, Cellular constitutive relation obtained with a planar tissue made of regular cells undergoing uniform areal stretching for different models considered in this study. Eq. 6.4, which assumes constant cortical tensions, is plotted for* $\gamma_l/\gamma_{ab} = 0.25$ *and* $k = 4/\sqrt{3}$ *(blue). The cellular constitutive relation accounting for cortical depletion using Eq. 6.21 is plotted for* $\gamma_{l,0}/\gamma_{ab,0} = 0.25$*,* $k = 4/\sqrt{3}$*, and* $\omega = 10$ *(red).*

The figure shows that, because of cortical depletion, the initial increase of tension with strain is followed by a strain-softening regime during which tension decreases with increasing strain.

6.3.3.4 Experimentally testing the strain-softening

Exogeneous induction of cortical dilution using latrunculin A proved uninformative because domes promptly collapsed, possibly because of weakening of cell-cell junctions. As an alternative, we locally triggered actin depolymerization using a photo-activatable derivative of cytochalasin D (see for details on the methods 8.4.12). Upon local activation, targeted cells increased their area without noticeable changes in the dome overall shape (Figure 48), indicating that cortical dilution is sufficient to cause large increases in cell area.

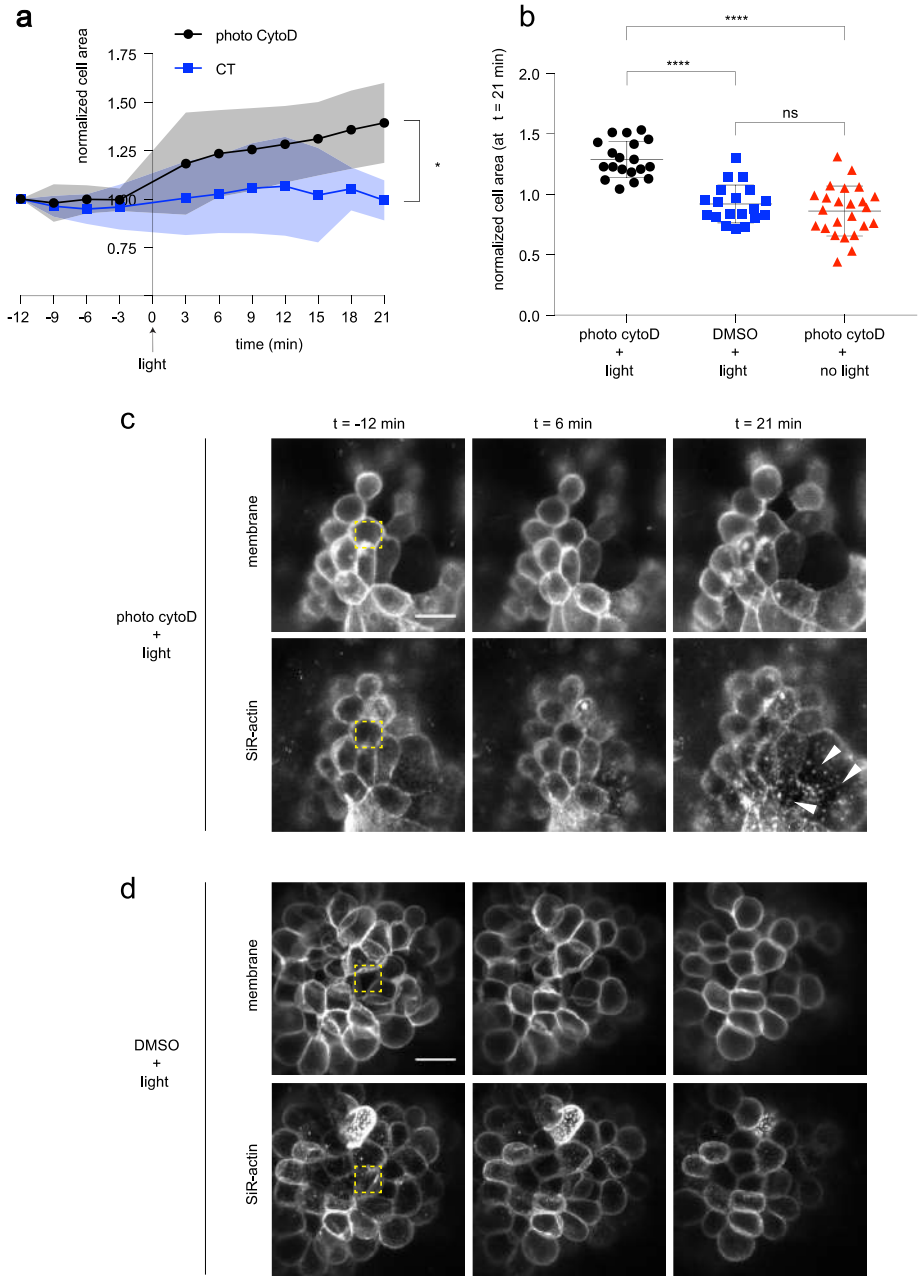

Figure 48: ***Local perturbation of the actin cortex using photoactivatable Cytochalasin D increases cell area. a*** *Time evolution of the normalized cell area in response to local*

*photoactivation of Cytochalasin D (black line, activation at t = 0 min, see methods, n = 5 domes). The blue line shows the time evolution of control cells (same illumination protocol but no photoactivatable Cytochalasin D in the medium, n = 8 domes). Area was normalized to the first time point. Solid lines and shaded areas indicate mean ± SD. At t = 21 min, normalized cell areas were significantly different (*P = 0.0159, two-tailed Mann-Whitney test).* ***b,*** *Normalized cell area 21 minutes after photoactivation in three experimental conditions: photoactivated cells (black circles, n = 19 cells from 5 domes), cells subjected to the same illumination protocol but without photoactivatable Cytochalasin D in the medium (blue squares, n = 19 cells from 8 domes), and cells with photoactivatable Cytochalasin D in the medium but without illumination (red triangles, n = 24 cells from 9 domes). Data include the immediate neighbors of the targeted cells because Cytochalasin D quickly diffused after activation. (****P<0.0001, ****P<0.0001, ns not significant, P = 0.4130, from left to right, two-tailed Mann-Whitney test. Data are shown as mean ± SD.* ***c,*** *Representative photoactivation experiments showing the apex of one dome before (-12 min) and after (6 min, 21 min) photoactivation of the cell marked with a yellow dashed rectangle (n=5). Top panels show the fluorescently labelled membrane and bottom panels show the SiR-actin channel. Note the increase in cell area and granulation in the SiR-actin channel (white arrowheads), indicating disruption of the actin cortex. Scale bar, 15 µm.* ***d,*** *Control experiment in which one cell at the apex of the dome (yellow dashed line) was subjected to the illumination protocol of* ***c*** *without photoactivatable Cytochalasin D in the medium (n=8). Top panels show the fluorescently labelled membrane and bottom panels show the SiR-actin channel. Scale bar, 15 µm.*

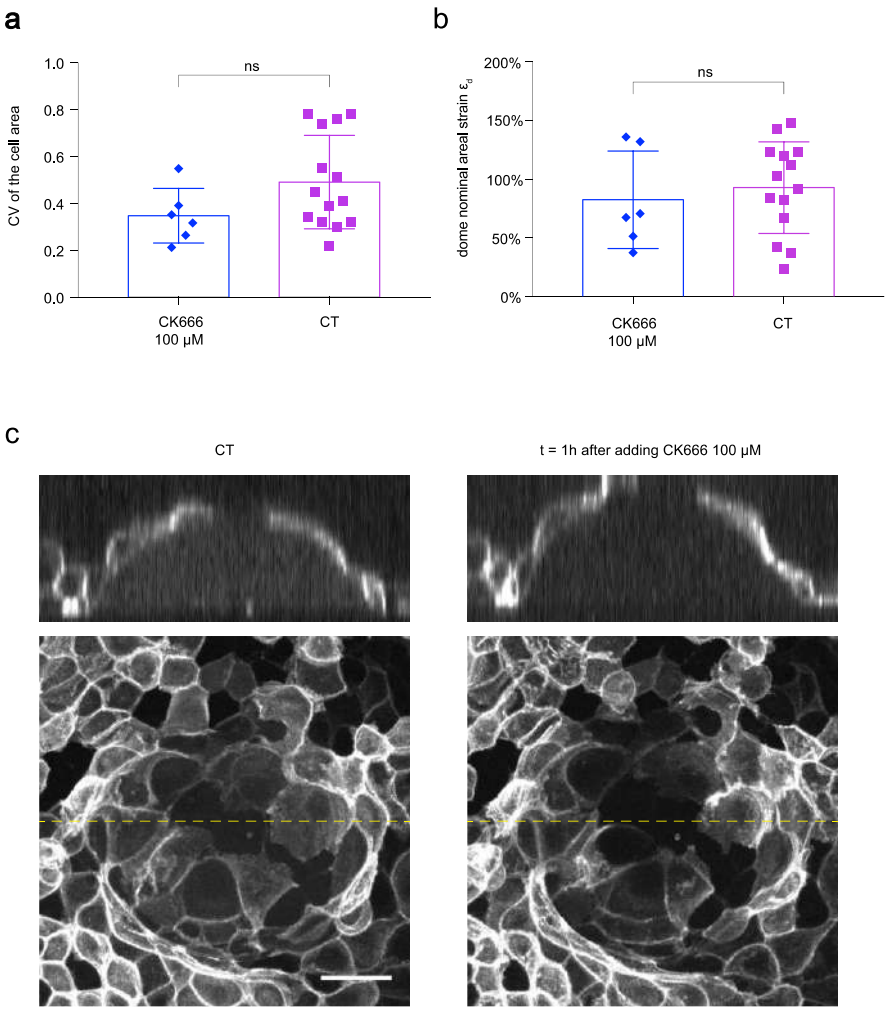

Figure 49: ***Inhibition of ARP2/3 does not affect area heterogeneity in MDCK domes. a,*** *Coefficient of variation of the cell area (CV, defined as standard deviation divided by the mean)*

in MDCK-CAAX domes treated with CK666 (100 µM for 60 minutes), compared to control domes. The coefficient of variation is a non-dimensional indicator of heterogeneity. The CV was calculated by measuring area of 10 cells in n = 6 domes treated with CK666 and in n = 14 control domes. ns, not significant (P = 0.1256). Two-tailed Mann-Whitney test. Data are shown as mean ± SD. ***b****, Dome nominal areal strain in MDCK-CAAX domes treated with CK666 (100 µM for 60 minutes, n=6), compared to control domes (n=14). ns, not significant, P = 0.7043. Two-tailed Mann-Whitney test. Data are shown as mean ± SD* ***c****, Maximum intensity projections and x-z sections of a representative control dome (left) and the same dome treated with CK666 100 µM (1 h). Scale bar, 25 µm.*

We then tested whether exogenously interfering with the actin cytoskeleton architecture. Impairing actin branching through ARP2/3 inhibitor CK666 (see 8.4.8 for details on the methods) did not affect significantly dome height and area heterogeneity (Figure 49).

Taken together, these results are consistent with our hypothesis that cortical dilution underlies cellular superstretching.

6.3.3.5 Strain localization due to an unbounded cell softening by cortical depletion

We next examine the structural consequences in a multicellular computational model of this strain-softening material behavior, understood here as a regime in which local tension decreases with deformation, resulting in a negative tangent stiffness. As shown in Figure 50, it leads to a phenomenon of strain-localization.

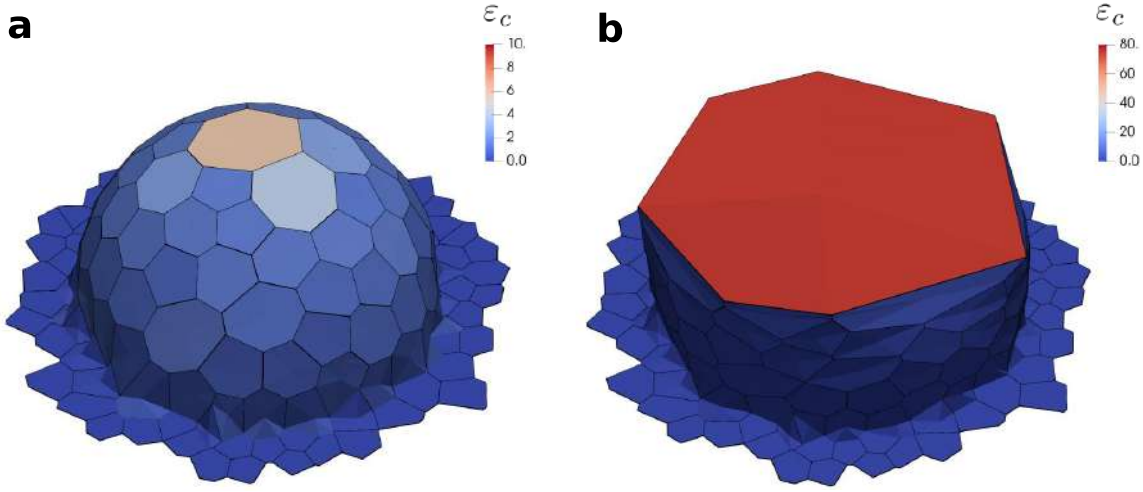

Figure 50: ***Strain localization due to an unbounded cell softening by cortical depletion****.* ***a-b,*** *A computational vertex model simulation of an expanding epithelial dome based on Eq. 6.18 accounting for cellular strain-softening.* ***a,*** *After an initial phase in which all cells are in a regime in which tension monotonously increases with strain, one cell reaches the strain-softening regime and thus is more easily further deformed.* ***b,*** *The softening cell localizes the deformation, relaxing neighboring cells. The simulation parameters are* $\gamma_{l,0}/\gamma_{ab,0} = 0.25$ *and* $\omega = 10$*. The strain-localization is obtained in* ***b*** *after imposing the enclosed volume increment* ΔV^* *on the equilibrated configuration in* ***a****.*

The emergence of strain localization, here the unbounded superstretching of a single cell in the dome, as a consequence of strain-softening is well-known[270]. However, this behavior is at odds with the observed cellular deformations (Figure 40) and it is not physically reasonable since it would lead to extreme thinning of cells, hence compressing the nucleus and other cytosolic objects, it would require very large amounts of membrane area, and it would stretch other cytoskeletal networks such as the intermediate filaments network (Figure 51). **In summary, above certain level of strain, cells will exhibit a re-stiffening that will avoid very extreme deformations**.

6.3.4 Re-stiffening at large cellular strains

A number of mechanisms can be invoked to introduce a re-stiffening of cells at very high strains. Any combination of these mechanisms should reflect in the model as an additional energy contribution penalizing large cellular deformations. Observations of the striking morphological transition in the intermediate filament (IF) network, and precisely for the keratin-18 network, from a relaxed state wrapping around the nucleus in barely stretched cells to a taught state in super-stretched cells (Figure 51, Figure 52), suggest a significant load-bearing role of IFs in super-stretched cells, but not in moderately stretched cells.

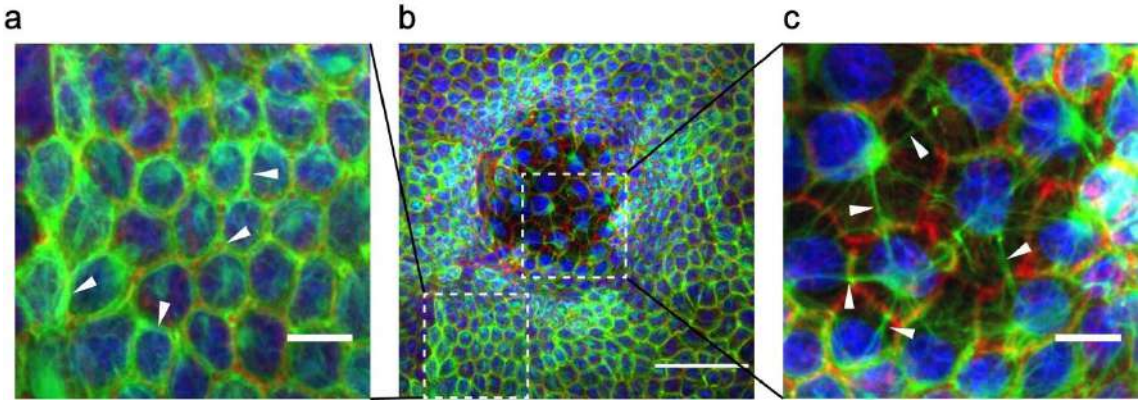

Figure 51: ***Intermediate filaments reorganize in superstretched cells. a-c****, MDCK keratin-18 (green) dome stained for F-Actin (phalloidin, red), and nuclei (Hoechst, blue) (n=3). Scale bar in* ***b****, 50 µm. Scale bar in* ***a,c****, 10 µm.*

6.3.4.1 Modeling the re-stiffening provided by the IFs

We include in the model a re-stiffening mechanism provided by the IFs by introducing a network of elastic springs. Inspired by the IF network morphology in super-stretched cells, these elastic springs connect the cell barycenter with the center of cell-cell junctions

and become active only after crossing an elongation threshold. We postulate an elastic energy per unit reference area for these springs of the form:

$$W_{ij}^{b} = \begin{cases} 0, & \varepsilon_{f,ij} < \varepsilon_{f,0} \\ \frac{1}{3A_{0,i}} k_f \left(\varepsilon_{f,ij} - \varepsilon_{f,0}\right)^3, & \varepsilon_{f,ij} \geq \varepsilon_{f,0} \end{cases} \tag{6.22}$$

where $\varepsilon_{f,ij}$ is the axial strain in the IF connecting the j −th edge-center to the barycenter of the i −th cell, $\varepsilon_{f,0}$ is the strain threshold after which the spring is activated, and k_f controls the steepness of the elastic penalty to elongation.

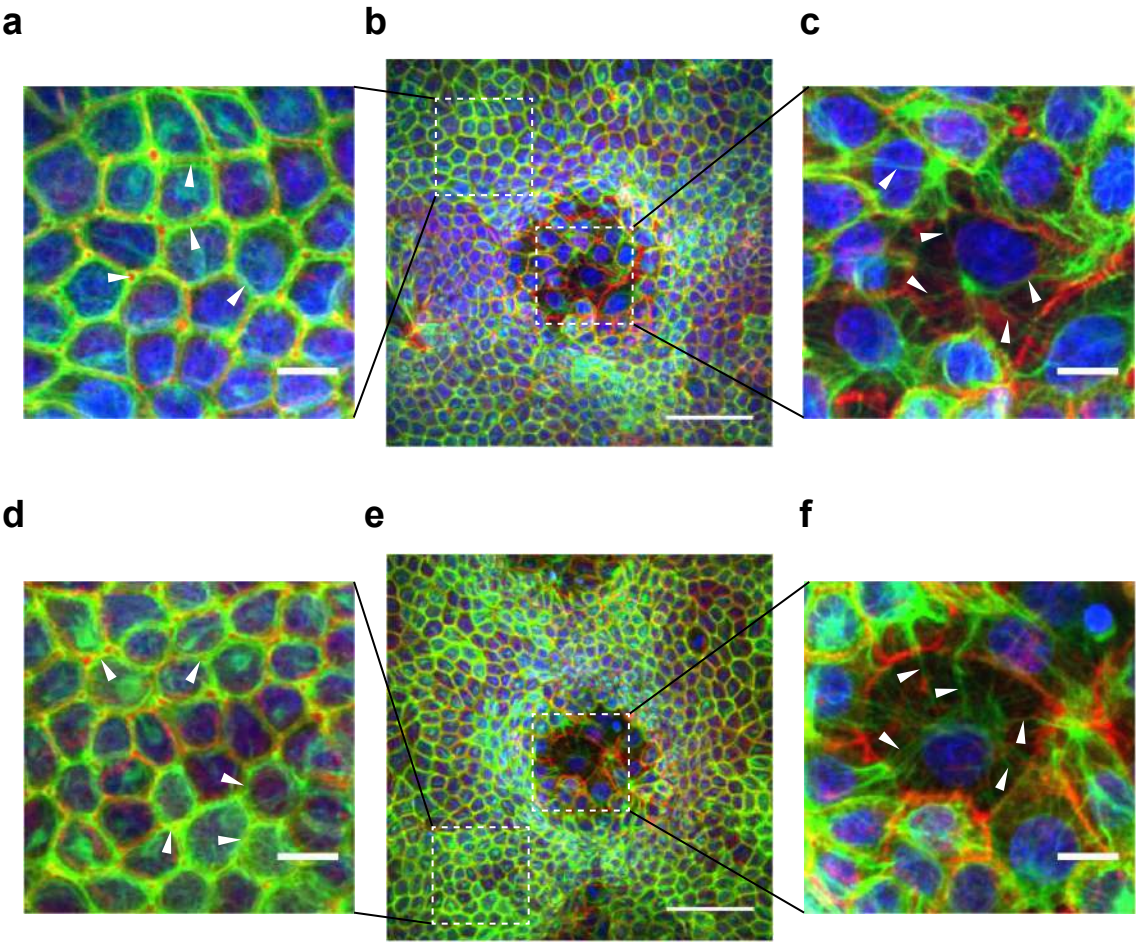

Figure 52: ***Intermediate filaments reorganize in superstretched cells. a-f****, Immunofluorescence micrographs (see methods in 8.4.9), represented using maximum intensity projection, of domes of MDCK keratin-18-GFP (in green) cells stained for F-Actin (phalloidin, red), and nuclei (Hoechst, blue), n=3. Scale bars, 50 µm.* ***a****,* ***d****, Zoomed area (marked with a dashed white square in* ***b****) showing that the keratin-18 filament network links neighboring cells and localizes at cell boundaries (white arrowheads). Scale bars, 10 µm.* ***c****,* ***f****, Zoomed area (marked with a dashed white square in* ***e****) showing that keratin-18 filaments are taut (white arrowheads) and have reorganized, with nodes at the cell center connecting different cells. Scale bars, 10 µm.*

With this model, we do not attempt to describe in detail the mechanics of the IF network. Despite recent advances in the mechanical characterization of individual IFs up to ~300% axial strains[271, 272], the constitutive behavior of a network of cross-linked IF bundles, which likely depends on progressive engagement of filaments, coordinated unfolding of the coiled-coil structure and filament sliding in a bundle, remains largely unknown. We note, however, that the results of the model are largely insensitive to the specific form of the potential beyond the threshold ($\varepsilon_{f,ij} \geq \varepsilon_{f,0}$), as long as it introduces a strong enough barrier to excessive cellular strains. This is further discussed later with Figure 61.

Accounting for the IF network with the potential in Eq. 6.22, the virtual work function per unit undeformed area of a cell is then $\delta W_i^t = \delta W_i + \sum_j \delta W_{ij}^b$, where δW_i is given in Eq. 6.18 and the summation is performed over all edges of a given cell.

Considering again a uniformly strained tissue made out of regular hexagonal cells, it is possible to express the tissue tension as $\sigma = \delta W^t / \delta \varepsilon_c$. The resulting cellular constitutive relation is shown in Figure 53.

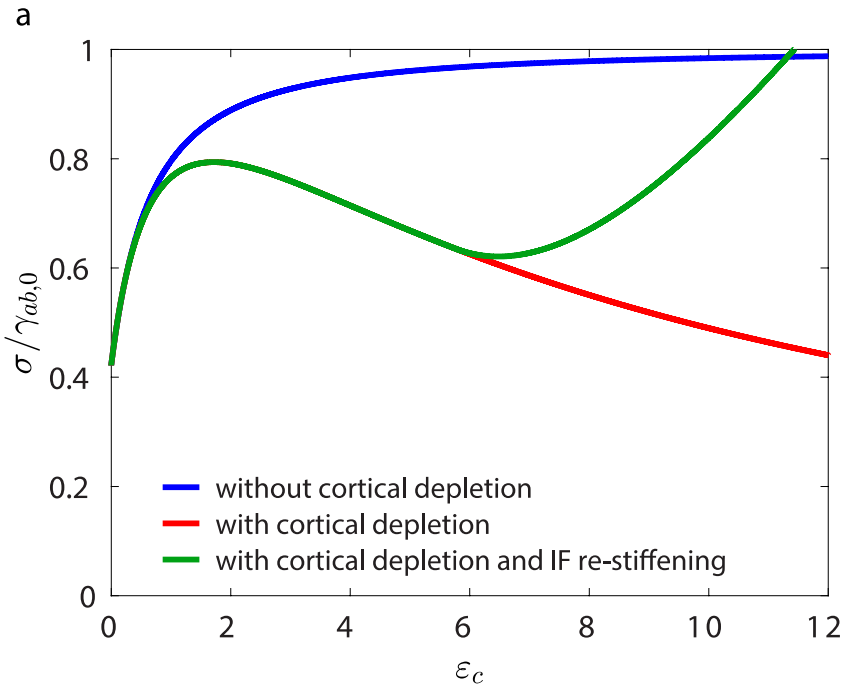

Figure 53: ***Cellular constitutive relations, with and without cortical depletion and with cortical depletion and re-stiffening****.* ***a****, Cellular constitutive relation obtained with a planar tissue made of regular cells undergoing uniform areal stretching for different models considered in this study. Eq. 6.4, which assumes constant cortical tensions, is plotted for* $\gamma_l/\gamma_{ab} = 0.25$ *and* $k = 4/\sqrt{3}$ *(blue). The cellular constitutive relation accounting for cortical depletion using Eq. 6.21 is plotted for* $\gamma_{l,0}/\gamma_{ab,0} = 0.25$, $k = 4/\sqrt{3}$, *and* $\omega = 10$ *(red). The cellular constitutive relation accounting for cortical depletion and re-stiffening at large strains is shown for* $\gamma_{l,0}/\gamma_{ab,0} = 0.25$, $k = 4/\sqrt{3}$, $\omega = 10$, $\varepsilon_{f,0} = 1.6$, *and* $k_f/\gamma_{ab,0}s_0^2 = 3$ *(green).*

After the strain-softening regime, it exhibits a mechanical re-stiffening due to the IF network. The computational implementation of the model using δW_i^t leads to the coexistence of super-stretched and barely stretched cells, with a sharp increase of cellular strain variance as tissue strain increases, and a tensional plateau (Figure 54).

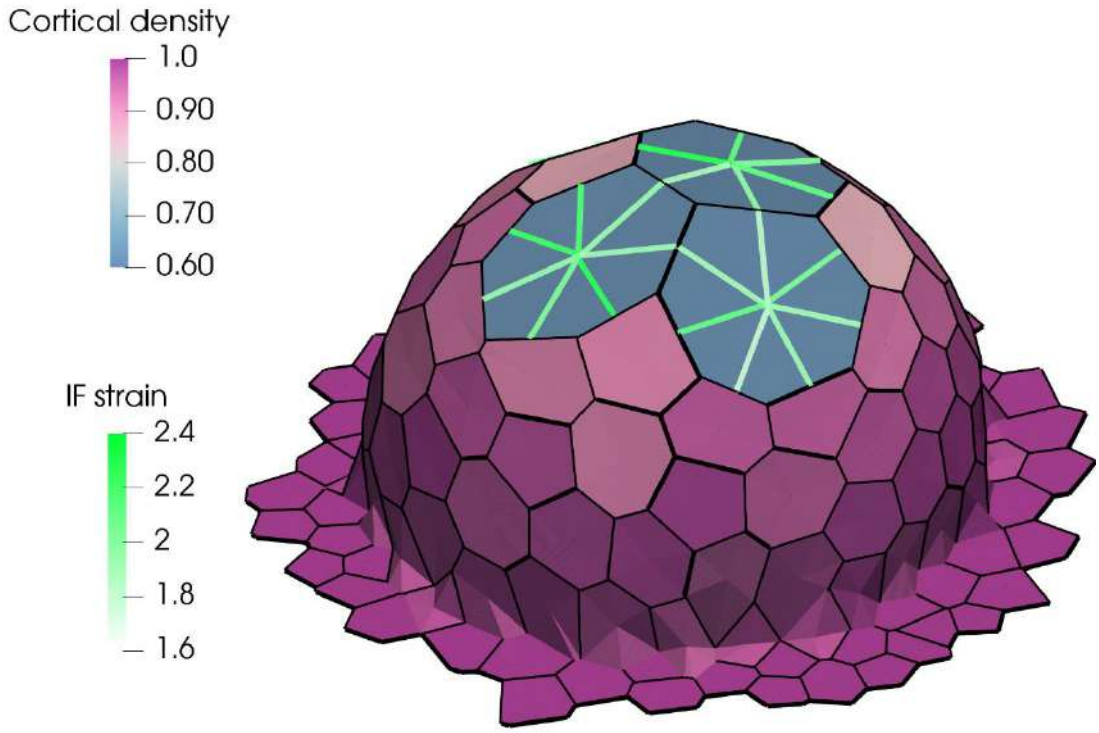

Figure 54: A computational vertex model simulation of epithelial dome expansion with individual cells exhibiting cortical depletion induced strain-softening and re-stiffening by IF network. Cells near the top of the dome undergo strain-softening due to cortical dilution and become superstretched. The IF network represented by green lines connecting cell barycenter with cell edges is activated beyond a threshold IF strain $\varepsilon_{f,0}$. The stiff response of the IF-network prevents excessive cellular deformation. The simulation parameters used are $\gamma_{l,0}/\gamma_{ab,0} = 0.25$, $\omega = 10$, $\varepsilon_{f,0} = 1.6$, and $k_f/\gamma_{ab,0}s_0^2 = 3$.

6.3.4.2 Experimentally testing the re-stiffening at large strains provided by the intermediate filaments

To further test this load bearing state, we performed laser ablation experiments, consisting in cutting with a laser beam, keratin-18 bundles in both superstretched cells and in barely stretched ones (Figure 55) (see detailed methods in 8.4.11).

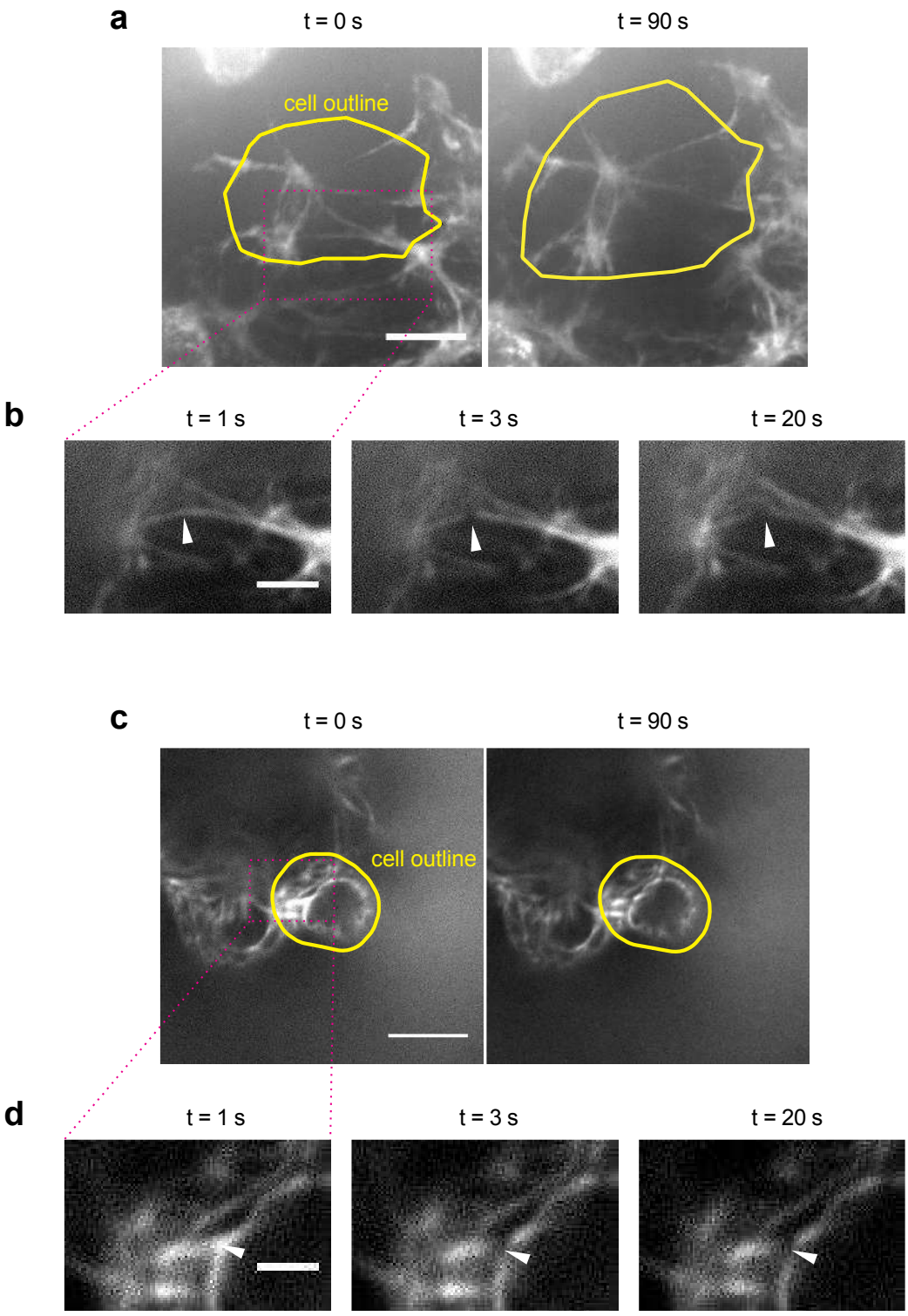

Figure 55: ***Intermediate filaments stabilize cell shape in superstretched cells. a,*** *Representative MDCK keratin-18-GFP superstretched cell at the apex of a dome before (0 s) and after (90 s) laser cutting the keratin filament bundle marked in* ***b*** *with a white arrowhead. The yellow line marks the outline of the cell measured with bright field imaging. Scale bar, 10 µm.* ***b,*** *Magnified view of the region labelled in* ***a*** *with a doted magenta rectangle. Scale bar, 5 µm.* ***c,*** *Representative MDCK keratin-18-GFP weakly stretched cell at the apex of a dome before (0 s) and after (90 s) laser cutting the keratin filament bundle shown in* ***d****. The yellow line marks the outline of the cell measured with bright field imaging. Scale bar, 10 µm.* ***d****, Magnified view of the region labelled in* ***c*** *with a doted magenta rectangle. The same laser cutting protocol and laser power were used to cut filaments in superstretched and weakly stretched cells. n=5. Scale bar, 5 µm.*

Following this experiment, we quantified the change in area for superstretched and for weakly stretched cells after laser ablating keratin bundles (Figure 56):

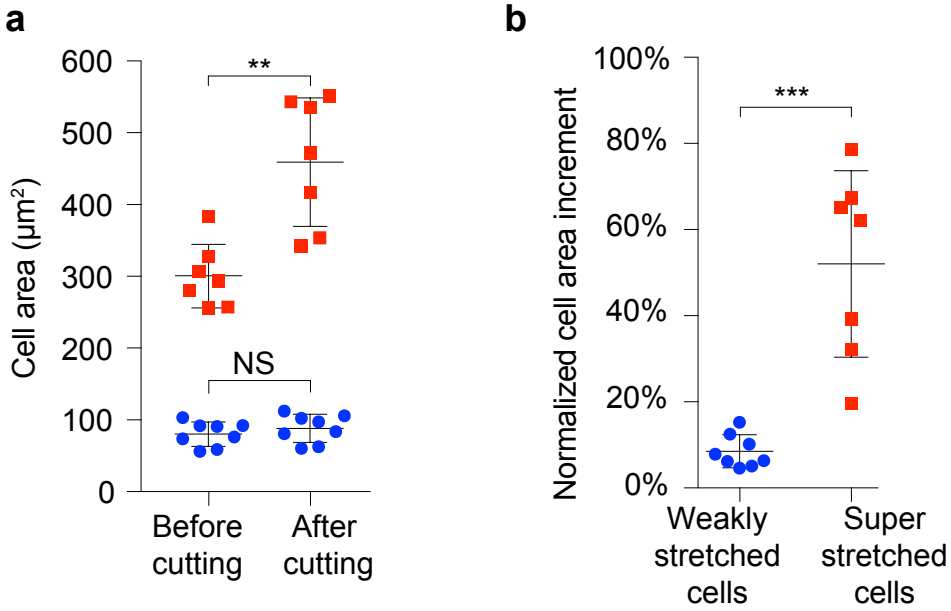

Figure 56: ***Changes in cell area after laser cuts of keratin bundles. a-b****, Changes in cell area following laser cuts of keratin bundles for weakly stretched (blue, n=8 cells) and superstretched cells (red, n=7 cells), represented as cell area before and after cuts (**a**, **P=0.0023; ns, non-significant, P=0.3282) and as normalized cell area increment (**b**, ***P<0.0003). Two-tailed Mann-Whitney tests. Mean ± SD.*

The results showed that there is no significant increase in area for weakly stretched cells but **there is a very significant areal increase after ablating a single bundle of keratin-18 for cells that were already in the superstretched phase. These observations agree with the notion that IFs act as a safety mechanism in cells against excessive deformations**[271-273].

6.3.5 Effective bi-stable energy landscape of active origin

The coexistence of low- and high-strain phases can be easily understood by examining Figure 57. It is clear that for either small or large applied tension (horizontal gray lines), there exists a single equilibrium state (a single intersection with the black line characterizing the cell constitutive response). Within a range, there are three intersections, and hence three equilibrium states.

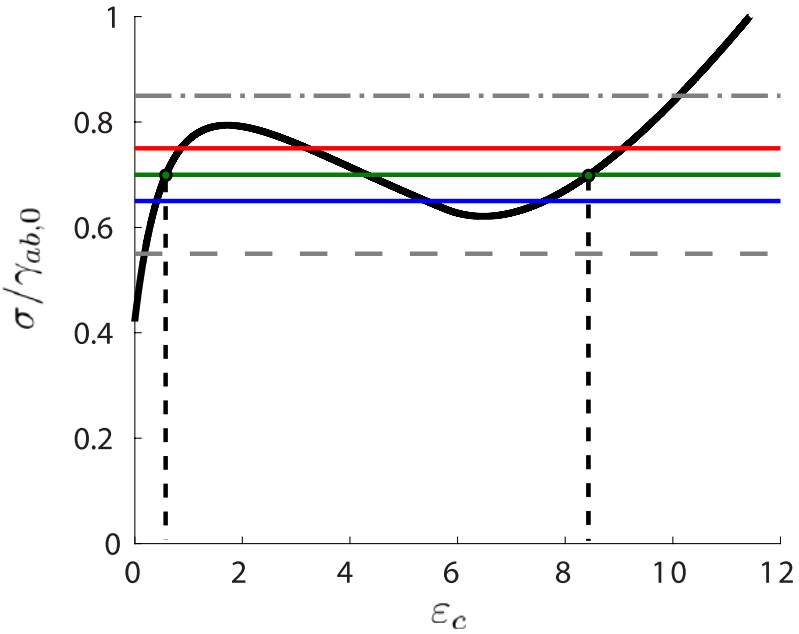

Figure 57: ***Cells can be in two strain states in a given range of high tension. a,*** *Cellular constitutive relation for a uniformly stretched tissue of regular hexagonal cells accounting for cortical depletion and re-stiffening at very high strains (black line) and various levels of applied tissue tension (horizontal lines). The parameters used are* $\gamma_{l,0}/\gamma_{ab,0} = 0.25$, $\omega = 10$, $\varepsilon_{f,0} = 1.6$, *and* $k_f/\gamma_{ab,0}s_0^2 = 3$.

To better establish the nature of these three equilibria, we develop next an effective energy to describe the system. We first note that the virtual work function in Eq. 6.1 can be obtained from the minimization of an effective energy function given by $W_i = \left(\gamma_{ab}A_i + \gamma_l A_{l,i}\right)/A_{0,i}$ because in this model γ_{ab} and γ_l are constant. In contrast, when we account for cortical dilution, ρ becomes deformation-dependent, Eq. 6.13, and as a result the virtual work function in Eq. 6.18 does not derive from an effective energy function. **The nonconservative nature of an active system can be expected in general**. However, under equibiaxial stretching of the cell monolayer, tissue tension can be expressed as $\sigma(\varepsilon_c)$, see Figure 57, a function of a scalar variable characterizing deformation (the areal cellular strain). Integration of this function:

$$W_{\text{effective}}(\varepsilon_c) = \int_0^{\varepsilon_c} \sigma(\varepsilon) d\varepsilon \tag{6.23}$$

defines an **effective energy landscape of active origin characterizing the mechanics of the system under equibiaxial deformation**, from which tension can be derived by differentiation, $\sigma = dW_{\text{effective}}/d\varepsilon_c$. Because $\sigma(\varepsilon_c)$ is non-monotonic, $W_{\text{effective}}(\varepsilon_c)$ is a

non-convex function. In Figure 58 we represent the effective potential energy density of the tissue under equibiaxial extension, $P(\varepsilon_c, \sigma) = W_{\text{effective}}(\varepsilon_c) - \sigma\varepsilon_c$, which includes the potential energy of the applied tension:

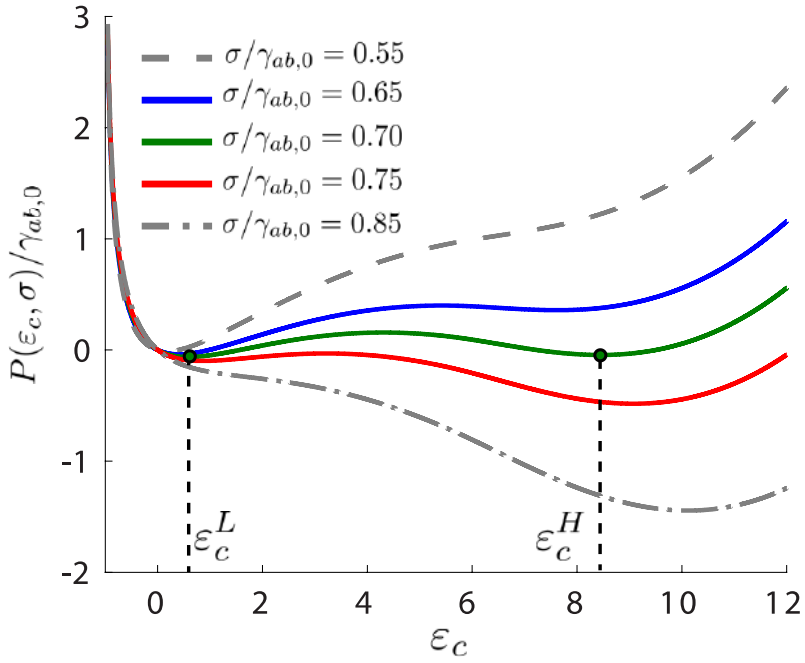

Figure 58: ***Effective energy landscape of active origin. a,*** *Effective potential energy density $P(\varepsilon_c, \sigma) = W_{effective}(\varepsilon_c) - \sigma\varepsilon_c$ of a single regular hexagonal cell accounting for the potential energy of the applied tension, for various levels of applied tension σ. Within a range of tensions, the effective potential energy has two local minima (red, green, and blue lines), corresponding to two stable phases of low and high areal strains. Outside this range, the potential energy has only one minimum (gray lines). The parameters used are $\gamma_{l,0}/\gamma_{ab,0} = 0.25$, $\omega = 10$, $\varepsilon_{f,0} = 1.6$, and $k_f/\gamma_{ab,0}s_0^2 = 3$.*

The equilibrium points found in Figure 57 as intersections of the constitutive black curve with horizontal lines are now the critical points of the energy landscape, i.e.~strains satisfying $\partial P/\partial\varepsilon_c = 0$. The non-convexity of the energy landscape is now apparent, with a two-well structure and three critical points in a range of intermediate tension. Interestingly, a bi-stable energy landscape was also identified by[255] in a region of parameter space of 3D vertex models of epithelial sheets, not associated to cortical depletion but rather to high negative lateral tension. It is clear from Figure 58 that only two of the equilibrium points in the colored curves are marginally stable (local minima of P), which correspond to the low- and the high-strain phases characterized by $\varepsilon_c^L < \varepsilon_c^H$ (labeled in Figure 58). **In precise analogy with the classical conceptual framework of superelasticity**[263]**, an epithelial dome with nominal strain $\boldsymbol{\varepsilon_d}$ in the interval $(\boldsymbol{\varepsilon_c^L}, \boldsymbol{\varepsilon_c^H})$ can lower its energy by developing a mixture of cells in the low- and in the high-strain energy wells rather than uniformly stretching all cells by a cellular strain**

ε_c close to the average dome strain ε_d. During this process of progressive switching of cells towards the high-strain phase, tension is nearly constant, as shown in Figure 59.

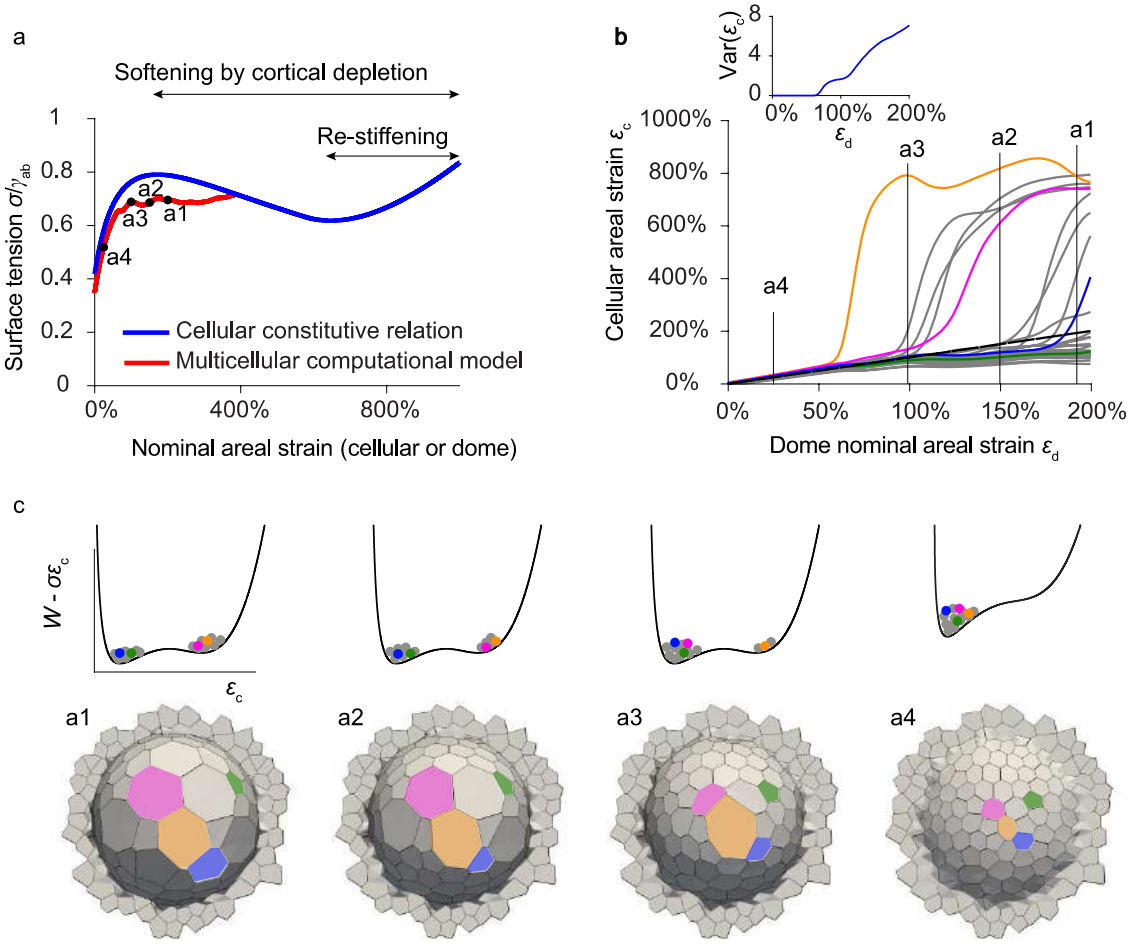

Figure 59: ***Cellular and dome mechanical behavior, exhibiting superelasticity.*** ***a****, Non-monotonic cellular constitutive relation predicted by the vertex model, accounting for softening by cortical depletion and re-stiffening at extreme cellular strains (blue line). Dome tension-strain relationship for the multicellular computational version of the same model (red line). a1 to a4 correspond to panels shown in* ***b*** *and* ***c.*** ***b****, ε_c versus ε_d from the vertex model. Variance of ε_c versus ε_d (inset).* ***c****, (bottom) Calculated geometries for a dome at 4 different strain stages of the deflation process represented in* ***a*** *(red). (top) Schematic representation of the effective potential energy landscape of active origin of the material. Tilted by tissue tension, it exhibits two wells at sufficiently high tension, corresponding to the barely stretched and superstretched states of cells. Color points represent the state of the individual cells depicted in bottom panels.*

This phenomenon is further illustrated in Figure 60, where a dome with regular hexagonal junctional network is considered to make a more quantitative comparison between the effective energy landscape of a uniform system and the numerical calculation. This figure shows the emergence of a bimodal cellular strain distribution peaked at ε_c^L and ε_c^H beyond the onset of switching. Note that in this swelling calculation, cells start to transit to the high-strain phase only when the energy well corresponding to the low-strain phase is

shallow. The situation in Figure 59 is reversed, since we model there a de-swelling event, and therefore highly stretched cells only transit to the low-strain state when the high-strain energy well is shallow.

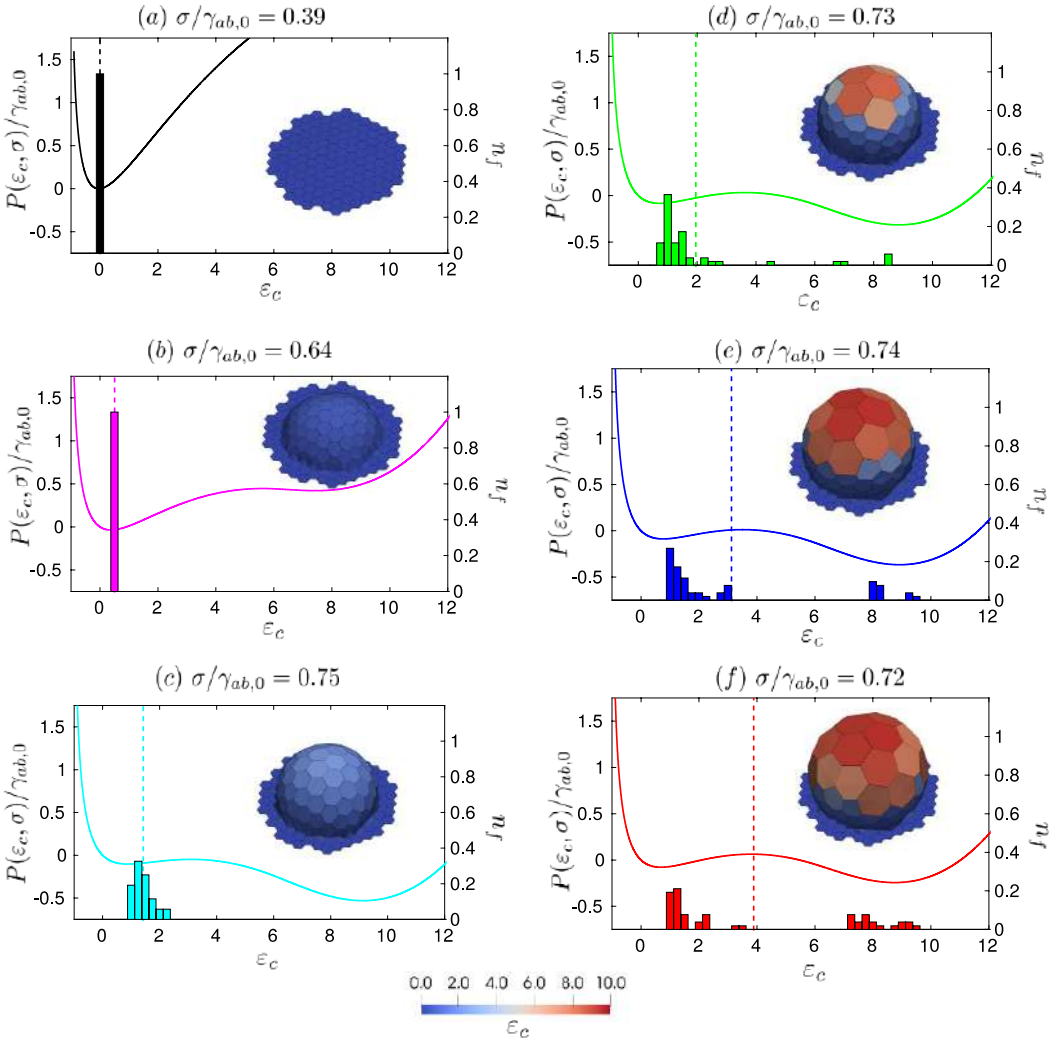

Figure 60: ***Progressive switching from low-strain to high-strain phases during dome swelling. a-f,*** *It is illustrated using the computational vertex model in a tissue made out of regular hexagonal cells. The dotted vertical lines correspond to the nominal dome strain ε_d. The cell areal strain ε_c is plotted on the $x-$axis. The effective potential energy density $P(\varepsilon_c,\sigma) = W_{effective}(\varepsilon_c) - \sigma\varepsilon_c$ of a regular hexagonal cell is plotted as solid lines referring to the left $y-$axis. The tissue tension σ, mentioned on the top of each subfigure, obtained from the computational model at a given ε_d, is used to evaluate $P(\varepsilon_c,\sigma)$. The histograms refer to the right $y-$axis and indicate the fraction of the cells in the dome n_f belonging to a given bin of cellular strain ε_c (of width 0.25). The progressive switching from low strain to high strain phase is apparent in* ***(d)-(f)*** *at nearly constant tissue tension σ. The simulation parameters used here are $\gamma_{l,0}/\gamma_{ab,0} = 0.25$, $\omega = 10$, $\varepsilon_{f,0} = 1.6$, and $k_f/\gamma_{ab,0}s_0^2 = 3$.*

According to this theoretical framework, as the nominal strain in the dome ε_d approaches ε_c^H, all cells will switch to the high-strain phase and the system will only be able to further

accommodate strain by stretching the high-strain phase, thereby exhausting the tension-buffering mechanism of the tissue. **In our experiments, we did not reach such high nominal strains, but we examined computationally this regime as reported in** Figure 61, where the model parameters are those used in Figure 59. In this case, we considered the equibiaxial stretching of a planar tissue to emphasize that epithelial **superelasticity should be a general mechanism**, not specific to the way the tissue is stretched by transmural pressure in our experiments:

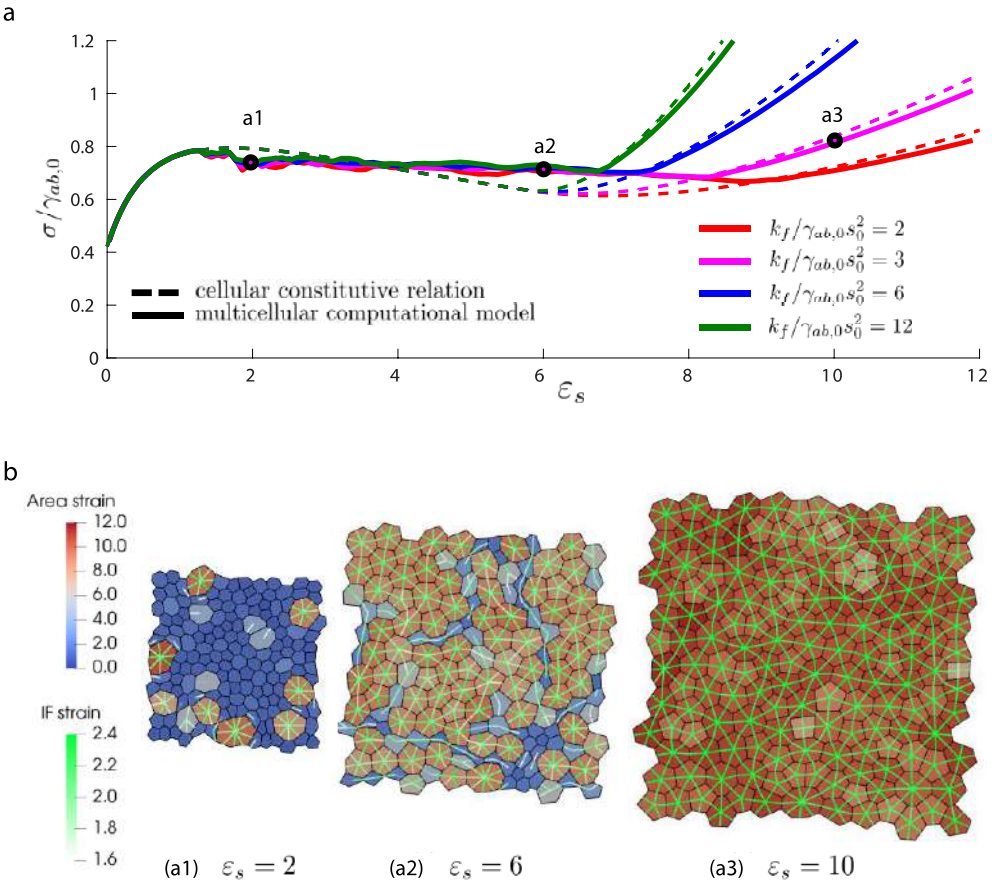

Figure 61: ***Exhaustion of the superelastic tension buffering****.* ***a****, Tissue tension as a function of areal strain obtained from the multicellular computational vertex model (solid) and for tissue made of regular hexagonal cells undergoing uniform areal stretching i.e. the cellular constitutive relation (dashed).* ***b****, In the computational vertex model, uniform biaxial stretch characterized by the areal strain ε_s is imposed on a biperiodic epithelial tissue by gradually increasing the box dimensions. The colormap in cells represents areal strain whereas the colormap on the dual network modeling the IFs represents linear strain. During stretching of epithelial sheet, when the tissue areal strain is in the range $1 \sim \varepsilon_c^L < \varepsilon_s < \varepsilon_c^H \sim 7$, the model predicts a wide tensional plateau during which the number of cells in the high strain phase gradually increases* ***(a1, a2)****. The tissue response in this region is unaffected by the details of the re-stiffening mechanism, which become relevant only after all cells have transitioned in to the high-strain phase for $\varepsilon_s > \varepsilon_c^H$. The onset of high-strain phase ε_c^H is determined by the re-stiffening parameters k_f and $\varepsilon_{f,0}$. For $\varepsilon_d > \varepsilon_c^H$, the dome exhibits positive stiffness as all cells in the dome are required to climb up the re-stiffening branch to accommodate a higher ε_s* ***(a3)****. The simulation parameters are the same as Figure 59, $\gamma_{l,0}/\gamma_{ab,0} = 0.25$, $\omega = 10, \varepsilon_{f,0} = 1.6$, and $k_f/\gamma_{ab,0}s_0^2 = \{2,3,6,12\}$.*

This figure suggests that by epithelial superelasticity, the tissue could increase its area by an order of magnitude at nearly constant tension. The mechanical response of the tissue is largely unaffected by the details of the re-stiffening model during the tensional plateau. Once the buffering mechanism is exhausted, the figure also shows that tension further increases at a rate given by the re-stiffening mechanism, whose details now become important. It is also interesting to compare the actual tension-strain response obtained computationally (solid lines) with the cellular constitutive relation obtained for a uniformly stretched tissue (dashed lines), which suggests that the height of the plateau is close to that given by the Maxwell equal area construction (which, for this system, is a horizontal straight line defined in the σ-ε plane, enforcing that the area enclosed in the two regions defined by the intersections of the horizontal line and the non-monotonic $\sigma(\varepsilon)$ are equal), albeit a bit higher. In fact, due to metastability of the low- and high-strain phases, superelasticity is often characterized by some degree of **hysteresis**, with a stress higher than that predicted by the Maxwell construction during loading and lower during unloading. We examined this in Figure 62 by loading and unloading the computational dome reported in Figure 59:

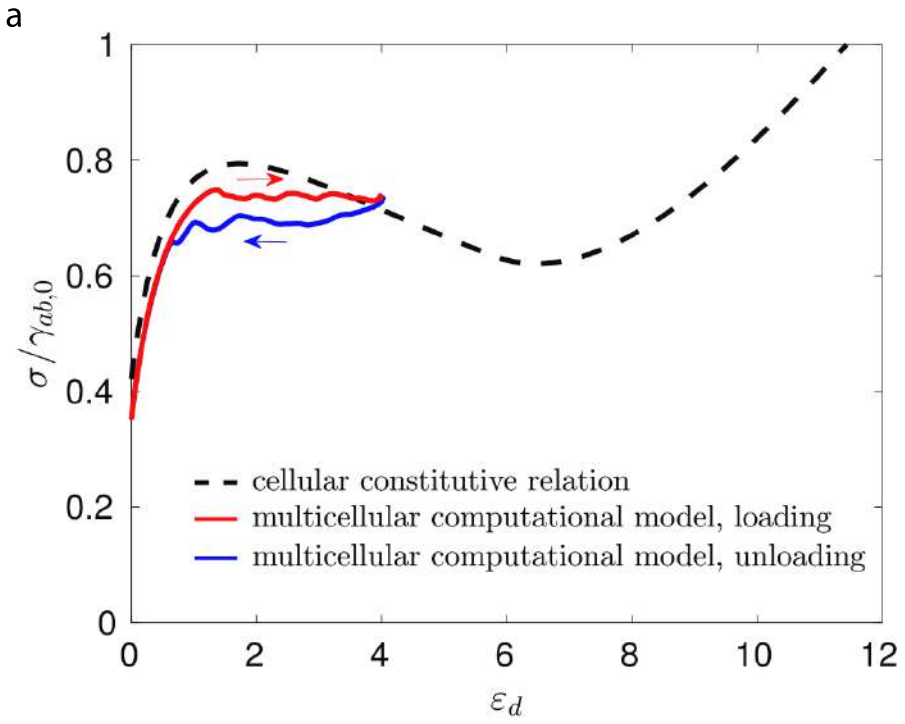

Figure 62: ***Loading-unloading of a dome using the multicellular computational vertex model reveals hysteresis****.* ***a****, The enclosed volume is increased to reach* $\varepsilon_d = 4$ *and then decreased at the same rate until* $\varepsilon_d = 0$*. The simulation parameters are the same as Figure 59,* $\gamma_{l,0}/\gamma_{ab,0} = 0.25$*,* $\omega = 10, \varepsilon_{f,0} = 1.6$*, and* $k_f/\gamma_{ab,0}s_0^2 = 3$*.*

Figure 62 shows that indeed our model produces some degree of hysteresis, with a lower tensional plateau upon unloading. Since the stress-strain curve for epithelial domes shown in Figure 32c of the section 6.1 is the result of various domes undergoing complex loading-unloading processes, hysteresis could be responsible in part for the higher degree of scatter observed beyond dome nominal strains of 100%.

6.4 Summary and discussion

Because the domes exhibit large volume fluctuations due to osmotic gradients, **we are able to measure and investigate the tension-strain relation of the curved epithelia at different levels of inflation** (represented as areal strain). We obtained an experimental mechanical constitutive relation, illustrated by the stress-strain curve (Figure 32 and Figure 33) that has the following main features:

- reversibility, meaning that the points on the curve correspond to different stages of swelling or deswelling of different domes.
- first regime, below 100% areal strain, that is close to a linear law, starting at ~1 mN/m.
- second regime (beyond 100% areal strain), with a tensional plateau at ~ 2 mN/m and larger scatter, reaching 300% areal strain which are very large deformations.

To better understand the measured epithelial tension-strain relation, we implemented a theoretical vertex model in 3D described in section 6.2.1.. By assuming constant cell volume[231] and idealizing cells as regular hexagons of uniform thickness under uniform equibiaxial strain, this model predicts that the effective surface tension of the tissue depends on cellular areal strain ε_c as described in Eq. 6.4., reproduced here:

$$\sigma = \gamma_{ab} - k\frac{\gamma_l}{(1+\varepsilon_c)^{3/2}}$$

where k is a non-dimensional constant. Remarkably, this active constitutive relation recapitulates the initial increase in tension and the subsequent plateau at larger areal strain observed experimentally (Figure 32c and Figure 39).

The tendency of tension to plateau at large strains emerges naturally from the fact that the area of lateral faces decreases with cell stretching and, hence, tissue tension converges to

apico-basal tension. To theoretically examine a situation closer to the experiments, we developed a 3D computational version of the vertex model shown in Figure 36. This model allowed us to study the tension-strain relation of computationally swollen and deswollen epithelial domes with junctional geometry obtained from experimental observations. The tension-strain law evaluated using this computational approach closely matched the analytical constitutive relation derived from a uniformly deformed planar tissue (Eq. 6.4, Figure 39).

This simple theoretical model missed an important experimental feature of the system which is the fact that above ~100% of dome strain (this is the second regime where there is the tensional plateau), there is no affinity between dome strain and individual cell strain. In this case, the variance of the cell strain increased sharply and barely stretched cells coexist with super-stretched ones. Putting everything together, **domes exhibit very large and reversible deformations at a constant tension, showing a strain heterogeneity among the constituent cells. They coexist in two states (barely and super- stretched ones). These are defining hallmarks of superelasticity**, which is a well-known material behavior of some metal alloys. Superelasticity requires a strain-softening mechanism that explains the phase transformation (seen as a mechanical instability) between the barely stretched cells to the superstretched ones at a nearly constant tension. As the cellular tension is mainly defined by the cellular cortex, we focused on it to find the possible strain-softening mechanism, which can be based on the fact that cells that are stretched up to very large deformations present also a diluted cortex. As the main component of the cortex we focused on actin, although cortical depletion could also affect actin cross-likers, polymerization agents and molecular motors. In our model, cortical thickness (or equivalently cortical surface density ρ) is determined by a balance between polymerization at the plasma membrane and depolymerization in the bulk of the actin gel[265, 266]. If the availability of dissolved cytoskeleton components ready for polymerization is infinite[265, 266], this model predicts that cortical density ρ and hence cortical tension γ are constant and independent of strain, leading to Eq. 6.4. If free cytoskeleton components are limited, however, the model predicts a progressive depletion of cortical density ρ with cellular areal strain, and hence **strain-softening** when the actin cortex becomes sufficiently thin[21] (Figure 43). From the experimental point of view, we first showed that **cell strain induces cortical dilution**. This has been shown in F-Actin stainings (fixed samples) but also in live using SiR-actin as a live imaging

probe for F-actin. In those experiments, F-actin cortical surface density decreased systematically with cell areal strain.

The next step is to very if the aforementioned cortical dilution (caused by cell strain) produces cell softening. If this implication is true, then softer cells placed over a dome that is in a uniform and isotropic state of tension, will be even more stretched and this is how the phase transformation works as a mechanical instability.

This mechanism cannot be tested using classical pharmacological treatments that affect all the cells as adding latrunculin, jasplakinolide or cytochalasin D to the medium that will affect the actin cytoskeleton or using any other treatment that will impair global contractility of myosin motors as blebbistatin or Y27632. The main reason is that for all these treatments, dome tension will globally drop, and we should point out that the phase transformation from barely stretched cells towards superstretched ones due to the strain-softening mechanism does only occur at high levels of tension.

Besides strain-softening, superelasticity also requires re-stiffening at large strains to confine the high-strain phase. Indeed, without a re-stiffening mechanism, the first cell reaching the softening regime would easily deform further, relaxing neighboring cells and eventually localizing deformation unboundedly[270]. Multiple mechanisms, generally neglected under moderate deformations, could stiffen cells subjected to extreme stretching, including exhaustion of the plasma membrane reservoir[274, 275], crowding of adhesion molecules in shrinking cell-cell adhesions[276], confinement of the stiff nucleus between two tensed cortices, or load transfer to the otherwise relaxed intermediate filament cytoskeleton[231]. Our experiments do not rule out any of these possibilities but they support the latter, as intermediate filaments in superstretched cells appeared unusually straight, suggesting load bearing (Figure 51, Figure 52).

To further test this mechanism, we laser-ablated keratin-18 filaments both in weakly stretched and superstretched cells. In weakly stretched cells, laser ablation did not induce changes in cell area. By contrast, laser ablation in superstretched cells resulted in a rapid increase in cell area, indicating that intermediate filaments in superstretched cells, but not in relaxed cells, bear tension (Figure 55, Figure 56).

By introducing re-stiffening at large strains into our computational vertex model, we were able to recapitulate our most salient experimental observations. At low levels of dome stretching, tissue tension increased with strain and cellular strain heterogeneity was low. By contrast, at high levels of stretching, the domes reached a tensional plateau and cellular strain heterogeneity rose sharply. Thus, **strain-softening by stretch-induced depletion**

of cortical components followed by re-stiffening at extreme stretches, configure an effective bistable energy landscape of active origin that explains the emergence of a stable high-strain phase of superstretched cells under sufficiently large tension.

Here one could rise the question 'can we predict which cells are (more likely) going to change phase?' The answer to it is that it is very hard to predict because there are several factors involved that could weight in a different way for different domes. Here we present a non-exhaustive list:

- The position of the cell on the dome. Despite domes are close to spherical caps, cells localized at dome's apex, that can be stretched in an equibiaxial way, are more strained than cells located at the boundary that can only be stretched in the meridional direction. This fact is already seen in the computational vertex model made of equal hexagons (see Figure 38c).
- Heterogeneities in the cortical surface density between cells.
- Number of neighbors and the initial shape and size of the cell.
- Different cortical dynamics between cells (because of the cell cycle stage or influenced by other biological cues as the actin network architecture).
- Possible different sizes of the cell nuclei.
- In general, mobilizing the re-stiffening mechanism (mediated by IF's, the plasma membrane, etc.) at different moments of cell deformation.

7 CONCLUSIONS AND FUTURE PERSPECTIVE

Active superelasticity provides a mechanism for epithelial tissues to undergo extreme and reversible deformations at nearly constant tension by progressive switching of individual cells to a superstretched state. Because the underlying subcellular mechanisms are rather universal, our study suggests a broad applicability *in vivo*. For example, epithelial superelasticity may mediate the spreading of superstretched extraembryonic tissues and their subsequent rapid compaction[277]. During these processes, tensional buffering would limit the corresponding Laplace pressure variations in the embryo, which could otherwise affect its shape. Active superelasticity may also enable the extreme cellular stretches in the trophectoderm during swelling and hatching of mammalian blastocysts[261, 262]. As superelastic materials, cells can finely tune their mechanical behavior by regulating expression levels of structural elements of the actin cortex or of their regulators, which ultimately control the threshold for strain-softening. Under conditions of excess availability of cortical elements, tissues may achieve tensional homeostasis without exhibiting cellular heterogeneity (Figure 39). Conversely, weakening the force-generation machinery at the actin cortex may overemphasize strain-softening, which could explain the emergence strain heterogeneity in modified embryonic tissues, leading eventually to tissue failure by strain localization in a few cells[278].

These measurements establish that epithelial monolayers exhibit active superelasticity, an unanticipated mechanical behavior that enables extreme deformations at nearly constant tension.

We reported here a new approach to precisely shape cell monolayers in 3D taking advantage of adhesive micropatterning and transmural pressure. Using this approach, we measured epithelial mechanics in a previously uncharted regime in terms of tissue geometry and stretch magnitude, of general relevance in curved tissues enclosing pressurized lumina. Our study identifies a new mechanism of tensional regulation -active superelasticity- by which epithelial tissues can accommodate extreme levels of stretching at nearly constant tension. Besides providing a framework to understand epithelial mechanics and morphogenesis in vivo, the material laws established here set the stage for a rational manipulation of cell monolayers in organoids and organ-on-a-chip technologies[279-281].

The main conclusions of the thesis are:

1. We reviewed the state-of-the-art on how to measure active mechanical stress in living tissues.
2. We implemented a new experimental approach to induce the formation of epithelial domes of controlled size and shape over PDMS using microcontact printing.
3. We found that epithelial domes very closely follow a spherical cap shape and their stress state can be assumed to be uniform and isotropic. This stress state can be fully described over all the dome by a scalar value σ which is a surface tension.
4. We were able to measure the tension over the dome by applying Laplace's law which is equivalent to consider the equilibrium equation of a thin axisymmetric membrane under uniform pressure. The tension σ can be computed as $2\sigma = R\Delta P$, where ΔP is the transmural pressure and R the radius of curvature of the spherical cap. ΔP coincides with the normal component of the traction vector $\boldsymbol{T}$ which is determined using Traction Force Microscopy ($\Delta P = \boldsymbol{T} \cdot \mathbf{n}$, with $\mathbf{n}$ being the normal vector to the gel surface inside dome's cavity) and R is obtained using confocal microscopy. We do not need to assume any constitutive behavior for the epithelial monolayer to obtain those tension values.
5. The dome setup represents a new micro-mechanical test for curved 3D epithelial tissues, analogous to a bulge test for inert materials. The surface tension σ can be computed at any instant and it can be related with the areal deformation (areal strain) to investigate epithelial rheology.
6. We tested that tension measurements were able to capture the time evolution of tension after applying the Rho Kinase inhibitor Y27632.
7. Dome swelling is caused by a passive water flow that equilibrates an osmotic imbalance. This imbalance is previously caused by an active ionic pumping that is transepithelial and in the apico-basal direction (from the external medium towards the internal cavity).
8. Dome volume dynamics can be modeled using Darcy's law adapted to a semipermeable membrane which withstands mechanical forces.
9. Osmolarity and water pressure can be assumed as uniform inside the dome and also in the external medium because of the timescales of volume dynamics.

Despite this fact, there is a jump in the osmolarity (caused by the active ionic pumping) and there is also a jump in the water pressure across the dome surface (caused by a dynamical resistance to water permeation).

10. We applied controlled hyperosmotic shocks to the dome and therefore we drove it from a given steady state to another one which is equilibrated to the new external osmolarity. We tracked the volume time evolution and from it, we computed the permeability for the MDCK epithelia. We found it in the order of magnitude of previous published data, obtained with other methods such electrical resistance.
11. Assuming the epithelial permeability as a known parameter (calculated before), we computed the absolute osmolarity inside the lumen. We also computed its time derivative which is the ionic pumping rate that was found nearly constant.
12. Using the developed micro-bulge test, we investigated the tension-strain relation for the curved 3D epithelia that form the domes. We found a tension-strain curve that is almost linear and well-defined for low strains and that reaches a tensional plateau with more scattering at large strains.
13. We found that the constituent cells of the dome exhibit strain heterogeneity at large dome deformations. Barely stretched cells coexist with super stretched ones.
14. We termed this new constitutive behavior for the epithelial tissue as active superelasticity, in analogy to superelasticity, a well-known material behavior of some metal alloys. The defining features are the capability to be largely deformed in a reversible manner at a constant tension thanks to a phase transformation of its micro-structure that coexists in two phases.
15. We found that superelasticity requires a strain-softening mechanism that explains the transformation between barely stretched cells to super-stretched ones and a re-stiffening at large deformation that impedes infinite deformations and that stabilizes the super-stretched phase.
16. We identified a stretch-induced cortical dilution as the strain-softening mechanism. We tested it experimentally by showing that more deformed cells systematically have a less dense actin cortex in fixed samples. We also showed the live cortical dilution using SiR-actin as a live probe. Finally, we locally disrupted the actin cortex to find evidence that a diluted cortex will result in a softer cell. We did this by using a photoactivatable Cytochalasin-D, which allowed a local disruption of the cortex without affecting the overall dome tension. The result was a significant increase of cell area.

17. We identified the intermediate filament network as part of the re-stiffening mechanism that avoids infinite deformations of cells that are in the super-stretched phase.
18. We integrated all these ingredients, namely the active superelastic behavior including the strain-softening mediated by cortical depletion and the re-stiffening at large strains by the action of the intermediate filaments, into a computational vertex model. The model is able to recapitulate the effective bistable energy landscape of active origin.

8 APPENDIX

8.1 Cell cultures reported to exhibit domes.

Tissue of origin	Cell line	Reference
Bladder	Rat bladder carcinoma	[283]
Cervix	Human cervical carcinoma	[284]
Choroid plexus	Primary rat choroid plexus	[285]
Colon	Human colon carcinoma (SW-48 cells)	[286]
Colon	Human colorectal adenocarcinoma (Caco2 cells)	[287]
Kidney	MDCK (dog kidney)	[235]
Kidney	LLC- PK1 (pig kidney)	[288]
Kidney	Opossum kidney proximal tubular (opossum kidney)	[289]
Lung	Primary pulmonary alveolar type II cells	[290]
Mammary	Primary neoplastic mouse mammary	[291]
Mammary	RAMA 25 (rat mammary)	[292]
Oral	Primary pig oral epithelia	[293]
Stomach	Primary rat glandular stomach	[294]

Table 2: This table shows different cell lines that are known and described to form domes. This list is not exhaustive. Adapted and updated from [282].

8.2 Viscous dissipation in the actin cortex

The actomyosin cortex is generally modeled as an active visco-elastic gel. At short time-scales, it is able to store elastic energy. At time-scales longer than actin turnover, however, it behaves like a viscous fluid[256, 265]. Because dome swelling takes place over the course of few hours, the elastic behavior of the cortical network is irrelevant. Furthermore, cortical viscosity produces very small forces at these rates of deformation, and only the active component of cortex rheology considered in previous sections plays a significant role. However, following the mechanical instability associated to strain-softening, cells should transit over a short time-scale towards the high-strain phase. Since the model presented so far is based on mechanical equilibrium alone, these transitions occur abruptly as cells suddenly snap from one stable phase to another. This contrasts with the smoother cell shape transitions observed experimentally (Figure 29 and Figure 30 in section 6.1). The dynamics of phase switching will be given by the relevant dissipative mechanisms, which could include not only cortical viscosity but also cytosolic viscosity or the drag forces associated to the rearrangement of the cell-cell adhesions. In the simulations presented in this work, we included the cortex viscosity though a viscous dissipation potential for the i −th cell of the form:

$$\mathcal{D}_i(\dot{\boldsymbol{r}}) = 2\int_{A_i} \mu[\|\boldsymbol{d}\|^2 + (\mathrm{tr}\,\boldsymbol{d})^2]\, t_c dS \tag{8.1}$$

where $\boldsymbol{d}$ is the interfacial rate-of-deformation tensor in the apico-basal surfaces, μ is the bulk shear viscosity coefficient[265] and $t_c = t_{c,0}\rho/\rho_0$ is the cortical thickness proportional to the normalized cortical surface density ρ/ρ_0 and $t_{c,0}$ is the cortical thickness in the reference configuration. The factor 2 accounts for the dissipation occurring in apical and basal cortical faces. Computationally, this functional is sampled at quadrature points in a barycentric triangulation of the polygon representing each cell. Given the state of the system at time t^{n-1} and following Onsager's variational principle[295], the configuration at time $t^n = t^{n-1} + \Delta t$ is obtained by minimizing the time-incremental work function:

$$\Delta W(\boldsymbol{r}) = \sum_{i=1}^{N} \left[\delta W_i^t(\boldsymbol{r^{n-1}}; \boldsymbol{r - r^{n-1}}) + \Delta t \mathcal{D}_i \left(\frac{\boldsymbol{r - r^{n-1}}}{\Delta t} \right) \right] \tag{8.2}$$

along with the constraint for enclosed volume under the dome, $V(\boldsymbol{r}) = V^*$.

The bulk viscosity coefficient is assumed to be $\mu = 4 \times 10^4$ Pa·s, in the range used in[296], with a reference cortex thickness $t_{c,0} = 0.2$ μm[297]. The time step corresponding to $\Delta V^* = 20 s_0^3$ is estimated as $\Delta t = 5.5 \mu s_0 / \gamma_{ab,0}$, to match the rate of change of enclosed volume observed in the experiments (Figure 29).

The modeling parameters used for various simulations in this study are summarized in the following table:

Table 3: Summary of the vertex model simulation parameters used for figures ranging from Figure 53 to Figure 62.

Parameter	Value
s_0	6.75 μm
$\gamma_{ab,0}$	5 mN/m
μ	4×10^4 Pa·s
ΔV^*	$20 s_0^3$
$\gamma_{l,0}$	$0.25 \gamma_{ab,0}$
ω	10
$\varepsilon_{f,0}$	1.6
k_f	$3.0 \gamma_{ab,0} / s_0^2$
Δt	$5.5 \mu s_0 / \gamma_{ab,0}$

8.3 Surface area calculations

8.3.1 Actual area from projected area

We used ImageJ plugins to z-project the maximum fluorescence intensity on the horizontal plane. With this technique, we obtain 2-D images with the projected areas. To retrieve the actual area of one cell, we use the fact that domes very closely follow a spherical cap geometry with known radius of curvature R (Figure 63). Under these conditions, the area of an infinitesimal region on the dome surface, dS, and its projection dS' are related by:

$$dS = \frac{dS'}{\cos\theta} \tag{8.3}$$

where the angle θ is depicted in the figure. In turn, the distance between the projected infinitesimal region and the projection of the north pole of the spherical cap, N', is given by:

$$r = R\sin\theta \tag{8.4}$$

which using the identity $\sin^2\theta + \cos^2\theta = 1$ leads to:

$$\frac{1}{\cos\theta} = \frac{1}{\sqrt{1-\left(\frac{r}{R}\right)^2}} \tag{8.5}$$

Combining the equations 8.3 and 8.5, it follows that the actual surface area of a region, S, can be computed over the plane of projection as:

$$S = \int_{S'} \frac{dS'}{\sqrt{1-\left(\frac{r}{R}\right)^2}} \tag{8.6}$$

As a result of imaging, projected cells on the horizontal plane are already discretized by pixels. Denoting by N_{pix} the number of pixels that belong to a given projected area,

e.g.~that of a cell, by A_p the area of one pixel, by R the radius of curvature of the dome and by r_i the distance between the center of the i-th pixel and the projection of the dome's north pole, we finally obtain the following computable approximation to the actual surface on the dome:

$$S = \sum_{i}^{N_{pix}} \frac{A_p}{\sqrt{1 - \left(\frac{r_i}{R}\right)^2}} = A_p \sum_{i}^{N_{pix}} \frac{1}{\sqrt{1 - \left(\frac{r_i}{R}\right)^2}} \tag{8.7}$$

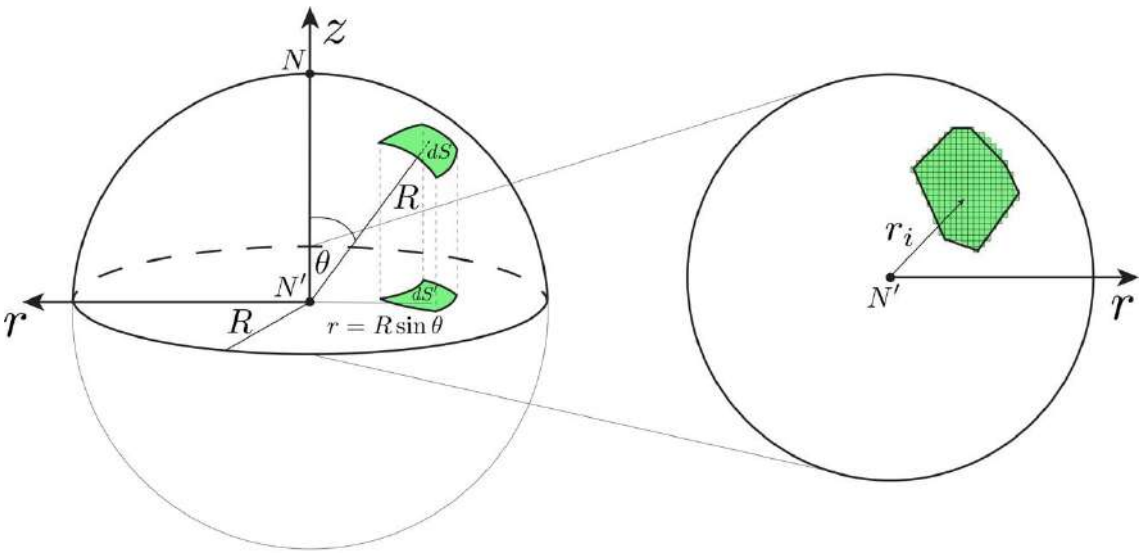

Figure 63: ***Actual area over a spherical surface and projected area on a horizontal plane****.*

This procedure to compute the actual area over domes from vertical projections over the horizontal plane has been used in all experiments of this work that involved values of apico-basal areas of cells from domes.

8.4 Methods

8.4.1 Fabrication of soft silicone gels (soft PDMS)

Soft elastomeric silicone gels were prepared using a protocol based on previous publications [298-301]. Briefly, a silicone elastomer was synthesized by mixing a 1:1 weight ratio of CY52-276A and CY52-276B polydimethylsiloxane (Dow Corning Toray). After degassing for 5 min, the gel was spin-coated on glass bottom dishes (35 mm, No. 0 coverslip thickness, Mattek) for 90 s at 400 rpm. The samples were then cured at 80 ºC for 1 h. The substrates were kept in a clean, dust-free and dry environment and they were always used before 4 weeks from fabrication.

8.4.2 Coating the soft PDMS substrate with fluorescent beads

After curing, the soft PDMS was treated with APTES ((3-Aminopropyl)triethoxysilane, Sigma-Aldrich, cat. No. A3648) diluted at 5% in absolute ethanol for 3 min, rinsed 3 times with ethanol 96%, and dried in the oven for 30 min at 60 ºC. Samples were incubated for 5 min with a filtered (220 nm) and sonicated solution of 200-nm-diameter red fluorescent carboxylate-modified beads (FluoSpheres, Invitrogen) in sodium tetraborate (3.8 mg/mL, Sigma-Aldrich), boric acid (5 mg/mL, Sigma-Aldrich) and 1-ethyl-3-(3-dimethylaminopropyl)carbodiimide (EDC, 0.1 mg/mL, Sigma-Aldrich), as described in [298]. Next, gels were rinsed 3 times with type-1 water and dried in the oven for 15 min at 60 ºC. Beads were passivated by incubating the samples with Tris-Buffered Saline (TBS, Sigma-Aldrich) solution for 20 min at room temperature. Finally, substrates were rinsed again 3 times with type-1 water and dried in the oven for 15 min at 60 ºC.

8.4.3 Soft PDMS stiffness measurements

Gel stiffness was measured by indenting the gel with a large metal sphere (diameter, 1000 μm) of known mass. The indentation caused by the weight of the sphere was determined using confocal microscopy. From the measured indentation and sphere mass, we obtained Young's modulus by applying Hertz theory corrected for the finite thickness of the gel[302]. We found a Young's Modulus of 2.9± 0.5 kPa (mean ±SD, n=6), in good agreement with published data[298-301, 303, 304].

8.4.4 Cell patterning on soft PDMS

PDMS patterning stamps were incubated with a fibronectin solution at 40 μg/mL (Fibronectin from human plasma, Sigma-Aldrich) for 1 h. Next, the protein was transferred to Poly Vinyl Alcohol (PVA, Sigma-Aldrich) membranes which were then placed in contact with the gel surface for 1 h. Membranes were dissolved and the surface was passivated at the same time using Pluronic F127 (Sigma-Aldrich) 0.2% w/v overnight at 4 ºC. Afterwards, the soft silicone gels were washed with Phosphate-Buffered Saline (PBS, Sigma-Aldrich) and incubated with cell culture medium for 30 min. For cell seeding, the culture medium was removed and a 70 μl drop containing ~150,000 cells was placed on the soft PDMS. 50 min after seeding, the unattached cells were washed away using PBS and more medium was added. Cells were seeded at least 48 h before experiments.

8.4.5 PDMS patterning stamps

Polydimethylsiloxane (PDMS, Sylgard, Dow Corning) stamps for micropatterning were fabricated. Briefly, SU8-50 masters containing cylinders of 80 μm or 100 μm in diameter were raised using conventional photolithography. Uncured PDMS was poured on the masters and cured for 2 h at 65 °C. PDMS was then peeled off from the master and kept at room temperature in a clean and dust-free environment until use.

8.4.6 3D traction microscopy

3D traction forces were computed using traction microscopy with finite gel thickness, [305, 306]. To account for both geometrical and material nonlinearities, a Finite Element Method (FEM) solution was implemented. Confocal stacks of the fluorescent beads covering the gel surface were taken with z-step = 0.3 μm and total depth of 15 μm. A 3D displacement field of the gel's top layer between any experimental time point and its relative reference image (obtained after cell trypsinization) were computed using home-made particle imaging velocimetry software based on an iterative algorithm with a dynamic interrogation window size and implementing convergence criteria based on image intensity as described in previous publications[307]. Results for the normal traction inside the dome were compared to analytical solutions for a liquid droplet over an elastic substrate with finite thickness[308-311].

8.4.7 Cell culture

Madin Darby canine kidney (MDCK) strain II and human epithelial colorectal adenocarcinoma (Caco-2) were used. To visualize specific cell structures the following stable fluorescent cell lines were used: MDCK expressing LifeAct-GFP (MDCK-LifeAct) to visualize the actin cytoskeleton, MDCK expressing CIBN-GFP-CAAX to visualize the plasma membrane (MDCK-CAAX), MDCK expressing keratin-18-GFP (MDCK-K18) to visualize intermediate filaments. All MDCK lines were cultured in minimum essential media with Earle's Salts and L-glutamine (Gibco) supplemented with 10% v/v fetal bovine serum (FBS; Gibco), 100 µg/ml penicillin and 100 µg/ml streptomycin. Selection antibiotic geneticin (ThermoFisher Scientific) was added at 0.5 mg/ml to LifeAct stable cell lines. Cells were maintained at 37 ºC in a humidified atmosphere with 5% CO2. Live imaging of F-actin was performed by incubating cells (12 h, 100 nM) using Live Cell Fluorogenic F-actin Labelling Probe (SiR-actin, Spirochrome). Caco-2 were imaged using Bodipy FL C16 dye (1 µM, 1h incubation, Thermo Fisher Scientific). MDCK-LifeAct cells were obtained from Prof Benoit Ladoux's lab. MDCK keratin-18-GFP cells were obtained from G. Charras lab. MDCK-CAAX were obtained by viral infection of CIBN-GFP-CAAX. CACO-2 cells were bought at Sigma Aldrich (86010202). Cell lines tested negative for mycoplasma contamination. All MDCK cell lines were authenticated by providing laboratories. CACO-2 cells were authenticated by the provider (Sigma Aldrich, from the ECACC).

8.4.8 Pharmacological interventions and osmotic shocks

To perturb actomyosin contractility cells were treated with Rho Kinase inhibitor Y-27632 (InSolutionTM Calbiochem, Merck-Millipore, 30 µM, 5 min incubation). To inhibit ARP2/3 complex cells were treated with CK666 (Sigma Aldrich, 100 µM, 1 h incubation). To perturb the osmolarity, D-mannitol (Sigma-Aldrich, final concentration 100 mM) was added to the medium. To weaken cell-cell junctions EGTA (Sigma Aldrich, final concentration 2 mM, 30 min) was added to the medium.

8.4.9 Cell immunofluorescence

MDCK cells were fixed with 4% paraformaldehyde in PBS for 10 min at room temperature and permeabilized using 0.1% Triton X100 (Sigma-Aldrich) in PBS for 10

min at room temperature. Cells were blocked in 1% Bovine Serum Albumin (BSA, Sigma-Aldrich) in PBS for 1 h (at room temperature). Phalloidin (Alexa FluorTM 555 Phalloidin, ThermoFisher Scientific) was then added at 1:1000 dilution in PBS and incubated for 30 min at room temperature. To identify nuclei, cells were then incubated for 10 min in a Hoechst solution (Hoechst® 33342, ThermoFisher Scientific) at 1:2500 dilution in PBS. Images were acquired with a Spinning Disk confocal microscope using a Nikon 60x oil 1.4 Numerical Aperture (NA) lens.

8.4.10 Time-lapse microscopy

Multidimensional acquisition for traction force measurements was performed using an inverted Nikon microscope with a spinning disk confocal unit (CSU-W1, Yokogawa), Zyla sCMOS camera (Andor, image size 2,048 x 2,048 pixels) using a Nikon 40× 0.75 NA air lens. The microscope was equipped with temperature control and CO2 control, using Andor iQ3 or Micro-Manager software[312].

8.4.11 Laser ablation

The set-up used is described in Colombelli *et al*[313]. Briefly, MDCK keratin-18-GFP cells were cultured on thin PDMS micropatterned substrates and allowed to form domes. We then used a sub-nanosecond UV pulsed laser to ablate individual filament bundles in weakly-stretched and superstretched cells. Immediately after ablation we monitored the time evolution of keratin filaments and we obtained bright field images of the domes to measure cell area. Experiments were performed at 37ºC and 5% CO2.

8.4.12 Photoactivatable Cytochalasin D

We used a phototriggerable derivative of Cytochalasin D (CytoD) that includes a nitroveratryloxycarbonyl (Nvoc) photoremovable group located at the hydroxyl group at C7 of CytoD. Attachment of the chromophore renders CytoD temporarily inactive. Upon light exposure, CytoD becomes active and causes local depolymerization of the actin cytoskeleton. For experiments, MDCK-CAAX domes were incubated with SiR-actin to visualize the cortical cytoskeleton. Individual cells were illuminated with a 405nm laser to activate CytoD. After the pulse, the cell area and actin cytoskeleton were visualized using time lapse microscopy (63× oil, Zeiss LSM 880).

8.4.13 Image analysis

ImageJ/Fiji software was used to perform the image analysis[314]. The pairwise stitching plugin was used to create 3D montages, the maximum intensity z-projection and the sum slices z-projection were used where appropriate. Actual cell areas were computed from z-projections using the methodology described in 8.3.

8.4.14 Code availability

MATLAB analysis procedures can be made available upon request to the corresponding author.

8.4.15 Data availability

The data that support the findings of this study are available from the corresponding author on reasonable request.

8.4.16 Animals

Animal care and experiments were carried out according to protocols approved by the Ethics Committee on Animal Research of the Science Park of Barcelona (PCB), Spain (Protocol number 7436). Outbred B6CBAF1/JRj mice (male and females of 5-6 weeks of age) were obtained from Janvier Labs. Mice were kept in a 12 h light/dark cycle (lights on 7:00 a.m.-7 p.m.) with ad libitum access to food and water.

8.4.17 Embryo collection and *in vitro* culture

For embryo collection, superovulation was induced in B6CBAF1/JRj females by intraperitoneal injection of 7.5 I.U. of pregnant mare serum gonadotropin (PMSG) followed, after 48h, by 7.5 I.U. of human chorionic gonadotropin (hCG). Superovulated females were then paired with male mice, and subsequently euthanized by cervical dislocation 20 h after hCG injection. Then, one-cell stage embryos (zygotes) were collected from the excised oviducts into medium containing 0.1% (w/v) hyaluronidase (Sigma) to remove cumulus cells under a dissection microscope. Recovered zygotes were cultured in micro-droplets of culture medium covered with mineral oil at 37°C and 5% CO2 until the blastocyst stage. No randomization nor blinding were performed as

experiments did not involve comparisons between groups. Experiments were reproduced four times.

8.4.18 Blastocyst immunofluorescence

Blastocysts at different degrees of development were fixed with 4% paraformaldehyde (PFA) (Aname) for 20 min at room temperature (RT). Then, fixed blastocysts were washed three times with PBS containing 1% bovine serum albumin (Sigma), 2% goat serum (Sigma) and 0.01% Triton X-100 (Sigma), referred as blocking buffer. Next, blastocysts were permeabilized with 2.5% Triton X-100 (Sigma) in PBS for 30 min at RT and subsequently washed three times with blocking buffer. Blastocysts were incubated overnight at 4ºC in anti-E-Cadherin primary antibody (610181, BD Biosciences) diluted 1:50 in blocking buffer. The following day, blastocysts were washed three times with blocking buffer and incubated for 90 min at 37ºC in Alexa Fluor (A) 488-conjugated secondary antibody (A21202, Thermo Fisher) diluted 1:200 in blocking buffer. Nuclei were counterstained with DAPI (D1306, Life Technologies) for 30 min. Image acquisition was performed in a SP5 Leica microscope or a Zeiss LSM780 confocal microscope using a plan-apochromat 40x/ oil DIC M27 objective.

9 REFERENCES

1. Thompson, D.A.W., *On growth and form*. 1917, Cambridge Eng.: University press. xv, 793 p.
2. Turing, A.M., *The chemical basis of morphogenesis.* Philosophical Transactions of the Royal Society of London. Series B, Biological Sciences, 1952. **237**(641): p. 37-72.
3. Elosegui-Artola, A., et al., *Mechanical regulation of a molecular clutch defines force transmission and transduction in response to matrix rigidity.* Nature Cell Biology, 2016. **18**(5): p. 540-548.
4. Schwarz, U.S. and M.L. Gardel, *United we stand: integrating the actin cytoskeleton and cell-matrix adhesions in cellular mechanotransduction.* J Cell Sci, 2012. **125**(Pt 13): p. 3051-60.
5. Engler, A.J., et al., *Matrix elasticity directs stem cell lineage specification.* Cell, 2006. **126**(4): p. 677-89.
6. Elosegui-Artola, A., et al., *Force Triggers YAP Nuclear Entry by Regulating Transport across Nuclear Pores.* Cell, 2017. **171**(6): p. 1397-1410 e14.
7. Trepat, X., et al., *Physical forces during collective cell migration.* Nature Physics, 2009. **5**(6): p. 426-430.
8. Sunyer, R., et al., *Collective cell durotaxis emerges from long-range intercellular force transmission.* Science, 2016. **353**(6304): p. 1157-1161.
9. Tambe, D.T., et al., *Collective cell guidance by cooperative intercellular forces.* Nature Materials, 2011. **10**(6): p. 469-475.
10. Brugués, A., et al., *Forces driving epithelial wound healing.* Nature Physics, 2014. **10**(9): p. 683-690.
11. Nelson, C.M., et al., *Microfluidic chest cavities reveal that transmural pressure controls the rate of lung development.* Development, 2017. **144**(23): p. 4328-4335.
12. Uroz, M., et al., *Regulation of cell cycle progression by cell-cell and cell-matrix forces.* Nature Cell Biology, 2018. **20**(6): p. 646-654.

13. Gudipaty, S.A., et al., *Mechanical stretch triggers rapid epithelial cell division through Piezo1.* Nature, 2017. **543**(7643): p. 118-121.
14. Eisenhoffer, G.T., et al., *Crowding induces live cell extrusion to maintain homeostatic cell numbers in epithelia.* Nature, 2012. **484**(7395): p. 546-9.
15. Guillot, C. and T. Lecuit, *Mechanics of epithelial tissue homeostasis and morphogenesis.* Science, 2013. **340**(6137): p. 1185-9.
16. Alberts, B., et al., *Molecular biology of the cell*. Sixth edition. ed. 2015, New York, NY: Garland Science, Taylor and Francis Group. xxxiv, 1342, 34, 53, 1 pages.
17. Elosegui-Artola, A., X. Trepat, and P. Roca-Cusachs, *Control of Mechanotransduction by Molecular Clutch Dynamics.* Trends Cell Biol, 2018. **28**(5): p. 356-367.
18. Suarez, C. and D.R. Kovar, *Internetwork competition for monomers governs actin cytoskeleton organization.* Nat Rev Mol Cell Biol, 2016. **17**(12): p. 799-810.
19. Mizuno, D., et al., *Nonequilibrium mechanics of active cytoskeletal networks.* Science, 2007. **315**(5810): p. 370-3.
20. Clark, A.G., et al., *Stresses at the cell surface during animal cell morphogenesis.* Curr Biol, 2014. **24**(10): p. R484-94.
21. Chugh, P., et al., *Actin cortex architecture regulates cell surface tension.* Nat Cell Biol, 2017. **19**(6): p. 689-697.
22. Jiang, H. and S.X. Sun, *Cellular pressure and volume regulation and implications for cell mechanics.* Biophys J, 2013. **105**(3): p. 609-19.
23. Mao, Y. and B. Baum, *Tug of war--the influence of opposing physical forces on epithelial cell morphology.* Dev Biol, 2015. **401**(1): p. 92-102.
24. Alt, S., P. Ganguly, and G. Salbreux, *Vertex models: from cell mechanics to tissue morphogenesis.* Philosophical Transactions of the Royal Society B: Biological Sciences, 2017. **372**(1720): p. 20150520.
25. Steinberg, M.S., *On the mechanism of tissue reconstruction by dissociated cells. I. Population kinetics, differential adhesiveness. and the absence of directed migration.* Proc Natl Acad Sci U S A, 1962. **48**: p. 1577-82.
26. Steinberg, M.S., *On the Mechanism of Tissue Reconstruction by Dissociated Cells, Iii. Free Energy Relations and the Reorganization of Fused, Heteronomic Tissue Fragments.* Proc Natl Acad Sci U S A, 1962. **48**(10): p. 1769-76.

27. Steinberg, M.S., *Mechanism of tissue reconstruction by dissociated cells. II. Time-course of events.* Science, 1962. **137**(3532): p. 762-3.
28. Foty, R.A., et al., *Liquid properties of embryonic tissues: Measurement of interfacial tensions.* Physical Review Letters, 1994. **72**(14): p. 2298-2301.
29. Foty, R.A. and M.S. Steinberg, *Cadherin-mediated cell-cell adhesion and tissue segregation in relation to malignancy.* Int J Dev Biol, 2004. **48**(5-6): p. 397-409.
30. Harris, A.K., *Is Cell sorting caused by differences in the work of intercellular adhesion? A critique of the Steinberg hypothesis.* J Theor Biol, 1976. **61**(2): p. 267-85.
31. Brodland, G.W., *The Differential Interfacial Tension Hypothesis (DITH): a comprehensive theory for the self-rearrangement of embryonic cells and tissues.* J Biomech Eng, 2002. **124**(2): p. 188-97.
32. Maitre, J.L., et al., *Adhesion functions in cell sorting by mechanically coupling the cortices of adhering cells.* Science, 2012. **338**(6104): p. 253-6.
33. Engl, W., et al., *Actin dynamics modulate mechanosensitive immobilization of E-cadherin at adherens junctions.* Nat Cell Biol, 2014. **16**(6): p. 587-94.
34. Manning, M.L., et al., *Coaction of intercellular adhesion and cortical tension specifies tissue surface tension.* Proc Natl Acad Sci U S A, 2010. **107**(28): p. 12517-22.
35. Gomez, G.A., R.W. McLachlan, and A.S. Yap, *Productive tension: force-sensing and homeostasis of cell-cell junctions.* Trends Cell Biol, 2011. **21**(9): p. 499-505.
36. Guillot, C. and T. Lecuit, *Mechanics of epithelial tissue homeostasis and morphogenesis.* Science, 2013. **340**(6137): p. 1185-1189.
37. Barker, N., *Adult intestinal stem cells: critical drivers of epithelial homeostasis and regeneration.* Nature Reviews Molecular Cell Biology, 2014. **15**(1): p. 19-33.
38. Krndija, D., et al., *Active cell migration is critical for steady-state epithelial turnover in the gut.* Science, 2019. **365**(6454): p. 705-710.
39. Northey, J.J., L. Przybyla, and V.M. Weaver, *Tissue Force Programs Cell Fate and Tumor Aggression.* Cancer Discovery, 2017. **7**(11): p. 1224-1237.
40. Nia, H.T., et al., *Solid stress and elastic energy as measures of tumour mechanopathology.* Nature Biomedical Enginnering, 2016. **1**.

41. Hannezo, E. and C.-P. Heisenberg, *Mechanochemical Feedback Loops in Development and Disease.* Cell, 2019. **178**(1): p. 12-25.
42. Benham-Pyle, B.W., et al., *Increasing beta-catenin/Wnt3A activity levels drive mechanical strain-induced cell cycle progression through mitosis.* eLIFE, 2016. **5**.
43. Crick, F.H.C. and A.F.W. Hughes, *The physical properties of cytoplasm.* Experimental Cell Research, 1950. **1**(1): p. 37-80.
44. Bausch, A.R., W. Möller, and E. Sackmann, *Measurement of local viscoelasticity and forces in living cells by magnetic tweezers.* Biophysical Journal, 1999. **76**(1 Pt 1): p. 573-579.
45. Ashkin, A., *Acceleration and Trapping of Particles by Radiation Pressure.* Physical Review Letters, 1970. **24**(4): p. 156-159.
46. Ashkin, A., et al., *Observation of a single-beam gradient force optical trap for dielectric particles.* Optics Letters, 1986. **11**(5): p. 288-290.
47. Wu, J., *Acoustical tweezers.* The Journal of the Acoustical Society of America, 1991. **89**(5): p. 2140-2143.
48. Binnig, G., C.F. Quate, and C. Gerber, *Atomic force microscope.* Physical Review Letters, 1986. **56**(9): p. 930-933.
49. Mitchison, J.M. and M.M. Swann, *The mechanical properties of the cell surface I. The cell elastimeter.* Journal of Experimental Biology, 1954. **31**(3): p. 443-460.
50. Zamir, E.A., et al., *Mechanical asymmetry in the embryonic chick heart during looping.* Annals of Biomedical Engineering, 2003. **31**(11): p. 1327-1336.
51. Brillouin, L., *Diffusion de la lumière et des rayons X par un corps transparent homogène.* Annales de Physique, 1922. **9**(17): p. 88-122.
52. Scarcelli, G. and S.H. Yun, *Confocal Brillouin microscopy for three-dimensional mechanical imaging.* Nature Photonics, 2007. **2**: p. 39-43.
53. Moore, A.R. and A.S. Burt, *On the locus and nature of the forces causing gastrulation in the embryos of Dendraster excentricus.* Journal of Experimental Zoology, 1939. **82**(1): p. 159-171.
54. Rehfeldt, F. and C.F. Schmidt, *Physical probing of cells.* Journal of Physics D: Applied Physics, 2017. **50**(46).
55. Basoli, F., et al., *Biomechanical Characterization at the Cell Scale: Present and Prospects.* Front Physiol, 2018. **9**: p. 1449.

56. Zhang, H. and K.-K. Liu, *Optical tweezers for single cells.* Journal of the Royal Society Interface, 2008. **5**(24): p. 671-690.
57. Favre-Bulle, I.A., et al., *Optical trapping in vivo: theory, practice, and applications.* Nanophotonics, 2019. **8**(6): p. 1023-1040.
58. Ozcelik, A., et al., *Acoustic tweezers for the life sciences.* Nature Methods, 2018. **15**(12): p. 1021-1028.
59. Krieg, M., et al., *Atomic force microscopy-based mechanobiology.* Nature Reviews Physics, 2018. **1**(1): p. 41-57.
60. Hochmuth, R.M., *Micropipette aspiration of living cells.* Journal of Biomechanics, 2000. **33**(1): p. 15-22.
61. González-Bermúdez, B., G.V. Guinea, and G.R. Plaza, *Advances in Micropipette Aspiration: Applications in Cell Biomechanics, Models, and Extended Studies.* Biophysical Journal, 2019. **116**(4): p. 587-594.
62. Campàs, O., *A toolbox to explore the mechanics of living embryonic tissues.* Seminars in Cell & Developmental Biology, 2016. **55**: p. 119-130.
63. Sugimura, K., P.-F. Lenne, and F. Graner, *Measuring forces and stresses in situ in living tissues.* Development, 2016. **143**(2): p. 186-196.
64. Roca-Cusachs, P., V. Conte, and X. Trepat, *Quantifying forces in cell biology.* Nature Cell Biology, 2017. **19**(7): p. 742-751.
65. Prevedel, R., et al., *Brillouin microscopy: an emerging tool for mechanobiology.* Nature Methods, 2019. **16**(10): p. 969-977.
66. Barresi, M.J.F. and S.F. Gilbert, *Developmental Biology*. 12th ed. 2019: Oxford University Press.
67. Pérez-González, C., et al., *Active wetting of epithelial tissues.* Nature Physics, 2019. **15**(1): p. 79-88.
68. Bergert, M., et al., *Confocal reference free traction force microscopy.* Nature Communications, 2016. **7**: p. 12814.
69. Latorre, E., et al., *Active superelasticity in three-dimensional epithelia of controlled shape.* Nature, 2018. **563**(7730): p. 203-208.
70. Ban, E., et al., *Mechanisms of Plastic Deformation in Collagen Networks Induced by Cellular Forces.* Biophysical Journal, 2018. **114**(2): p. 450-461.
71. Girardo, S., et al., *Standardized microgel beads as elastic cell mechanical probes.* Journal of Materials Chemistry B, 2018. **6**(39): p. 6245-6261.

72. Saw, T.B., et al., *Topological defects in epithelia govern cell death and extrusion.* Nature, 2017. **544**(7649): p. 212-216.
73. Wang, N., et al., *Cell prestress. I. Stiffness and prestress are closely associated in adherent contractile cells.* American Journal of Physiology-Cell Physiology, 2002. **282**(3): p. C606-C616.
74. Harris, A.K., P. Wild, and D. Stopak, *Silicone rubber substrata: a new wrinkle in the study of cell locomotion.* Science, 1980. **208**(4440): p. 177-179.
75. Lee, J., et al., *Traction forces generated by locomoting keratocytes.* Journal of Cell Biology, 1994. **127**(6 Pt 2): p. 1957-1964.
76. Oliver, T., M. Dembo, and K. Jacobson, *Traction forces in locomoting cells.* Cell Motility and the Cytoskeleton, 1995. **31**(3): p. 225-240.
77. Dembo, M., et al., *Imaging the traction stresses exerted by locomoting cells with the elastic substratum method.* Biophysical Journal, 1996. **70**(4): p. 2008-2022.
78. Dembo, M. and Y.-L. Wang, *Stresses at the Cell-to-Substrate Interface during Locomotion of Fibroblasts.* Biophysical Journal, 1999. **76**(4): p. 2307-2316.
79. Schwarz, U.S. and J.R.D. Soiné, *Traction force microscopy on soft elastic substrates: A guide to recent computational advances.* Biochimica et Biophysica Acta, 2015. **1853**(11 Pt B): p. 3095-3104.
80. Style, R.W., et al., *Traction force microscopy in physics and biology.* Soft Matter, 2014. **10**(23): p. 4047-4055.
81. Polio, S.R., et al., *A micropatterning and image processing approach to simplify measurement of cellular traction forces.* Acta Biomaterialia, 2012. **8**(1): p. 82-88.
82. Butler, J.P., et al., *Traction fields, moments, and strain energy that cells exert on their surroundings.* American Journal of Physiology-Cell Physiology, 2002. **282**(3): p. C595-C605.
83. del Álamo, J.C., et al., *Spatio-temporal analysis of eukaryotic cell motility by improved force cytometry.* Proceedings of the National Academy of Sciences of the United States of America, 2007. **104**(33): p. 13343-13348.
84. Schwarz, U.S., et al., *Calculation of Forces at Focal Adhesions from Elastic Substrate Data: The Effect of Localized Force and the Need for Regularization.* Biophysical Journal, 2002. **83**(3): p. 1380-1394.

85. Sabass, B., et al., *High resolution traction force microscopy based on experimental and computational advances.* Biophysical Journal, 2008. **94**(1): p. 207-220.

86. Huang, Y., et al., *Traction force microscopy with optimized regularization and automated Bayesian parameter selection for comparing cells.* Scientific Reports, 2019. **9**(1): p. 539.

87. Yang, Z., et al., *Determining substrate displacement and cell traction fields--a new approach.* Journal of Theoretical Biology, 2006. **242**(3): p. 607-616.

88. Griffin, B.P., et al., *A novel method for quantifying traction forces on hexagonal micropatterned protein features on deformable poly-dimethyl siloxane sheets.* MethodsX, 2019. **6**: p. 1343-1352.

89. Burton, K. and D.L. Taylor, *Traction forces of cytokinesis measured with optically modified elastic substrata.* Nature, 1997. **385**(6615): p. 450-454.

90. Balaban, N.Q., et al., *Force and focal adhesion assembly: a close relationship studied using elastic micropatterned substrates.* Nature Cell Biology, 2001. **3**(5): p. 466-472.

91. Serra-Picamal, X., et al., *Mechanical waves during tissue expansion.* Nature Physics, 2012. **8**(8): p. 628-634.

92. Kim, J.H., et al., *Propulsion and navigation within the advancing monolayer sheet.* Nature Materials, 2013. **12**(9): p. 856-863.

93. Park, J.-A., et al., *Unjamming and cell shape in the asthmatic airway epithelium.* Nature Materials, 2015. **14**(10): p. 1040-1048.

94. Uroz, M., et al., *Traction forces at the cytokinetic ring regulate cell division and polyploidy in the migrating zebrafish epicardium.* Nature Materials, 2019. **18**(9): p. 1015-1023.

95. Jerison, E.R., et al., *Deformation of an elastic substrate by a three-phase contact line.* Physical Review Letters, 2011. **106**(18): p. 186103.

96. Xu, Y., et al., *Imaging in-plane and normal stresses near an interface crack using traction force microscopy.* Proceedings of the National Academy of Sciences of the United States of America, 2010. **107**(34): p. 14964-14967.

97. Casares, L., et al., *Hydraulic fracture during epithelial stretching.* Nature Materials, 2015. **14**(3): p. 343-351.

98. Oria, R., et al., *Force loading explains spatial sensing of ligands by cells.* Nature, 2017. **552**(7684): p. 219-224.

99. Nguyen, D.T., et al., *Surface Pressure and Shear Stress Fields within a Frictional Contact on Rubber.* The Journal of Adhesion, 2011. **87**(3): p. 235-250.

100. Chateauminois, A. and C. Fretigny, *Local friction at a sliding interface between an elastomer and a rigid spherical probe.* The European Physical Journal E Soft Matter, 2008. **27**(2): p. 221-227.

101. del Álamo, J.C., et al., *Three-dimensional quantification of cellular traction forces and mechanosensing of thin substrata by fourier traction force microscopy.* PLoS One, 2013. **8**(9): p. e69850.

102. Álvarez-González, B., et al., *Cytoskeletal Mechanics Regulating Amoeboid Cell Locomotion.* Applied Mechanics Reviews, 2014. **66**(5): p. 050804.

103. Tan, J.L., et al., *Cells lying on a bed of microneedles: an approach to isolate mechanical force.* Proceedings of the National Academy of Sciences of the United States of America, 2003. **100**(4): p. 1484-1489.

104. Saez, A., et al., *Rigidity-driven growth and migration of epithelial cells on microstructured anisotropic substrates.* Proceedings of the National Academy of Sciences of the United States of America, 2007. **104**(20): p. 8281-8286.

105. Legant, W.R., et al., *Microfabricated tissue gauges to measure and manipulate forces from 3D microtissues.* Proceedings of the National Academy of Sciences of the United States of America, 2009. **106**(25): p. 10097-10102.

106. Boudou, T., et al., *A microfabricated platform to measure and manipulate the mechanics of engineered cardiac microtissues.* Tissue Engineering: Part A, 2012. **18**(9-10): p. 910-919.

107. du Roure, O., et al., *Force mapping in epithelial cell migration.* Proceedings of the National Academy of Sciences of the United States of America, 2005. **102**(7): p. 2390-2395.

108. Rabodzey, A., et al., *Mechanical forces induced by the transendothelial migration of human neutrophils.* Biophysical Journal, 2008. **95**(3): p. 1428-1438.

109. Reffay, M., et al., *Interplay of RhoA and mechanical forces in collective cell migration driven by leader cells.* Nature Cell Biology, 2014. **16**(3): p. 217-23.

110. Saez, A., et al., *Traction forces exerted by epithelial cell sheets.* Journal of Physics: Condensed Matter, 2010. **22**(19): p. 194119.

111. Yang, B., et al., *Stopping transformed cancer cell growth by rigidity sensing.* Nature Materials, 2020. **19**(2): p. 239-250.
112. Schoen, I., et al., *Probing cellular traction forces by micropillar arrays: contribution of substrate warping to pillar deflection.* Nano Letters, 2010. **10**(5): p. 1823-1830.
113. Liu, Z., et al., *Mechanical tugging force regulates the size of cell-cell junctions.* Proceedings of the National Academy of Sciences of the United States of America, 2010. **107**(22): p. 9944-9949.
114. Bastounis, E., et al., *Cooperative cell motility during tandem locomotion of amoeboid cells.* Molecular Biology of the Cell, 2016. **27**(8): p. 1262-1271.
115. Maruthamuthu, V., et al., *Cell-ECM traction force modulates endogenous tension at cell-cell contacts.* Proceedings of the National Academy of Sciences of the United States of America, 2011. **108**(12): p. 4708-4713.
116. Ng, M.R., et al., *Mapping the dynamics of force transduction at cell-cell junctions of epithelial clusters.* eLIFE, 2014. **3**: p. e03282.
117. Tambe, D.T., et al., *Monolayer stress microscopy: limitations, artifacts, and accuracy of recovered intercellular stresses.* PLoS One, 2013. **8**(2): p. e55172.
118. Moussus, M., et al., *Intracellular stresses in patterned cell assemblies.* Soft Matter, 2014. **10**(14): p. 2414-2423.
119. Nier, V., et al., *Inference of Internal Stress in a Cell Monolayer.* Biophysical Journal, 2016. **110**(7): p. 1625-1635.
120. Serrano, R., et al., *Three-Dimensional Monolayer Stress Microscopy.* Biophysical Journal, 2019. **117**(1): p. 111-128.
121. Timoshenko, S. and S. Woinowsky-Krieger, *Theory of Plates and Shells*. Second ed. 1959.
122. Vishwakarma, M., et al., *Mechanical interactions among followers determine the emergence of leaders in migrating epithelial cell collectives.* Nature Communications, 2018. **9**(1): p. 3469.
123. Harris, A.R., et al., *Characterizing the mechanics of cultured cell monolayers.* Proceedings of the National Academy of Sciences of the United States of America, 2012. **109**(41): p. 16449-16454.
124. Khalilgharibi, N., et al., *Stress relaxation in epithelial monolayers is controlled by the actomyosin cortex.* Nature Physics, 2019. **15**(8): p. 839-847.

125. Harris, A.R., et al., *Generating suspended cell monolayers for mechanobiological studies.* Nature Protocols, 2013. **8**(12): p. 2516-2530.
126. Merzouki, A., O. Malaspinas, and B. Chopard, *The mechanical properties of a cell-based numerical model of epithelium.* Soft Matter, 2016. **12**(21): p. 4745-4754.
127. Wyatt, T.P.J., et al., *Emergence of homeostatic epithelial packing and stress dissipation through divisions oriented along the long cell axis.* Proceedings of the National Academy of Sciences of the United States of America, 2015. **112**(18): p. 5726-5731.
128. Xu, G.-K., Y. Liu, and Z. Zheng, *Oriented cell division affects the global stress and cell packing geometry of a monolayer under stretch.* Journal of Biomechanics, 2016. **49**(3): p. 401-407.
129. Wyatt, T.P.J., et al., *Actomyosin controls planarity and folding of epithelia in response to compression.* Nature Materials, 2020. **19**(1): p. 109-117.
130. Fouchard, J., et al., *Curling of epithelial monolayers reveals coupling between active bending and tissue tension.* bioRxiv, 2019.
131. Khalilgharibi, N., et al., *Stress relaxation in epithelial monolayers is controlled by the actomyosin cortex.* Nature Physics, 2019.
132. Bloom, R.J., et al., *Mapping local matrix remodeling induced by a migrating tumor cell using three-dimensional multiple-particle tracking.* Biophysical Journal, 2008. **95**(8): p. 4077-4088.
133. Hur, S.S., et al., *Live Cells Exert 3-Dimensional Traction Forces on Their Substrata.* Cell and Molecular Bioengineering, 2009. **2**(3): p. 425-436.
134. Álvarez-González, B., et al., *Three-dimensional balance of cortical tension and axial contractility enables fast amoeboid migration.* Biophysical Journal, 2015. **108**(4): p. 821-832.
135. Maskarinec, S.A., et al., *Quantifying cellular traction forces in three dimensions.* Proceedings of the National Academy of Sciences of the United States of America, 2009. **106**(52): p. 22108-22113.
136. Toyjanova, J., et al., *High resolution, large deformation 3D traction force microscopy.* PLoS One, 2014. **9**(4): p. e90976.
137. Delanoë-Ayari, H., J.P. Rieu, and M. Sano, *4D traction force microscopy reveals asymmetric cortical forces in migrating Dictyostelium cells.* Physical Review Letters, 2010. **105**(24): p. 248103.

138. Gordon, V.D., et al., *Measuring the mechanical stress induced by an expanding multicellular tumor system: a case study.* Experimental Cell Research, 2003. **289**(1): p. 58-66.
139. Zhou, J., et al., *Force production and mechanical accommodation during convergent extension.* Development, 2015. **142**(4): p. 692-701.
140. Legant, W.R., et al., *Measurement of mechanical tractions exerted by cells in three-dimensional matrices.* Nature Methods, 2010. **7**(12): p. 969-971.
141. Steinwachs, J., et al., *Three-dimensional force microscopy of cells in biopolymer networks.* Nature Methods, 2016. **13**(2): p. 171-176.
142. Mark, C., et al., *Collective forces of tumor spheroids in three-dimensional biopolymer networks.* bioRxiv, 2019.
143. Alessandri, K., et al., *Cellular capsules as a tool for multicellular spheroid production and for investigating the mechanics of tumor progression in vitro.* Proceedings of the National Academy of Sciences of the United States of America, 2013. **110**(37): p. 14843-8.
144. Leonavicius, K., et al., *Mechanics of mouse blastocyst hatching revealed by a hydrogel-based microdeformation assay.* Proceedings of the National Academy of Sciences of the United States of America, 2018. **115**(41): p. 10375-10380.
145. Aung, A., et al., *3D traction stresses activate protease-dependent invasion of cancer cells.* Biophysical Journal, 2014. **107**(11): p. 2528-2537.
146. Yeh, Y.-T., et al., *Three-dimensional forces exerted by leukocytes and vascular endothelial cells dynamically facilitate diapedesis.* Proceedings of the National Academy of Sciences of the United States of America, 2018. **115**(1): p. 133-138.
147. Álvarez-González, B., et al., *Two-Layer Elastographic 3-D Traction Force Microscopy.* Scientific Reports, 2017. **7**: p. 39315.
148. Navis, A. and M. Bagnat, *Developing pressures: fluid forces driving morphogenesis.* Current Opinion in Genetics & Development, 2015. **32**: p. 24-30.
149. Hales, S., *Statical Essays: containing haemastaticks; or, an account of some hydraulick and hydrostatical experiments made on the blood and blood-vessels of animals*. 1733, London: W. Innys and R. Manby.
150. Wiederhielm, C.A., et al., *Pulsatile Pressures in the Microcirculation of Frog's Mesentery.* American Journal of Physiology, 1964. **207**(1): p. 173-176.

151. Petrie, R.J. and H. Koo, *Direct measurement of intracellular pressure.* Current Protocols in Cell Biology, 2014. **63**(1): p. 12.9.1-12.9.9.

152. Falchuk, K.H. and R.W. Berliner, *Hydrostatic pressures in peritubular capillaries and tubules in the rat kidney.* American Journal of Physiology, 1971. **220**(5): p. 1422-1426.

153. Kelly, S.M. and P.T. Macklem, *Direct measurement of intracellular pressure.* American Journal of Physiology, 1991. **260**(3 Pt 1): p. C652-C657.

154. Petrie, R.J., H. Koo, and K.M. Yamada, *Generation of compartmentalized pressure by a nuclear piston governs cell motility in a 3D matrix.* Science, 2014. **345**(6200): p. 1062-1065.

155. Myers, R.R., et al., *Proximodistal gradient in endoneurial fluid pressure.* Experimental Neurology, 1988. **102**(3): p. 368-370.

156. Wit, H.P., E.O. Thalen, and F.W.J. Albers, *Dynamics of inner ear pressure release, measured with a double-barreled micropipette in the guinea pig.* Hearing Research, 1999. **132**(1-2): p. 131-139.

157. Avila, M.Y., et al., *Reliable measurement of mouse intraocular pressure by a servo-null micropipette system.* Investigative Ophthalmology & Visual Science, 2001. **42**(8): p. 1841-1846.

158. Hu, N., H.J. Yost, and E.B. Clark, *Cardiac morphology and blood pressure in the adult zebrafish.* The Anatomical Record, 2001. **264**(1): p. 1-12.

159. Tanner, C., D.A. Frambach, and D.S. Misfeldt, *Transepithelial transport in cell culture. A theoretical and experimental analysis of the biophysical properties of domes.* Biophysical Journal, 1983. **43**(2): p. 183-190.

160. Hu, N., et al., *Structure and function of the developing zebrafish heart.* The Anatomical Record, 2000. **260**(2): p. 148-157.

161. Stekelenburg-de Vos, S., et al., *Systolic and diastolic ventricular function assessed by pressure-volume loops in the stage 21 venous clipped chick embryo.* Pediatric Research, 2005. **57**(1): p. 16-21.

162. Desmond, M.E., M.L. Levitan, and A.R. Haas, *Internal luminal pressure during early chick embryonic brain growth: descriptive and empirical observations.* The Anatomical Record Part A: Discoveries in Molecular, Cellular, and Evolutionary Biology, 2005. **285**(2): p. 737-747.

163. Chan, C.J., et al., *Hydraulic control of mammalian embryo size and cell fate.* Nature, 2019. **571**(7763): p. 112-116.

164. Mosaliganti, K.R., et al., *Size control of the inner ear via hydraulic feedback.* eLIFE, 2019. **8**.

165. Lorenz, J.N., *Micropuncture of the kidney: a primer on techniques.* Comprehensive Physiology, 2012. **2**(1): p. 621-637.

166. Campàs, O., et al., *Quantifying cell-generated mechanical forces within living embryonic tissues.* Nature Methods, 2014. **11**(2): p. 183-189.

167. Vorselen, D., et al., *Microparticle traction force microscopy reveals subcellular force exertion patterns in immune cell-target interactions.* Nature Communications, 2020. **11**(1): p. 20.

168. Serwane, F., et al., *In vivo quantification of spatially varying mechanical properties in developing tissues.* Nature Methods, 2017. **14**(2): p. 181-186.

169. Ingremeau, F., et al., *Optical sensing of mechanical pressure based on diffusion measurement in polyacrylamide cell-like barometers.* Soft Matter, 2017. **13**(23): p. 4210-4213.

170. Dolega, M.E., et al., *Cell-like pressure sensors reveal increase of mechanical stress towards the core of multicellular spheroids under compression.* Nature Communications, 2017. **8**: p. 14056.

171. Mohagheghian, E., et al., *Quantifying compressive forces between living cell layers and within tissues using elastic round microgels.* Nature Communications, 2018. **9**(1): p. 1878.

172. Bar-Kochba, E., et al., *A Fast Iterative Digital Volume Correlation Algorithm for Large Deformations.* Experimental Mechanics, 2014. **55**(1): p. 261-274.

173. Shen, J., L.-D. Sun, and C.-H. Yan, *Luminescent rare earth nanomaterials for bioprobe applications.* Dalton Transactions, 2008(42): p. 5687-5697.

174. Mehlenbacher, R.D., et al., *Nanomaterials for in vivo imaging of mechanical forces and electrical fields.* Nature Reviews Materials, 2017. **3**(2): p. 17080.

175. Wisser, M.D., et al., *Strain-induced modification of optical selection rules in lanthanide-based upconverting nanoparticles.* Nano Letters, 2015. **15**(3): p. 1891-1897.

176. Lay, A., et al., *Upconverting Nanoparticles as Optical Sensors of Nano- to Micro-Newton Forces.* Nano Letters, 2017. **17**(7): p. 4172-4177.

177. Humar, M. and S.H. Yun, *Intracellular microlasers.* Nature Photonics, 2015. **9**(9): p. 572-576.

178. Schubert, M., et al., *Monitoring contractility in single cardiomyocytes and whole hearts with biointegrated microlasers.* bioRxiv, 2019.
179. Lucio, A.A., et al., *Spatiotemporal variation of endogenous cell-generated stresses within 3D multicellular spheroids.* Scientific Reports, 2017. **7**(1): p. 12022.
180. Traeber, N., et al., *Polyacrylamide Bead Sensors for in vivo Quantification of Cell-Scale Stress in Zebrafish Development.* Scientific Reports, 2019. **9**(1): p. 17031.
181. Gayrard, C. and N. Borghi, *FRET-based Molecular Tension Microscopy.* Methods, 2016. **94**: p. 33-42.
182. Yasunaga, A., Y. Murad, and I.T.S. Li, *Quantifying molecular tension-classifications, interpretations and limitations of force sensors.* Physical Biology, 2019. **17**(1): p. 011001.
183. Meng, F., T.M. Suchyna, and F. Sachs, *A fluorescence energy transfer-based mechanical stress sensor for specific proteins in situ.* The FEBS journal, 2008. **275**(12): p. 3072-3087.
184. Grashoff, C., et al., *Measuring mechanical tension across vinculin reveals regulation of focal adhesion dynamics.* Nature, 2010. **466**(7303): p. 263-266.
185. Förster, T., *Zwischenmolekulare Energiewanderung und Fluoreszenz.* Annalen der Physik, 1948. **437**(1-2): p. 55-75.
186. Conway, D.E., et al., *Fluid shear stress on endothelial cells modulates mechanical tension across VE-cadherin and PECAM-1.* Current Biology, 2013. **23**(11): p. 1024-1030.
187. Cai, D., et al., *Mechanical feedback through E-cadherin promotes direction sensing during collective cell migration.* Cell, 2014. **157**(5): p. 1146-1159.
188. Price, A.J., et al., *Mechanical loading of desmosomes depends on the magnitude and orientation of external stress.* Nature Communications, 2018. **9**(1): p. 5284.
189. Borghi, N., et al., *E-cadherin is under constitutive actomyosin-generated tension that is increased at cell-cell contacts upon externally applied stretch.* Proceedings of the National Academy of Sciences of the United States of America, 2012. **109**(31): p. 12568-12573.
190. Narayanan, V., et al., *Osmotic Gradients in Epithelial Acini Increase Mechanical Tension across E-cadherin, Drive Morphogenesis, and Maintain Homeostasis.* Current Biology, 2020. **30**(4): p. 624-633.

191. Eder, D., K. Basler, and C.M. Aegerter, *Challenging FRET-based E-Cadherin force measurements in Drosophila.* Scientific Reports, 2017. **7**(1): p. 13692.

192. Stabley, D.R., et al., *Visualizing mechanical tension across membrane receptors with a fluorescent sensor.* Nature Methods, 2011. **9**(1): p. 64-67.

193. Colombelli, J. and J. Solon, *Force communication in multicellular tissues addressed by laser nanosurgery.* Cell and Tissue Research, 2013. **352**(1): p. 133-147.

194. Zulueta-Coarasa, T. and R. Fernandez-Gonzalez, *Laser ablation to investigate cell and tissue mechanics in vivo*, in *Integrative Mechanobiology: Micro- and Nano- Techniques in Cell Mechanobiology*, D.K. Y. Sun, & C. Simmons, Editor. 2015, Cambridge University Press: Cambridge. p. 128-147.

195. Bonnet, I., et al., *Mechanical state, material properties and continuous description of an epithelial tissue.* Journal of the Royal Society Interface, 2012. **9**(75): p. 2614-2623.

196. Etournay, R., et al., *Interplay of cell dynamics and epithelial tension during morphogenesis of the Drosophila pupal wing.* eLIFE, 2015. **4**: p. e07090.

197. Hutson, M.S., et al., *Forces for morphogenesis investigated with laser microsurgery and quantitative modeling.* Science, 2003. **300**(5616): p. 145-149.

198. Ma, X., et al., *Probing embryonic tissue mechanics with laser hole drilling.* Physical Biology, 2009. **6**(3): p. 036004.

199. Hutson, M.S., et al., *Combining laser microsurgery and finite element modeling to assess cell-level epithelial mechanics.* Biophysical Journal, 2009. **97**(12): p. 3075-3085.

200. Kiehart, D.P., et al., *Multiple forces contribute to cell sheet morphogenesis for dorsal closure in Drosophila.* Journal of Cell Biology, 2000. **149**(2): p. 471-490.

201. Solon, J., et al., *Pulsed forces timed by a ratchet-like mechanism drive directed tissue movement during dorsal closure.* Cell, 2009. **137**(7): p. 1331-1342.

202. Hunter, G.L., et al., *Ion channels contribute to the regulation of cell sheet forces during Drosophila dorsal closure.* Development, 2014. **141**(2): p. 325-334.

203. Fernandez-Gonzalez, R. and J.A. Zallen, *Wounded cells drive rapid epidermal repair in the early Drosophila embryo.* Molecular Biology of the Cell, 2013. **24**(20): p. 3227-3237.

204. Campinho, P., et al., *Tension-oriented cell divisions limit anisotropic tissue tension in epithelial spreading during zebrafish epiboly.* Nature Cell Biology, 2013. **15**(12): p. 1405-1414.

205. Maître, J.-L., et al., *Asymmetric division of contractile domains couples cell positioning and fate specification.* Nature, 2016. **536**(7616): p. 344-348.

206. Maître, J.-L., et al., *Pulsatile cell-autonomous contractility drives compaction in the mouse embryo.* Nature Cell Biology, 2015. **17**(7): p. 849-855.

207. Yang, X., et al., *Correlating cell shape and cellular stress in motile confluent tissues.* Proceedings of the National Academy of Sciences of the United States of America, 2017. **114**(48): p. 12663-12668.

208. Cranston, P.G., et al., *Cinemechanometry (CMM): A method to determine the forces that drive morphogenetic movements from time-lapse images.* Annals of Biomedical Engineering, 2010. **38**(9): p. 2937-47.

209. Farhadifar, R., et al., *The influence of cell mechanics, cell-cell interactions, and proliferation on epithelial packing.* Current Biology, 2007. **17**(24): p. 2095-2104.

210. Ishihara, S., et al., *Comparative study of non-invasive force and stress inference methods in tissue.* The European Physical Journal E Soft Matter, 2013. **36**(4): p. 9859.

211. Ishihara, S. and K. Sugimura, *Bayesian inference of force dynamics during morphogenesis.* Journal of Theoretical Biology, 2012. **313**: p. 201-211.

212. Stein, M.B. and R. Gordon, *Epithelia as bubble rafts: A new method for analysis of cell shape and intercellular adhesion in embryonic and other epithelia.* Journal of Theoretical Biology, 1982. **97**(4): p. 625-639.

213. Hayashi, T. and R.W. Carthew, *Surface mechanics mediate pattern formation in the developing retina.* Nature, 2004. **431**(7009): p. 647-652.

214. Chiou, K.K., L. Hufnagel, and B.I. Shraiman, *Mechanical stress inference for two dimensional cell arrays.* PLoS Computational Biology, 2012. **8**(5): p. e1002512.

215. Brodland, G.W., et al., *CellFIT: a cellular force-inference toolkit using curvilinear cell boundaries.* PLoS One, 2014. **9**(6): p. e99116.

216. Kong, W., et al., *Experimental validation of force inference in epithelia from cell to tissue scale.* Scientific Reports, 2019. **9**(1): p. 14647.

217. Veldhuis, J.H., et al., *Practical aspects of the cellular force inference toolkit (CellFIT).* Methods in Cell Biology, 2015. **125**: p. 331-351.

218. Veldhuis, J.H., et al., *Inferring cellular forces from image stacks.* Philosophical Transactions of the Royal Society B: Biological Sciences, 2017. **372**(1720): p. 20160261.

219. Chen, H.H. and G.W. Brodland, *Cell-level finite element studies of viscous cells in planar aggregates.* Transactions-American Society of Mechanical Engineers Journal of Biomechanical Engineering, 2000. **122**(4): p. 394-401.

220. Brodland, G.W., D. Viens, and J.H. Veldhuis, *A new cell-based FE model for the mechanics of embryonic epithelia.* Computer Methods in Biomechanics and Biomedical Engineering, 2007. **10**(2): p. 121-128.

221. Brodland, G.W., et al., *Video force microscopy reveals the mechanics of ventral furrow invagination in Drosophila.* Proceedings of the National Academy of Sciences of the United States of America, 2010. **107**(51): p. 22111-22116.

222. Sugimura, K. and S. Ishihara, *The mechanical anisotropy in a tissue promotes ordering in hexagonal cell packing.* Development, 2013. **140**(19): p. 4091-4101.

223. Xu, M., et al., *A scheme for 3-dimensional morphological reconstruction and force inference in the early C. elegans embryo.* PLoS One, 2018. **13**(7): p. e0199151.

224. Nestor-Bergmann, A., et al., *Decoupling the Roles of Cell Shape and Mechanical Stress in Orienting and Cueing Epithelial Mitosis.* Cell Reports, 2019. **26**(8): p. 2088-2100 e4.

225. Krens, S.F.G., et al., *Interstitial fluid osmolarity modulates the action of differential tissue surface tension in progenitor cell segregation during gastrulation.* Development, 2017. **144**(10): p. 1798-1806.

226. Mongera, A., et al., *A fluid-to-solid jamming transition underlies vertebrate body axis elongation.* Nature, 2018. **561**(7723): p. 401-405.

227. Notbohm, J., et al., *Three-dimensional analysis of the effect of epidermal growth factor on cell-cell adhesion in epithelial cell clusters.* Biophysical Journal, 2012. **102**(6): p. 1323-1330.

228. Tambe, D.T., et al., *Collective cell guidance by cooperative intercellular forces.* Nat Mater, 2011. **10**(6): p. 469-75.

229. Vincent, R., et al., *Active Tensile Modulus of an Epithelial Monolayer.* Phys Rev Lett, 2015. **115**(24): p. 248103.

230. Sunyer, R., et al., *Collective cell durotaxis emerges from long-range intercellular force transmission.* Science, 2016. **353**(6304): p. 1157-61.

231. Harris, A.R., et al., *Characterizing the mechanics of cultured cell monolayers.* Proc Natl Acad Sci U S A, 2012. **109**(41): p. 16449-54.

232. Rabito, C.A., et al., *Distribution and characteristics of the occluding junctions in a monolayer of a cell line (MDCK) derived from canine kidney.* J Membr Biol, 1978. **43**(4): p. 351-65.

233. Cereijido, M., et al., *Fluxes, junctions, and blisters in cultured monolayers of epithelioid cells (MDCK).* Ann N Y Acad Sci, 1981. **372**: p. 422-41.

234. Thomas, S.R., S.G. Schultz, and J.E. Lever, *Stimulation of dome formation in MDCK kidney epithelial cultures by inducers of differentiation: dissociation from effects on transepithelial resistance and cyclic AMP levels.* J Cell Physiol, 1982. **113**(3): p. 427-32.

235. Leighton, J., et al., *Secretory activity and oncogenicity of a cell line (MDCK) derived from canine kidney.* Science, 1969. **163**(3866): p. 472-3.

236. Leighton, J., et al., *A cell line derived from normal dog kidney (MDCK) exhibiting qualities of papillary adenocarcinoma and of renal tubular epithelium.* Cancer, 1970. **26**(5): p. 1022-8.

237. Lever, J.E., *Inducers of mammalian cell differentiation stimulate dome formation in a differentiated kidney epithelial cell line (MDCK).* Proc Natl Acad Sci U S A, 1979. **76**(3): p. 1323-7.

238. Lever, J.E., *Regulation of dome formation in differentiated epithelial cell cultures.* J Supramol Struct, 1979. **12**(2): p. 259-72.

239. Sugahara, K., J.H. Caldwell, and R.J. Mason, *Electrical currents flow out of domes formed by cultured epithelial cells.* J Cell Biol, 1984. **99**(4 Pt 1): p. 1541-4.

240. Tanner, C., D.A. Frambach, and D.S. Misfeldt, *Transepithelial transport in cell culture. A theoretical and experimental analysis of the biophysical properties of domes.* Biophys J, 1983. **43**(2): p. 183-90.

241. Hill, R., *C. A theory of the plastic bulging of a metal diaphragm by lateral pressure.* The London, Edinburgh, and Dublin Philosophical Magazine and Journal of Science, 1950. **41**(322): p. 1133-1142.

242. Machado, G., D. Favier, and G. Chagnon, *Membrane Curvatures and Stress-strain Full Fields of Axisymmetric Bulge Tests from 3D-DIC Measurements.*

Theory and Validation on Virtual and Experimental results. Experimental Mechanics, 2011. **52**(7): p. 865-880.

243. Buerzle, W., et al., *Multiaxial mechanical behavior of human fetal membranes and its relationship to microstructure.* Biomech Model Mechanobiol, 2013. **12**(4): p. 747-62.
244. Hardin, C., et al., *Glassy dynamics, cell mechanics, and endothelial permeability.* J Phys Chem B, 2013. **117**(42): p. 12850-6.
245. Rao, P.V., et al., *Modulation of aqueous humor outflow facility by the Rho kinase-specific inhibitor Y-27632.* Invest Ophthalmol Vis Sci, 2001. **42**(5): p. 1029-37.
246. Dasgupta, S., et al., *Physics of lumen growth.* Proc Natl Acad Sci U S A, 2018. **115**(21): p. E4751-E4757.
247. Kosmalska, A.J., et al., *Physical principles of membrane remodelling during cell mechanoadaptation.* Nat Commun, 2015. **6**: p. 7292.
248. Olbrich, K., et al., *Water permeability and mechanical strength of polyunsaturated lipid bilayers.* Biophys J, 2000. **79**(1): p. 321-7.
249. Matsui, H., et al., *Osmotic water permeabilities of cultured, well-differentiated normal and cystic fibrosis airway epithelia.* J Clin Invest, 2000. **105**(10): p. 1419-27.
250. Farinas, J. and A.S. Verkman, *Cell volume and plasma membrane osmotic water permeability in epithelial cell layers measured by interferometry.* Biophys J, 1996. **71**(6): p. 3511-22.
251. Lavelle, J.P., et al., *Low permeabilities of MDCK cell monolayers: a model barrier epithelium.* Am J Physiol, 1997. **273**(1 Pt 2): p. F67-75.
252. Simmons, N.L., *Ion transport in 'tight' epithelial monolayers of MDCK cells.* J Membr Biol, 1981. **59**(2): p. 105-14.
253. Wyatt, T.P., et al., *Emergence of homeostatic epithelial packing and stress dissipation through divisions oriented along the long cell axis.* Proc Natl Acad Sci U S A, 2015. **112**(18): p. 5726-31.
254. Alt, S., P. Ganguly, and G. Salbreux, *Vertex models: from cell mechanics to tissue morphogenesis.* Philos Trans R Soc Lond B Biol Sci, 2017. **372**(1720).
255. Hannezo, E., J. Prost, and J.F. Joanny, *Theory of epithelial sheet morphology in three dimensions.* Proc Natl Acad Sci U S A, 2014. **111**(1): p. 27-32.

256. Salbreux, G., G. Charras, and E. Paluch, *Actin cortex mechanics and cellular morphogenesis.* Trends Cell Biol, 2012. **22**(10): p. 536-45.
257. Schwarz, U.S. and S.A. Safran, *Physics of adherent cells.* Reviews of Modern Physics, 2013. **85**(3): p. 1327-1381.
258. Loiseau, E., et al., *Shape remodeling and blebbing of active cytoskeletal vesicles.* Sci Adv, 2016. **2**(4): p. e1500465.
259. Murisic, N., et al., *From discrete to continuum models of three-dimensional deformations in epithelial sheets.* Biophys J, 2015. **109**(1): p. 154-63.
260. MATLAB, *version 9.1.0.441655 (R2016b)*. 2016, Natick, Massachusetts: The MathWorks Inc.
261. Hildebrand, S., et al., *The E-cadherin/AmotL2 complex organizes actin filaments required for epithelial hexagonal packing and blastocyst hatching.* Sci Rep, 2017. **7**(1): p. 9540.
262. Deglincerti, A., et al., *Self-organization of the in vitro attached human embryo.* Nature, 2016. **533**(7602): p. 251-4.
263. Otsuka, K. and C.M. Wayman, *Shape memory materials*. 1998, Cambridge: Cambridge University Press.
264. Burke, T.A., et al., *Homeostatic actin cytoskeleton networks are regulated by assembly factor competition for monomers.* Curr Biol, 2014. **24**(5): p. 579-85.
265. Turlier, H., et al., *Furrow constriction in animal cell cytokinesis.* Biophys J, 2014. **106**(1): p. 114-23.
266. Joanny, J.F., et al., *The actin cortex as an active wetting layer.* Eur Phys J E Soft Matter, 2013. **36**(5): p. 52.
267. Fritzsche, M., et al., *Actin kinetics shapes cortical network structure and mechanics.* Sci Adv, 2016. **2**(4): p. e1501337.
268. Malik-Garbi, M., et al., *Scaling behaviour in steady-state contracting actomyosin networks.* Nat Phys, 2019. **15**(5): p. 509-516.
269. Ennomani, H., et al., *Architecture and Connectivity Govern Actin Network Contractility.* Curr Biol, 2016. **26**(5): p. 616-26.
270. Jirásek, M. and Z.P. Bazant, *Inelastic analysis of structures*. 2002, Chichester, West Sussex, England ; New York, NY: Wiley. xxi, 734 p.
271. Koster, S., et al., *Intermediate filament mechanics in vitro and in the cell: from coiled coils to filaments, fibers and networks.* Curr Opin Cell Biol, 2015. **32**: p. 82-91.

272. Block, J., et al., *Nonlinear Loading-Rate-Dependent Force Response of Individual Vimentin Intermediate Filaments to Applied Strain.* Phys Rev Lett, 2017. **118**(4): p. 048101.

273. Herrmann, H., et al., *Intermediate filaments: from cell architecture to nanomechanics.* Nat Rev Mol Cell Biol, 2007. **8**(7): p. 562-73.

274. Sinha, B., et al., *Cells respond to mechanical stress by rapid disassembly of caveolae.* Cell, 2011. **144**(3): p. 402-13.

275. Raucher, D. and M.P. Sheetz, *Characteristics of a membrane reservoir buffering membrane tension.* Biophys J, 1999. **77**(4): p. 1992-2002.

276. Maitre, J.L. and C.P. Heisenberg, *Three functions of cadherins in cell adhesion.* Curr Biol, 2013. **23**(14): p. R626-33.

277. Hilbrant, M., et al., *The beetle amnion and serosa functionally interact as apposed epithelia.* Elife, 2016. **5**.

278. Martin, A.C., et al., *Integration of contractile forces during tissue invagination.* J Cell Biol, 2010. **188**(5): p. 735-49.

279. Cruz-Acuna, R., et al., *Synthetic hydrogels for human intestinal organoid generation and colonic wound repair.* Nat Cell Biol, 2017. **19**(11): p. 1326-1335.

280. Gjorevski, N., et al., *Designer matrices for intestinal stem cell and organoid culture.* Nature, 2016. **539**(7630): p. 560-564.

281. Clevers, H., *Modeling Development and Disease with Organoids.* Cell, 2016. **165**(7): p. 1586-1597.

282. Taub, M., *Tissue culture of epithelial cells*. 1985, New York: Plenum Press. xxii, 288 p.

283. Toyoshima, K., et al., *Conditions of cultivation required for the formation of hemicysts in vitro by rat bladder carcinoma R-4909.* Cancer Res, 1976. **36**(8): p. 2800-6.

284. Auersperg, N., *Histogenetic behavior of tumors. I. Morphologic variation in vitro and in vivo of two related human carcinoma cell lines.* J Natl Cancer Inst, 1969. **43**(1): p. 151-73.

285. Cameron, G., *Secretory activity of the chorioid plexus in tissue culture.* Anat Rec, 1953. **117**(1): p. 115-25.

286. McCombs, W.B., 3rd, et al., *Morphologic and immunologic studies of a human colon tumor cell line (SW-48).* Cancer, 1976. **38**(6): p. 2316-27.

287. Grasset, E., et al., *Epithelial properties of human colonic carcinoma cell line Caco-2: electrical parameters.* Am J Physiol, 1984. **247**(3 Pt 1): p. C260-7.

288. Mullin, J.M., et al., *Sugar transport in the LLC-PK1 renal epithelial cell line: similarity to mammalian kidney and the influence of cell density.* J Cell Physiol, 1980. **104**(3): p. 375-89.

289. Rizzoli, R. and J.P. Bonjour, *Effect of dexamethasone on parathyroid hormone stimulation of cyclic AMP in an opossum kidney cell line.* J Cell Physiol, 1987. **132**(3): p. 517-23.

290. Mason, R.J., et al., *Transepithelial transport by pulmonary alveolar type II cells in primary culture.* Proc Natl Acad Sci U S A, 1982. **79**(19): p. 6033-7.

291. McGrath, C.M., *Cell Organization and Responsiveness to Hormones in vitro: Genesis of Domes in Mammary Cell Cultures.* American Zoologist, 1975. **15**(2): p. 231-236.

292. Lever, J.E., *Cyclic AMP and inducers of mammalian cell differentiation stimulate dome formation in mammary and renal epithelial cell cultures, in: Hormones and Cell Culture, Book B*. Vol. 6. 1979, New York: Cold Spring Harbor Laboratory.

293. Birek, C., et al., *Dome formation by oral epithelia in vitro.* In Vitro, 1982. **18**(4): p. 382-92.

294. Huh, N., T. Takaoka, and H. Katsuta, *Establishment of epithelial cell lines from rat glandular stomachs.* Jpn J Exp Med, 1977. **47**(5): p. 413-24.

295. Arroyo, M., Walani, N., Torres-Sánchez, A. & Kaurin, D., *Onsager's variational principle in soft matter: introduction and application to the dynamics of adsorption of proteins onto fluid membranes*, in *The Role of Mechanics in the Study of Lipid Bilayers*. 2018, Springer, Cham. p. 287-332.

296. Bergert, M., et al., *Force transmission during adhesion-independent migration.* Nat Cell Biol, 2015. **17**(4): p. 524-9.

297. Clark, A.G., K. Dierkes, and E.K. Paluch, *Monitoring actin cortex thickness in live cells.* Biophys J, 2013. **105**(3): p. 570-80.

298. Style, R.W., et al., *Traction force microscopy in physics and biology.* Soft Matter, 2014. **10**(23): p. 4047-55.

299. Style, R.W., et al., *Surface tension and contact with soft elastic solids.* Nat Commun, 2013. **4**: p. 2728.

300. Mertz, A.F., et al., *Cadherin-based intercellular adhesions organize epithelial cell-matrix traction forces.* Proc Natl Acad Sci U S A, 2013. **110**(3): p. 842-7.
301. Vedula, S.R., et al., *Epithelial bridges maintain tissue integrity during collective cell migration.* Nat Mater, 2014. **13**(1): p. 87-96.
302. Long, R., et al., *Effects of gel thickness on microscopic indentation measurements of gel modulus.* Biophys J, 2011. **101**(3): p. 643-50.
303. Mertz, A.F., et al., *Scaling of traction forces with the size of cohesive cell colonies.* Phys Rev Lett, 2012. **108**(19): p. 198101.
304. Bergert, M., et al., *Confocal reference free traction force microscopy.* Nat Commun, 2016. **7**: p. 12814.
305. del Alamo, J.C., et al., *Three-dimensional quantification of cellular traction forces and mechanosensing of thin substrata by fourier traction force microscopy.* PLoS One, 2013. **8**(9): p. e69850.
306. Alvarez-Gonzalez, B., et al., *Three-dimensional balance of cortical tension and axial contractility enables fast amoeboid migration.* Biophys J, 2015. **108**(4): p. 821-32.
307. Bar-Kochba, E., et al., *A Fast Iterative Digital Volume Correlation Algorithm for Large Deformations.* Exp Mech, 2014. **55**(1): p. 261-274.
308. Yu, Y.S. and Y.P. Zhao, *Elastic deformation of soft membrane with finite thickness induced by a sessile liquid droplet.* J Colloid Interface Sci, 2009. **339**(2): p. 489-94.
309. Das, S., et al., *Elastic deformation due to tangential capillary forces.* Phys Fluids, 2011. **23**(7).
310. Lubarda, V.A., *Mechanics of a liquid drop deposited on a solid substrate.* Soft Matter, 2012. **8**(40).
311. Yu, Y.-s., *Substrate elastic deformation due to vertical component of liquid-vapor interfacial tension.* Appl Math Mech, 2012. **33**(9): p. 1095-1114.
312. Edelstein, A.D., et al., *Advanced methods of microscope control using muManager software.* J Biol Methods, 2014. **1**(2).
313. Colombelli, J., S.W. Grill, and E.H.K. Stelzer, *Ultraviolet diffraction limited nanosurgery of live biological tissues.* Rev Sci Instrum, 2004. **75**(2): p. 472-478.
314. Schindelin, J., et al., *Fiji: an open-source platform for biological-image analysis.* Nat Methods, 2012. **9**(7): p. 676-82.